NON-PLANAR WINGS IN NON-PLANAR GROUND EFFECT

Thesis by

Joseph Eugene Davis

In Partial Fulfillment of the Requirements
For the Degree of
Doctor of Philosophy

California Institute of Technology
Pasadena, California
1972
(Submitted September 17, 1971)

ACKNOWLEDGEMENTS

The inspiration for this attempt to develop methods for solving problems dealing with wings in non-planar ground effect was provided by Dr. Gordon L. Harris. Not only is the original conception of the ideas involved attributable to him, but the execution of these ideas were only possible with the aid of his guidance and encouragement.

The author also wishes to express his gratitude to Dr. Homer J. Stewart for his invaluable assistance and advice with regard to many critical analytical problems, and to Elizabeth Fox for her assistance in the preparation of the thesis in its present form.

ABSTRACT

A numerical method is developed for solving the problem of a wing in arbitrary non-planar ground effect. The linearized equations of unsteady motion for an arbitrary non-planar wing in non-planar ground effect are presented. Numerical calculations were made to determine all the aerodynamic characteristics and stability derivatives for various thin, uncambered planar and non-planar wings (including two wings connected in tandem) in planar and non-planar ground effect. These calculations were incorporated into the equations of unsteady motion to determine the dynamic stability characteristics of these wings in the various ground effect situations. Several wings were found to be longitudinally stable, but only in rare cases were they found to be laterally stable.

An experiment was conducted to compare some of the numerical calculations with reality. The agreement was reasonable.

TABLE OF CONTENTS

TABLE OF CONTENTS (Cont'd)

TABLE OF CONTENTS (Cont'd)

PAGE

TABLE OF CONTENTS (Cont'd)

LIST OF SYMBOLS

A_f = Aspect ratio of front wing

A_r = Aspect ratio of rear wing

b_f = Distance between the $\frac{1}{4}$ chord of the front wing and the c. g. of the vehicle

b_r = Distance between the $\frac{1}{4}$ chord of the rear wing and the c. g. of the vehicle

C_f = Chord length of front wing

C_r = Chord length of rear wing

C_{D_f} = Drag coefficient of front wing $= \dfrac{D_f}{\frac{1}{2}\rho U^2 S_f}$

C_{D_r} = Drag coefficient of rear wing $= \dfrac{D_r}{\frac{1}{2}\rho U^2 S_r}$

C_{L_f} = Lift coefficient of front wing $= \dfrac{L_f}{\frac{1}{2}\rho U^2 S_f}$

C_{L_r} = Lift coefficient of rear wing $= \dfrac{L_r}{\frac{1}{2}\rho U^2 S_r}$

$$(C_{\ell_f}, C_{M_f}, C_{N_f}) = \left(\frac{L_{M_f}}{\frac{1}{2}\rho U^2 S_f c_f}, \frac{M_f}{\frac{1}{2}\rho U^2 S_f c_f}, \frac{N_f}{\frac{1}{2}\rho U^2 S_f c_f}\right)$$

$$(C_{\ell_r}, C_{M_r}, C_{N_r}) = \left(\frac{L_{M_r}}{\frac{1}{2}\rho U^2 S_r c_r}, \frac{M_r}{\frac{1}{2}\rho U^2 S_r c_r}, \frac{N_r}{\frac{1}{2}\rho U^2 S_r c_r}\right)$$

$$(C_{\ell_{f_{L.E.}}}, C_{M_{f_{L.E.}}}, C_{N_{f_{L.E.}}}) = \left(\frac{L_{M_{f_{L.E.}}}}{\frac{1}{2}\rho U^2 S_f c_f}, \frac{M_{f_{L.E.}}}{\frac{1}{2}\rho U^2 S_r c_r}, \frac{N_{f_{L.E.}}}{\frac{1}{2}\rho U^2 S_f c_f}\right)$$

$$(C_{\ell_{r_{L.E.}}}, C_{M_{r_{L.E.}}}, C_{N_{r_{L.E.}}}) = \left(\frac{L_{M_{r_{L.E.}}}}{\frac{1}{2}\rho U^2 S_r c_r}, \frac{M_{r_{L.E.}}}{\frac{1}{2}\rho U^2 S_r c_r}, \frac{N_{r_{L.E.}}}{\frac{1}{2}\rho U^2 S_r c_r}\right)$$

$C_{y_f} = \left(\frac{Y_f}{\frac{1}{2}\rho U^2 S_f}\right)$

$C_{y_r} = \left(\frac{Y_r}{\frac{1}{2}\rho U^2 S_r}\right)$

D_f = Total drag of the front wing

D_r = Total drag of the rear wing

g = Acceleration due to gravity

h_f = Height of the $\frac{1}{4}$ chord of the front wing above the ground at any instant in time

h_{f_o} = Equilibrium height of the $\frac{1}{4}$ chord of the front wing above the ground

h_r = Height of the $\frac{1}{4}$ chord of the rear wing above the ground at any instant in time

h_{r_o} = Equilibrium height of the $\frac{1}{4}$ chord of the rear wing above the ground

i_f = Angle of incidence between the front wing and the reference line of the vehicle

i_r = Angle of incidence between the rear wing and the reference line of the vehicle

$i_{xx} = \frac{I_{xx}}{\frac{1}{2}\rho c_f^5}$

$i_{xz} = \dfrac{I_{xz}}{\frac{1}{2}\rho c_f^5}$

$i_{yy} = \dfrac{I_{yy}}{\frac{1}{2}\rho c_f^5}$

$i_{zz} = \dfrac{I_{zz}}{\frac{1}{2}\rho c_f^5}$

I_{xx} = Moment of inertia of the vehicle about the x-axis at the c. g. of the vehicle

I_{xz} = Product of inertia of the vehicle at the c. g. of the vehicle

I_{yy} = Moment of inertia of the vehicle about the y-axis at the c. g. of the vehicle

I_{zz} = Moment of inertia of the vehicle about the z-axis at the c. g. of the vehicle

ℓ_f = Distance between the c. p. of the front wing and the c. g. of the vehicle

ℓ_r = Distance between the c. p. of the rear wing and the c. g. of the vehicle

L_f = Lift due to the front wing

L_r = Lift due to the rear wing

(L, M, N) = Moment vector at the c. g. of the vehicle as measured in the coord. system attached to the vehicle and rotating with it

(L_{M_f}, M_f, N_f) = Instantaneous roll, pitch, and yaw moments about the vehicle c. g. due to the front wing as measured in the coord. system attached to the vehicle and rotating with it

$L_{M_r}, M_r, N_r)$ = Instantaneous roll, pitch, and yaw moments about the vehicle c. g. due to the rear wing as measured in the coord. system attached to the vehicle and rotating with it

$(L_{M_{f_{L.E.}}}, M_{f_{L.E.}}, N_{f_{L.E.}})$ = Instantaneous roll, pitch, and yaw moments due to the front wing taken about the leading edge of the front wing and measured in the coord. system attached to the vehicle and rotating with it

$(L_{M_{r_{L.E.}}}, M_{r_{L.E.}}, N_{r_{L.E.}})$ = Instantaneous roll, pitch, and yaw moments due to the rear wing taken about the leading edge of the rear wing and measured in the coord. system attached to the vehicle and rotating with it

m = Mass of the vehicle

(p, q, r) = Angular rate vector about the c. g. of the vehicle as measured in the undisturbed coord. system

S_f = Planform area of the front wing

S_r = Planform area of the rear wing

t = Time

$(U+u, v, w)$ = Velocity vector of the vehicle in the coord. system attached to the vehicle and rotating with it

U = Equilibrium forward speed of the vehicle

(x, y, z) = Position vector of the vehicle relative to $t = 0$ and with respect to the coord. system attached to the vehicle and rotating with it

(x_o, y_o, z_o) = Coordinates at time $t = 0$

(X, Y, Z) = Force vector acting on the vehicle referenced to the coordinate system attached to the vehicle and rotating with it

$x_{c.p._f}$ = The x-coordinate position of the center of pressure of the front wing measured relative to the x-coordinate position of the leading edge of the front wing

$x_{c.p._r}$ = The x-coordinate position of the center of pressure of the rear wing measured relative to the x-coordinate position of the leading edge of the rear wing

$(x_{L.E._f}, y_{L.E._f}, z_{L.E._f})$ = The vector position of the leading edge of the front wing measured relative to the origin at the vehicle c. g.

$(x_{L.E._r}, y_{L.E._r}, z_{L.E._r})$ = The vector position of the leading edge of the rear wing measured relative to the origin at the vehicle c. g.

Y_f = Lateral force due to the front wing measured in the coord. system attached to the vehicle and rotating with it

Y_r = Lateral force due to the rear wing measured in the coord. system attached to the vehicle and rotating with it

α_{f_o} = Undisturbed angle of attack of front wing

α_f = Instantaneous angle of attack of the front wing

α_r = Instantaneous angle of attack of the rear wing

β_f = Angle between the x-axis attached to the vehicle and the instantaneous wind direction measured at the front Wing = sideslip angle of front wing

β_r = Angle between the x-axis attached to the vehicle and the instantaneous wind direction measured at the rear wing = sideslip angle of rear wing

δ = $\int_0^t \psi(\tau)d\tau$

ε = Downwash angle at the rear wing induced by the presence of the front wing

ζ = $\int_0^t \phi(\tau)d\tau$

θ_o = Angle between the gravity axis and the unperturbed z-axis of the coordinate system attached to the vehicle and rotating with it

θ = Perturbation in the pitch angle measured as the angle between the instantaneous z-axis attached to the vehicle and rotating with it during longitudinal motion and the undisturbed z-axis

κ = $\int_0^t \theta(\tau)d\tau$

λ_i = Roots of the characteristic eqn. of the longitudinal or lateral eqns. of unsteady motion

μ = $\frac{m}{\frac{1}{2}\rho c_f^3}$

ρ = Density of the fluid in which the vehicle is traveling

$\Delta\tau$ = Time taken for the vehicle to travel a distance $l_f + l_r$

ϕ = Perturbation in roll angle measured as the angle between the instantaneous z-axis attached to the vehicle and rotating with it during lateral motion and the undisturbed z-axis

ψ = Perturbation in yaw angle measured as the angle between the instantaneous x-axis attached to the vehicle and rotating with it during lateral motion, and the undisturbed x-axis

$(\dot{\ })$ = $\frac{d}{dt}(\ )$

LIST OF FIGURES

LIST OF TABLES

INTRODUCTION

The search for new high-speed ground transportation water and rough terrain vehicles has spread in many directions. One of these directions involves the use of aerodynamic lift to support and stabilize a high-speed vehicle above a planar or non-planar (regular or irregular) ground surface. The ram wing and the terrafoil are the most popular names associated with this mode of transportation. A ram wing can be described as a vehicle which is geometrically similar to a large low-aspect-ratio airfoil flying close to the ground and being subject to aerodynamic ground effects. Various ram wing configurations are shown in figure 1. A detailed description of a terrafoil vehicle is presented in reference 1. In general, it can be described as a tandem winged vehicle subject to close ground effect and which aerodynamically interacts with the surface or guideway to achieve static and dynamic stability. Various terrafoil configurations are shown in figure 2.

The ram wing and terrafoil concepts for multi-terrain travel have several advantages over other proposed guided and multi-terrain vehicles, such as the air-cushion vehicle. Among these advantages are: 1) the utilization of ground augmented dynamic lift at high speeds, 2) the reduction in induced aerodynamic drag due to the presence of ground effect, 3) the reduction of wave and spray drag over water since these vehicles will in general (and particularly at high speeds) fly appreciably higher than the corresponding air cushion vehicle, 4) the elimination of momentum or sink drag, which is the equivalent of induced drag for a wing, 5) the capability of being integrated with a captured air-bubble lift augmentation system, and 6) the capability for negotiating drastic changes in height above the ground to facilitate travel over very rough terrain or for obstacle avoidance.

There have been, however, some major difficulties which have held back the development of these vehicles for use in high-speed surface transportation. One of these difficulties has been the absence of any analytical or numerical methods for solving the problem of the completely arbitrary non-planar wing flying in the presence of any arbitrary non-planar ground situation. Another difficulty stems from the fact that there has been a lack of investigations into the static and dynamic stability characteristics of three-dimensional wings in arbitrary ground effect.

It is therefore the purpose of this investigation to develop a suitable numerical method for solving the problem of completely arbitrary wings flying in the close proximity to any arbitrary planar or non-planar ground, and to present the linearized equations of unsteady motion for non-planar wings in non-planar ground effect. Chapter I states the analytical problem, reviews the previous attempts at solutions for wings in ground effect and introduces the generalities of the present solution technique. In Chapter II the aerodynamic analysis using this solution technique is presented and applied to two and then three-dimensional problems, and compared with other solution techniques. Included in this chapter are the numerical results involving the aerodynamic characteristics of various planar and non-planar wings in planar and non-planar ground effect. Chapter

III is concerned with the development of the linearized equations of unsteady motion (longitudinal and lateral) for arbitrary wings in arbitrary ground effect. Solutions to these equations are presented for most of the wings and ground effect situations discussed in Chapter II. Finally, Chapter IV presents an experimental investigation of a non-planar wing in planar and non-planar ground effect and comparisons are made with the numerical solution to similar problems.

CHAPTER I

A. Statement of the Analytical Problem

1. Principal Assumptions

Before an attempt can be made to consider the analytical problem, it is helpful to discuss some of the basic underlying assumptions with regard to the flow field around a wing in ground effect. First, it is assumed that the flow field about all the wings and ground planes investigated satisfy Laplace's equation. That is,

$$\nabla^2 \varphi = 0 \qquad (1)$$

where φ is the velocity potential. Second, it is assumed that the Kutta condition is satisfied at the trailing edge of all wings investigated. That is, it is assumed that the velocity is continuous at the trailing edge of these wings. With these assumptions in mind, the remaining boundary conditions on the flow field can now be written.

2. Boundary Conditions

a. Boundary Condition on the Wing

We wish to write down the boundary condition on an arbitrary wing surface that satisfies the condition that the fluid flow is tangent to the wing surface at the wing surface. The unit normal vector to the wing surface is

$$\bar{n}_w = n_{w_1}\bar{i} + n_{w_2}\bar{j} + n_{w_3}\bar{k}$$

The velocity at any point in the flow field is

$$\bar{V} = (U_\infty + u)\bar{i} + (V_\infty + v)\bar{j} + (W_\infty + w)\bar{k}$$

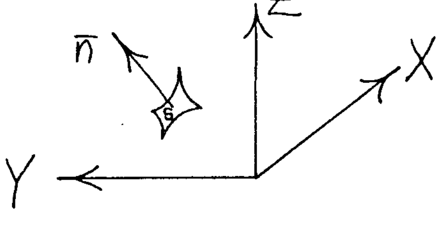

where $\overline{V}_\infty = (U_\infty, V_\infty, W_\infty)$ = External freestream velocity accounting for rigid body motion in translation and rotation. This also accounts for the velocity induced by other objects in the flow field whose pressure distribution is already known.

$\overline{V} = (u, v, w)$ = Velocity induced by the lifting surface and the velocity induced by any planar or non-planar ground.

The wing boundary condition is satisfied if

$$\overline{V} \cdot \overline{n}_w = 0$$

b. Boundary Condition on the Ground

The boundary condition on an arbitrary non-planar ground plane must satisfy the condition that the fluid flow is tangent to the ground on the ground surface. The unit normal vector to the ground surface is

$$\overline{n}_g = n_{g_1} \overline{i} + n_{g_2} \overline{j} + n_{g_3} \overline{k}$$

The velocity at any point in the flow field is

$$\overline{V} = u\overline{i} + v\overline{j} + w\overline{k}$$

where $\overline{V}$ is defined as above. However, $\overline{V}$ can also be split into its two components; that is, the velocity induced by the lifting surface and the velocity induced by the ground. Hence,

$$\bar{V} = \bar{V}_w + \bar{V}_g = (u_w + u_g)\bar{i} + (v_w + v_g)\bar{j} + (w_w + w_g)\bar{k}$$

Now, the ground boundary condition is satisfied if

$$\bar{V} \cdot \bar{n}_g = 0$$

B. Analytical Solutions

Although, in general, it is not possible to solve, in closed form, the problem of an arbitrary non-planar wing in non-planar ground effect, it is useful to review the results of those special cases where analytical solutions have been presented.

1. Analytic Solutions in Two Dimensions

The first "exact" solution dealing with two-dimensional wings in potential flow was that given by Tomotika et al. (ref. 2) in 1933 for a flat wing. The solution was arrived at through the conformal transformation of a flat wing and ground plane into the outer and inner boundaries, respectively, of an annular region in the complex plane. The flow in this annular region is known, hence the pressures on the annular region were calculated and transformed back to the coordinate system of the flat plate with ground plane, and the lift was then determined. In general, the results showed that the increase in lift on a flat two-dimensional wing in ground effect decreases as the angle of attack is made larger. Tomotika later extended his solution to include all Joukowski-type airfoils.

A more recent analytical solution for the two-dimensional wing in ground effect was presented by Widnall and Barrows (ref. 19) in 1969 using the method of matched asymptotic expansions. In general, the solution for the flow in the region above the wing was matched to the solutions at the leading and trailing edges and to the channel flow solution beneath the wing. Results obtained by this method were fairly accurate for height to chord ratios less than 0.5.

Widnall later extended this solution to the case of a sinusoidal ground plane (ref. 14).

2. Analytic Solutions in Three Dimensions

Using the method of matched asymptotic expansions, Widnall and Barrows (refs. 14 and 19) have presented approximate analytical solutions for the case of an optimally loaded flat elliptical wing with a straight trailing edge in planar ground effect and in the presence of a ground plane with sinusoidal bumps of small amplitude. In addition, they have presented approximate solutions for a nearly optimally-loaded wing in a tube and for a ram wing in a rectangular shaped trough where the flow is nearly two-dimensional. All of these solutions are, of course, for very special cases and, in addition, are valid for certain limited regions of aspect ratio and ground clearance.

There have been other investigations into the problem of a wing in a fully confined space such as a tube or a wind tunnel, but it is expedient to limit the present discussion to wings in semi-confined spaces.

C. Numerical Solution Techniques

1. Introduction

Since it is essentially impossible to analytically solve the flow field around the arbitrary wing in the presence of an arbitrarily non-planar ground, it is essential to make use of numerical techniques in order to solve the average problem.

There are a multitude of satisfactory numerical techniques available for representing and solving potential flow problems involving wings. These techniques usually involve the use of vortex distributions, source/sink distributions, doublet distributions, or a combination of these distributions to represent the presence of a wing in a flow field.

One of the simplest and most direct methods of representing a wing is the vortex-lattice method. This method consists of subdividing the upper and lower surface of a wing into quadrilateral patches. A horseshoe vortex is placed along the line one-fourth the length of the patch from the front of the patch. The flow tangency boundary condition on the wing surface is satisfied at the midpoint of the line which is three-fourths the length of the patch from the front of the patch. These patches are distributed in the chordwise and spanwise directions. The strengths of the individual vortices are determined by applying the wing boundary condition at as many points on the wing surface as there are vortices. A system of simultaneous equations is then solved to determine the horseshoe-vortex strength. Although the Kutta condition is not explicitly accounted for in this method, numerical results indicate that it is satisfied nonetheless. One of the features of this method is that it eliminates the need for spanwise and chordwise loading functions. The origin of the vortex-lattice method is usually attributed to Falkner (ref. 20). Since its inception, it has been used by many investigators, including most recently Giesing (ref. 21). The two-dimensional special case of this method has been rigorously investigated by James (ref. 22) and has proven to be remarkably accurate for two-dimensional airfoils.

Another successful, although more complicated, method is that used by Watkins et al. (ref. 4). This method numerically solves the integral equation relating the lift and downwash distributions for thin wings in subsonic flow. The unknown lift distribution is represented by the product of chordwise and spanwise modes of lift, each given an unknown weighting factor. The relation between the downwash and the lift distribution is then applied to as many points as assumed modes of lift. This gives a set of simultaneous algebraic equations to solve for the weighting factors. The aerodynamic coefficients are then determined by numerically integrating the pressure distribution over the wing surface. Saunders (ref. 5) has used a modification of this method to numerically compute the aerodynamic coefficients of some thin wings in planar ground effect.

Previous to the present investigation, the only method used to represent a ground plane for use in calculations of wings in ground effect, was the imaging method. It consists of placing an identical wing in mirror image fashion on the opposite side of the plane designated as the ground plane. In this way, the boundary condition on the ground surface is automatically satisfied because the equal and opposite flow velocities exactly cancel at the plane designated as the ground plane. Kohlman (ref. 24) used the imaging method in conjunction with a discrete vortex digital computer program to determine the ground effect on wings of arbitrary planform. Saunders (ref. 5) also used the imaging method and the kernel function wing representation of Watkins (ref. 4) to determine the ground effect on some thin flat wings as well as thin non-planar wings with sweep and taper ratio. Most recently, Kalman (ref. 23) used this method with the vortex-lattice method to compute the ground effect on thin flat rectangular wings of various aspect ratio. The results obtained by all three methods seem to be in general agreement with each other as well as with experimental data.

However, there have been no investigations conducted that have considered the problem of the arbitrary non-planar ground. All numerical investigations have only considered the case of wings in planar ground effect. The reason for this is obvious; the imaging method cannot be extended to the arbitrary non-planar ground problem. Therefore, if any solutions are to be obtained for the problem of an arbitrary wing in arbitrary non-planar ground effect, they can only be obtained by developing a new method for representing ground interference.

2. The Present Technique — Generalities

The main considerations involved in choosing the numerical technique used in this investigation were simplicity, flexibility, and cost minimization. Therefore, the method chosen for the simulation of the presence of a wing in the flow field was the vortex-lattice method. This method can be used for any arbitrary wing shape, since the Kutta condition is automatically satisfied. The method also generates the proper singularity at the leading edge automatically. In addition, the simple calculations involved in satisfying the boundary condition on the wing, which avoided any problems with singularities, were very attractive.

However, a new method had to be developed for representing the presence of the ground in the flow field. This method had to be equivalent to the method of images for two-dimensional and three-dimensional planar ground problems, but had to have the capability of being extended to three-dimensional non-planar ground problems. Therefore, it was decided to represent the presence of the ground in the flow field by a distribution of mass sources and sinks. The distribution of sources and sinks were placed on the ground surface and the boundary condition prescribing that there be no normal flow through the ground was satisfied at a discrete number of points. The strengths of the sources or sinks at these discrete points as well as the strengths of the horseshoe vortices representing the wing were then determined by solving a set of simultaneous equations developed by satisfying the boundary conditions on the wing and ground. A rigorous mathematical development of this technique is shown later in this section. There were many problems associated with this technique. Among them was the need to truncate the ground plane rather than extending it to $\pm \infty$. Another problem evolved in the choice of locations on the ground plane for which the boundary condition on the ground was to be satisfied. This problem was especially critical in the region beneath the wing and in regions near any corners in the ground plane. Additional problems also arose due to the singular nature of the source strength directly at the corners on the ground plane. The details as well as the resolution of these and other problems involved with this method are discussed in section II-B, part 3.

An entirely different technique for representing a non-planar ground plane was also developed. This technique was actually an extension of the principles of images and is thus referred to as multiple imaging. It involves the placement of more than one image of a given wing in the flow field to represent the effect of a non-planar ground. This method, however, was only useful for solving problems where the non-planar ground consisted of two straight infinite ground planes intersecting each other at a certain angle. However, the development of this technique was essential in order to check some of the results of the source/sink distribution technique. The mathematical treatment of this technique and those mentioned previously will now be presented. First, the mathematical treatment of the source/sink distribution technique in conjunction with the vortex-lattice method as applied to two-dimensional flows will be discussed. Then the imaging method in conjunction with the vortex-lattice method as applied to two-dimensional flows will be shown. The mathematical treatment of these methods will then be applied to three-dimensional planar ground problems, and finally, the treatment of the former method and the multiple imaging method will be applied to three-dimensional non-planar ground problems.

CHAPTER II

A. Application to Two-Dimensional Problems:

The coordinate system for the two-dimensional flow of a wing in ground effect using the source/sink distribution method in conjunction with the two-dimensional vortex-lattice method (often called the Weissinger approximation) is shown in figure 3.

In two dimensions the vortex-lattice method of representing the wing consists of subdividing the wing into equal chordwise segments. A two-dimensional point vortex is placed in each segment at a point one-fourth the length of the segment from the front of the segment. The flow tangency boundary condition on the wing surface is satisfied at one point in each segment. This point is at a distance of three-fourths the length of the segment from the front of the segment. This situation is depicted in detail in figure 3. It is of interest to note here that James (ref. 22) has rigorously proved the validity of this method in two dimensions for a wing in an unbounded fluid. In fact, in an unbounded fluid, he has shown that the correct value of the lift and moment is obtained regardless of the number of segments into which the wing is subdivided so long as the downwash is everywhere bounded on the wing. In ground effect, this last conclusion does not hold true. However, the correct value for the lift and moment calculated by this method for a wing in ground effect is asymptotically approached as the number of subdivisions is increased. The closer the wing approaches the ground, the more subdivisions are required for an accurate answer. This fact has been verified by numerical calculations which are explained and expressed in detail in part C-1. We will now develop an expression for the lift on a two-dimensional wing in ground effect using the source/sink distribution method in conjunction with the vortex-lattice method.

Nomenclature:

C = length of chord of airfoil

$\gamma(\mu)$ = circulation per unit length of vortex distribution

$\eta(\xi)$ = efflux rate per unit length of line source

$P(x,y)$ = field point at which we wish to evaluate the velocity induced by the line source and the vortex distribution

$\gamma d\mu$ = elemental vortex with circulation $\gamma d\mu$

$\eta d\xi$ = elemental source of strength $\eta d\xi$

μ = distance along X-axis from origin to $\gamma d\mu$

$\sigma(\mu)$ = distance along Y-axis from origin to $\gamma d\mu$

ξ = distance along X-axis from origin to $\eta d\xi$

R = distance from incremental source to $P(x,y)$

β = angle between R and X-axis

U_∞ = velocity of freestream

α = local angle of vortex distribution to freestream

1. Source Distribution Method

The elemental stream function due to the line source is,

$$d\psi_s = -\frac{\eta\, d\xi\, \beta}{2\pi}$$

The complete stream function resulting from the entire line source extending from $-\infty$ to $+\infty$ is

$$\psi_s = -\int_{-\infty}^{\infty} \frac{\eta}{2\pi}\beta\, d\xi .$$

or

$$\psi_s = -\int_{-\infty}^{\infty} \frac{\gamma}{2\pi} \tan^{-1}\left(\frac{y}{x-\xi}\right) d\xi$$

The elemental stream function due to the vortex distribution is,

$$d\psi_v = \frac{\gamma d\mu}{2\pi} \ln\left[(x-\mu)^2 + (y-\sigma(\mu))^2\right]^{1/2}$$

The complete stream function resulting from the entire vortex distribution extending from $\mu = 0$ to $\mu = C$ is,

$$\psi_v = \int_0^C \frac{\gamma d\mu}{2\pi} \ln\left[(x-\mu)^2 + (y-\sigma(\mu))^2\right]^{1/2}$$

We can relate σ to μ in the following way:

$$\sigma = h + f(\mu) \quad \text{on the airfoil}$$

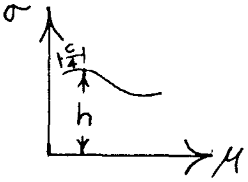

The stream function for the freestream is,

$$\psi_F = U_\infty y$$

The total stream function from all components is then

$$\psi_T = \psi_s + \psi_v + \psi_F$$

$$\psi_T = -\int_{-\infty}^{\infty} \frac{\gamma}{2\pi} \tan^{-1}\left(\frac{y}{x-\xi}\right) d\xi + \int_0^C \frac{\gamma d\mu}{2\pi} \ln\left[(x-\mu)^2 + (y-\sigma)^2\right]^{1/2} + U_\infty y$$

The following boundary conditions must be met:

1) There is no flow through the ground. That is,

$$\left.\frac{\partial \psi_T}{\partial x}\right|_{y=0} = 0$$

2) On the airfoil surface the flow must be tangential to the surface. That is,

$$-\alpha(x,y) = -\frac{v}{U_\infty + u} = \frac{\dfrac{\partial \psi_T}{\partial x}}{\dfrac{\partial \psi_T}{\partial y}} \quad \text{on the airfoil surface}$$

Conforming to the first boundary condition we find the following:

$$\frac{\partial \psi_T}{\partial x} = \frac{1}{2\pi}\int_{-\infty}^{\infty} \frac{\eta y \, d\xi}{[(x-\xi)^2 + y^2]} + \frac{1}{2\pi}\int_0^c \frac{\gamma (x-\mu)\, d\mu}{[(x-\mu)^2 + (y-\sigma)^2]}$$

As $y \to 0$, it can be shown that the integral on the left approaches

$$\frac{1}{2}\int_{-\infty}^{\infty} \eta \, \delta(x-\xi)\, d\xi = \frac{\eta(x)}{2}$$

Hence

$$\left.\frac{\partial \psi_T}{\partial x}\right|_{y=0} = \frac{\eta(x)}{2} + \frac{1}{2\pi}\int_0^c \frac{\gamma (x-\mu)\, d\mu}{[(x-\mu)^2 + \sigma^2]} = 0$$

Therefore we have an expression for $\eta(x)$, namely,

$$\eta(x) = -\frac{1}{\pi}\int_0^c \frac{\gamma(x-\mu)\,d\mu}{[(x-\mu)^2+\sigma^2]}$$

Hence

$$\psi_T = \frac{1}{2\pi^2}\int_{-\infty}^{\infty}\left(\int_0^c \frac{\gamma(\xi-\mu)\,d\mu}{[(\xi-\mu)^2+\sigma^2]}\right)\tan^{-1}\left(\frac{y}{x-\xi}\right)d\xi + \int_0^c \frac{\gamma\,d\mu}{2\pi}\ln\left[(x-\mu)^2+(y-\sigma)^2\right]^{1/2} + U_\infty y$$

In order to determine the vortex strength distribution, we must now satisfy the boundary condition on the wing surface. At this point we will discretize the wing surface in the manner prescribed by the vortex-lattice method. Hence the boundary condition on the wing surface in discrete form is expressed as,

$$\frac{v(x_j,y_j)}{U_\infty + u(x_j,y_j)} = -\alpha(x_j,y_j) \quad \text{for each j}$$

where the coordinates x_j, y_j are the points at which the boundary condition is satisfied on the wing surface. Hence

$$v(x_j,y_j) + \alpha(x_j,y_j)\,u(x_j,y_j) = -\alpha(x_j,y_j)\,U_\infty$$

Shortening the notation, so that x_j, y_j is replaced by j, and expressing the velocity in terms of its components, we have

$$\sum_i v_i(j) + v'(j) + \alpha(j)\left[\sum u_i(j) + u'(j)\right] = -\alpha(j)\,U_\infty$$

The subscript i refers to the velocity induced by the i^{th} discrete point vortex on the j^{th} matching point. Also $v'(j)$ and $u'(j)$ are the contributions to the velocity induced at the matching point by the infinite line source. They can be expressed as,

$$v'(j) = \frac{1}{2\pi^2}\int_{-\infty}^{\infty}\left(\sum_i \frac{\gamma_i(\xi-\mu_i)\Delta\mu_i}{(\xi-\mu_i)^2+\sigma_i^2}\right)\frac{y_j\,d\xi}{[(x-\xi)^2+y_j^2]}$$

$$u'(j) = \frac{1}{2\pi^2}\int_{-\infty}^{\infty}\left(\sum_i \frac{\gamma_i(\xi-\mu_i)\Delta\mu_i}{(\xi-\mu_i)^2+\sigma_i^2}\right)\frac{(x_j-\xi)\,d\xi}{[(x_j-\xi)^2+y_j^2]}$$

Changing the order of integration and summation, we can express $u'(j)$ and $v'(j)$ in terms of a shortened notation. That is,

$$u'(j) = \sum_i u_i'(j) \qquad ; \qquad v'(j) = \sum_i v_i'(j)$$

where the definitions of $u_i'(j)$ and $v_i'(j)$ are obvious by reference to the two previous equations.

Hence, we can rewrite the boundary condition on the wing as,

$$\sum_i \left[v_i(j) + v_i'(j) + \alpha(j)\left(u_i(j) + u_i'(j)\right)\right] = -\alpha(j)\,U_\infty$$

Since the velocity induced by each vortex is proportional to the circulation γ_i of that vortex, we can define

$$\tilde{v}_i(j) = \frac{1}{\gamma_i}v_i(j) \qquad ; \qquad \tilde{u}_i(j) = \frac{1}{\gamma_i}u_i(j)$$

$$\tilde{v}_i'(j) = \frac{1}{\gamma_i}v_i'(j) \qquad ; \qquad \tilde{u}_i'(j) = \frac{1}{\gamma_i}u_i'(j)$$

and we can rewrite the equation as

$$\sum_i \gamma_i \left[\tilde{v}_i(j) + \tilde{v}_i'(j) + \alpha(j)\left(\tilde{u}_i(j) + \tilde{u}_i'(j)\right)\right] = -\alpha(j)\, U_\infty$$

This gives us a j^{th} order set of simultaneous linear algebraic equations to solve for the discrete point vortex strengths γ_i .

Assuming that this can be done, we can calculate the lift as,

$$L = \sum_k \rho\left(U_\infty + u(k)\right) \gamma_k \cos(\alpha(k))$$

where $\quad u(k) = \sum_i u_i(k) \quad + u'(k)$

and k refers to the velocity induced at the k^{th} discrete vortex by all other vortices and the line source. The moment is expressed as,

$$M = \sum_k \rho\left(U_\infty + u(k)\right) \gamma_k \left[x_k \cos(\alpha(k)) - y_k \sin(\alpha(k))\right]$$

We will now develop expressions for the lift and moment for the same problem using the method of images in conjunction with the vortex-lattice technique.

2. Image Method

The complete stream function resulting from the entire vortex distribution of both the real wing and the image wing and from the freestream is,

$$\psi_T = \int_0^c \frac{\gamma}{2\pi}\left[\ln\left[(x-\mu)^2 + (y-\sigma(\mu))^2\right]^{1/2} + \ln\left[(x-\mu)^2 + (y+\sigma(\mu))\right]^{1/2}\right] d\mu$$

$$+\, U_\infty y$$

The method of images automatically satisfies the boundary condition of no normal flow through the ground; hence, we have only to satisfy the boundary condition on the wing. That is,

$$v(x_j, y_j) + \alpha(x_j, y_j)\, u(x_j, y_j) = -\alpha(x_j, y_j)\, U_\infty$$

In a manner similar to that of the source distribution method, we now write

$$\sum_i \left[v_i(j) + v_i''(j) + \alpha(j)\left(u_i(j) + u_i''(j)\right)\right] = -\alpha(j)\, U_\infty$$

where
$$u_i''(j) = \frac{1}{2\pi} \sum_i \frac{\gamma_i (y_i+\sigma)\,\Delta\mu}{\left[(x_j-\mu)^2 + (y_j+\sigma)^2\right]}$$

$$v_i''(j) = \frac{1}{2\pi} \sum_i \frac{\gamma_i (x_j-\mu)\,\Delta\mu}{\left[(x_j-\mu)^2 + (y_j+\sigma)^2\right]}$$

We then follow the same procedure as with the source distribution method and arrive at similar expressions for the lift and moment. However,
$$u(k) = \sum_i u_i(k) + u''(k)$$

3. Equivalence of the Source Method and the Image Methods

In order to prove that the source distribution method is exactly equivalent to the image method for representing the presence of the ground in two dimensions, it is only necessary to prove that the velocity induced by a single point vortex together with an infinite line source, whose source strength distribution satisfies the condition that there is no normal flow through it, is the same as the velocity induced by a point vortex and its image. This would be sufficient, since any arbitrary airfoil can be expressed in terms of a point vortex distribution along its upper and lower surface.

This proof is found in Appendix A. The definite integral over the source distribution is evaluated by complex variable contour integration. The velocity induced by this source distribution is shown to be exactly the velocity induced by a vortex image.

B. Application to Three-Dimensional Problems

1. Source Distribution Method

The coordinate system for the three-dimensional flow of a wing in planar or non-planar ground effect using the source distribution method in conjunction with the three-dimensional vortex-lattice method is shown in figure 4.

a. Wing Representation

In three dimensions the vortex-lattice method of representing the wing consists of subdividing the wing into spanwise and chordwise segments. A three-dimensional horseshoe point vortex is placed in each segment so that the bound portion of the horseshoe vortex lies along the line joining the one-quarter chord points of the chordwise edges of each segment. This situation is illustrated in figure 4. The flow tangency boundary condition on the wing surface is satisfied at the midpoint of the line joining the three-quarter chord points of the chordwise edges of each segment. There are some restrictions on the shape of a given segment. A segment can be a quadrilateral or a triangle. If it is a quadrilateral, the two chordwise edges must be parallel to the plane defined by the freestream direction and the unit normal to the wing surface at that chordwise edge. If it is a triangle (a degenerate case of the quadrilateral) the single chordwise edge must be parallel to this plane. This is illustrated in figure 5.

The accuracy associated with representing wings in this manner has been found to be excellent. For a more detailed discussion of the method as well as many comparisons with experimental data, the reader is referred to Kalman (ref. 23). In fact, a comparison of this method and the method of Saunders for calculating the forces on thin flat rectangular wings in ground effect and thin wings with dihedral in ground effect is presented in the reference. The agreement was excellent.

We will now develop expressions for the forces and moments on an arbitrary three-dimensional wing in arbitrary planar or non-planar ground effect using the source distribution method in conjunction with the vortex-lattice method.

b. Source Distribution Ground Representation

Theoretical Development

Nomenclature:

$P(x, y, z)$ = field point at which we wish to evaluate the total potential

(ξ, μ, ζ) = coordinates of a differential element of the source sheet ground plane

$\eta(\xi, \mu)$ = efflux rate per unit area of source sheet

$\eta \, d\xi \, d\mu$ = elemental 3-D source of strength $\eta \, d\xi \, d\mu$

R = distance from incremental source to $P(x, y)$

(x_i, y_i, z_i) = coordinates of 1/4-chord point of i^{th} horseshoe vortex patch

(x_m, y_m, z_m) = coordinates of 3/4-chord point of i^{th} horseshoe vortex patch

Γ_i = circulation of horseshoe vortex

φ_T = total potential induced by freestream, source sheet ground plane and system of horseshoe vortices

φ_s = potential due to the presence of the source sheet ground plane

φ_{s_n} = potential due to the n^{th} segment of the source sheet ground plane where the infinite source sheet is divided into several spanwise segments

$\varphi_{F.S.}$ = potential due to presence of the freestream

$\varphi_{H.V.}$ = potential due to the system of horseshoe vortices

$\bar{\nabla}\varphi_T$ = velocity at any point in the flow field

Potential at any Point P in the Flow Field:

The velocity potential due to the presence of the source sheet ground plane of infinitesimal thickness is:

$$\varphi_s = -\frac{1}{4\pi}\int_{-\infty}^{\infty}\int_{-\infty}^{\infty}\frac{\gamma(\xi,\mu)\,d\xi\,d\mu}{\sqrt{(x-\xi)^2+(y-\mu)^2+(z-\zeta)^2}}$$

Assume that the shape of the source sheet does not vary in the X-direction, but does vary in the Y-direction.

We can write the ζ-coordinate of any incremental source in the source sheet in terms of the μ-coordinate.

Let $\zeta = f(\mu)$ where f is known and is at least piecewise continuous.

Hence, we can write φ_s as,

$$\varphi_s = -\frac{1}{4\pi}\int_{-\infty}^{\infty}\int_{-\infty}^{\infty}\frac{\gamma(\xi,\mu)\,d\xi\,d\mu}{\sqrt{(x-\xi)^2+(y-\mu)^2+(z-f(\mu))^2}}$$

Furthermore, if we divide the source sheet ground plane into several spanwise segments, say r segments, such that for any given segment,

$$\varphi_{s_n} = -\frac{1}{4\pi}\int_{-\infty}^{\infty}\int_{\mu_{n_l}}^{\mu_{n_u}}\frac{\gamma(\xi,\mu)\,d\xi\,d\mu}{\sqrt{(x-\xi)^2+(y-\mu)^2+(z-f(\mu))^2}}$$

Then $\varphi_s = \sum_{n=1}^{r} \varphi_{s_n}$

We now add the potential due to the system of discrete horseshoe vortices and the freestream. For the present we shall refer to these potentials as $\varphi_{H.V.}$ and $\varphi_{F.S.}$.

Hence, the total potential for the flow field is,

$$\varphi_T = \sum_{n=1}^{r} \varphi_{s_n} + \varphi_{H.V.} + \varphi_{F.S.}$$

Boundary Condition of No Flow Through the Ground:

In order to simulate the presence of a ground plane by the source sheet, we must satisfy the condition that there can be no flow through the ground. That is,

$\bar{V}\cdot\bar{n}_g = 0$ on the ground plane

In other words,

$$\left(\bar{\nabla}\varphi_T\Big|_{z=f(y)}\right)\cdot\bar{n}_g = 0 \qquad \bar{\nabla} = \frac{\partial}{\partial x}\bar{i} + \frac{\partial}{\partial y}\bar{j} + \frac{\partial}{\partial z}\bar{k}$$

where

$$\bar{n}_g = n_{g_1}\bar{i} + n_{g_2}\bar{j} + n_{g_3}\bar{k}$$

at the point where the boundary condition is being satisfied. We can rewrite $\bar{\nabla}\varphi_T$ as

$$\bar{\nabla}\varphi_T = \sum_{n=1}^{r}\bar{\nabla}\varphi_{s_n} + \bar{\nabla}\varphi_{H.V.} + \bar{\nabla}\varphi_{F.S.}$$

A detailed derivation of the velocity induced by an arbitrary horseshoe vortex is given in Appendix C. We must now calculate $\bar{\nabla}\varphi_{s_n}$. But first, let us subdivide the ground source distribution into segments so that any arbitrary non-planar ground plane can be represented by a finite set of straight segments placed at the appropriate position in the ground plane to approximate the desired ground shape. However, for the purposes of the configurations considered in this investigation we need only to generalize the non-planar ground plane to account for non-planarity in the y-z plane. Hence all ground planes considered in this investigation will not have any variation in the x-direction. In other words, the normal to the ground plane can be expressed as $\bar{n}_g = n_{g_2}\bar{j} + n_{g_3}\bar{k}$

Consider the velocity induced at a point on a given segment by the three-dimensional source distribution placed on that segment. We will refer to the potential of the source distribution on the segment where we are satisfying the ground boundary condition at a given point by $\varphi_{s_{B.C.}}$. Then we can write $\bar{\nabla}\varphi_{s_{B.C.}}$ as,

$$\bar{\nabla}\varphi_{s_{B.C.}} = \frac{\partial \varphi_{s_{B.C.}}}{\partial x}\bar{i} + \frac{\partial \varphi_{s_{B.C.}}}{\partial y}\bar{j} + \frac{\partial \varphi_{s_{B.C.}}}{\partial z}\bar{k}$$

$$\frac{\partial \varphi_{s_{B.C.}}}{\partial x} = \frac{1}{4\pi}\int_{-\infty}^{\infty}\int_{\mu_{B.C._l}}^{\mu_{B.C._u}} \frac{\eta(\xi,\mu)(x-\xi)\,d\xi\,d\mu}{\left[(x-\xi)^2+(y-\mu)^2+(z-f_{B.C.}(\mu))^2\right]^{3/2}}$$

$$\frac{\partial \varphi_{s_{B.C.}}}{\partial y} = \frac{1}{4\pi}\int_{-\infty}^{\infty}\int_{\mu_{B.C._l}}^{\mu_{B.C._u}} \frac{\eta(\xi,\mu)(y-\mu)\,d\xi\,d\mu}{\left[(x-\xi)^2+(y-\mu)^2+(z-f_{B.C.}(\mu))^2\right]^{3/2}}$$

$$\frac{\partial \varphi_{s_{B.C.}}}{\partial z} = \frac{1}{4\pi}\int_{-\infty}^{\infty}\int_{\mu_{B.C._l}}^{\mu_{B.C._u}} \frac{\eta(\xi,\mu)(z-f_{B.C.}(\mu))\,d\xi\,d\mu}{\left[(x-\xi)^2+(y-\mu)^2+(z-f_{B.C.}(\mu))^2\right]^{3/2}}$$

Since $\frac{\partial \varphi_{s_{B.C.}}}{\partial x}$ does not enter into the boundary condition, we need only concentrate on the $\frac{\partial \varphi_{s_{B.C.}}}{\partial y}$ and $\frac{\partial \varphi_{s_{B.C.}}}{\partial z}$.

To evaluate these velocities at the source sheet we let z approach $f_{B.C.}(y)$.

From previous work in two dimensions we know that we can evaluate these two integrals by analogy to the delta function. We transform our coordinates into coordinates perpendicular to and parallel to the segment of the source sheet at which we are satisfying the boundary condition. We call these coordinates $\tilde{x}, \tilde{y}, \tilde{z}$. We then evaluate the velocity normal to the source sheet at the source sheet.

$$-\frac{\partial \varphi_{s_{B.C.}}}{\partial \tilde{z}}\bigg|_{\tilde{z}=\tilde{f}} = -\frac{1}{4\pi}\left[\int_{-\infty}^{\infty}\int_{\tilde{\mu}_{B.C._L}}^{\tilde{\mu}_{B.C._U}} \frac{\eta(\tilde{\xi},\tilde{\mu})(\tilde{z}-\tilde{f})\,d\tilde{\xi}\,d\tilde{\mu}}{\left[(\tilde{x}-\tilde{\xi})^2+(\tilde{y}-\tilde{\mu})^2+(\tilde{z}-\tilde{f})^2\right]^{3/2}}\right] = \frac{\eta(\tilde{x},\tilde{y})}{2}$$

We see that $\eta(\tilde{x},\tilde{y}) = \eta(x, y, f_{B.C.}(y))$

$$\frac{\eta(x,y,f_{B.C.}(y))}{2} = -\sum_{n\neq n_{B.C.}} \bar{\nabla}\varphi_{s_n}\cdot\bar{n}_g - \bar{\nabla}\varphi_{H.V.}\cdot\bar{n}_g$$

We must now calculate the velocities induced by the other segments of the source sheet evaluated at the point where we are satisfying the boundary condition. Thus, for all φ_{s_n} other than the one at which we are satisfying the boundary condition, we have

$$\frac{\partial \varphi_{s_n}}{\partial y}\bigg|_{z=f_{B.C.}(y)} = \frac{1}{4\pi}\int_{-\infty}^{\infty}\int_{\mu_{n_L}}^{\mu_{n_U}} \frac{\eta_n(\xi,\mu)(y-\mu)\,d\xi\,d\mu}{\left[(x-\xi)^2+(y-\mu)^2+(f_{B.C.}(y)-f_n(\mu))^2\right]^{3/2}}$$

Similarly,

$$\frac{\partial \varphi_{s_n}}{\partial z}\bigg|_{z=f_{B.C.}(y)} = \frac{1}{4\pi}\int_{-\infty}^{\infty}\int_{\mu_{n_L}}^{\mu_{n_U}} \frac{\eta_n(\xi,\mu)(f_{B.C.}(y)-f_n(\mu))\,d\xi\,d\mu}{\left[(x-\xi)^2+(y-\mu)^2+(f_{B.C.}(\mu)-f_n(\mu))^2\right]^{3/2}}$$

Hence, we can write the boundary condition of no flow through the source sheet as,

$$0 = \frac{\eta(x,y,f_{B.C.}(y))}{2} + \left\{ \sum_{n \neq n_{B.C.}} \left[\frac{1}{4\pi} \left(\int_{-\infty}^{\infty} \int_{\mu_{n_L}}^{\mu_{n_U}} \frac{\eta_n(\xi,\mu)(y-\mu)\, d\xi\, d\mu}{\left[(x-\xi)^2+(y-\mu)^2+(f_{B.C.}(y)-f_n(\mu))^2\right]^{3/2}} \right) \cdot n_{g_2} \right. \right.$$

$$\left. \left. + \frac{1}{4\pi} \left(\int_{\infty}^{\infty} \int_{\mu_{n_L}}^{\mu_{n_U}} \frac{\eta_n(\xi,\mu)(f_{B.C.}(y)-f_n(\mu))\, d\xi\, d\mu}{\left[(x-\xi)^2+(y-\mu)^2+(f_{B.C.}(y)-f_n(\mu))^2\right]^{3/2}} \right) \cdot n_{g_3} \right] + \frac{\partial \varphi_{H.V.}}{\partial y} n_{g_2} + \frac{\partial \varphi_{H.V.}}{\partial z} n_{g_3} \right\}$$

In order to determine the source strength distribution on the ground plane and the vortex distribution on the wing we must also satisfy the boundary condition on the wing surface. We would like to generalize this wing boundary condition to include the case where the wing may be given an arbitrary roll, pitch, or yaw rate. The detailed derivation describing the motion of a given point on the wing surface undergoing an arbitrary translation and rotation rate is given in Appendix B.

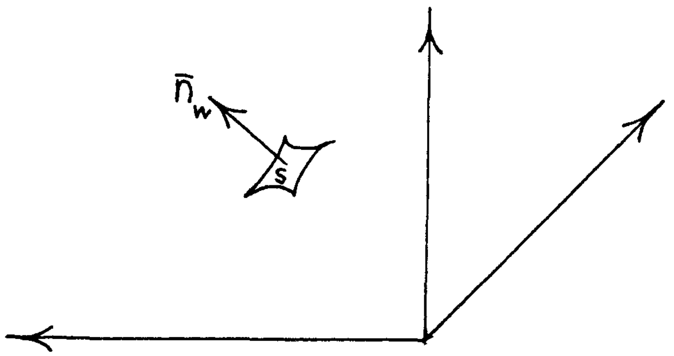

Hence, consider the boundary condition on an arbitrary wing surface that satisfies the condition that the fluid flow induced by all elements of the flow is tangent to the wing surface at the wing surface. The unit normal to the wing surface is

$$\bar{n}_w = n_{w_1}\bar{i} + n_{w_2}\bar{j} + n_{w_3}\bar{k}$$

The velocity at any point in the flow field is

$$\bar{V} = (U_\infty + u)\bar{i} + (V_\infty + v)\bar{j} + (W_\infty + w)\bar{k}$$

where $(U_\infty, V_\infty, W_\infty)$ = The velocity induced by the wing translation and rotation relative to a fixed coordinate system. This velocity accounts for the speed of the wing and accounts for the roll rate of the wing.

(u, v, w) = The velocity induced by the wing on which the boundary condition is being satisfied plus the velocity induced by the presence of any ground plane.

The wing boundary condition is satisfied if $\bar{V}\cdot\bar{n}_w = 0$. That is,

$$u n_{w_1} + v n_{w_2} + w n_{w_3} = -U_\infty n_{w_1} - V_\infty n_{w_2} - W_\infty n_{w_3}$$

Suppose we have a wing which is translating and rotating through space with velocity (U_0, V_0, W_0) and rotation rate $\bar{\omega} = (p, q, r)$. Let the distance from the center of rotation to any point on the wing surface be denoted by $\bar{r}_r = (r_{r_1}, r_{r_2}, r_{r_3})$ where the center of rotation is $\bar{r}_c$.

Then, in a coordinate system translating and rotating with the wing, the velocity induced by the wing's rotation and translation is

$$(U_\infty, V_\infty, W_\infty) = (U_0 - q r_{r_3} + r r_{r_2})\bar{i} + (V_0 + p r_{r_3} - r r_{r_1})\bar{j} + (W_0 + q r_{r_1} - p r_{r_2})\bar{k}$$

Hence the boundary condition on the wing with arbitrary angular rates and translation rates included is,

$$u n_{w_1} + v n_{w_2} + w n_{w_3} = -(U_0 - q r_{r_3} + r r_{r_2}) n_{w_1} - (p r_{r_3} - r r_{r_1} + V_0) n_{w_2}$$
$$- (q r_{r_1} - p r_{r_2} + W_0) n_{w_3}$$

The velocity vector (u, v, w) can be decomposed into the velocities induced by horseshoe vortices and the velocities induced by the ground source distribution. In addition, the boundary condition on the wing is satisfied at only a finite number of points dictated by the vortex-lattice method. Using the symbol "j" to denote the coordinates (x_j, y_j, z_j) of a given point at which the boundary condition is being satisfied, and using the symbol "i" to denote the velocity induced by the i^{th} horseshoe vortex at the j^{th} matching point, we write the wing boundary condition in the following discretized manner:

$$\sum_i \left[u_i(j) n_{w_1} + v_i(j) n_{w_2} + w_i(j) n_{w_3} \right] + u'(j) n_{w_1} + v'(j) n_{w_2} + w'(j) n_{w_3}$$
$$= -(U_0 - q r_{r_3} + r r_{r_2}) n_{w_1} - (V_0 + p r_{r_3} - r r_{r_1}) n_{w_2} - (W_0 + q r_{r_1} - p r_{r_2}) n_{w_3}$$

where $(u'(j), v'(j), w'(j))$ is the velocity induced by the source distribution representing the ground.

In order to numerically satisfy this boundary condition, and the boundary condition on the ground, we must discretize the integrals over the source distribution on the ground.

Discretization of the Source Distribution

The boundary condition on the wing and the boundary condition on the ground represent a coupled set of integral equations for the unknown vortex strengths Γ_j and source strength distribution $\eta(\xi,\mu)$. An excellent means of numerically solving these equations is to represent the integrals over the source distribution as a finite sum. Then satisfying the wing and ground boundary conditions at "n" discrete points gives "n" algebraic equations in "n" unknowns. The unknown vortex and source strengths are then solved for by any of the many available methods for systems of linear algebraic equations. Given these vortex and source strengths it is then possible to determine the forces and moments on the wing.

The mathematical treatment of the aforementioned process is now presented. Recall that the expressions for the velocities $(u'(j), v'(j), w'(j))$ can be written as,

$$u'(j) = \frac{1}{4\pi} \int_{-\infty}^{\infty}\int_{-\infty}^{\infty} \frac{\eta(\xi,\mu)(x_j-\xi)\,d\xi\,d\mu}{\left[(x_j-\xi)^2+(y_j-\mu)^2+(z_j-f(\mu))^2\right]^{3/2}}$$

$$u'(j) = \frac{1}{4\pi} \int_{-\infty}^{\infty} \sum_{n=1}^{r} \int_{\mu_{n_L}}^{\mu_{n_u}} \frac{\eta_n(\xi,\mu)(x_j-\xi)\, d\mu\, d\xi}{\left[(x_j-\xi)^2+(y_j-\mu)^2+(z_j-f_n(\mu))^2\right]^{3/2}}$$

Let us represent the integral by a double summation over a finite number of intervals. Using Simpson's rule as the basis for the summation, we get,

$$u'(j) = \frac{1}{4\pi} \sum_{k=1}^{NPX} \sum_{n=1}^{r} \sum_{\ell=1}^{NPY_n} c_\ell d_k g_{n_u}(x_j, y_j, z_j, \xi_k, \mu_\ell)\, \eta_n(\xi_k, \mu_\ell) \frac{\Delta\xi\Delta\mu}{9}$$

where $g_{n_u}(x_j, y_j, z_j, \xi_k, \mu_k) = \dfrac{x_j - \xi_k}{\left[(x_j-\xi_k)^2+(y_j-\mu_\ell)^2+(z_j-f_n(\mu_\ell))^2\right]^{3/2}}$

$\Delta\xi, \Delta\mu$ = step size of integration interval

and c_ℓ, d_k = weighting functions for Simpson's $\frac{1}{3}$ rule of integration.

If, in addition, we wish to be able to vary the step size of integration in certain regions, we must make some modifications to the above formula.

If NDX and NDY are the number of regions in the X and Y directions, then

$$u'(j) = \frac{1}{4\pi} \sum_{m=1}^{NDX} \sum_{k=1}^{NPX_m} \sum_{n=1}^{r} \sum_{p=1}^{NDY_n} \sum_{\ell=1}^{NPY_{n,p}} c_\ell d_k g_{n_u}(x_j, y_j, z_j, \xi_k, \mu_\ell)\, \eta_n(\xi_k, \mu_\ell) \frac{\Delta\xi_m \Delta\mu_p}{9}$$

Let $q = (k-1)NPYT + \ell$ where $NPYT$ = total number of points in the Y -direction

Writing $u'(j)$ in more compact notation gives

$$u'(j) = \frac{1}{4\pi}\sum_{q} e_q\, g_{jq_u} \frac{\Delta\xi_q \Delta\mu_q}{q} \eta_q \qquad \text{where} \qquad g_{jq_u} = g_u(j,q)$$

$$e_q = c_\ell d_k$$

Similarly

$$v'(j) = \frac{1}{4\pi}\sum_{q} e_q\, g_{jq_v} \frac{\Delta\xi_q \Delta\mu_q}{q} \eta_q \qquad \text{where} \quad g_{jq_v} = \frac{(y_j - \mu_\ell)}{\left[(x_j-\xi_k)^2 + (y_j-\mu_\ell)^2 + (z_j - f_n(\mu_\ell))^2\right]^{3/2}}$$

and

$$w'(j) = \frac{1}{4\pi}\sum_{q} e_q\, g_{jq_w} \frac{\Delta\xi_q \Delta\mu_q}{q} \eta_q \quad \text{where} \quad g_{jq_w} = \frac{z_j - f_n(\mu_\ell)}{\left[(x_j-\xi_k)^2 + (y_j-\mu_\ell)^2 + (z_j - f_n(\mu_\ell))^2\right]^{3/2}}$$

Substituting these relations for the velocities into the equation for the boundary condition on the wing, we get

$$\sum_{i} \left[u_i(j)\, n_{w_1} + v_i(j)\, n_{w_2} + w_i(j)\, n_{w_3} \right]$$

$$+ \frac{1}{4\pi}\sum_{q} \frac{\Delta\xi_q \Delta\mu_q}{q} \left[e_q g_{jq_u} \eta_q n_{w_1} + e_q g_{jq_v} \eta_q n_{w_2} + e_q g_{jq_w} \eta_q n_{w_3} \right] =$$

$$-(U_0 - q r_{r_3} + r r_{r_2}) n_{w_1} - (V_0 + p r_{r_3} - r r_{r_1}) n_{w_2} - (W_0 + q r_{r_1} - p r_{r_2}) n_{w_3}$$

Since the velocity induced by the vortices is proportional to the circulation Γ_i , we can write,

$$u_i(j) = \Gamma_i \tilde{u}_i(j)$$

$$v_i(j) = \Gamma_i \tilde{v}_i(j)$$

$$w_i(j) = \Gamma_i \tilde{w}_i(j)$$

Hence, we can rewrite the boundary condition equation as,

$$\sum_i \Gamma_i \left[\tilde{u}_i(j) n_{w_1} + \tilde{v}_i(j) n_{w_2} + \tilde{w}_i(j) n_{w_3} \right]$$

$$+ \sum_q \eta_q \left[\frac{\Delta\xi_q \Delta\mu_q e_q}{36\pi} \left(g_{jq_u} n_{w_1} + g_{jq_v} n_{w_2} + g_{jq_w} n_{w_3} \right) \right] = \text{R.H.S.}$$

Let $C_{jq} = \frac{\Delta\xi_q \Delta\mu_q e_q}{36\pi} \left(g_{jq_u} n_{w_1} + g_{jq_v} n_{w_2} + g_{jq_w} n_{w_3} \right)$

and $D_{ji} = \tilde{u}_i(j) n_{w_1} + \tilde{v}_i(j) n_{w_2} + \tilde{w}_i(j) n_{w_3}$

Then the equation for the condition of no flow through the wing can be written as,

$$\sum_q C_{jq} \eta_q + \sum_i D_{ji} \Gamma_i = \text{R.H.S.} \qquad \text{for all } j$$

This gives us j equations for $q+j$ unknown. Hence, we must get the remaining q equations from the boundary condition of no flow through the ground.

The boundary condition of no flow through the ground is stated as follows:

$$0=\frac{\eta(x,y,f_{B.C.}(y))}{2}+\frac{1}{4\pi}\int_{-\infty}^{\infty}\sum_{n\neq n_{B.C.}}\left[\left(\int_{\mu_{n_L}}^{\mu_{n_u}}\frac{\eta_n(\xi,\mu)(y-\mu)\,d\xi\,d\mu}{\left[(x-\xi)^2+(y-\mu)^2+(f_{B.C.}(y)-f_n(\mu))^2\right]^{3/2}}\right)n_{g_2}\right.$$

$$\left.+\left(\int_{\mu_{n_L}}^{\mu_{n_u}}\frac{\eta_n(\xi,\mu)(f_{B.C.}(y)-f_n(\mu))\,d\xi\,d\mu}{\left[(x-\xi)^2+(y-\mu)^2+(f_{B.C.}(y)-f_n(\mu))^2\right]^{3/2}}\right)n_{g_3}\right]+\frac{\partial\varphi_{H.V.}}{\partial y}n_{g_2}+\frac{\partial\varphi_{H.V.}}{\partial z}n_{g_3}$$

where $\bar{n}$ = unit vector normal to ground surface = $n_2\bar{j}+n_3\bar{k}$

Now, as before, we represent the integrals in the above equation by a double summation over a finite number of intervals. We evaluate the integrand at the same points on the ground plane that we used to evaluate the integrand for the previous boundary condition. Hence, using the notation previously introduced, we can rewrite the ground boundary condition as,

$$0 = \frac{\eta_j}{2} + \frac{1}{4\pi} \sum_{m=1}^{NDX} \sum_{k=1}^{NPX_m} \sum_{n=1}^{r} \sum_{p=1}^{NDY_n} \sum_{\ell=1}^{NPY_{p,n}} c_\ell d_k \left(g_{jk\ell_v} \eta_{k\ell} n_{g_2} + g_{jk\ell_w} \eta_{k\ell} n_{g_3} \right) \frac{\Delta\xi_m \Delta\mu_p}{9}$$

$$+ \sum_i \Gamma_i \left(\tilde{v}_i(j) n_{g_2} + \tilde{w}_i(j) n_{g_3} \right) \qquad \text{for all } j$$

Or, rewriting in more compact form

$$0 = \frac{\eta_j}{2} + \sum_q \eta_q \left[\frac{e_q \Delta\xi_q \Delta\mu_q}{36\pi} \left(g_{jq_v} n_{g_2} + g_{jq_w} n_{g_3} \right) \right]$$

$$+ \sum_i \Gamma_i \left[\tilde{v}_i(j) n_{g_2} + \tilde{w}_i(j) n_{g_3} \right]$$

Let $A_{jq} = \frac{e_q \Delta\xi_q \Delta\mu_q}{36\pi} \left(g_{jq_v} n_{g_2} + g_{jq_w} n_{g_3} \right)$

and $B_{ji} = \tilde{v}_i(j) n_{g_2} + \tilde{w}_i(j) n_{g_3}$

Hence, we can write the boundary condition of no flow through the ground in the form

$$\frac{\eta_j}{2} + \sum_q A_{jq} \eta_q + \sum_i B_{ji} \Gamma_i = 0$$

We now have a total of $q+j$ equations for $q+j$ unknowns.

Special Source Strength Approximation

In order to accurately simulate the presence of a reasonably complex wing flying in the presence of a given non-planar ground, a large number of wing vortices and ground boundary condition matching points will be required. Every discrete point at which the wing or ground boundary condition is satisfied represents a linear algebraic equation. The sum total of all the equations produced by matching the boundary conditions represents a set of simultaneous linear algebraic equations in the unknowns γ_i and Γ_i. These equations must be solved numerically. However, the computing time required to do this increases as N^3 where N is the number of equations to be solved. Therefore, it is essential to minimize the number of equations that must be solved. An excellent means for reducing the number of equations is to express some of the unknown source strengths in terms of the other unknown source strengths by means of an interpolation polynomial. This does not reduce the accuracy of the overall method since the kernel functions in the integrands of the integrals vary much more sharply than the source strength distribution. Therefore, a second order interpolation polynomial was developed to approximate the variation of the source strength distribution. This was incorporated into the source sheet distribution method by subdividing the ground integration interval into several segmented integration intervals. Each segmented integration interval consisted of five ground boundary condition matching points. However, the second and fourth points were expressed in terms of the first, third, and fifth points by means of the second-order interpolation polynomial. This approximation reduced the number of equations in each direction by a factor of two, thereby reducing the total number of equations by a factor of four. The accuracy of the overall method was not impaired since the sub-intervals of integration could be made as small as desired.

Calculation of Forces and Moments

The previous equations when solved give both the distribution of circulation on the wing, and the distribution of source strength on the ground plane.

Assuming that this linear system of $q+j$ equations can be solved, we can calculate the forces and moments. Assuming that the freestream velocity points in the $+X$ -direction,

$$L = \sum_{i} 2 t_i \rho u(x_i, y_i, z_i) \Gamma_i n_{w_3}$$

But

$$u(x_i, y_i, z_i) = U_\infty + \sum_{j} u_j(i) + \sum_{q} u'_q(i)$$

$$u_j(i) = \Gamma_j \tilde{u}_j(i)$$

$$u'_q(i) = \eta_q e_q g_{iq_u} \frac{\Delta\xi_q \Delta\mu_q}{36\pi}$$

yielding

$$L = 2\rho \sum_i t_i \Big(U_\infty + \sum_{j \neq i} \Gamma_j \tilde{u}_j(i) + \sum_q \eta_q e_q g_{iq_u} \frac{\Delta\xi_q \Delta\mu_q}{36\pi} \Big) \Gamma_i n_{w_3}$$

Non-dimensionalizing with respect to the chord C , we get

$$C_L = 2 \frac{c}{S} \sum_i \frac{t_i}{c} \Big(1 + \sum_{j \neq i} \frac{\Gamma_j \tilde{u}_j(i)}{U_\infty c} + \sum_q \frac{\eta_q}{U_\infty} e_q c^2 g_{iq_u} \frac{\frac{\Delta\xi_q}{c} \frac{\Delta\mu_q}{c}}{36\pi} \Big) \frac{\Gamma_i}{U_\infty c} n_{w_3}$$

Similarly, we can write expressions for the other forces and moments as,

$$C_D = 2 \frac{c}{S} \sum_i \frac{t_i}{c} \Big(\sum_{j \neq i} \frac{\Gamma_j \tilde{w}_j(i)}{U_\infty c} + \sum_q \frac{\eta_q}{U_\infty} e_q c^2 g_{iq_w} \frac{\frac{\Delta\xi_q}{c} \frac{\Delta\mu_q}{c}}{36\pi} \Big) \frac{\Gamma_i}{U_\infty c}$$

Note: This obviously is an expression for the induced drag only.

$$C_Y = 2 \frac{c}{S} \sum \frac{t_i}{c} \Big(1 + \frac{u(i)}{U_\infty} + \frac{u'(i)}{U_\infty} \Big) \frac{\Gamma_i}{U_\infty c} n_{w_2}$$

Defining $C_{\ell_{L.E.}}$ as the roll moment coefficient about the midpoint of the leading edge

$$C_{\ell_{L.E.}} = 2\frac{c}{S}\sum_{i}\frac{t_i}{c}\left(1+\frac{u(i)}{U_\infty}+\frac{u'(i)}{U_\infty}\right)\left(\left(\frac{y_i-y_{L.E.}}{c}\right)n_{w_3}-\left(\frac{z_i-z_{L.E.}}{c}\right)n_{w_2}\right)\frac{\Gamma_i}{U_\infty c}$$

where (x_i, y_i, z_i) are the coordinates of the midpoint of the bound vortex in the segment "i".

Similarly, the pitch and yaw moment coefficients about the midpoint of the leading edge are written as,

$$C_{M_{L.E.}} = 2\frac{c}{S}\sum_{i}\frac{t_i}{c}\frac{\Gamma_i}{U_\infty c}\Big[\left(\frac{z_i-z_{L.E.}}{c}\right)\left(\frac{w(i)}{U_\infty}+\frac{w'(i)}{U_\infty}\right)$$

$$-\left(\frac{x_i-x_{L.E.}}{c}\right)\left(1+\frac{u(i)}{U_\infty}+\frac{u'(i)}{U_\infty}\right)n_{w_3}\Big]$$

$$C_{N_{L.E.}} = 2\frac{c}{S}\sum_{i}\frac{t_i}{c}\frac{\Gamma_i}{U_\infty c}\Big[\left(\frac{x_i-x_{L.E.}}{c}\right)\left(1+\frac{u(i)}{U_\infty}+\frac{u'(i)}{U_\infty}\right)n_{w_3}$$

$$-\left(\frac{y_i-y_{L.E.}}{c}\right)\left(\frac{w(i)}{U_\infty}+\frac{w'(i)}{U_\infty}\right)\Big]$$

2. Multiple Image Method

a. Generalities

The value of the multiple image method for solving non-planar ground effect problems stems from the fact that this method automatically satisfies the boundary condition of no normal flow through the ground. Therefore, we only need to satisfy the boundary condition of no flow through the wing. This provides us with a second independent method of solving certain non-planar ground effect problems, thus providing an excellent check on the source/sink distribution method.

However, it is obvious that the multiple image method is limited to solving only a certain class of problems. That is, it can only represent non-planar ground planes which can be described as two straight semi-infinite ground segments intersecting at certain angles. This type of problem is illustrated in figure 6. The method consists of placing n identical wings in the flow field. These wings are placed so that they are all facing the freestream direction but are at an angle $\beta_i = \frac{360}{n}(i-1)$ to the horizontal and equidistant from a line which is parallel to the freestream direction. This represents the problem of a wing flying in the presence of a non-planar ground consisting of two semi-infinite segments which intersect at an angle $\frac{360}{n}$ degrees in the y-z plane. The ground plane is uniform in the X-direction. Since we can only place an integer number of wings $n = 2,3,4,\ldots$ the ground planes cannot intersect at any arbitrary angle, but only at those angles that can be expressed as $\frac{360}{n}$ for $n \geq 2$. The case $n=1$ is, of course, representative of a wing flying in an infinite medium. The case $n=2$ represents the planar ground effect problems.

Let us now develop expressions for the forces and moments on a wing in non-planar ground effect using the multiple-image method in conjunction with the vortex-lattice method. We first consider the boundary condition on the wing.

b. Boundary Condition on the Wing

The general expression for the boundary condition on the wing is the same as before. That is,

$$u n_{w_1} + v n_{w_2} + w n_{w_3} = -(U_0 - q r_{r_3} + r r_{r_2}) n_{w_1}$$
$$-(p r_{r_3} - r r_{r_1} + V_0) n_{w_2} - (q r_{r_1} - p r_{r_2} + W_0) n_{w_3}$$

But now,

$$u(x_j, y_j, z_j) = \sum_i \Gamma_i \sum_n \tilde{u}_{n_i}(j)$$

Similarly,

$$v(x_j, y_j, z_j) = \sum_i \Gamma_i \sum_n \tilde{v}_{n_i}(j)$$
$$w(x_j, y_j, z_j) = \sum_i \Gamma_i \sum_n w_{n_i}(j)$$

where $(u_n(j), v_n(j), w_n(j))$ are the velocity components induced by the n^{th} wing in the image system. Also, since all n wings are identical, they each have the same circulation distribution. Hence, the velocity induced by each discrete vortex and its images can be summed with the Γ_i being a common factor.

Substituting these facts and the above relations into the wing boundary condition, we get an equation for each point at which we satisfy this boundary condition. That is,

$$\sum_i \Gamma_i \Big[\sum_n \big(\tilde{u}_{n_i}(j) n_{w_1} + \tilde{v}_{n_i}(j) n_{w_2} + \tilde{w}_{n_i}(j) n_{w_3} \big) \Big] = \text{R.H.S.}$$

The system of equations represented by this equation when solved gives the vortex strength distribution on the wing. We can then calculate the forces and moments as follows:

$$L = \sum_{i} 2 t_i \rho u(x_i, y_i, z_i) \Gamma_i n_{w_3}$$

where, in this case,

$$u(x_i, y_i, z_i) = U_0 + \sum_{n} u_n(x_j, y_j, z_j)$$

$$D = \sum_{i} 2 t_i \rho w(x_i, y_i, z_i) \Gamma_i$$

and

$$w(x_i, y_i, z_i) = W_0 + \sum_{n} w_n(x_j, y_j, z_j)$$

The calculation of the other forces and moments follows in a similar manner.

3. Equivalence of the Source Method and the Image Method

In order to prove that the source distribution method is exactly equivalent to the image method for representing the presence of the ground in three dimensions, it is only necessary to prove that the velocity induced by a single horseshoe vortex together with an infinite source sheet, whose source strength distribution satisfies the condition that there is no normal flow through it, is the same as the velocity induced by a single horseshoe vortex and its image (for planar ground problems) or images (for non-planar ground problems). This is sufficient, since any arbitrary three-dimensional wing can be expressed in terms of a horseshoe vortex distribution.

In two dimensions we were able to show this proof analytically.

However, in three dimensions the integrals that must be evaluated are extremely difficult if not impossible to evaluate. Therefore, it was necessary to numerically compare the solutions. This was done by numerically computing the forces and moments on various wings in ground effect as well as computing the vortex strength distributions on the wing surface and the source strength distribution on the ground planes using both the source sheet distribution method and the imaging method. Although the results showed that the agreement between the two methods was excellent in all cases, it was found that there are three inherent difficulties with the source distribution method. First, it was very difficult numerically to extend a source sheet distribution to infinity; therefore, the ground plane had to be truncated at a certain finite radius in all directions for ease of computation. Second, in order to accurately represent the integrand of the integrals in the equations describing the boundary conditions on the wing and ground, the ground boundary condition matching points had to be placed at specific locations and with specific spacing in the ground region beneath the wing. Third, since the source strength on the ground goes to infinity at any corners in the ground plane, the matching points near the corners had to be placed very carefully also.

Detailed numerical investigations were carried out to determine how to correctly handle each of these difficulties. The description of these investigations and the results obtained from them are presented in Appendix D. In general, three important results were obtained. 1) The size of the source sheet distribution required to accurately represent an infinite ground plane depended on the height above the ground at which the velocity induced by the source sheet was calculated. It also depended on the particular component of the velocity being calculated. It was found for a flat ground that a source sheet distribution extended to a radius of 3 times H in all directions simulated the velocity induced in a direction normal to the ground plane within an error of 5%, where H is the height above the ground at which the velocity is evaluated. A source sheet distribution extended to a radius of about 7 times H in all directions simulated the velocity induced in a direction parallel to the ground plane within the same error bound. Furthermore, these results for a flat ground were found to be applicable to any arbitrary non-planar ground situation so long as the source sheet distribution is placed in accordance with the distance normal to the particular ground segment whose induced velocity is being calculated, and in accordance with the component of the velocity being calculated.

2) In order to accurately represent the contribution of the source sheet ground plane distribution in the equation describing the boundary condition on the wing and in the equation describing the forces and moments on the wing, the discrete points at which the integrand of the integrals in these equations is evaluated must be placed according to certain rules. These rules specify that integrand evaluation points must be placed beneath the midpoint of the 1/4 and 3/4 line of each wing segment (for non-planar ground they would be placed at the points on the ground which minimize the distance between those points and the midpoints of the 1/4 and 3/4 line of

each wing segment). In addition, the spacing must be about 1/2 or less for at least the next two points in all directions. The development of these rules is more fully understood by a close reading of Appendix D. 3) Although the source strength becomes unbounded at any corners in the ground plane (that is, places where two ground segments intersect at an angle), the mass flux contributed to the flow field is zero at the singularity. Therefore, the singularities at the corners do not adversely affect the flow field. For a detailed mathematical treatment of the corner singularities see Appendix D.

c. Numerical Results and Comparisons

The numerical solution techniques outlined in sections II-A, and II-B were formulated in several computer programs. In fact, separate programs were written for two-dimensional wings using the method of images, three-dimensional wings using the method of simple and multiple images, and three-dimensional wings using the source sheet distribution method. These programs were written in FORTRAN IV language for use on an IBM 370/155 computer at Caltech, and for use on an IBM 360/91 at UCLA.

It would be impossible, economically, to numerically solve all the possible airfoil and wing shapes and all the possible planar and non-planar ground shapes. Therefore, the choice was made to numerically investigate several examples of only a single class of wings and only a few types of ground plane situations. The class of wings investigated was thin planar and non-planar wings without camber or twist. The ground planes investigated were flat ground planes, in two and three dimensions, and three types of three-dimensional non-planar ground situations representing three possible high-speed ground transportation vehicle guideways.

The results of these numerical investigations are divided into three sections. The first section is devoted to two-dimensional wings; the second section to wings in planar ground effect; and the third section to wings in non-planar ground effect. Only the calculations of force and moment coefficients are presented in these sections, and compared to experiments or other theories whenever possible. More broad results dealing with stability derivatives and dynamic stability characteristics of most of these wings are deferred to Chapter III where a stability analysis is developed.

1. Results for Two-Dimensional Wings

Numerical calculations were carried out to determine the lift on a two-dimensional thin flat wing in ground effect. Cases were solved for wings represented by 1, 2, and 3 vortices, at angles of attack of 2°, 10°, and 14°, and for heights ranging from one chord length down to the height where the trailing edge touched the ground. The angle of attack is defined here and in the rest of Chapter II as the angle between the surface of the wing and the horizontal. This is important to note because in Chapter III the angle of attack is defined as the angle between the surface of the wing and the instantaneous wind vector. The difference between these two definitions is discussed in Chapter III. Figures 7, 8, and 9 show the ratio of the lift at the height h/c_o to the lift at $h = \infty$ as a function of the height of the quarter chord above the ground for the various numbers of vortices and angles of attack. The figures also show the exact values of the lift derived by Tomotika (ref. 2).

The calculations showed that the two-dimensional vortex-lattice method develops a different value for the lift depending on the number of vortices used to represent the wing. This is contrary to the situation in an unbounded fluid where the same value for the lift is developed independent of the number of vortices used to represent the wing. However, as the number of vortices is increased, the numerical solution asymptotically approaches the exact value. The calculations also indicate that the solution diverged when the airfoils were placed very close to the ground. However, the onset of the divergence occurred increasingly close to the ground as the number of vortices was increased.

2. Results for Three-Dimensional Wings in Planar Ground Effect

Numerical calculations were carried out to determine the forces and moments on various three-dimensional thin, uncambered wings at angle of attack. For the purpose of brevity, these wings were separated into three main categories: 1) single planar wings; 2) single non-planar wings; and 3) tandem planar wings. Results concerning only the rudimentary aerodynamic parameters, such as lift coefficient, induced drag coefficient, lift curve slope, moment curve slope, and center of gravity location are presented in this section. This is because experimental and other theoretical results exist for these parameters for some wings in ground effect. More general results concerning the static stability derivatives and dynamic stability characteristics of these wings are presented in

Chapter III.

a. Single Planar Wings

Calculations of lift-curve slope C_{L_α}, the induced drag coefficient C_{D_i}, and the quarter-chord moment-curve slope $C_{M_{\alpha_{1/4}}}$ were made for thin flat rectangular wings of aspect ratio 1, 2, and 4, angles of attack 2.5° and 5°, and heights above the ground ranging from .05 chords to ∞. Consistent with the definition of the angle of attack as used in all of Chapter II, the lift-curve slope C_{L_α}, and the moment curve slope $C_{M_{\alpha_{1/4}}}$ are defined as the changes in the lift and moment with changes in the angle between the wing surface and the ground. The lift and moment curve slopes are presented this way in this chapter because all experiments with wings in ground effect measure the variation of lift and moment with a variation in the angle between the wing surface and the ground. These calculations were performed to compare the results to previous numerical calculations and experimental data, and to determine the number of vortices required to adequately represent a wing in ground effect by the vortex-lattice method in conjunction with imaging.

Figure 10 shows the lift-curve slope vs. aspect ratio for thin flat rectangular wings in an unbounded fluid. The results of various numerical solutions and experiments agree well with the vortex-lattice method. This indicates that a rather modest number of vortices, such as 30 to 50, are required to adequately represent a wing, and that more accurate results are obtainable merely by increasing the number of vortices used to represent the wing.

Comparisons of calculations and experimental data on the lift-curve-slope in ground effect are shown in figure 11. The experimental data are for 11% thick airfoils with camber. Since thickness causes a negative contribution to the lift in ground effect, the experimental data points, as expected, were below the numerical calculations for thin, uncambered wings. The numerical results by Kalman shown in figure 11 were achieved using the same vortex-lattice procedure as used in this investigation. His results for angle of attack compare excellently with Saunders' kernel function procedure. The present results for $\alpha = 2.5°$ and $\alpha = 5°$ compare very well with the other calculations. In addition, the results obtained using only 12 vortices were reasonably close to the results obtained using 36 vortices. This further indicates that the vortex-lattice method converges quickly to a consistent result. All the results illustrate the most fundamental property of ground effect. That is, the lift on a wing in ground effect increases dramatically as the ground is approached. Another less obvious property of ground effect illustrated in this figure is that the lift-curve slope is not a constant with angle of attack. In fact, it varies with height above the ground, the pitch angle, and aspect ratio. It also varies very strongly with the position about which the wing is pitched. An illustration of the variation of the lift-curve slope as a function of angle of attack for a wing in ground effect is shown in the results of figure 12. These results are for a thin flat rectangular wing of aspect ratio 1. The lift-curve slope is plotted as a function of angle of attack for various heights above the ground. The center of rotation for pitch was the one-quarter chord. All heights were also measured at the one-quarter chord. The results show the lift-curve slope to be a concave upward function of pitch angle. However, if the trailing edge were chosen as the center of rotation, the lift-curve slope would have been a convex upward function of the pitch angle. A center of rotation position most likely exists such that the lift-curve slope is a constant. However, this position obviously varies with height, pitch angle, and aspect ratio, as well as the wing geometry. Still another important property of ground effect is shown in figure 13, where the induced drag coefficient of thin flat rectangular wings is plotted as a function of height for the previous aspect ratios and angles of attack. The induced drag coefficient increases as a wing of a given aspect ratio approaches the ground at constant angle of attack. However, it decreases as the wing approaches the ground if the lift coefficient is held constant. The total drag on a wing in ground effect held at constant lift coefficient may increase or decrease relative to the same wing in an infinite medium. This is because the density varies with altitude, and the drag depends linearly on density, so that the total drag will vary accordingly.

Figure 14 shows the variation of the quarter-chord moment-curve slope with height above the ground, aspect ratio, and angle of attack. Results of the same previous numerical investigations shown in figure 11 are compared with the present results. Kalman (ref. 23) used the same vortex-lattice method as in the present investigation. His results for $\alpha = 0$ compare very well with Saunders' kernel function method. The results of the present investigation indicate that the moment curve slopes at the quarter chord vary significantly with angle of attack and height above the ground, whereas in an infinite medium it is nearly a constant with angle of attack.

Calculations of the stability derivatives for various thin flat rectangular wings in planar ground effect are presented in table 1. The dynamic stability characteristics of these wings are discussed in Chapter III.

b. Single Non-planar Wings

Numerical calculations were carried out to determine the forces and moments on various single non-planar wings in planar ground effect. All wings considered were thin, uncambered, and untwisted.

Wings with dihedral:

The lift curve slope of a thin rectangular wing with dihedral, having an aspect ratio of 4 and angle of attack of 5° is plotted as a function of dihedral angle for a vertex height of 0.5 chords above the ground and is shown in figure 15. The results are compared with the previous calculations of Saunders and Kalman for $\alpha = 0°$. As mentioned previously, Kalman used the same vortex-lattice method as is being used in the present investigation. His results compare very well with Saunders' kernel function method except when the wing tips touch the ground. The kernel function method breaks down at this point because it incorrectly forces the loading to go to zero at the wing tips. In general, the lift-curve slope in all cases increases as the dihedral angle is decreased. It is interesting to note that even when the wing is represented by only 4 vortices, the results are in reasonable agreement with the more accurate results.

Rectangular wings with end plates:

Numerical calculations of the aerodynamic coefficients and center of pressure location as a function of the height above the ground for thin rectangular wings with two types of end plates are shown in figures 17, 18, and 19. The two types of end plates considered were triangular end plates extended beneath the main wing with the bottom edge parallel to the ground, and rectangular end plates with top and bottom edges parallel to the ground. Illustrations of these two end plated wings are shown in figure 16. The various configurations investigated were wings of aspect ratio 0.5, 1, and 2 at angles of attack 2.5°, 5°, and 10°. The only rectangular end-plated cases considered were those for an aspect ratio of 0.5 at an angle of attack of 10°. These were the only rectangular end-plated cases considered because it was expected that these cases would best illustrate any significant deviation from the triangular end-plated cases.

The results indicate that the lift-curve slope is decreased with the use of triangular end plates for the wings of aspect ratio 0.5 and 1, but is slightly increased for the wing of aspect ratio 2. The lift and drag coefficients were, of course, increased with the use of either type of end plates except for the 10° angle of attack case. It is evident that the numerical solution becomes inaccurate for these higher angles of attack. This inaccuracy probably stems from the approximation that the trailing vortices shed straight back from the wing. For high angles of attack this is a poor approximation, especially for low-aspect-ratio wings. Hence, the comparisons between wings with and without end plates for the aspect ratio 0.5, angle of attack 10° case are probably not correct.

The presence of end plates also retards the rearward travel of the center of pressure in ground effect for the wings of aspect ratio 0.5 and 1. However, as the aspect ratio increases, this retarding effect diminishes and in fact reverses itself. Hence, for the wing of aspect ratio 2, the presence of end plates tended to cause the center of pressure to be slightly rearward of the c.p. of the flat wing without end plates. These results could have been expected since end plates affect lower aspect ratio wings far more than the higher aspect ratio wings. Furthermore, the peculiar shape of the end plates caused their effects to be more prominent near the leading edge of the wing rather than the trailing edge.

Far more comprehensive results on wings with end plates are shown and discussed in Chapter III where static and dynamic stability is discussed. Numerical calculations of the stability derivatives for various thin rectangular wings with end plates are presented in table 2.

Flat Wing with End Plates at Angle of Attack:

Calculations were made of the lift coefficient as a function of the height above the ground for the non-planar wing shown in figure 20. The horizontal wing segment had an average aspect ratio of 0.2564 and was placed with an angle of attack of 2.5°. The two end plates were 0.154 chords in average width and were also placed at an angle of attack of 2.5° to the X-Z plane. The bottom edges of the end plates were parallel to the ground plane. The results were compared to an experiment which was performed as part of the investigation. The details of the experiment can be found in Chapter IV. The agreement between the numerical calculations and the experiment were excellent at all heights except where the bottom edges of the wing touched the ground. At this height, the turbulent boundary layer beneath the wing caused the ground plane to become effectively closer to the wing thereby creating higher lifts. In fact, correction factors were applied to the experimental result to account for this effect and the corrected results were much closer to the theoretically predicted result.

Additional calculations were made to determine the lift coefficient as a function of angle of attack at a height of 0.2123 chords. These results were compared to experimental measurements of the same situation and are presented in figure 21. The numerical results were slightly below the experimental results, but were within the expected accuracy of the experiment. The lift-curve slope at this height at an angle of attack of 2.5° was computed numerically and from the experiment and were found to compare quite well considering the accuracy of the experiment.

Flat Rectangular Wings in Tandem

Numerical calculations were made for a pair of thin flat rectangular wings in tandem. The downwash on the rear wing due to the presence of the front wing was accounted for automatically by the trailing vortex portions of the horseshoe vortices used to represent the wing. The only assumption necessary with regard to these trailing vortices was that they shed from the front wing surface parallel to the ground. This is a very good approximation in close ground effect for low angles of attack. The results presented in references (10) and (15) verify the validity of this assumption. The only uncertainty arising in this calculation is whether the distribution of trailing vortices, used to mathematically represent the wake, accurately represent the downwash induced by the wing. In order to verify the accuracy of this representation, numerical calculations were made to determine the downwash induced by an elliptical planform wing in an unbounded fluid. These numerical calculations were then compared with theoretical predictions of the downwash induced by the elliptical planform wing. The results were found to be excellent. The numerical results became inaccurate near the tips of the wake, but this was to be expected since the theory predicts a discontinuity in downwash at the tips. A detailed description of these downwash calculations for the elliptical wing and comparisons with theory can be found in Appendix E.

With these results firmly established, the validity of the trailing vortex distribution for representing the wake was assumed to extend to wings in ground effect. The lift-curve slope, induced drag coefficient, and leading edge moment coefficient as functions of the height above the ground for flat rectangular wings in tandem are presented in figures 22 and 23. Calculations were made for identical wings of aspect ratio 1, 2, and 4, with each wing at an angle of attack of 2.5°. The wings were rigidly attached by a thin fuselage and were placed 3 and 4 chords apart. The centers of gravity and rotation were placed at the vehicle center of pressure.

The numerically calculated values for the lift-curve slope became astoundingly large as the ground was approached. This was due to the fact that the rotation arm was large and the center of pressure was closer to the front wing than to the rear wing. A plot of the vehicle center of pressure location as a function of height above the ground, aspect ratio, and separation distance is shown in figure 24. Small rotations about the vehicle c.p. caused large variations in the height of the rear wing, and also caused large variations in the downwash induced on the rear wing. The result of these variations was a large lift-curve slope.

The results further indicated that the downwash did not vary significantly with the separation distance between the two wings. This is indicated by the fact that the lift-curve slope and induced drag did not change significantly with separation distance.

Calculations of the stability derivatives for various thin flat rectangular wings in tandem are presented in table 3. The static and dynamic stability characteristics of these wings are discussed in Chapter III.

3. Results for Three-Dimensional Wings in Non-Planar Ground Effect

Numerical results were obtained for three types of non-planar ground effect geometries. Schematics of these three geometries are shown in figure 25. Two cases were solved with the same ground geometry but with slightly different wings. In addition, a simplified check case was run to compare the numerical results obtained by the source distribution method with the results obtained by the multiple image method for the same problem. The check case is presented first, and then the results of the important cases are presented separately.

a. Check Case

Figures 26 and 27 present a detailed description of the non-planar ground effect situation simulated to compare the results of the two methods for solving wings in non-planar ground effect.

The figure shows a thin wing flying in the presence of two semi-infinite ground planes intersecting at a 90° angle. The wing has an aspect ratio of 2, an angle of attack of 7.1°, and is flying at a height of 0.5 chords above the intersection of the ground planes.

This problem was solved by the multiple image method by placing the actual wing and three image wings into the flow at 90° angles to each other. The problem was then solved by the source distribution method by placing a finite source sheet along the desired ground plane. The source sheet extended 2.576 chords in each spanwise direction, and it extended from -1.4 chords to 2.25 chords along the X-direction where the origin of the coordinate system is on the ground directly beneath the leading edge of the wing.

Plots of the load distribution on the wing calculated by each method are shown in figure 28. The two sets of curves are nearly identical. The lift and moment coefficients were also nearly identical.

b. Slanted Channel — Wing with Dihedral

Calculations were performed on a wing of aspect ratio 2 with

45° dihedral at a height of 0.5 chords above the vertex of a slanted channel ground plane. Plots of the lift coefficient, the leading edge moment coefficient, the induced drag coefficient, the lateral force coefficient, and the leading edge roll moment coefficient as a function of angle of attack, roll angle, and lateral deflection from equilibrium are shown in figures 29 and 30. There are three important features of these results. The first is that the lateral force and roll moment are nearly linear with roll angle and lateral shift from equilibrium even for relatively large perturbations from equilibrium. This indicates that a linearized approximation for the equations of dynamic stability would be very suitable at least for the roll and lateral deflections from equilibrium. The second important feature of these results is the fact that the longitudinal forces and moments seem to be decoupled from the lateral perturbations. This is very important since it means that the equations of dynamic stability can be decoupled into the longitudinal equations of motion and the lateral equations of motion which will simplify the analysis greatly. It was expected that this configuration could not be decoupled because of the peculiar oblique type of ground effect. Since, however, it is apparent that the equations of motion can even be decoupled for this case, it can be concluded that the equations of motion can be decoupled for most non-planar ground effect situations within reason. The third important result is that the lateral force with a perturbation in roll angle is unexpectedly destabilizing. This shows that the change in the direction of the normal force coefficient is a larger effect than is the change in the lift due to the change in proximity to the ground for roll perturbations.

The source strength distribution on the ground for the slanted ground case is shown in figures 31 and 32. The source strength as a function of X is consistent with the expected downwash distribution induced by a wing at angle of attack. The source distribution as a function of Y is also consistent. However, at the corners, the source strengths are peaked. This phenomena has already been explained in section II-B, part 3.

c. Rectangular Rail - End Plates at Angle of Attack Beneath the Wing

Figure 25c illustrates this non-planar ground effect situation. The top segment has an average aspect ratio of 0.2564 measured at the midchord. Cases were solved with the top segment at an angle of attack of 2.5° at various heights above the ground. Cases were also solved for this wing in the presence of planar ground effect and were discussed in part 2 of this section. Another non-planar ground case was solved with the top wing segment at 5° and at a quarter chord height of 0.2452 chords above the ground. The end plates have average aspect ratios of 0.2014 and 0.2233 for each case and were placed at 2.5° lateral angle of attack in both cases. The end plates are 0.0783 chords from the side walls measured at the quarter chord. The bottom edge of the end plates are parallel to the plane. The rectangular rail is 0.1323 chords high and 0.1215 chords wide.

A plot of the load distribution along the center line of the top wing segment is shown in Chapter IV in figure 73 and compared with experimental measurements for the 2.5° angle of attack case at a height of 0.2123 chords. In addition, plots of the aerodynamic coefficients as a function of height above the ground are shown in figure 33. The calculations of the lift coefficient are compared with experimental measurements for the 2.5° angle of attack case also in Chapter IV in figure 68.

Due to computer storage limitations, the ground plane was only extended to a distance of 0.2 chords in the $\pm Y$-direction and from -0.45 to 1.2 chords in the X-direction. From results of calculations on finite ground planes discussed in section II-B, part 3, this should have caused the results for the lifts and moments to be 10 to 15% lower than if the ground plane were extended to infinity, and the same percentage higher for the drags. This conclusion is consistent with the comparisons to the experimental measurements. In addition, the experimental measurements were probably too high due to boundary layer effects on the simulated ground. These effects are explained in detail in Chapter IV.

Calculations of all the stability derivatives for the case of $h = 0.2123$, angle of attack 2.5, and the case of $h = 0.2452$, angle of attack 5° are presented in tables 4 and 5, and the dynamic stability characteristics for these cases are presented in Chapter III.

Comparisons of the 2.5° angle of attack case in the presence of a non-planar ground with the same wing in the presence of a planar ground show that the presence of the non-planar ground piece adds at least 10% to the lift. In fact, the increase is probably 20 to 25% because the non-planar ground case was solved with an extremely truncated ground plane.

d. Rectangular Channel — End Plates at Angle of Attack Above the Wing

Figure 25d illustrates this non-planar ground situation. The top segment has an average aspect ratio of 0.2936 measured at mid-chord, an angle of attack of 2.5°, and the quarter chord is 0.1327 chords above the channel bottom. The end plates are of average aspect ratio 0.13098 also measured at the quarter chord, and at a 2.5° lateral angle of attack. The end plates are also 0.1327 chords from the side walls. The top edge of the end plates are parallel to the X-Y plane. The channel is 0.537 chords wide and 0.2419 chords deep.

The aerodynamic coefficients and stability derivatives for this case are presented in table 6, and the dynamic stability characteristics are discussed in Chapter III.

In general, the lift on the wing was not as large with the end plates above the wing as it was with the end plates below the wing. This is consistent with the results of the planar ground situation for wings with parallel side plates. Evidently, the end plates below the wing increase the pressure far more significantly than the end plates above the wing decrease the pressure.

The results of this non-planar ground case are expected to be very accurate because the ground plane was extended 0.57 chords in the $\pm Y$-direction and from -0.6375 to 1.44 in the X-direction. These dimensions are at least 3 times larger in any direction than the height of the wing from the ground.

e. Discussion of Wings in Tandem in Non-Planar Ground Effect

One of the most complicated problems with regard to wings in ground effect is the situation where two planar or non-planar wings are flying in tandem in the presence of a non-planar ground. Complications occur as a result of the peculiar downwash field induced by the front wing on the rear wing. The approximation that the trailing vortices shed straight back from the wing is probably not very accurate. In the actual situation, the trailing vortices most likely shed at some angle to the X-axis. This angle has a lateral as well as a vertical component. To further complicate the situation, the trailing vortices most likely also have a significant amount of curvature. The positioning of these trailing vortices in relation to the rear wing may or may not significantly affect the values of the overall aerodynamic characteristics such as the lift, induced drag, and moment coefficients. However, this positioning will undoubtedly affect the values of the various stability derivatives. This is especially true for the stability derivatives with respect to w, v, θ, and ψ, the vertical and lateral velocities and the pitch and yaw perturbation angles. Depending on the particular type of non-planar ground situation, the trailing vortices will shift in direction as a result of a perturbation in any of these velocities or angles. However, it is not clear in most cases what magnitude or direction this shift will take. Hence, it is not clear how the downwash distribution at the rear wing will be disturbed with a perturbation in any of these velocities or angles. But since results of calculations on tandem wings in planar ground effect indicate that the stability derivatives with respect to w and θ are controlled mainly by the variation in the downwash distribution at the rear wing, then calculations of these derivatives in non-planar ground situations using the same approximations as with planar ground will probably be significantly in error.

Therefore, a more generalized approach is required for representing the position of the trailing vortices in non-planar ground situations. One such approach would consist of representing the trajectory of each trailing vortex by several straight segments. The angles of each segment could be determined by an iterative procedure. The trailing vortex segments would initially be directed straight back parallel with the freestream direction. The flow field could be solved using the usual vortex-lattice method in conjunction with the source distribution method. The flow direction of the velocity vector would then be calculated at the midpoint of each trailing vortex segment. The angle of the segment would be set parallel to this direction and the flow field would be solved again. This procedure would be continued until further change in the angle of each segment was no longer necessary.

A slightly more complicated approach would consist of representing the trajectory of each trailing vortex by a second order polynomial. The same type of iterative procedure would be used to solve for the proper trailing vortex trajectory, but more complicated equations would be involved.

CHAPTER III

A. Introduction

The results presented in the previous chapter gave an indication of the equilibrium performance capabilities of various planar and non-planar wings in planar and non-planar ground effect. However, these equilibrium parameters (the lift, moment, and induced drag coefficients) do not provide any information about the static and dynamic stability characteristics of these vehicles. An understanding of these stability characteristics is of paramount importance to a complete description of the properties of a wing in ground effect. There have been some previous investigations of the stability characteristics of wings in ground effect, but these investigations have not been very satisfactory. A derivation of the general equations of longitudinal dynamic stability by Kumar (ref. 13) for a wing in ground effect has been found to be erroneous due to the misinterpretation of the stability derivatives with respect to the angle of attack $\frac{w}{U}$ and pitch angle θ, and due to the absence of θ in the equation $\frac{\dot{h}}{U} = \theta - \frac{w}{U}$. These errors tended to underestimate the pitching motion in ground effect. The equations of lateral motion have been presented by Kumar for planar ground effect, but these equations have never been presented for non-planar ground effect. Widnall et al. (ref. 14) have presented a simplified longitudinal stability analysis for the nearly 2-D flow of a ram wing in a channel. However, the X-equation of motion was neglected in this analysis. This led to the erroneous result that single wings are neutrally stable in ground effect.

Therefore, the purpose of this chapter is to investigate the generalized longitudinal and lateral stability of the various wings presented in the results of Chapter II by solving the linearized equations of unsteady motion as applied to planar or non-planar wings in planar or non-planar ground effect. These equations are developed by considering the forces and moments on a wing in a state slightly perturbed from equilibrium.

B. Theoretical Analysis

This perturbed state is illustrated in figures 34, 35, and 36. The coordinate system in which the equations are expressed is one which is rigidly attached to the vehicle. The linearized equations of unsteady motion for arbitrary single or tandem non-planar wings in planar or non-planar ground effect are basically an extension of the equations of motion for wings flying in an infinite medium. However, now there are also force derivatives with respect to such variables as θ, z, κ, y, ϕ, ψ, δ, and ζ. The equations are as follows:

$$\frac{\partial X}{\partial u} u + \frac{\partial X}{\partial w} w + \frac{\partial X}{\partial q} q + \theta\left(\frac{\partial X}{\partial \theta} - mg\cos\theta_o\right) + z\frac{\partial X}{\partial z} + \kappa\frac{\partial X}{\partial \kappa} = m\dot{u}$$

$$\frac{\partial Y}{\partial y} y + \frac{\partial Y}{\partial v} v + \frac{\partial Y}{\partial \dot{v}} \dot{v} + \frac{\partial Y}{\partial p} p + \frac{\partial Y}{\partial r} + \frac{\partial Y}{\partial \phi}\phi + \frac{\partial Y}{\partial \psi}\psi + \frac{\partial Y}{\partial \zeta}\zeta + \frac{\partial Y}{\partial \delta}\delta +$$

$$+ \phi\, mg\cos\theta_o + \psi\, mg\sin\theta_o = m(\dot{v} + rU)$$

$$\frac{\partial Z}{\partial z} z + \frac{\partial Z}{\partial u} u + \frac{\partial Z}{\partial w} w + \frac{\partial Z}{d\dot{w}}\dot{w} + \frac{\partial Z}{\partial q} q + \frac{\partial Z}{\partial \theta}\theta + \frac{\partial Z}{\partial \kappa}\kappa - \theta\, mg\sin\theta_o = m(\dot{w} - qU)$$

$$\frac{\partial L}{\partial y} y + \frac{\partial L}{\partial v} v + \frac{\partial L}{\partial \dot{v}}\dot{v} + \frac{\partial L}{\partial p} p + \frac{\partial L}{\partial r} r + \frac{\partial L}{\partial \phi}\phi + \frac{\partial L}{\partial \psi}\psi + \frac{\partial L}{\partial \zeta}\zeta + \frac{\partial L}{\partial \delta}\delta = I_{xx}\dot{p} - I_{xz}\dot{r}$$

$$\frac{\partial M}{\partial z} z + \frac{\partial M}{\partial u} u + \frac{\partial M}{\partial w} w + \frac{\partial M}{\partial \dot{w}}\dot{w} + \frac{\partial M}{\partial q} q + \frac{\partial M}{\partial \theta}\theta + \frac{\partial M}{\partial \kappa}\kappa = I_{yy}\dot{q}$$

$$\frac{\partial N}{\partial y} y + \frac{\partial N}{\partial v} v + \frac{\partial N}{\partial \dot{v}}\dot{v} + \frac{\partial N}{\partial p} p + \frac{\partial N}{\partial r} r + \frac{\partial N}{\partial \phi}\phi + \frac{\partial N}{\partial \psi}\psi + \frac{\partial N}{\partial \zeta}\zeta + \frac{\partial N}{\partial \delta}\delta = I_{zz}\dot{r} - I_{xz}\dot{p}$$

The (X, Z, M) equations are the longitudinal equations, while the (Y, L, N) are the lateral equations of motion. The two sets of equations are completely decoupled to this approximation, and hence can be solved separately. The derivatives of the forces and moments with respect to the dependent variables appearing in these equations are determined in the following manner. Let the angles of attack of the front and rear wings (we will consider the special case of a single wing later) be α_f and α_r, and let the angles of sideslip be denoted by β_f and β_r. Then,

$$\alpha_f = \alpha_{f_o} + \frac{w}{U} - \frac{q\ell_f}{U}$$

$$\alpha_r = \alpha_{r_o} + \frac{w}{U} - \varepsilon + i_r - i_f + \frac{q\ell_r}{U}$$

$$\beta_f = \frac{v}{U} + \frac{r\ell_f}{U}$$

$$\beta_r = \frac{v}{U} + \sigma - \frac{r\ell_r}{U}$$

where

$$\varepsilon = \varepsilon_o + \frac{\partial\varepsilon}{\partial\alpha_f} d\alpha_f + \frac{\partial\varepsilon}{\partial\dot{\alpha}_f} d\dot{\alpha}_f + \frac{\partial\varepsilon}{\partial h_f} dh_f + \frac{d\varepsilon}{\partial h_r} dh_r + \frac{\partial\varepsilon}{\partial\dot{h}_f} d\dot{h}_f + \frac{\partial\varepsilon}{\partial\theta} d\theta$$

and

$$\sigma = \frac{\partial\sigma}{\partial\beta_f}\beta_f + \frac{\partial\sigma}{\partial\dot{\beta}_f}\dot{\beta}_f + \frac{\partial\sigma}{\partial d_f} d_f + \frac{\partial\sigma}{\partial d_r} d_r + \frac{\partial\sigma}{\partial\dot{\alpha}_f}\dot{\alpha}_f + \frac{\partial\sigma}{\partial p} p + \frac{\partial\sigma}{\partial\phi}\phi + \frac{\partial\sigma}{\partial\psi}\psi$$

It is important to point out the distinction between the angle of attack defined on the plots of the results in Chapter II, and the angle of attack defined in Chapter III. In Chapter II, the angle of attack was defined as the angle between the wing surface and the ground with the wind vector being always parallel to the ground. Hence the lift-curve slope $\frac{\partial C_L}{\partial\alpha}$, and the moment curve slope $\frac{\partial C_m}{\partial\alpha}$ as used in Chapter II refer to the change in lift and moment resulting from a change in the angle between the wing surface and the ground with the wind vector always parallel to the ground. However, in this chapter, the angle of attack is defined as the angle between the wing surface and the relative wind vector. It is possible to have a change in the angle between the wing surface and the relative wind without having a change in the angle between the wing surface and the ground. This would occur when the wing is experiencing a perturbation in vertical velocity only. In terms of the nomenclature of Chapter III, the angle of attack as used in Chapter II is defined as θ . But the change in a quantity with a change in θ with the wind being kept parallel to the ground is defined as

$$\left.\frac{\partial}{\partial\theta}\right|_{\theta = w}$$

In other words, changes in the angle between the wing surface and the ground with the wind always parallel to the ground are changes in θ with w being kept equal to θ . Therefore,

$$\left.\frac{\partial}{\partial\theta}\right|_{\theta = w} = \left.\frac{\partial}{\partial w}\right|_{\theta} + \left.\frac{\partial}{\partial\theta}\right|_{w}$$

where $\left.\frac{\partial}{\partial w}\right|_{\theta}$ is the change in a quantity with a change in the angle between the wing surface and the relative wind with the angle between the wing surface and the ground being kept constant, and $\left.\frac{\partial}{\partial\theta}\right|_{w}$ is the change in a quantity with a change in the angle between the wing surface and the ground with the angle between the wing surface and the relative wind being kept constant. All experimental measurements of changes in aerodynamic characteristics with changes in angles of attack for wings in ground effect have actually been measurements of $\frac{\partial}{\partial\theta}\Big|_{\theta=w}$. These have been measurements of the sum of two effects, $\frac{\partial}{\partial\theta}\Big|_{w}$ and $\frac{\partial}{\partial w}\Big|_{\theta}$. The first effect is a measure of the influence of a change in the geometric orientation of the wing with the external wind direction relative to the wing surface held constant. This effect disappears as $h \rightarrow \infty$. The second effect is a measure of the influence of a change in the angle of attack with the geometric orientation to the ground held constant. This effect approaches the conventional $\frac{\partial}{\partial\alpha}$ as $h \rightarrow \infty$.

The terms $q\ell_f/U$, $q\ell_r/U$, $r\ell_f/U$, $r\ell_r/U$ are included in the expressions for the angles of attack and sideslip only when the separation distances ℓ_f and ℓ_r are much greater than c_f and c_r respectively. Otherwise, the stability derivatives with respect to q must be calculated taking the variation of velocity with chordwise position into account, and the terms $q\ell_f/U$, $q\ell_r/U$, $r\ell_f/U$, $r\ell_r/U$ are no longer included in the angles of attack and sideslip.

Also let h_f and h_r be the heights of the 1/4 chord of the front and rear wings above the ground, and let d_f and d_r be the lateral deflections from equilibrium as measured at the 1/4 chord of the front and rear wings. Then,

$$h_f = h_{f_o} + \int_o^t U\theta(\tau)d\tau - (z - z_o)_{c.g.} + b_f\theta$$

$$h_r = h_{r_o} + \int_o^t U\theta(\tau)d\tau - (z - z_o)_{c.g.} + b_r\theta$$

$$d_f = \int_o^t U\psi(\tau)d\tau + y_{c.g.} + b_f\psi$$

$$d_f = \int_o^t U\psi(\tau)d\tau + y_{c.g.} - b_r\psi$$

Using these relationships, the force and moment derivatives can easily be determined. We define the instantaneous (X, Y, Z) forces and (L_M, M, N) moments as follows:

$$X \approx -\Big((C_{D_f}S_f + C_{D_r}S_r) - (C_{L_f}S_f(\frac{w-\dot{\theta}\ell_f}{U}) + C_{L_r}S_r(\frac{w+\dot{\theta}\ell_r}{U})\Big)\tfrac{1}{2}\rho U^2$$

$$Y = (C_{y_f}S_f + C_{y_r}S_r)\tfrac{1}{2}\rho U^2$$

$$Z \approx -(C_{L_f}S_f + C_{L_r}S_r)\tfrac{1}{2}\rho U^2$$

$$L = (C_{\ell_f}S_f c_f + C_{\ell_r}S_r c_r)\tfrac{1}{2}\rho U^2$$

$$M = (C_{M_f}S_f c_f + C_{M_r}S_r c_r)\tfrac{1}{2}\rho U^2$$

$$N = (C_{N_f}S_f c_f + C_{N_r}S_r c_r)\tfrac{1}{2}\rho U^2$$

where the subscripts f and r refer to the front and rear wings respectively. Hence the force and moment derivatives can be expressed as follows:

$$\frac{\partial X}{\partial u} = -\frac{2}{U}(C_{D_f}S_f + C_{D_r}S_r)\tfrac{1}{2}\rho U^2$$

$$\frac{\partial X}{\partial w} = -\left[\left(\frac{\partial C_{D_f}}{\partial \alpha_f}\left(\frac{1}{U}\right) - \frac{\partial C_{D_f}}{\partial \dot{h}_f} - \frac{C_{L_f}}{U}\right)S_f + \left(\frac{\partial C_{D_r}}{\partial \alpha_r}\left(\frac{1}{U}\left(1 - \frac{\partial \varepsilon}{\partial \alpha_f}\right) - \frac{\partial \varepsilon}{\partial \dot{h}_f}\right) - \frac{\partial C_{D_r}}{\partial \dot{h}_r}\right.\right.$$
$$\left.\left. + \frac{\partial C_{D_r}}{\partial \dot{\alpha}_r}\left(\frac{\partial \varepsilon}{\partial h_f} + \frac{\partial \varepsilon}{\partial h_r}\right) - \frac{C_{L_r}}{U}\right) S_r\right] \tfrac{1}{2}\rho U^2$$

$$\frac{\partial X}{\partial q} = -\left[\left(-\frac{\partial C_{D_f}}{\partial \alpha_f}\left(\frac{\ell_f}{U}\right) + \frac{\partial C_{D_f}}{\partial \dot{h}_f} b_f + C_{L_f}\frac{\ell_f}{U} + \boxed{\frac{\partial C_{D_f}}{\partial q}}\right)S_f + \left(\frac{\partial C_{D_r}}{\partial \alpha_r}\left(-\frac{\partial \varepsilon}{\partial \alpha_f}\left(\frac{\ell_f}{U}\right) +\right.\right.\right.$$
$$\left. + \frac{\partial \varepsilon}{\partial \dot{h}_f} b_f + \frac{\ell_r}{U}\right) + \frac{\partial C_{D_r}}{\partial \dot{\alpha}_r}\left(-\frac{\partial \varepsilon}{\partial h_f} b_f + \frac{\partial \varepsilon}{\partial h_r} b_r + \frac{\partial \varepsilon}{\partial \dot{h}_f} U - \left.\frac{\partial \varepsilon}{\partial \theta}\right|_{h_f, h_r, \alpha_r, \alpha_f}\right)$$
$$\left.\left. - \frac{\partial C_{D_r}}{\partial \dot{h}_r} b_r - \frac{C_{L_r}\ell_r}{U}\right) S_r\right] \tfrac{1}{2}\rho U^2$$

$$\frac{\partial Z}{\partial \theta} = -\left[\left(\frac{\partial C_{D_f}}{\partial h_f} b_f + \frac{\partial C_{D_f}}{\partial \dot{h}_f} U + \left.\frac{\partial C_{D_f}}{\partial \theta}\right|_{h_f,\alpha_f}\right)S_f + \left(\frac{\partial C_{D_r}}{\partial \alpha_r}\left(-\frac{\partial \varepsilon}{\partial h_f} b_f +\right.\right.\right.$$
$$\left.\left. + \frac{\partial \varepsilon}{\partial h_r} b_r + \frac{\partial \varepsilon}{\partial \dot{h}_f} U - \left.\frac{\partial \varepsilon}{\partial \theta}\right|_{h_f, h_r, \alpha_f, \alpha_r}\right) - \frac{\partial C_{D_r}}{\partial h_r} b_r \left.\frac{\partial C_{D_r}}{\partial \theta}\right|_{h_f, h_r, \alpha_r, \alpha_f}\right.$$
$$\left.\left. + \frac{\partial C_{D_r}}{\partial \dot{h}_r} U + \frac{\partial C_{D_r}}{\partial \dot{\alpha}_r}\left(\frac{\partial \varepsilon}{\partial h_f} + \frac{\partial \varepsilon}{\partial h_r}\right)U\right)S_r\right]\tfrac{1}{2}\rho U^2$$

$$\frac{\partial Z}{\partial z} = -\left[-\frac{\partial C_{D_f}}{2h_f} S_f + \left(-\frac{\partial C_{D_r}}{\partial h_r} + \frac{\partial C_{D_r}}{\partial \alpha_r}\left(\frac{\partial \varepsilon}{\partial h_f} + \frac{\partial \varepsilon}{\partial h_r}\right)\right)S_r\right]\tfrac{1}{2}\rho U^2$$

$$\frac{\partial Z}{\partial u} = -\frac{2}{U}(C_{L_f}S_f + C_{L_r}S_r)\tfrac{1}{2}\rho U^2$$

$$\frac{\partial Z}{\partial w} = -\left[\left(\frac{\partial C_{L_f}}{\partial \alpha_f}\left(\frac{1}{U}\right) - \frac{\partial C_{L_f}}{\partial \dot{h}_f}\right) S_f + \left(\frac{\partial C_{L_r}}{\partial \alpha_r}\left(\frac{1}{U}\left(1 - \frac{\partial \varepsilon}{\partial \alpha_f}\right) + \frac{\partial \varepsilon}{\partial \dot{h}_f}\right) - \frac{\partial C_{L_r}}{\partial \dot{h}_r} + \right.\right.$$

$$\left.\left. + \frac{\partial C_{L_r}}{\partial \dot{\alpha}_r}\left(\frac{\partial \varepsilon}{\partial h_f} + \frac{\partial \varepsilon}{\partial h_r}\right)\right) S_r\right] \tfrac{1}{2}\rho U^2$$

$$\frac{\partial Z}{\partial q} = -\left[\left(-\frac{\partial C_{L_f}}{\partial \alpha_f}\left(\frac{\ell_f}{U}\right) + \frac{\partial C_{L_f}}{\partial \dot{h}_f} b_f + \boxed{\frac{\partial C_{D_f}}{\partial q}}\right) S_f + \left(\frac{\partial C_{L_r}}{\partial \alpha_r}\left(-\frac{\partial \varepsilon}{\partial \alpha_f}\left(\frac{\ell_f}{U}\right) + \right.\right.\right.$$

$$+ \frac{\partial \varepsilon}{\partial \dot{h}_f} b_f + \frac{\ell_r}{U}\Big) + \frac{\partial C_{L_r}}{\partial \dot{\alpha}_r}\Big(\frac{\partial \varepsilon}{\partial \dot{h}_f} U + \frac{\partial \varepsilon}{\partial \dot{h}_r} U - \frac{\partial \varepsilon}{\partial h_f} b_f + \frac{\partial \varepsilon}{\partial h_r} b_r -$$

$$\left.\left.\left. - \frac{\partial \varepsilon}{\partial \theta}\Big|_{h_f, h_r, \alpha_f, \alpha_r}\right) - \frac{\partial C_{L_r}}{\partial \dot{h}_r} b_r\right) S_r\right] \tfrac{1}{2}\rho U^2$$

$$\frac{\partial Z}{\partial \theta} = -\left[\left(\frac{\partial C_{L_f}}{\partial h_f} b_f + \frac{\partial C_{L_f}}{\partial \dot{h}_f} U + \frac{\partial C_{L_f}}{\partial \theta}\Big|_{h_f, h_r, \alpha_f, \alpha_r}\right) S_f + \left(\frac{\partial C_{L_r}}{\partial \alpha_r}\left(-\frac{\partial \varepsilon}{\partial h_f} b_f + \right.\right.\right.$$

$$\left. + \frac{\partial \varepsilon}{\partial h_r} b_r + \frac{\partial \varepsilon}{\partial \dot{h}_f} U - \frac{\partial \varepsilon}{\partial \theta}\Big|_{h_f, h_r, \alpha_f, \alpha_r}\right) - \frac{\partial C_{L_r}}{\partial h_r} b_r +$$

$$+ \frac{\partial C_{L_r}}{\partial \theta}\Big|_{h_f, h_r, \alpha_f, \alpha_r} + \frac{\partial C_{L_r}}{\partial \dot{h}_r} U +$$

$$\left.\left. + \frac{\partial C_{L_r}}{\partial \dot{\alpha}_r}\left(\frac{\partial \varepsilon}{\partial h_f} + \frac{\partial \varepsilon}{\partial h_r}\right) U\right) S_r\right] \tfrac{1}{2}\rho U^2$$

$$\frac{\partial Z}{\partial z} = -\left(-\frac{\partial C_{L_f}}{\partial h_f} S_f + \left(-\frac{\partial C_{L_r}}{\partial h_r} + \frac{\partial C_{L_r}}{\partial \alpha_r}\left(\frac{\partial \varepsilon}{\partial h_f} + \frac{\partial \varepsilon}{\partial h_r}\right)\right) S_r\right) \tfrac{1}{2}\rho U^2$$

$$\frac{\partial Z}{\partial \dot{w}} = -\left[\frac{\partial C_{L_f}}{\partial \dot{\alpha}_f}\left(\frac{S_f}{U}\right) + \left(\frac{\partial C_{L_r}}{\partial \dot{\alpha}_r}\left(\frac{1}{U} - \frac{\partial \varepsilon}{\partial \alpha_f}\left(\frac{1}{U}\right) + \frac{\partial \varepsilon}{\partial \dot{h}_f}\right) - \right.\right.$$

$$\left.\left. - \frac{\partial C_{L_r}}{\partial \alpha_r} \frac{\partial \varepsilon}{\partial \dot{\alpha}_f} \frac{1}{U}\right) S_r\right] \tfrac{1}{2}\rho U^2$$

$\frac{\partial M}{\partial u} \approx 0$ because at equilibrium $C_{M_f} S_f C_f + C_{M_r} S_r C_r \cong 0$

$$\frac{\partial M}{\partial w} = \Bigg[\Bigg(\frac{\partial C_{M_f}}{\partial \alpha_f}\left(\frac{1}{U}\right) - \frac{\partial C_{M_f}}{\partial \dot{h}_f}\Bigg) S_f C_f + \Bigg(\frac{\partial C_{M_r}}{\partial \alpha_r}\left(\frac{1}{U}\left(1 - \frac{\partial \varepsilon}{\partial \alpha_f}\right) + \frac{\partial \varepsilon}{\partial \dot{h}_f}\right)$$

$$- \frac{\partial C_{M_r}}{\partial \dot{h}_r} + \frac{\partial C_{M_r}}{\partial \dot{\alpha}_r}\left(\frac{\partial \varepsilon}{\partial h_f} + \frac{\partial \varepsilon}{\partial h_r}\right)\Bigg) S_r C_r\Bigg] \tfrac{1}{2}\rho U^2$$

$$\frac{\partial M}{\partial q} = \Bigg[\Bigg(- \frac{\partial C_{M_f}}{\partial \alpha_f}\left(\frac{\ell_f}{U}\right) + \frac{\partial C_{M_f}}{\partial \dot{h}_f} b_f + \boxed{\frac{\partial C_{M_f}}{\partial q}}\Bigg) S_f C_f + \Bigg(\frac{\partial C_{M_r}}{\partial \alpha_r}\Bigg(- \frac{\partial \varepsilon}{\partial \alpha_f}\left(\frac{\ell_f}{U}\right) +$$

$$+ \frac{\partial \varepsilon}{\partial \dot{h}_f} b_f + \frac{\ell_r}{U}\Bigg) + \frac{\partial C_{M_r}}{\partial \dot{\alpha}_r}\Bigg(\frac{-\partial \varepsilon}{\partial \dot{h}_f} U + \frac{\partial \varepsilon}{\partial \dot{h}_r} U -$$

$$- \frac{\partial \varepsilon}{\partial h_f} b_f + \frac{\partial \varepsilon}{\partial h_r} b_r - \frac{\partial \varepsilon}{\partial \theta}\bigg|_{h_f, h_r, \alpha_f, \alpha_r}\Bigg) - \frac{\partial C_{M_r}}{\partial \dot{h}_r} b_r\Bigg) S_r C_r\Bigg] \tfrac{1}{2}\rho U^2$$

$$\frac{\partial M}{\partial \theta} = \Bigg[\Bigg(\frac{\partial C_{M_f}}{\partial h_f} b_f + \frac{\partial C_{M_f}}{\partial \dot{h}_f} U + \frac{\partial C_{M_f}}{\partial \theta}\bigg|_{h_f, h_r, \alpha_f, \alpha_r}\Bigg) S_f C_f +$$

$$+ \Bigg(\frac{\partial C_{M_r}}{\partial \alpha_r}\Bigg(- \frac{\partial \varepsilon}{\partial h_f} b_f + \frac{\partial \varepsilon}{\partial h_r} b_r + \frac{\partial \varepsilon}{\partial \dot{h}_f} U - \frac{\partial \varepsilon}{\partial \theta}\bigg|_{h_f, h_r, \alpha_f, \alpha_r}\Bigg) -$$

$$- \frac{\partial C_{M_r}}{\partial h_r} b_r + \frac{\partial C_{M_r}}{\partial \theta}\bigg|_{h_f, h_r, \alpha_f, \alpha_r} + \frac{\partial C_{M_r}}{\partial \dot{h}_r} U +$$

$$+ \frac{\partial C_{M_r}}{\partial \dot{\alpha}_r}\left(\frac{\partial \varepsilon}{\partial h_r} + \frac{\partial \varepsilon}{\partial h_f}\right) U\Bigg) S_r C_r\Bigg] \tfrac{1}{2}\rho U^2$$

$$\frac{\partial M}{\partial z} = \Bigg[- \frac{\partial C_{M_f}}{\partial h_f} S_f C_f + \Bigg(\frac{-\partial C_{M_r}}{\partial h_r} + \frac{\partial C_{M_r}}{\partial \alpha_r}\left(\frac{\partial \varepsilon}{\partial h_f} + \frac{\partial \varepsilon}{\partial h_r}\right)\Bigg) S_r C_r\Bigg] \tfrac{1}{2}\rho U^2$$

$$\frac{\partial M}{\partial \dot{w}} = \Bigg[\frac{\partial C_{M_f}}{\partial \dot{\alpha}_f}\left(\frac{S_f C_f}{U}\right) + \Bigg(\frac{\partial C_{M_r}}{\partial \dot{\alpha}_r}\left(\frac{1}{U} - \frac{\partial \varepsilon}{\partial \alpha_f}\left(\frac{1}{U}\right) + \frac{\partial \varepsilon}{\partial \dot{h}_f}\right) - \frac{\partial C_{M_r}}{\partial \alpha_r}\frac{\partial \varepsilon}{\partial \dot{\alpha}_f}\left(\frac{1}{U}\right)\Bigg) S_r C_r\Bigg] \tfrac{1}{2}\rho U^2$$

$$\frac{\partial Y}{\partial y} = \left(\frac{\partial C_{y_f}}{\partial d_f} S_f + \left(\frac{\partial C_{y_r}}{\partial \alpha_r} + \frac{\partial C_{y_r}}{\partial \beta_r} \left(\frac{\partial \sigma}{\partial d_f} + \frac{\partial \sigma}{\partial d_r} \right) S_r \right) \right) \tfrac{1}{2} \rho U^2$$

$$\frac{\partial Y}{\partial v} = \left(\left(\frac{1}{U} \frac{\partial C_{y_f}}{\partial \beta_f} + \frac{\partial C_{y_f}}{\partial \dot{d}_f} \right) S_f + \left(\frac{\partial C_{y_r}}{\partial \beta_r} \left(\frac{1}{U} + \frac{1}{U} \frac{\partial \sigma}{\partial \beta_f} + \frac{\partial \sigma}{\partial \dot{d}_f} \right) + \right. \right.$$

$$\left. \left. + \frac{\partial C_{y_r}}{\partial \dot{\beta}_r} \left(\frac{\partial \sigma}{\partial d_f} + \frac{\partial \sigma}{\partial d_r} \right) + \frac{\partial C_{y_r}}{\partial \dot{d}_r} \right) S_r \right) \tfrac{1}{2} \rho U^2$$

$$\frac{\partial Y}{\partial \dot{v}} = \left(\frac{\partial C_{y_f}}{\partial \dot{\beta}_f} \frac{1}{U} S_f + \left(\frac{\partial C_{y_r}}{\partial \dot{\beta}_r} \left(\frac{1}{U} + \frac{\partial \sigma}{\partial \beta_f} \frac{1}{U} + \frac{\partial \sigma}{\partial \dot{d}_f} \right) + \frac{\partial C_{y_r}}{\partial \beta_r} \frac{\partial \sigma}{\partial \dot{\beta}_f} \frac{1}{U} \right) S_r \right) \tfrac{1}{2} \rho U^2$$

$$\frac{\partial Y}{\partial p} = \left(\frac{\partial C_{y_f}}{\partial p} S_f + \left(\frac{\partial C_{y_r}}{\partial p} + \frac{\partial C_{y_r}}{\partial \beta_r} \frac{\partial \sigma}{\partial p} \right) S_r \right) \tfrac{1}{2} \rho U^2$$

$$\frac{\partial Y}{\partial r} = \left(\left(\frac{\partial C_{y_f}}{\partial \beta_f} \frac{\ell_f}{U} + \frac{\partial C_{y_f}}{\partial \dot{d}_f} b_f + \boxed{\frac{\partial C_{y_f}}{\partial r}} \right) S_f + \left(\frac{\partial C_{y_r}}{\partial \beta_r} \left(- \frac{\ell_r}{U} + \frac{\partial \sigma}{\partial b_f} \frac{\ell_f}{U} + \frac{\partial \sigma}{\partial \dot{d}_f} b_f \right) + \right. \right.$$

$$\left. \left. + \frac{\partial C_{y_r}}{\partial \dot{\beta}_r} \left(\frac{\partial \sigma}{\partial \dot{d}_f} U + \frac{\partial \sigma}{\partial d_f} b_f - \frac{\partial \sigma}{\partial d_r} b_r + \frac{\partial \sigma}{\partial \psi} \right) - \frac{\partial C_{y_r}}{\partial \dot{d}_r} \right) S_r \right) \tfrac{1}{2} \rho U^2$$

$$\frac{\partial Y}{\partial \phi} = \left(\frac{\partial C_{y_f}}{\partial \phi} S_f + \left(\frac{\partial C_{y_r}}{\partial \phi} + \frac{\partial C_{y_r}}{\partial \beta_r} \frac{\partial \sigma}{\partial \phi} \right) S_r \right) \tfrac{1}{2} \rho U^2$$

$$\frac{\partial Y}{\partial \psi} = \left(\left(\frac{\partial C_{y_f}}{\partial d_f} b_f + \frac{\partial C_{y_f}}{\partial \dot{d}_f} U + \left. \frac{\partial C_{y_f}}{\partial \psi} \right|_{\beta_f, d_f} \right) S_f + \left(- \frac{\partial C_{y_r}}{\partial \alpha_r} b_r + \right. \right.$$

$$+ \frac{\partial C_{y_r}}{\partial \beta_r} \left(\frac{\partial \sigma}{\partial d_f} b_f - \frac{\partial \sigma}{\partial d_r} b_r + \frac{\partial \sigma}{\partial \dot{d}_f} U + \frac{\partial \sigma}{\partial \psi} \right) +$$

$$\left. \left. + \left. \frac{\partial C_{y_r}}{\partial \psi} \right|_{\beta_r, d_r, d_f, \beta_f} + \frac{\partial C_{y_r}}{\partial \dot{d}_r} U + \frac{\partial C_{y_r}}{\partial \dot{\beta}_r} \left(\frac{\partial \sigma}{\partial d_f} U + \frac{\partial \sigma}{\partial d_r} U \right) \right) S_r \right) \tfrac{1}{2} \rho U^2$$

$$\frac{\partial Y}{\partial \zeta} = 0$$

$$\frac{\partial Y}{\partial \delta} = \left(\frac{\partial C_{y_f}}{\partial d_f} U S_f + (\frac{\partial C_{y_r}}{\partial d_r} U + \frac{\partial C_{y_r}}{\partial \beta_r} U (\frac{\partial \sigma}{\partial d_f} + \frac{\partial \sigma}{\partial d_r})) S_r \right) \tfrac{1}{2} \rho U^2$$

$$\frac{\partial L}{\partial y} = \left(\frac{\partial C_{\ell_f}}{\partial d_f} S_f C_f + (\frac{\partial C_{\ell_r}}{\partial d_r} + \frac{\partial C_{\ell_r}}{\partial \beta_r} (\frac{\partial \sigma}{\partial d_f} + \frac{\partial \sigma}{\partial d_r}) S_r C_r \right) \tfrac{1}{2} \rho U^2$$

$$\frac{\partial L}{\partial v} = \left((\frac{1}{U} \frac{\partial C_{\ell_f}}{\partial \beta_f} + \frac{\partial C_{\ell_f}}{\partial \dot{d}_f}) S_f C_f + (\frac{\partial C_{\ell_r}}{\partial \beta_r} (\frac{1}{U} + \frac{1}{U} \frac{\partial \sigma}{\partial \beta_f} + \frac{\partial \sigma}{\partial \dot{d}_f}) \right.$$

$$\left. + \frac{\partial C_{\ell_r}}{\partial \dot{\beta}_r} (\frac{\partial \sigma}{\partial d_f} + \frac{\partial \sigma}{\partial d_r}) + \frac{\partial C_{\ell_r}}{\partial \dot{d}_r}) S_r C_r \right) \tfrac{1}{2} \rho U^2$$

$$\frac{\partial L}{\partial \dot{v}} = \left(\frac{\partial C_{\ell_f}}{\partial \dot{\beta}_f} \frac{1}{U} S_f C_f + (\frac{\partial C_{\ell_r}}{\partial \dot{\beta}_r} (\frac{1}{U} + \frac{\partial \sigma}{\partial \beta_f} \frac{1}{U} + \frac{\partial \sigma}{\partial \dot{d}_f}) + \frac{\partial C_{\ell_r}}{\partial \beta_r} + \frac{\partial \sigma}{\partial \dot{\beta}_f} \frac{1}{U}) S_r C_r \right) \tfrac{1}{2} \rho U^2$$

$$\frac{\partial L}{\partial p} = \left(\frac{\partial C_{\ell_f}}{\partial p} S_f C_f + (\frac{\partial C_{\ell_r}}{\partial p} + \frac{\partial C_{\ell_r}}{\partial p_r} \frac{\partial \sigma}{\partial p}) S_r C_r \right) \tfrac{1}{2} \rho U^2$$

$$\frac{\partial L}{\partial r} = \left((\frac{\partial C_{\ell_f}}{\partial \beta_f} \frac{\ell_f}{U} + \frac{\partial C_{\ell_f}}{\partial \dot{d}_f} b_f + \boxed{\frac{\partial C_{\ell_f}}{\partial r}}) S_f C_f + (\frac{\partial C_{\ell_r}}{\partial \beta_r} (- \frac{\ell_r}{U} + \frac{\partial \sigma}{\partial \beta_f} \frac{\ell_f}{U} + \frac{\partial \sigma}{\partial \dot{d}_f} b_f) \right.$$

$$\left. + \frac{\partial C_{\ell_r}}{\partial \dot{\beta}_r} (\frac{\partial \sigma}{\partial \dot{d}_f} U + \frac{\partial \sigma}{\partial d_f} b_f - \frac{\partial \sigma}{\partial d_r} b_r + \frac{\partial \sigma}{\partial \psi}) - \frac{\partial C_{\ell_r}}{\partial \dot{d}_r} b_r) S_r C_r \right) \tfrac{1}{2} \rho U^2$$

$$\frac{\partial L}{\partial \phi} = \left(\frac{\partial C_{\ell_f}}{\partial \phi} S_f C_f + (\frac{\partial C_{\ell_r}}{\partial \phi} + \frac{\partial C_{\ell_r}}{\partial \beta_r} \frac{\partial \sigma}{\partial \phi}) S_r C_r \right) \tfrac{1}{2} \rho U^2$$

$$\frac{\partial L}{\partial \psi} = \left((\frac{\partial C_{\ell_f}}{\partial d_f} b_f + \frac{\partial C_{\ell_f}}{\partial \dot{d}_f} U + \left. \frac{\partial C_{\ell_f}}{\partial \psi} \right|_{d_f, \beta_f}) S_f C_f + (- \frac{\partial C_{\ell_r}}{\partial d_r} b_r + \right.$$

$$+ \frac{\partial C_{\ell_r}}{\partial \beta_r} (\frac{\partial \sigma}{\partial d_f} b_f - \frac{\partial \sigma}{\partial d_r} b_r + \frac{\partial \sigma}{\partial \dot{d}_f} U + \frac{\partial \sigma}{\partial \psi}) + \left. \frac{\partial C_{\ell_r}}{\partial \psi} \right|_{\beta_r, d_r, d_f, \beta_f} +$$

$$\left. + \frac{\partial C_{\ell_r}}{\partial \dot{d}_r} U + \frac{\partial C_{\ell_r}}{\partial \dot{\beta}_r} (\frac{\partial \sigma}{\partial d_f} U + \frac{\partial \sigma}{\partial d_r} U)) S_r C_r \right) \tfrac{1}{2} \rho U^2$$

$$\frac{\partial L}{\partial \zeta} = 0$$

$$\frac{\partial L}{\partial \delta} = \left(\frac{\partial C_{\ell_f}}{\partial d_f} U S_f C_f + (\frac{\partial C_{\ell_r}}{\partial d_r} U + \frac{\partial C_{\ell_r}}{\partial \beta_r} U (\frac{\partial \sigma}{\partial d_f} + \frac{\partial \sigma}{\partial d_r})) S_r C_r \right) \tfrac{1}{2} \rho U^2$$

$$\frac{\partial N}{\partial y} = \left(\frac{\partial C_{n_f}}{\partial d_f} S_f C_f + (\frac{\partial C_{n_r}}{\partial d_r} + \frac{\partial C_{n_r}}{\partial \beta_r} (\frac{\partial \sigma}{\partial d_f} + \frac{\partial \sigma}{\partial d_r}) S_r C_r \right) \tfrac{1}{2} \rho U^2$$

$$\frac{\partial N}{\partial v} = \left((\frac{1}{U} \frac{\partial C_{n_f}}{\partial \beta_f} + \frac{\partial C_{n_f}}{\partial \dot{d}_f}) S_f C_f + (\frac{\partial C_{n_r}}{\partial \beta_r} (\frac{1}{U} + \frac{1}{U} \frac{\partial \sigma}{\partial \beta_f} + \frac{\partial \sigma}{\partial \dot{d}_f}) \right.$$
$$\left. + \frac{\partial C_{n_r}}{\partial \dot{\beta}_r} (\frac{\partial \sigma}{\partial d_f} + \frac{\partial \sigma}{\partial d_r}) + \frac{\partial C_{n_r}}{\partial \dot{d}_r}) S_r C_r \right) \tfrac{1}{2} \rho U^2$$

$$\frac{\partial N}{\partial \dot{v}} = \left(\frac{\partial C_{n_f}}{\partial \dot{\beta}_f} \frac{1}{U} S_f C_f + (\frac{\partial C_{n_r}}{\partial \dot{\beta}_r} (\frac{1}{U} + \frac{\partial \sigma}{\partial \beta_f} \frac{1}{U} + \frac{\partial \sigma}{\partial \dot{d}_f}) + \frac{\partial C_{n_r}}{\partial \beta_r} \frac{\partial \sigma}{\partial \dot{\beta}_f} \frac{1}{U}) S_r C_r \right) \tfrac{1}{2} \rho U^2$$

$$\frac{\partial N}{\partial p} = \left(\frac{\partial C_{n_f}}{\partial p} S_f C_f + (\frac{\partial C_{n_r}}{\partial p} + \frac{\partial C_{n_r}}{\partial \beta_r} \frac{\partial \sigma}{\partial p}) S_r C_r \right) \tfrac{1}{2} \rho U^2$$

$$\frac{\partial N}{\partial r} = \left((\frac{\partial C_{n_f}}{\partial \beta_f} \frac{\ell_f}{U} + \frac{\partial C_{\ell_f}}{\partial \dot{d}_f} b_f + \boxed{\frac{\partial C_{N_f}}{\partial r}}) S_f C_f + (\frac{\partial C_{n_r}}{\partial \beta_r} (- \frac{\ell_r}{U} + \frac{\partial \sigma}{\partial \beta_r} \frac{\ell_f}{U} + \frac{\partial \sigma}{\partial \dot{d}_f} b_f) \right.$$
$$\left. + \frac{\partial C_{n_r}}{\partial \dot{\beta}_r} (\frac{\partial \sigma}{\partial \dot{d}_f} U + \frac{\partial \sigma}{\partial d_f} b_f - \frac{\partial \sigma}{\partial d_r} b_r + \frac{\partial \sigma}{\partial \psi}) - \frac{\partial C_{n_r}}{\partial \dot{d}_r} b_r) S_r C_r \right) \tfrac{1}{2} \rho U^2$$

$$\frac{\partial N}{\partial \phi} = \left(\frac{\partial C_{n_f}}{\partial \phi} S_f C_f + (\frac{\partial C_{n_r}}{\partial \phi} + \frac{\partial C_{n_r}}{\partial \beta_r} \frac{\partial \sigma}{\partial \phi}) S_r C_r \right) \tfrac{1}{2} \rho U^2$$

$$\frac{\partial N}{\partial \psi} = \left((\frac{\partial C_{n_f}}{\partial d_f} b_f + \frac{\partial C_{n_f}}{\partial \dot{d}_f} U + \frac{\partial C_{n_f}}{\partial \psi} \Big|_{\beta_f, d_f}) S_f C_f + (- \frac{\partial C_{n_r}}{\partial d_r} b_r \right.$$
$$+ \frac{\partial C_{n_r}}{\partial \beta_r} (\frac{\partial \sigma}{\partial d_f} b_f - \frac{\partial \sigma}{\partial d_r} b_r + \frac{\partial \sigma}{\partial \dot{d}_f} U + \frac{\partial \sigma}{\partial \psi}) + \frac{\partial C_{n_r}}{\partial \dot{d}_r} U +$$

$$+ \frac{\partial C_{n_r}}{\partial \dot{\beta}_r} \left(\frac{\partial \sigma}{\partial d_f} U + \frac{\partial \sigma}{\partial d_r} U\right) + \frac{\partial C_{n_r}}{\partial \psi} \Bigg|_{\beta_r, d_r, d_f, \beta_f} \Big) S_r C_r \Bigg) \tfrac{1}{2} \rho U^2$$

$$\frac{\partial N}{\partial \zeta} = 0$$

$$\frac{\partial N}{\partial \delta} = \left(\frac{\partial C_{n_f}}{\partial d_f} U S_f C_f + \Big(\frac{\partial C_{n_r}}{\partial d_r} U + \frac{\partial C_{n_r}}{\partial \beta_r} U \Big(\frac{\partial \sigma}{\partial d_f} + \frac{\partial \sigma}{\partial d_r} \Big)\Big) S_r C_r \right) \tfrac{1}{2} \rho U^2$$

Note the terms that are within dashed blocks in the equations involving $\partial/\partial q$, $\partial/\partial r$. These terms are included only for single wings or for tandem wings whose distances from the vehicle c. g. are not large compared to their chord lengths so that the vehicle as a whole must be given a perturbation in p, q, or r to determine the overall vehicle stability derivatives with respect to p, q, r. Furthermore, we must set $C_r = 0$ and set $\ell_f = \ell_r = 0$ for these single wings or closely spaced tandem wing vehicles.

All stability derivatives are calculated at the equilibrium position for any given vehicle and assumed to be constant throughout the small perturbations from equilibrium. However, since the reduced frequency for the motion is assumed to be small, the stability derivatives

$$\frac{\partial C_{L_f}}{\partial \dot{\alpha}_f}, \frac{\partial C_{L_r}}{\partial \dot{\alpha}_r}, \frac{\partial C_{L_f}}{\partial \ddot{h}_f}, \frac{\partial C_{L_r}}{\partial \ddot{h}_r}, \frac{\partial C_{M_f}}{\partial \dot{\alpha}_f}, \frac{\partial C_{M_r}}{\partial \dot{\alpha}_r}, \frac{\partial C_{M_f}}{\partial \ddot{h}_f}, \frac{\partial C_{M_r}}{\partial \ddot{h}_r}, \frac{\partial C_{D_f}}{\partial \dot{\alpha}_f},$$

$$\frac{\partial C_{D_r}}{\partial \dot{\alpha}_r}, \frac{\partial C_{D_f}}{\partial \ddot{h}_f}, \frac{\partial C_{D_r}}{\partial \ddot{h}_r}, \frac{\partial C_{y_f}}{\partial \dot{\beta}_f}, \frac{\partial C_{y_r}}{\partial \dot{\beta}_r}, \frac{\partial C_{y_f}}{\partial \ddot{d}_f}, \frac{\partial C_{y_r}}{\partial \ddot{d}_r}, \frac{\partial C_{\ell_f}}{\partial \dot{\beta}_f}, \frac{\partial C_{\ell_r}}{\partial \dot{\beta}_r},$$

$$\frac{\partial C_{\ell_f}}{\partial \ddot{h}_f}, \frac{\partial C_{\ell_r}}{\partial \ddot{h}_r}, \frac{\partial C_{N_f}}{\partial \dot{\beta}_f}, \frac{\partial C_{N_r}}{\partial \dot{\beta}_r}, \frac{\partial C_{N_f}}{\partial \ddot{h}_f}, \frac{\partial C_{N_r}}{\partial \ddot{h}_r}$$

are neglected. All remaining stability derivatives were calculated by the aerodynamic lifting surface computer program.

Now, the linearized equations of unsteady motion are two systems of linear first-order differential equations with initial conditions. This type of system is most easily solved by Laplace transform methods. The resulting solutions can be expressed as:

$$u = \sum_{i=1}^{6} A_{\text{long}_i} e^{\lambda_{\text{long}_i} t}$$

$$z = \sum_{i=1}^{6} B_{\text{long}_i} e^{\lambda_{\text{long}_i} t}$$

$$\kappa = \sum_{i=1}^{6} C_{\text{long}_i} e^{\lambda_{\text{long}_i} t}$$

$$\theta = \sum_{i=1}^{6} \lambda_{\text{long}_i} C_{\text{long}_i} e^{\lambda_{\text{long}_i} t}$$

$$y = \sum_{j=1}^{8} A_{\text{lat}_j} e^{\lambda_{\text{lat}_j} t}$$

$$\zeta = \sum_{j=1}^{8} B_{\text{lat}_j} e^{\lambda_{\text{lat}_j} t}$$

$$\delta = \sum_{j=1}^{8} C_{\text{lat}_j} e^{\lambda_{\text{lat}_j} t}$$

$$\phi = \sum_{j=1}^{8} \lambda_{\text{lat}_j} B_{\text{lat}_j} e^{\lambda_{\text{lat}_j} t}$$

$$\psi = \sum_{j=1}^{8} \lambda_{\text{lat}_j} C_{\text{lat}_j} e^{\lambda_{\text{lat}_j} t}$$

The λ_{long_i}'s and λ_{lat_i}'s are the roots of the characteristic equation for each system, and A_{long_i}'s, B_{long_i}'s, C_{long_i}'s, A_{lat_i}'s, B_{lat_i}'s, and C_{lat_i}'s are determined from the initial conditions. The characteristic equations for the longitudinal and lateral equations will now be presented. Note that each first term is negative.

$$\lambda_{long}^{6}\{+I_{yy}m(Z_{\dot{w}}-m)\} +$$

$$\lambda_{long}^{5}\{-M_{q}m(Z_{\dot{w}}-m)-I_{yy}(X_{u}(Z_{\dot{w}}-m)-mZ_{w})+(Z_{q}+mU)mM_{\dot{w}}\} +$$

$$\lambda_{long}^{4}\{M_{q}(X_{u}(Z_{\dot{w}}-m)-mZ_{w})-I_{yy}(X_{u}Z_{w}-mZ_{z}-Z_{u}X_{w})-M_{\theta}m(Z_{\dot{w}}-m)$$

$$+(Z_{q}+mU)(-X_{u}M_{\dot{w}}+mM_{w})+\widetilde{Z}_{\theta}mM_{\dot{w}}+X_{q}(Z_{u}M_{\dot{w}}-M_{u}(Z_{\dot{w}}-m))\} +$$

$$\lambda_{long}^{3}\{M_{q}(X_{u}Z_{w}-mZ_{z}-Z_{u}X_{w})-I_{yy}(X_{u}Z_{z}-Z_{u}X_{z})+M_{\theta}(X_{u}(Z_{\dot{w}}-m)-mZ_{w})$$

$$-M_{\kappa}m(Z_{\dot{w}}-m)+(Z_{q}+mU)(M_{u}X_{w}-X_{u}M_{w}+mM_{z})+\widetilde{Z}_{\theta}(-X_{u}M_{\dot{w}}+mM_{w})$$

$$+Z_{\kappa}mM_{\dot{w}}+X_{q}(Z_{u}M_{w}-M_{u}Z_{w})+\widetilde{X}_{\theta}(Z_{u}M_{\dot{w}}-M_{u}(Z_{\dot{w}}-m))\} +$$

$$\lambda_{long}^{2}\{M_{q}(X_{u}Z_{z}-Z_{u}X_{z})+M_{\theta}(X_{u}Z_{w}-mZ_{z}-Z_{u}X_{w})+M_{\kappa}(X_{u}(Z_{\dot{w}}-m)-mZ_{w})$$

$$+(Z_{q}+mU)(M_{u}X_{z}-X_{u}M_{z})+\widetilde{Z}_{\theta}(M_{u}X_{w}-X_{u}M_{w}+mM_{z}) +$$

$$+(Z_{\kappa}(-X_{u}M_{\dot{w}}+mM_{w})$$

$$+X_{q}(Z_{u}M_{z}-M_{u}Z_{z})+\widetilde{X}_{\theta}(Z_{u}M_{w}-M_{u}Z_{w})+X_{\kappa}(Z_{u}M_{\dot{w}}-M_{u}(Z_{\dot{w}}-m))\} +$$

$$\lambda_{long}\{M_{\theta}(X_{u}Z_{z}-Z_{u}X_{z})+M_{\kappa}(X_{u}Z_{w}-mZ_{z}-Z_{u}X_{w})+\widetilde{Z}_{\theta}(M_{u}X_{z}-X_{u}M_{z})$$

$$+Z_{\kappa}(M_{u}X_{w}-X_{u}M_{w}+mM_{z})+\widetilde{X}_{\theta}(Z_{u}M_{z}-M_{u}Z_{z})+X_{\kappa}(Z_{u}M_{w}-M_{u}Z_{w})\} +$$

$$\{M_{\kappa}(X_uZ_z-Z_uX_z)+Z_{\kappa}(M_uX_z-X_uM_z)+X_{\kappa}(Z_uM_z-M_uZ_z)\}$$

$$= 0$$

where $\widetilde{X}_{\theta} = X_{\theta}-mg \cos \theta_o$ and $\widetilde{Z}_{\theta} = Z_{\theta}-mg \sin \theta_o$
and where $\widetilde{Y}_{\phi} = Y_{\phi} + mg \cos \theta_o$ and $\widetilde{Y}_{\psi} = Y_{\psi} + mg \sin \theta_o$

$$\lambda_{lat}^8((Y_{\dot{v}}-m)(I_{xx}I_{zz}-I_{xz}^2)) +$$

$$\lambda_{lat}^7((Y_{\dot{v}}-m)(-N_rI_{xx}-I_{zz}L_p-L_rI_{xz}-N_pI_{xz})+Y_v(I_{xx}I_{zz}-I_{xz}^2)+$$

$$+Y_p(I_{xz}N_{\dot{v}}+L_{\dot{v}}I_{zz})+(Y_r-m)(L_{\dot{v}}I_{xz}+I_{xx}N_{\dot{v}})) +$$

$$\lambda_{lat}^6((Y_{\dot{v}}-m)(-I_{xx}N_{\psi}+L_pN_r-I_{zz}L_{\phi}-L_rN_p-I_{xz}N_{\phi}-L_{\psi}I_{xz})+$$

$$Y_v(-N_rI_{xx}-I_{zz}L_p-L_rI_{xz}-N_pI_{xz})+$$

$$+Y_y(I_{xx}I_{zz}-I_{xz}^2)+Y_p(L_rN_{\dot{v}}+I_{xz}N_v-L_{\dot{v}}N_r+L_vI_{zz})+\widetilde{Y}_{\phi}(I_{xz}N_{\dot{v}}+L_{\dot{v}}I_{zz})$$

$$+(Y_r-m)(L_{\dot{v}}N_p+L_vI_{xz}+I_{xx}N_v-L_pN_{\dot{v}})+\widetilde{Y}_{\psi}(L_{\dot{v}}I_{xz}+I_{xx}N_{\dot{v}}))+$$

$$\lambda_{lat}^5((Y_{\dot{v}}-m)(-I_{xx}N_{\delta}+L_pN_{\psi}+L_{\phi}N_r-I_{zz}L_{\zeta}-I_{xz}N_{\zeta}-L_rN_{\phi}-L_{\psi}N_p-L_{\delta}I_{xz})$$

$$+Y_v(-I_{xx}N_{\psi}+L_pN_r-I_{zz}L_{\phi}-L_rN_p-I_{xz}N_{\phi}-L_{\psi}I_{xz})$$

$$+Y_y(-N_rI_{xx}-I_{zz}L_p-L_rI_{xz}-N_pI_{xz})+Y_p(I_{xz}N_y+L_rN_v+L_{\psi}N_{\dot{v}}-$$

$$-L_{\dot{v}}N_{\psi}-L_vN_r+I_{zz}L_y)+\widetilde{Y}_{\phi}(L_rN_{\dot{v}}+I_{xz}N_v-L_{\dot{v}}N_r+L_vI_{zz})+$$

$$+Y_{\zeta}(I_{xz}N_{\dot{v}}+L_{\dot{v}}I_{zz})+(Y_r-m)(L_{\dot{v}}N_{\phi}-L_vN_p+L_yI_{xz}+I_{xx}N_y-$$

$$-L_pN_v-L_{\phi}N_{\dot{v}})+\widetilde{Y}_{\psi}(L_{\dot{v}}N_p+L_vI_{xz}+I_{xx}N_v-L_pN_{\dot{v}})+Y_{\delta}(L_{\dot{v}}I_{xz}+I_{xx}N_{\dot{v}}))+$$

$$
\begin{aligned}
&\lambda_{lat}^{4}((Y_{\dot{v}}-m)(L_pN_\delta+L_\phi N_\psi+L_\zeta N_r-L_rN_\zeta-L_\psi N_\phi-L_\delta N_p)+Y_v(-I_{xx}N_\delta+L_pN_\psi+\\
&\quad +L_\phi N_r-I_{zz}L_\zeta-I_{xz}N_\zeta-L_rN_\phi-L_\psi N_p-L_\delta I_{xz})+Y_y(-I_{xx}N_\psi+L_pN_r-I_{zz}L_\phi-\\
&\quad -L_rN_p-I_{xz}N_\phi-L_\psi I_{xz})+Y_p(L_rN_y+L_\psi N_v+L_\delta N_{\dot{v}}-L_{\dot{v}}N_\delta-L_vN_\psi-L_yN_r)+\\
&\quad +\widetilde{Y}_\phi(I_{xz}N_y+L_rN_v+L_\psi N_{\dot{v}}-L_{\dot{v}}N_\psi-L_vN_r+I_{zz}L_y)+Y_\zeta(L_rN_{\dot{v}}\\
&\quad +I_{xz}N_v-L_{\dot{v}}N_r+L_vI_{zz})+(Y_r-m)(L_{\dot{v}}N_\zeta+L_vN_\phi+L_yN_p-L_p\ N_y-L_\phi N_v-\\
&\quad -L_\zeta N_{\dot{v}})+\widetilde{Y}_\psi(L_{\dot{v}}N_\phi+L_vN_p+L_yI_{xz}+I_{xx}N_y-L_pN_v-L_\phi N_{\dot{v}})+Y_\delta(L_{\dot{v}}N_p+\\
&\quad +L_vI_{xz}+I_{xx}N_v-L_pN_{\dot{v}}))+\\
&\lambda_{lat}^{3}((Y_{\dot{v}}-m)(L_\phi N_\delta+L_\zeta N_\psi-L_\psi N_\zeta-L_\delta N_\phi)+Y_v(L_pN_\delta+L_\phi N_\psi+L_\zeta N_r-L_rN_\zeta-\\
&\quad -L_\psi N_\phi-L_\delta N_p)+Y_y(-I_{xx}N_\delta+L_p\ N_\psi\ +L_\phi N_r-I_{zz}L_\zeta-I_{xz}N_\zeta\ -L_rN_\phi\\
&\quad -L_\psi N_p-L_\delta I_{xz})+Y_p(L_\psi N_y+L_\delta N_v-L_vN_\delta-L_yN_v)+\widetilde{Y}_\phi(L_rN_y+L_\psi N_v+L_\delta N_{\dot{v}}\\
&\quad -L_{\dot{v}}N_\delta-L_vN_\psi-L_yN_r)+Y_\zeta(I_{xz}N_y+L_rN_v+L_\psi N_{\dot{v}}-L_{\dot{v}}N_\psi-L_vN_r+I_{zz}L_y)+\\
&\quad +(Y_r-m)(L_vN_\zeta+L_yN_\phi-L_\phi N_y-L_\zeta N_v)+\widetilde{Y}_\psi(L_{\dot{v}}N_\zeta+L_vN_\phi+L_yN_p-L_pN_y-\\
&\quad -L_\phi N_v-L_\zeta N_{\dot{v}})+Y_\delta(L_{\dot{v}}N_\phi+L_vN_p+L_yI_{xz}+I_{xx}N_y-L_pN_v-L_\phi N_{\dot{v}}))\ +\\
&\lambda_{lat}^{2}((Y_{\dot{v}}-m)(L_\zeta N_\delta-L_\delta N_\zeta)+Y_v(L_\phi N_\delta+L_\zeta N_\psi-L_\psi N_\zeta-L_\delta N_\phi)+Y_y(L_pN_\delta\ +\\
&\quad +L_\phi N_\psi+L_\zeta N_r-L_rN_\zeta-L_\psi N_\phi-L_\delta N_p)+Y_p(L_\delta N_y-L_yN_\delta)+\widetilde{Y}_\phi(L_\psi N_y+\\
&\quad +L_\delta N_v-L_vN_\delta-L_yN_\psi)+Y_\zeta(L_rN_y+L_\psi N_v+L_\delta N_{\dot{v}}-L_{\dot{v}}N_\delta-L_vN_\psi-L_yN_r)+\\
&\quad +(Y_r-m)(L_yN_\zeta-L_\zeta N_y)+\widetilde{Y}_\psi(L_vN_\zeta+L_yN_\phi-L_\phi N_y-L_\zeta N_v)+Y_\delta(L_{\dot{v}}N_\zeta\ +\\
&\quad +L_vN_\phi+L_yN_p-L_pN_y-L_\phi N_v-L_\zeta N_{\dot{v}}))+\\
&\lambda_{lat}(Y_v(L_\zeta N_\delta-L_\delta N_\zeta)+Y_y(L_\phi N_\delta+L_\zeta\ N_\psi\ -L_\psi N_\zeta-L_\delta N_\phi)+\widetilde{Y}_\phi(L_\delta N_y-L_yN_\delta)+\\
&\quad +Y_\zeta(L_\psi N_y+L_\delta N_v-L_vN_\delta-L_yN_\psi)+\widetilde{Y}_\psi(L_yN_\zeta-L_\zeta N_y)+Y_\delta(L_vN_\zeta+L_yN_\phi\\
&\quad -L_\phi N_y-L_\zeta N_v))+Y_y(L_\zeta N_\delta-L_\delta N_\zeta)+Y_\zeta(L_\delta N_y-L_yN_\delta)+Y_\delta(L_yN_\zeta-L_\zeta N_y)=0
\end{aligned}
$$

Note that the last term of the longitudinal equation is identically zero and the last two terms of the lateral equation are identically zero. This can be verified by noting that the force and moment derivatives with respect to z and y are the same as the force and moment derivatives with respect to κ and δ. Also, the partial derivatives with respect to ζ are zero. Therefore, the characteristic equation for longitudinal motion can be reduced to a fifth-order polynomial and the characteristic equation for the lateral motion can be reduced to a sixth order polynomial. Routh's criteria can be applied to these equations to determine whether the roots are stable. However, for these large polynomials, the criteria is long and tedious. Details for applying Routh's criteria to these equations can be found in ref. (13). It is of interest to note that, in satisfying Routh's criteria for dynamic stability, the criteria for static stability is also necessarily satisfied. The coefficients multiplying the first power of λ_{long} and λ^2_{lat} must be less than zero in order that static stability be achieved. These terms are the constant terms after the characteristic equations are reduced to fifth and sixth order polynomials respectively. For wings flying in an infinite medium the characteristic equations reduce to fourth order polynomials and the criterion for static stability for longitudinal motion reduces to the familiar criteria $C_L > 0$, $\frac{\partial C_M}{\partial w} < 0$.

The equations presented above were used as a basis for investigating the dynamic stability of wings in planar and non-planar ground effect. Solutions to these equations were obtained for most of the wings mentioned in section II-C. The roots of the characteristic equations were calculated by computer program and are presented in the following sections. For the tandem wings, the time history of the motion was also calculated.

Crude estimates of the parasitic drag of each of the wings were made, because the total drag, not just the induced drag, was required in the equations of motion. The parasitic drag estimates are presented in Appendix F.

All radii of gyration (except for the tandem wings) were determined assuming a uniform mass distribution while neglecting the mass of all end plates.

The vehicle Froude numbers (U^2/cg) were 21 for the single flat and end-plated wings, 250 for the tandem wings, and 12.5 for the non-planar wings in non-planar ground effect. These Froude numbers represent typical high-speed ground transportation parameters best suited for each type of wing. Since there already were a large number of variable parameters, the Froude numbers were not varied.

C. Results

1. Single Flat Rectangular Wings

Numerical calculations were carried out to determine the stability characteristics of single flat rectangular wings flying in planar ground effect. Cases were solved for aspect ratios of 0.5, 1, 2, and 4, heights ranging from 0.05 to ∞, and angles of attack of 2.5°, 5°, and 10°. The c.g. was placed at the center of pressure on the wing surface.

Root-locus diagrams depicting the variation of the roots of the characteristic equation with height, aspect ratio, and angle of attack are shown in figures 37 through 44. It was found that the flat rectangular wings were not longitudinally stable at any height, aspect ratio, or angle of attack. They were also laterally unstable except for the wings of aspect ratio 0.5 at angle of attack 10°. The fact that the calculations indicated lateral stability for these configurations is surprising. In fact, it is probable that the high angle of attack case for aspect ratio 0.5 was inaccurate. The reason for the inaccuracy is discussed in section II-c, part 2, a.

2. Single Flat Rectangular Wings with End Plates

Numerical calculations were carried out to determine the stability characteristics of ram wing models consisting of a single flat rectangular wing with triangular and rectangular end plates flying in planar ground effect. For the triangular end-plated wing, cases were solved for aspect ratios of 0.5, 1.0, 2.0, heights ranging from 0.05 to 0.5, and angles of attack of 2.5°, 5°, 10°. In each case, the c.g. was placed at the center of pressure on the wing surface; and the end plates were always shaped so that the bottom edge was parallel to the ground in the equilibrium position.

It was decided that the differences between the triangular and rectangular end plates would be brought out more clearly for the high angle of attack, low aspect ratio cases. So these were the only cases solved for the wing with rectangular end plates.

Root-locus diagrams depicting the variation of the roots of the characteristic equation with height, aspect ratio, and angle of attack are shown in figures 45 through 50. In general, it is seen that the ram wing was longitudinally stable below a certain height. This height, however, varied with aspect ratio and angle of attack, as shown in figure 51 for the triangular end-plated wing. Similar behavior is exhibited by the rectangular end-plated wing. In fact, very little difference is found between the triangular end-plated wing and the rectangular end-plated wing. The only basic differences between the behavior of the two types of wings was that the lift developed by the triangular end-plated wing was higher, and the frequency of oscillation for the rectangular end-plated wing was slightly higher than for the triangular end-plated wing in longitudinal motion. However, as previously mentioned, the results for the 10° angle of attack, aspect ratio 0.5 case are probably inaccurate.

The results for lateral stability were completely negative. Regardless of the height above ground, the aspect ratio, angle of attack, and end plating, there was no configuration for which stick-fixed lateral stability was achieved. The laterally unstable character was due principally to the yaw instability of the ram wing.

3. Flat Rectangular Wings Connected in Tandem

Plots of the time required to damp to 1/10 of the original perturbation from equilibrium are shown in figures 52 and 53 for two identical, flat rectangular wings of aspect ratio 1, 2, 4, at angle of attack 2.5°, heights above the ground ranging from 0.05 to 0.3 chords given an initial perturbation of 0.05 chords vertical displacement. Figure 52 is for a wing separation distance of 4 chords. The c.g. was placed at the center of pressure of the over-all vehicle. It is seen that for a given aspect ratio there is an optimum height for which the damping time is minimized. This optimum height decreases with decreasing aspect ratio and also decreases with decreasing wing separation distance. A plot of this optimum height versus aspect ratio and separation distance is shown in figure 54.

It is also seen from figure 55 that for a given aspect ratio there is a critical height above which instability occurs. This critical height decreases with decreasing aspect ratio and also decreases with decreasing wing separation distance. Root-locus diagrams depicting the variation of the roots of the characteristic equation with height, aspect ratio, and separation distance are also shown in figures 56 a, b, c through 58 a, b, c.

4. Non-Planar Wings in Non-Planar Ground Effect

Numerical calculations were carried out to determine the stability characteristics of three cases of single non-planar wings in non-planar ground effect. Schematics of these three cases are shown in Chapter II in figure 25b, c, d. The geometrical details concerning the wing and ground dimensions are explained in section II-C, parts 3c and 3d. Root-locus diagrams depicting the variation of the roots of the characteristic equation for these three cases are shown in figures 59 and 60. Figure 59 shows the roots of the longitudinal equations, while figure 60 shows the roots of the lateral equations.

The root-locus diagram for longitudinal stability shows that all three configurations are unstable. For the two cases with end plates below the wing at angle of attack, an increase in the angle of attack of the top wing segment was longitudinally destabilizing. This is concluded from the fact that the real parts of the roots shifted positively. In fact, the smallest real root went from negative to positive with the change to 5° angle of attack. It is clearly possible that the case with end plates above the wing would become stable if the wing were closer to the ground. This is concluded from the fact that the roots at -1.92 and 0.17 go together and would approach each other as the height above the ground is decreased.

The root locus diagram for lateral stability indicates that all three situations are unstable. Again, an increase in angle of attack is destabilizing. However, in this case it is not clear that a decrease in height for the case with the end plates above the wing would be stabilizing. It would be stabilizing if the roots at -6.1 and 0.29 went together.

CHAPTER IV

In order to investigate the validity of some of the assumptions and idealizations used in the numerical calculations presented in the previous chapters, an experiment was conducted.

This experiment consisted of a wind tunnel study where measurements were taken of the lift and drag on a non-planar wing in planar and non-planar ground effect. This wing was also investigated numerically so that a valuable check could be made between theory and experiment.

The details of this experiment are now presented.

A. Introduction

It was important to investigate the accuracy of the numerical calculations made in Chapters II and III for the most general case possible. It was equally important to be able to investigate the accuracy of the ground representation and the accuracy of the wing representation separately. Therefore, it was decided to make experimental measurements of a non-planar wing model in both planar and non-planar ground effect. Since the method of images was used for planar ground effect, the accuracy of the wing representation could be investigated very well from the planar ground measurements. Then the accuracy of the source distribution method for representing a non-planar ground could be investigated in the experimental measurements with the non-planar ground.

The non-planar wing model used for the experimental measurements is shown in figure 25c. It was described in section II-C, part 2, b and in section II-C, part 3, b as the "Thin Rectangular Wing with End Plates at Angle of Attack Extending Beneath the Wing." The non-planar ground situation investigated was the one described in section II-C, part 3, b. A detailed description of the experimental wing, the wind tunnel, and the ground plane model now follows.

B. Wing Model

A schematic of the experimental wing model is shown in figures 61 and 62. Schematics of the wing supports are shown in figures 63 and 64. Photographs of the model in position in the wind tunnel in close proximity to the non-planar ground model are shown in figure 65. The main requirements for the model besides having the correct planform shape were that it be uncambered and as thin as possible. Therefore, the chordwise thickness distribution was made to resemble a thin wedge. The model was 15" long with a maximum width of 4.5". The maximum thickness was about 1.25%. In the original configuration, the leading edge was given a circular radius of 3/32". The trailing edge was about 1/32" thick. The upper and lower surfaces were straight between the leading and trailing edges but were at an angle to each other. During the course of the experiment, however, the upper surface of the leading edge had to be sanded down to a more streamlined shape to eliminate a small separation bubble which appeared near the leading edge. The new leading edge shape is shown as a dashed line in figure 61. The effects of this change in leading edge were shown mainly in the drag. This will be discussed in more detail in the results of this chapter.

The model was constructed out of aluminum and the supports were constructed out of steel. The side supports were placed so that the model rotated about the one-quarter chord line of the top wing segment. This was consistent with the center of rotation in the numerical calculations. The rear support was placed beneath the centerline of the top wing at about 11.75" to the rear of the leading edge. All supports were streamlined to minimize interference effects.

C. The Wind Tunnel

The wind tunnel used for this study was the Merrill Wind Tunnel at the Graduate Aeronautical Laboratory of the California Institute of Technology. The test section measures 46 by 32 inches and is 9 feet in length. The tunnel is a closed return, constant operating tunnel capable of speeds in excess of 200 feet per second. However, to obtain high enough Reynolds numbers, a speed of 185 ft. per second was used in the tests.

The effect of the wind tunnel walls might be expected to be significant. However, the influence of these walls can be crudely estimated by placing wake system images above and below and on the two sides of the actual wake system. These images induce insignificant velocities at the airfoil locations for two reasons. First, the vorticity representing the various wake image boundaries are of opposite direction and also of nearly equal strength. Therefore, the induced velocity of the pair nearly cancels. Secondly, the image systems are at a distance of at least two chords from the airfoil at their nearest point. This distance results in small induced velocities at the airfoil when compared to the velocity induced by the wake system immediately behind the airfoils. Due to these factors, the wall influences were expected to be small.

D. Ground Plane Model

Schematics of the experimental simulation of the planar and non-planar ground are shown in figures 66 and 67. In general, it resembles a flat plate airfoil, but it is more than 4 times longer than the wing model, and about 9 1/2 times wider. From the numerical results of section II-C, part 2, d we can estimate that the wing model can be as high as 0.45 chords (based on the wing model length) above the experimental ground plane before the finiteness of the ground plane begins to cause significant effects. Holes were made for the wing supports. This was necessary because the balance system for measuring the forces was beneath the test section. A spanwise suction slot was placed at a position about 7 inches in front of the wing model leading edge. The slot, about 0.03" wide, was used to remove the boundary layer on the simulated ground plane. It was placed as close to the wing model leading edge as was possible without disturbing the pressure distribution on the ground plane induced by the model. The ground plane itself was placed in the wind tunnel at a position about 19 inches from the top of the test section. The three suction slot pumping hoses and the wing model supports were inserted through holes in the bottom of the test section. The non-planar segment of the ground plane was about 1.8 inches by 2 inches and was removable so that planar ground as well as non-planar ground measurements could be taken with the same ground plane. The angle of attack of the ground plane was set so the pressures on the top and bottom surfaces were equal.

E. Experimental Measurements

Measurements were taken of the lift and drag on the non-planar wing model at various heights above the simulated ground plane and at various angles of attack. In the planar ground configuration, measurements were taken at heights (measured at the one-quarter chord of the chordwise centerline of the top wing surface) of 0.33 chords, 0.215 chords, and 0.17 chords, and at angles of attack ranging from -5° to 8°. The range of angles of attack was limited by the angles at which the bottom edges of the side plates contacted the ground. In fact, for the 0.17 chord height, only the measurement at the designed angle of attack of 2.5° could be taken because the bottom edges were nearly touching the ground. In the non-planar ground configuration, measurements were taken at heights of 0.33 chords, 0.283 chords, and 0.215 chords, and through a similar range of angles of attack.

In addition, measurements of the pressure distribution along the centerline of the top of the non-planar ground piece, and the pressure distribution along the centerline of the upper and lower surfaces of the top wing segment were taken at the 0.215 chord height. The pressures were measured by a piece of plastic tubing about 0.08 inches in diameter. A small hole was cut into the tubing for static pressure measurements.

All measurements were taken at a wind tunnel dynamic pressure of 38.7 lbs/ft^2. This was equivalent to a velocity of 185.4 ft/sec. Measurements of the dynamic pressure were taken with a calibrated pitot-static pressure measuring device.

The flow Reynolds number based on the chord length of the wing model was 1.35 x 10^6.

F. Experimental Results

Experimental measurements of the lift coefficients as functions of angle of attack and height above the ground are shown in figures 68 through 71 for the planar and non-planar cases. The theoretically predicted results for these cases are also shown in the figures. The above measurements were taken for two different wing model leading edge shapes. This was necessary because the original leading edge shape (a semicircle of radius 3/32 of an inch) produced a small separation bubble about 2 inches in length near the leading edge. This bubble occurred because the flow had a much larger local angle of attack beneath the leading edge than the 2.5° to the freestream. The flow between the wing and ground was slowed down as it attempted to pass through the converging channel produced by the wing and ground. Therefore, the flow near the leading edges went around rather than through the channel. This produced the higher local angle of attack near the leading edge. A second set of measurements were taken with a different leading edge shape. This shape was streamlined to eliminate the separation bubble. As expected, the drag was reduced significantly with the second shape. The lift, however, was not changed significantly except at very high angles of attack.

The measurements taken at the lowest heights for both the planar and non-planar ground were significantly affected by the boundary layer displacement thickness on the ground plane. In the planar ground case, the boundary layer was completely removed 7" ahead of the wing leading edge; however, the extremely large adverse pressure gradient on the ground just ahead of the leading edge of the wing caused transition of the boundary layer to occur. In the non-planar ground case, the boundary layer was not completely removed due to limitations in the suction slot on the non-planar ground piece. Therefore, a turbulent boundary layer developed before the large adverse pressure gradient was encountered. Then the adverse pressure gradient undoubtedly thickened the boundary layer substantially. In both the planar and non-planar cases these effects were very significant. In fact, in the planar ground case, an estimate can be made of this effect. We can assume that the boundary layer became turbulent about two inches ahead of the leading edge of the wing. This assumption is made by considering the plot of the pressure distribution along the centerline of the non-planar ground piece shown in figure 72. The pressure distribution along the centerline of the planar ground situation was expected to be quite similar with the peak in the pressure gradient occurring further upstream. Using the 1/7th power law as a crude approximation for the profile of the turbulent boundary layer, the growth of the displacement thickness can be written as

$$\delta^*(x) \approx 0.00288\, x^{4/5}$$

where x is measured in feet from the origin of the turbulent boundary layer (2 inches upstream of the leading edge of the wing model). This displacement thickness caused an effective ground plane shape which was tilted up at 0.147 degrees. It also decreased the effective height of the wing by 0.0011 chords. However, the numerical solution calculated for this problem in Chapter II indicated that the slope of the curve of the lift as a function of height is approximately 65 at the height of 0.165 chords above the ground (see figure 20). In addition, the partial derivative $\left.\frac{\partial C_L}{\partial \theta}\right|_W$ was approximately 20 at this height. Hence, a simple correction to the measurement can be made as follows:

$$\Delta C_L \approx \frac{\partial C_L}{\partial h}\Delta h + \frac{\partial C_L}{\partial \theta}\Delta\theta \approx .1233$$

This conservative estimate reduces the measured value of the lift coefficient substantially.

This simple type of correction cannot be easily applied to the non-planar ground situation because it was not clear where the turbulent boundary layer effectively originated. In addition, Elder (ref. 16) indicates that transition of the boundary layer occurs earlier on a finite flat plate than on a 2-D flat plate, but it is not clear how the boundary layer grows. Also, the effect of the highly adverse pressure gradient cannot be determined beyond the qualitative deduction that it causes the boundary layer to thicken more rapidly than it would under zero pressure gradient conditions. A plot of the load distribution along the centerline of the top wing segment is shown in figure 73. The numerically predicted load distribution is shown also. The difference in the two distributions is most prominent near the trailing edge where the experimentally predicted load distribution is much larger than expected. This indicates that the rear portion of the wing is effectively closer to the ground than indicated by the numerical results. Hence, the measurement at the height of 0.215 chords in the presence of the non-planar ground is not a valid comparison to the equivalent numerical results.

The experimental measurements were also affected by the wing leading edge shape. A semi-circular leading edge shape caused a separation bubble to occur near the leading edge, whereas the streamlined leading edge introduced a small amount of camber. Both shapes should have caused the experimental lift coefficients to be higher than expected. The separation bubble introduced both an effective thickness and camber near the leading edge which should have caused a shift upward in the lift vs. angle of attack curve at each height above the ground. The streamlined leading edge also introduced some camber at the leading edge, and so the lift curves should have been shifted upward by the same reasoning. In general, however, these effects were significant only at the smallest heights above the ground.

The numerically predicted results were in good agreement with the experimental results in all cases considering that the numerical results were for a truncated ground plane which reduced the lift augmentation of the ground. The greatest deviations were at the wing positions nearest the ground. However, in the planar ground case these deviations were accounted for in a simple manner, and in the non-planar ground case the deviations can be explained at least qualitatively.

APPENDIX A

Nomenclature:

γ = efflux rate per unit length of line source

$P(x,y)$= field point at which we wish to find the effect of the line source and point vortex

$\gamma d\xi$ = elemental source of strength $\gamma d\xi$

d = distance of point vortex above the line $y=0$

Γ = circulation about the origin of the point vortex

ℓ = distance of vortex from Y-axis

R = distance from incremental source to $P(x,y)$

β = angle between R and the X-axis

It is the purpose of this appendix to prove that the velocity induced by a single point vortex together with an infinite line source, whose source strength distribution satisfies the condition that there is no normal flow through it, is equivalent to the velocity induced by a point vortex and its image.

The stream function associated with the incremental source (see figure 74) is

$$d\psi = -\frac{\gamma d\xi \beta}{2\pi}$$

The complete stream function resulting from the entire line source from $-A$ to A is found by integrating from $\xi=-A$ to $\xi=A$

$$\psi = \int_{-A}^{A} -\frac{\gamma}{2\pi}\beta d\xi$$

but $$\beta = \tan^{-1}\left(\frac{y}{x-\xi}\right)$$

Hence $$\psi = \int_{-A}^{A} \frac{\gamma(\xi)}{2\pi} \tan^{-1}\left(\frac{y}{x-\xi}\right) d\xi$$

So, $$\psi_T = -\frac{1}{2\pi}\int_{-A}^{A} \gamma(\xi) \tan^{-1}\left(\frac{y}{x-\xi}\right) d\xi + \frac{\Gamma}{2\pi} \ln\left[(x-\ell)^2 + (y-d)^2\right]^{1/2}$$

and
$$\frac{\partial \psi_T}{\partial x} = \frac{1}{2\pi}\int_{-A}^{A} \frac{\gamma(\xi)\, y\, d\xi}{\left[(x-\xi)^2 + y^2\right]} + \frac{\Gamma}{2\pi}\, \frac{(x-\ell)}{\left[(x-\ell)^2 + (y-d)^2\right]}$$

Note that the function

$$f(x) = \frac{\varepsilon}{(x-\xi)^2 + \varepsilon^2}$$

has for small ε a very sharp peak (resonance) at $\xi = x$

Furthermore

$$\int f(x)\, d\xi = \int_{-C}^{C} \frac{\varepsilon\, d\xi}{(x-\xi)^2 + \varepsilon^2} = \int_{-C}^{C} \frac{\frac{d\xi}{\varepsilon}}{\left(\frac{x-\xi}{\varepsilon}\right)^2 + 1}$$

where C is any arbitrary end point of integration

Let $\tau = \frac{\xi - x}{\varepsilon}$; $\xi = -C \Longrightarrow \tau = -\left(\frac{C+x}{\varepsilon}\right)$

$d\tau = \frac{d\xi}{\varepsilon}$; $\xi = C \Longrightarrow \tau = \frac{C-x}{\varepsilon}$

Hence substituting into the above integral we get

$$\int_{-\left(\frac{C+x}{\varepsilon}\right)}^{\frac{C-x}{\varepsilon}} \frac{d\tau}{\tau^2 + 1} = \tan^{-1}\tau \Big|_{-\left(\frac{C+x}{\varepsilon}\right)}^{\frac{C-x}{\varepsilon}}$$

The limits are proportional to $1/\varepsilon$ and hence as $\varepsilon \to 0$, the value of the integral is

$$\tan^{-1}\tau \Big|_{-\infty}^{\infty} = \pi$$

consequently

$$\lim_{\varepsilon \to 0} \frac{\varepsilon}{\pi[(x-\xi)^2+\varepsilon^2]} = \delta(x-\xi)$$

where $\delta(x-\xi)$ is the delta function

Hence letting $y \to 0$ in $\frac{\partial \psi_T}{\partial x}$ we get

$$\left.\frac{\partial \psi_T}{\partial x}\right|_{y=0} = \frac{1}{2}\int_{-A}^{A} \gamma(\xi)\,\delta(x-\xi)\,d\xi + \frac{\Gamma}{2\pi}\,\frac{(x-\ell)}{[(x-\ell)^2+d^2]} = 0$$

Hence

$$0 = \frac{\gamma(x)}{2} + \frac{\Gamma}{2\pi}\,\frac{(x-\ell)}{[(x-\ell)^2+d^2]}$$

Hence

$$\psi_T = \frac{\Gamma}{2\pi^2}\int_{-A}^{A}\frac{(\xi-\ell)}{[(\xi-\ell)^2+d^2]}\tan^{-1}\left(\frac{y}{x-\xi}\right)d\xi + \frac{\Gamma}{2\pi}\ln\left[(x-\ell)^2+(y-d)^2\right]^{1/2}$$

Now, we write the equivalent total stream function for the point vortex and its image. Figure 75 shows the appropriate coordinate system.

The stream function associated with each vortex is (see figure 75)

$$\psi = \frac{\Gamma}{2\pi}\ln r$$

where r is the distance from the point P to the origin of the vortex

Hence the total stream function for the vortex pair is

$$\psi_T = \frac{\Gamma}{2\pi}\left[\ln[(x-l)^2+(y-d)^2]^{1/2} - \ln[(x-l)^2+(y+d)^2]^{1/2}\right]$$

Comparison of the Two Solutions

The stream function solution for the point vortex near a line source was

$$\psi_T = \frac{\Gamma}{2\pi^2}\int_{-A}^{A}\frac{(\xi-l)}{[(\xi-l)^2+d^2]}\tan^{-1}\left(\frac{y}{x-\xi}\right)d\xi + \frac{\Gamma}{2\pi}\ln[(x-l)^2+(y-d)^2]^{1/2}$$

The stream function solution for the vortex pair was

$$\psi_T = \frac{\Gamma}{2\pi}\left[\ln[(x-l)^2+(y-d)^2]^{1/2} - \ln[(x-l)^2+(y+d)^2]^{1/2}\right]$$

We are interested in comparing the two solutions for $y \geq 0$ to determine if they are equal. Indeed, for $A \to \infty$ the two solutions should be equal for $y \geq 0$. Hence, by inspecting the two solutions we see that for the two solutions to be equal as $A \to \infty$ and $y \geq 0$, the following must be true.

$$\frac{\Gamma}{2\pi^2}\int_{-\infty}^{\infty}\frac{(\xi-l)}{[(\xi-l)^2+d^2]}\tan^{-1}\left(\frac{y}{x-\xi}\right)d\xi = -\ln[(x-l)^2+(y+d)^2]^{1/2}$$

This integral is very difficult to evaluate. However, we can make the integral easier by noting that

$$\frac{\partial \psi_T}{\partial x}_{\substack{\text{vortex}\\ + \\ \text{line source}}} = \frac{\partial \psi_T}{\partial x}_{\substack{\text{vortex}\\ \text{pair}}} \qquad \text{as } A \to \infty \,, y \geq 0$$

Therefore, the following must be true:

$$\frac{1}{\pi}\int_{-\infty}^{\infty} \frac{(\xi-\ell)y\,d\xi}{[(\xi-\ell)^2+d^2][(x-\xi)^2+y^2]} = \frac{(x-\ell)}{[(x-\ell)^2+(y+d)^2]}$$

Integration of the above integral will be done by using the residue theorems of complex variables.

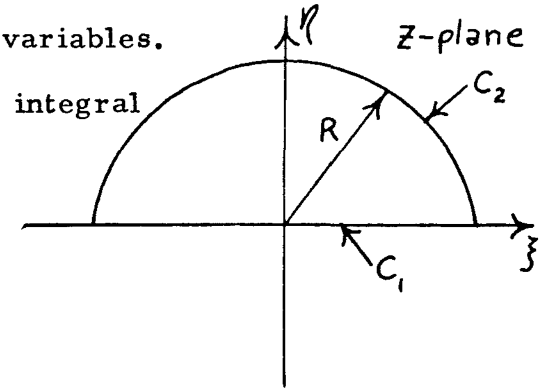

Consider the following integral

$$\frac{1}{\pi}\int_{C} \frac{(z-\ell)y\,dz}{[(z-\ell)^2+d^2][(x-z)^2+y^2]}$$

where $z = \xi + i\eta$

and the contour of integration is the closed semi-circle in the top half of the z -plane as shown in the figure. The integral can be aplit up into two integrals. One along the ξ -axis and the other around the edge of the semi-circle so that

$$\frac{1}{\pi}\int_{C} \frac{(z-\ell)y\,dz}{[(z-\ell)^2+d^2][(x-z)^2+y^2]} = \frac{1}{\pi}\int_{C_1} \frac{(\xi-\ell)y\,d\xi}{[(\xi-\ell)^2+d^2][(x-\xi)^2+y^2]}$$

$$+ \frac{1}{\pi}\int_{C_2} \frac{(z-\ell)y\,dz}{[(z-\ell)^2+d^2][(x-z)^2+y^2]}$$

Consider the integral around the entire curve C. We can determine the poles of the integrand by setting the terms in the brackets in the denominator equal to zero. That is,

$$(z-l)^2 + d^2 = 0$$

$$\Rightarrow \quad z = \frac{2l \pm \sqrt{4l^2 - 4(l^2+d^2)}}{2} = l \pm id$$

$$(x-z)^2 + y^2 = 0$$

$$z = \frac{2x \pm \sqrt{4x^2 - 4(x^2+y^2)}}{2} = x \pm iy$$

Hence the integrand has four simple poles $x \pm iy$ and $l \pm id$

By the Cauchy Integral theorem

$$\int_C f(z)dz = 2\pi i\left(\sum_i K_i\right) \qquad \text{where} \sum_i K_i = \text{sum of the residues of the poles of the integrand}$$

But since we are only interested in the top half of the plane, we need only consider the poles at $x+iy$ and $l+id$.

The integral can now be rewritten as

$$\frac{1}{\pi}\int_C \frac{(z-l)\,y\,dz}{[z-(l+id)][z-(l-id)][z-(x+iy)][z-(x-iy)]} = 2i(K_1+K_2)$$

The residue at the pole $x+iy$ is

$$K_1 = \frac{-i\left[(x-\ell)+iy\right]}{2\left[(x-\ell)+i(y-d)\right]\left[(x-\ell)+i(y+d)\right]}$$

The residue at the pole $\ell + id$ is

$$K_2 = \frac{y}{2\left[(\ell-x)+i(d-y)\right]\left[(\ell-x)+i(d+y)\right]}$$

The value of the integral is then

$$2i(K_1+K_2) = \frac{(x-\ell)}{\left[(\ell-x)^2+(y+d)^2\right.}$$

Hence it has been shown that

$$\frac{1}{\pi}\int_C \frac{(z-\ell)\,y\,dz}{\left[(z-\ell)^2+d^2\right]\left[(x-z)^2+y^2\right]} = \frac{(x-\ell)}{\left[(\ell-x)^2+(y+d)^2\right]}$$

Now consider the integral along the path C_2.

$$\int_{C_2} \frac{(z-\ell)y\,dz}{[(z-\ell)^2+d^2][(x-z)^2+y^2]}$$

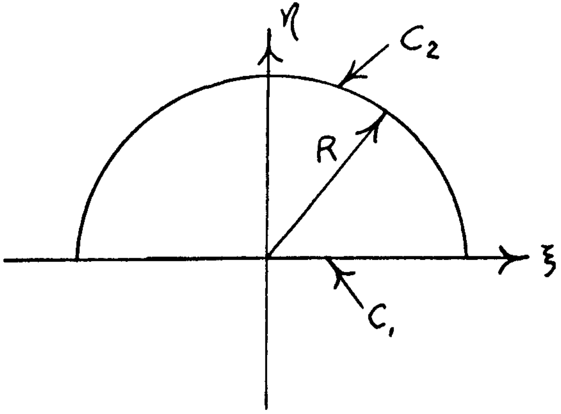

On C_2 , $z = Re^{i\theta}$

$$dz = iRe^{i\theta}d\theta$$

Hence
$$\int_{C_2} \frac{(z-\ell)y\,dz}{[(z-\ell)^2+d^2][(x-z)^2+y^2]} = \int_0^{\pi} \frac{}{[(Re^{i\theta}-\ell)^2+d^2][(x-Re^{i\theta})^2+y^2]}$$

$$\leq \frac{(R-\ell)Ry\pi R}{[(R-\ell)^2-d^2][(x-R)^2-y^2]}$$

Therefore as $R \to \infty$

$$\int_{C_2} \frac{(z-\ell)y\,dz}{[(z-\ell)^2+d^2][(x-z)^2+y^2]} \longrightarrow 0$$

Therefore, we see that as $R \to \infty$

$$\lim_{R\to\infty} \frac{1}{\pi}\int_{C_1} \frac{(\xi-\ell)y\,d\xi}{[(\xi-\ell)^2+d^2][(x-\xi)^2+y^2]} \to \frac{1}{\pi}\int_{-\infty}^{\infty} \frac{(\xi-\ell)y\,d\xi}{[(\xi-\ell)^2+d^2][(x-\xi)^2+y^2]}$$

Therefore we can conclude that

$$\frac{1}{\pi}\int_{-\infty}^{\infty}\frac{(\xi-l)y\,d\xi}{[(\xi-l)^2+d^2][(x-\xi)^2+y^2]}=\frac{(x-l)}{[(l-x)^2+(y+d)^2]}$$

We have shown that the $\frac{\partial\psi_T}{\partial x}$ for both stream functions are equal. If we can also show that $\frac{\partial\psi_T}{\partial y}$ for both stream functions are equal then we can say that both stream functions are equal.

For the point vortex near a line source, as $A\to\infty$

$$\frac{\partial\psi_T}{\partial y}=\frac{\Gamma}{2\pi^2}\int_{-\infty}^{\infty}\frac{}{[(\xi-l)^2+d^2][(x-\xi)^2+y^2]}+\frac{\Gamma(y-d)}{2\pi[(x-l)^2+(y-d)^2}$$

For the vortex pair,

$$\frac{\partial\psi_T}{\partial y}=\frac{\Gamma}{2\pi}\left[\frac{(y-d)}{[(x-l)^2+(y-d)^2]}-\frac{(y+d)}{[(x-l)^2+(y+d)^2]}\right.$$

Hence, we must show that as $A\to\infty$, and for $y\geq 0$

$$\frac{1}{\pi}\int_{-\infty}^{\infty}\frac{(\xi-l)(x-\xi)\,d\xi}{[(\xi-l)^2+d^2][(x-\xi)^2+y^2]}=-\frac{y+d}{[(x-l)^2+(y+d)^2]}$$

To solve the integral on the left hand side we will use the same method as was used in the previous integration, that is Cauchy's Integral theorem. The procedure is quite similar to that of the previous equations, so only the algebra will be shown without explanation until the answer is obtained.

$$K_1 = \frac{-[(x-l)+iy]}{[(x-l)+i(y-d)][(x-l)+i(y+d)]2}$$

$$K_2 = \frac{[(x-l)-id]}{2[(l-x)+i(d-y)][(l-x)+i(d+y)]}$$

$$2i(K_1+K_2) = -\frac{(d+y)}{[(x-l)^2+(y+d)^2]}$$

Therefore $\frac{\partial \psi_T}{\partial y}$ is the same for both stream functions.

Hence we have shown that $\frac{\partial \psi_T}{\partial x}$ and $\frac{\partial \psi_T}{\partial y}$ are the same for both the point vortex near a line source and the vortex pair for $y \geq 0$ given the boundary condition that there is no flow through $y=0$. Therefore it must be true that the stream functions for the two problems are the same for $y \geq 0$ and $|A| \to \infty$.

That is,

$$\frac{\Gamma}{2\pi^2}\int_{-\infty}^{\infty}\frac{(\xi-l)\tan^{-1}\left(\frac{y}{x-\xi}\right)d\xi}{[(\xi-l)^2+d^2]} + \frac{\Gamma}{2\pi}\ln\left[(x-l)^2+(y-d)^2\right]^{1/2}$$

$$= \frac{\Gamma}{2\pi}\ln\left[\left(\frac{(x-l)^2+(y-d)^2}{(x-l)^2+(y+d)^2}\right)^{1/2}\right]$$

APPENDIX B

Arbitrary Velocity of a Point in Space:

Suppose we have a rotating coordinate system with rotation rates (p, q, r). We wish to find the velocity of any point in space relative to the non-rotating coordinate system.

$$\bar{r} = \bar{r}_o + \bar{r}_r$$

$$\dot{\bar{r}} = \dot{\bar{r}}_o + \bar{v}_r + \bar{\omega} \times \bar{r}_r$$

where $\dot{\bar{r}}_o$ = velocity of origin O' relative to O

$\bar{v}_r$ = velocity measured in (x', y', z') coord. system

Let $\bar{r}_r = r_{r_1}\bar{i} + r_{r_2}\bar{j} + r_{r_3}\bar{k} = r'_{r_1}\bar{i}' + r'_{r_2}\bar{j}' + r'_{r_3}\bar{k}'$

$$\Rightarrow \dot{\bar{r}} = \dot{\bar{r}}_o + \bar{v}_r + (p\bar{i} + q\bar{j} + r\bar{k}) \times (r_{r_1}\bar{i} + r_{r_2}\bar{j} + r_{r_3}\bar{k})$$

$$\Rightarrow \dot{\bar{r}} = \dot{\bar{r}}_o + \bar{v}_r + (q r_{r_3} - r r_{r_2})\bar{i} + (r r_{r_1} - p r_{r_3})\bar{j} + (p r_{r_2} - q r_{r_1})\bar{k}$$

APPENDIX C

The velocity induced by the finite length line vortex between (X_1, Y_1, Z_1) and (X_2, Y_2, Z_2) is (see figure 76)

$$\bar{V} = \frac{\Gamma}{4\pi} \frac{\bar{r}_1 \times \bar{r}_2}{|\bar{r}_1 \times \bar{r}_2|^2} \bar{r}_0 \cdot \left(\frac{\bar{r}_1}{|\bar{r}_1|} - \frac{\bar{r}_2}{|\bar{r}_2|} \right)$$

where

$$\bar{r}_0 = (X_2 - X_1 \,,\, Y_2 - Y_1 \,,\, Z_2 - Z_1)$$

$$\bar{r}_1 = (X - X_1 \,,\, Y - Y_1 \,,\, Z - Z_1)$$

$$\bar{r}_2 = (X - X_2 \,,\, Y - Y_2 \,,\, Z - Z_2)$$

Now, let $$\frac{Y_2 - Y_1}{X_2 - X_1} = \tan\beta$$

$$\frac{Z_2 - Z_1}{X_2 - X_1} = \tan\alpha$$

Then, we can write the induced velocity as

$$\bar{V} = \frac{\Gamma}{4\pi} \left[\left(\frac{(Y-Y_1)(Z-Z_2) - (Y-Y_2)(Z-Z_1)}{D} \right) \bar{i} + \left(\frac{(Z-Z_1)(X-X_2) - (Z-Z_2)(X-X_1)}{D} \right) \bar{j} \right.$$

$$\left. + \left(\frac{(X-X_1)(Y-Y_2) - (X-X_2)(Y-Y_1)}{D} \right) \bar{k} \right] \left[\frac{(X_2-X_1)(X-X_1) + (Y_2-Y_1)(Y-Y_1) + (Z_2-Z_1)(Z-Z_1)}{\sqrt{(X-X_1)^2 + (Y-Y_1)^2 + (Z-Z_1)^2}} \right.$$

$$\left. - \frac{(X_2-X_1)(X-X_2) + (Y_2-Y_1)(Y-Y_2) + (Z_2-Z_1)(Z-Z_2)}{\sqrt{(X-X_2)^2 + (Y-Y_2)^2 + (Z-Z_2)^2}} \right]$$

where $$D = \left[(Y-Y_1)(Z-Z_2)-(Y-Y_2)(Z-Z_1)\right]^2 + \left[(Z-Z_1)(X-X_2)-(Z-Z_2)(X-X_1)\right]^2 + \left[(X-X_1)(Y-Y_2)-(X-X_2)(Y-Y_1)\right]^2$$

We want to have (X_2, Y_2, Z_2) all go to infinity while preserving the angles α and β. Hence, we must put all terms involving (X_2, Y_2, Z_2) in terms of α and β. Then we will let $X_2 \to \infty$. This gives,

$$\bar{V} = \frac{\Gamma}{4\pi}\left[\frac{\left[-(Y-Y_1)\tan\alpha+(Z-Z_1)\tan\beta\right]\bar{i}+\left[-(Z-Z_1)+(X-X_1)\tan\alpha\right]\bar{j}+\left[-(X-X_1)\tan\beta+(Y-Y_1)\right]\bar{k}}{\left[-(Y-Y_1)\tan\alpha+(Z-Z_1)\tan\beta\right]^2+\left[-(Z-Z_1)+(X-X_1)\tan\alpha\right]^2+\left[-(X-X_1)\tan\beta+(Y-Y_1)\right]^2}\right] \cdot$$

$$\left[\frac{(X-X_1)+(Y-Y_1)\tan\beta+(Z-Z_1)\tan\alpha}{\sqrt{(X-X_1)^2+(Y-Y_1)^2+(Z-Z_1)^2}} + \sqrt{1+\tan^2\alpha+\tan^2\beta}\right]$$

We are now ready to write down the complete velocity induced by a single horseshoe vortex. This consists of the velocities induced by the bound portion and the two trailing portions. See figure 77.

The total velocity induced by the horseshoe vortex shown on figure 77 is,

$$\bar{V}=\frac{\Gamma}{4\pi}\left[\frac{[(Y-Y_1)(Z-Z_2)-(Y-Y_2)(Z-Z_1)]\bar{i}+[(Z-Z_1)(X-X_2)-(Z-Z_2)(X-X_1)]\bar{j}+[(X-X_1)(Y-Y_2)-(X-X_2)(Y-Y_1)]\bar{k}}{[(Y-Y_1)(Z-Z_2)-(Y-Y_2)(Z-Z_1)]^2+[(Z-Z_1)(X-X_2)-(Z-Z_2)(X-X_1)]^2+[(X-X_1)(Y-Y_2)-(X-X_2)(Y-Y_1)}\right]\cdot$$

$$\left[\frac{(X_2-X_1)(X-X_1)+(Y_2-Y_1)(Y-Y_1)+(Z_2-Z_1)(Z-Z_1)}{\sqrt{(X-X_1)^2+(Y-Y_1)^2+(Z-Z_1)^2}}-\frac{(X_2-X_1)(X-X_2)+(Y_2-Y_1)(Y-Y_2)+(Z_2-Z_1)(Z-Z_2)}{\sqrt{(X-X_2)^2+(Y-Y_2)^2+(Z-Z_2)^2}}\right]$$

$$+\frac{\Gamma}{4\pi}\left[\frac{[(Y-Y_1)\tan\alpha_1-(Z-Z_1)\tan\beta_1]\bar{i}+[(Z-Z_1)-(X-X_1)\tan\alpha_1]\bar{j}+[(X-X_1)\tan\beta_1-(Y-Y_1)]\bar{k}}{[(Z-Z_1)\tan\beta_1-(Y-Y_1)\tan\alpha_1]^2+[(X-X_1)\tan\alpha_1-(Z-Z_1)]^2+[(Y-Y_1)-(X-X_1)\tan\beta_1]^2}\right]\cdot$$

$$\left[\frac{(X-X_1)+(Y-Y_1)\tan\beta_1+(Z-Z_1)\tan\alpha_1}{\sqrt{(X-X_1)^2+(Y-Y_1)^2+(Z-Z_1)^2}}+\sqrt{1+\tan^2\alpha_1+\tan^2\beta_1}\right]$$

$$-\frac{\Gamma}{4\pi}\left[\frac{[(Y-Y_2)\tan\alpha_2-(Z-Z_2)\tan\beta_2]\bar{i}+[(Z-Z_2)-(X-X_2)\tan\alpha_2]\bar{j}+[(X-X_2)\tan\beta_2-(Y-Y_2)]\bar{k}}{[(Z-Z_2)\tan\beta_2-(Y-Y_2)\tan\alpha_2]^2+[(X-X_2)\tan\alpha_2-(Z-Z_2)]^2+[(Y-Y_2)-(X-X_2)\tan\beta_2]^2}\right]\cdot$$

$$\left[\frac{(X-X_2)+(Y-Y_2)\tan\beta_2+(Z-Z_2)\tan\alpha_2}{\sqrt{(X-X_2)^2+(Y-Y_2)^2+(Z-Z_2)^2}}+\sqrt{1+\tan^2\alpha_2+\tan^2\beta_2}\right]$$

This is the velocity induced by a single horseshoe vortex whose trailing vortices are at arbitrary angles to the direction of the freestream.

APPENDIX D

INVESTIGATION OF THE INTEGRAND OF THE VARIOUS INTEGRAL EQUATIONS INVOLVED IN THE REPRESENTATION OF A NON-PLANAR GROUND PLANE (3-D) BY A DISTRIBUTION OF SOURCES AND SINKS

Introduction:

When a non-planar ground plane is represented by a distribution of sources and sinks, one is faced with solving integral equations in order to determine the source strength distribution of the ground plane. Also, after solving for the distribution then, in order to calculate the forces and moments on a wing, one must evaluate an integral representing the effect of the ground plane on the flow at any point in the flow field. Thus it is very important to have an accurate knowledge of the integrand of the various integrals and integral equations before being able to discretize them and numerically calculate solutions on a computer. Therefore, the purpose of this investigation was to gain this desired knowledge.

There are three types of integral equations involved with non-planar wings in non-planar ground effect. One is the integral equation which arises when we attempt to determine the effect of the ground on the surface of the wing when satisfying the boundary condition of no normal flow through the wing surface. Another integral equation arises when we determine the effect of the ground plane when satisfying the boundary condition of no normal flow through the ground. The third integral of importance is the one which must be evaluated when determining the effect of the ground on the horizontal velocity at the quarter chord of each vortex patch. This arises when calculating the lift L. These three integrals are investigated in this appendix.

Integral Equation Arising from Boundary Conditions on the Wing:

In order to calculate the forces and moments on an inviscid representation of a 3-dimensional thin non-planar wing in non-planar ground effect, we must satisfy two boundary conditions in the flow field. One of these boundary conditions is that the flow must be tangential to the wing surface. This boundary condition is expressed mathematically as,

$$(U_\infty+u)n_{w_1}+(V_\infty+v)n_{w_2}+(W_\infty+w)n_{w_3}=0$$

for each point j at which the boundary condition is satisfied

Since we will be solving this equation numerically, we must discretize the wing and satisfy the boundary condition at a finite number of points on the boundary, thereby solving for a finite number of unknowns (that is, a finite number of points in the circulation and source strength distributions).

Therefore we must have an accurate picture of the functions we are discretizing so as to accurately represent them.

But, at each point on the wing surface which we use to satisfy the boundary conditions there is a contribution to the velocity at that point from two different places. That is, the wing induces a velocity at the point and the ground induces a velocity at the point. At this time, we will investigate the velocity induced by the ground at the point.

Since the ground is defined as a set of sources lying at points along the ground, and at each source point there is a different source strength, then we must integrate the effect of all these source points. Mathematically, this integral for each velocity component is,

$$u_g(x_j,y_j,z_j)=\frac{1}{4\pi}\int_{-\infty}^{\infty}\int_{-\infty}^{\infty}\frac{\eta(\xi,\mu,\zeta)(x_j-\xi)\,d\xi\,d\mu\,d\zeta}{[(x_j-\xi)^2+(y_j-\mu)^2+(z_j-\zeta)^2]^{3/2}}$$

$$v_g(x_j,y_j,z_j)=\frac{1}{4\pi}\int_{-\infty}^{\infty}\int_{-\infty}^{\infty}\frac{\eta(\xi,\mu,\zeta)(y_j-\mu)\,d\xi\,d\mu\,d\zeta}{[(x_j-\xi)^2+(y_j-\mu)^2+(z_j-\zeta)^2]^{3/2}}$$

$$w_g(x_j,y_j,z_j)=\frac{1}{4\pi}\int_{-\infty}^{\infty}\int_{-\infty}^{\infty}\frac{\eta(\xi,\mu,\zeta)(z_j-\zeta)\,d\xi\,d\mu\,d\zeta}{[(x_j-\xi)^2+(y_j-\mu)^2+(z_j-\zeta)^2]^{3/2}}$$

However, we want to study the integrals as they appear in the equations for the boundary conditions so we want to consider the integral

$$\int_{-\infty}^{\infty}\int_{-\infty}^{\infty}\eta(\xi,\mu,\zeta)\left[\frac{(x_j-\xi)n_{w_1}+(y_j-\mu)n_{w_2}+(z_j-\zeta)n_{w_3}}{[(x_j-\xi)^2+(y_j-\mu)^2+(z_j-\zeta)^2]^{3/2}}\right]d\xi\,d\mu\,d\zeta$$

It is not necessary to solve a major problem to study this integral. The important thing to notice is that the integrand is the product of two different functions. One function is $\gamma(\xi,\mu,\zeta)$ and the other we will call the kernel function. This kernel function is of a form such that as $(\xi,\mu,\zeta)\rightarrow(x_j,y_j,z_j)$ the kernel function $\rightarrow\infty$. But (x_j,y_j,z_j) are coordinates on the ground. Hence, for a wing boundary condition matching point near the ground, the kernel function has the form of an approximate delta function centered at (x_j,y_j,z_j).

However, $\gamma(\xi,\mu,\zeta)$ depends on the overall gamma distribution of the wing. Hence it should not have as much variation as will the kernel function. So the entire integrand should vary much like the kernel function varies.

To verify this hypothesis, some numerical calculations were made for a wing represented by a single horseshoe vortex flying at 5° angle of attack at a 1/4 chord height of 0.2 chords above the ground. A flat ground plane was used for these calculations. On figures 78 and 79 we see plots of the kernel function and $\gamma(\xi,\mu,\zeta)$ vs. x and y on the ground plane. The matching point for the boundary condition on the wing was at the 3/4 chord so that the matching point was 0.15645 chords above the flat ground plane. We see that the kernel function is quite peaked at $(x=0.75, y=0, z=0)$ which is the smallest possible distance from the matching point. Also $\gamma(\xi,\mu,\zeta)$ varies rapidly near the 1/4 chord, but the kernel function is so small here that it is not very important. Hence, we see that the kernel function definitely dominates the integrand. It has a very large peak near the matching point and dies off very quickly in all directions.

For matching points higher above the ground the peaking is much less pronounced but then the integrand does not die off relative to the peak value so quickly.

Further numerical calculations were made to determine the size of the source sheet distribution required to accurately simulate an infinite ground plane. The results of these calculations indicate that there are several factors which affect the accuracy and the amount of computation time taken to numerically integrate and predict the solution of the horseshoe vortex in ground effect. These factors are: 1) The ratio of the height above the ground to the radius of integration away from the field point being solved, 2) The number of intervals in the area of integration needed to obtain the proper accuracy, and 3) The accuracy required in the actual integration process. We will consider each of these factors in more depth.

Before the study began it was decided that an error of less than 5% was tolerable. Therefore in all phases of the study, 5% was used as the proper error criteria.

It was found that the proper ratio of integration radius to height above the ground was on the order of about 3 in the Y-direction and about 1.75 in the X-direction. These ratios caused errors of about 4% to 5% while all other sources of error were held constant. A graph of the error in the ground induced vertical velocity vs. the ratio of the Y-limits of the finite ground plane to the height above the ground at which the vertical velocity is evaluated, is shown in figure 80.

Integral Equation Arising from Boundary Condition on Ground:

The other boundary condition which must be satisfied when solving inviscid non-planar wings in non-planar ground effect is the condition that there can be no flow through the surface of the ground. This boundary condition is expressed mathematically as (see section titled "Applications to Non-Planar Ground Effect"),

$$\frac{\eta(x_j,y_j,z_j)}{2}+\frac{1}{4\pi}\int_{-\infty}^{\infty}\int_{-\infty}^{\infty}\eta(\xi,\mu,\zeta)\left[\frac{(y_j-\mu)n_{g_2}+(z_j-\zeta)n_{g_3}}{[(x_j-\xi)^2+(y_j-\mu)^2+(z_j-\mu)^2]^{3/2}}\right]d\xi\, d\mu\, d\zeta$$

$$+\frac{\partial\varphi_{H.V.}}{\partial y}n_{g_2}+\frac{\partial\varphi_{H.V.}}{\partial z}n_{g_3}=0$$

This equation results from satisfying, $\bar{V}\cdot\bar{n}=0$ on the ground surface, where $\bar{n}$ = outward normal from the ground surface.

The velocity induced by the ground at any other point on the ground is represented by the integral in the above equation. At the moment we are interested only in this integral. That is, we are concerned with the profile of $\eta(\xi,\mu,\zeta)$ and the kernel function and the product of the two which makes up the entire integrand. Therefore, consider the integral

$$\int_{-\infty}^{\infty}\int_{-\infty}^{\infty}\eta(\xi,\mu,\zeta)\left[\frac{(y_j-\mu)n_{g_2}+(z_j-\zeta)n_{g_3}}{[(x_j-\xi)^2+(y_j-\mu)^2+(z_j-\zeta)^2]^{3/2}}\right]d\xi\, d\mu\, d\zeta$$

As with the wing boundary condition we see that the kernel function of the integrand $\rightarrow\infty$ as $(\xi,\mu,\zeta)\rightarrow(x_j,y_j,z_j)$. Hence the integrand should have a sharp peak where there are corners on the ground plane or discontinuities in the slope of the ground plane. From the nature of the numerator of the kernel function we see that the peaks should be sharper as a function of μ and ρ than as a function of ξ . Also, the integrand as a whole should vary much the same as the kernel function varies.

To verify these hypotheses, some numerical calculations were made for a wing with 45° dihedral, aspect ratio = 4 and angle of attack = 5°, represented by 2 horseshoe vortices, and flying above a non-planar ground plane whose shape resembled a V with each side being 45° to the horizontal. The figure below illustrates the problem.

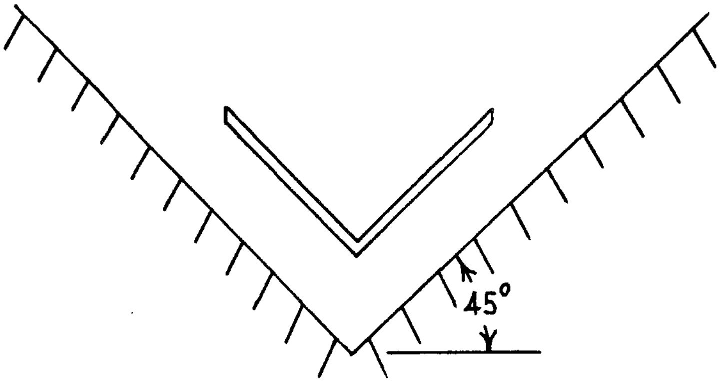

Front View

After observing the numerical calculations it was found that the kernel function of the integral involved in the ground boundary condition did exhibit the distribution that was expected. It was found that the peak of the kernel function occurred at a distance from the corner about equal to the distance of the matching point from the corner along the opposite wall of the ground plane. As the matching point approached the corner, the peak became higher and sharper. In fact, if the matching point is placed at the corner, a singularity occurs in the kernel function at the corner. But if the matching point is not at the corner, then the kernel function goes to zero at the corner. Therefore, we see that the kernel function is a non-uniformly convergent function in the closed region from the corner to infinity. It is a uniformly convergent function in the open interval from the corner to infinity.

It is also apparent from the graphs that if d is the minimum distance of the matching point from the opposing ground plane, then the integration limits need to extend about 4d from the point on the opposing ground plane where the minimum distance occurs from the matching point. This is illustrated more clearly in the figures below.

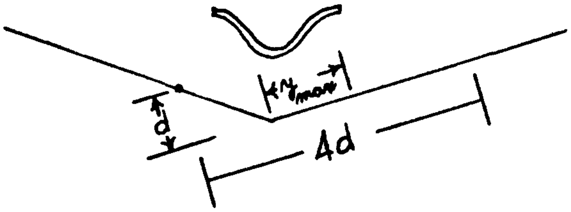

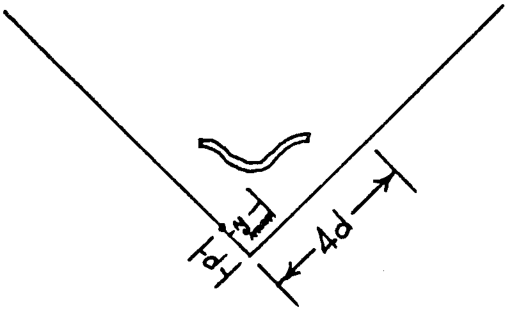

η_{max} = distance from corner to peak of kernel function.

The only location where the kernel function may cause difficulties is at a corner. As mentioned previously, a singularity occurs in the kernel function at the corner. It is important to determine what effect this singularity might have on the flow field. Therefore, let us investigate the boundary condition on the ground at a corner in greater detail. We first investigate the corner boundary condition for two dimensions and then for three dimensions.

Boundary Condition at a Corner in Two Dimensions:

Consider a pair of 2-d point vortices in the presence of an infinite boundary with a corner. The figure below illustrates the problem. Let us represent the presence of the wall by a distribution of sources and sinks all along the wall. Assume we know the strength of the vortices $\pm\Gamma$. Then the only unknown is the source strength distribution along the wall. To determine this distribution we must satisfy the boundary condition at the wall that there can be no normal flow through the wall. Let $\eta(x)$ and $\eta(y)$ be the source strength along x or y. Then

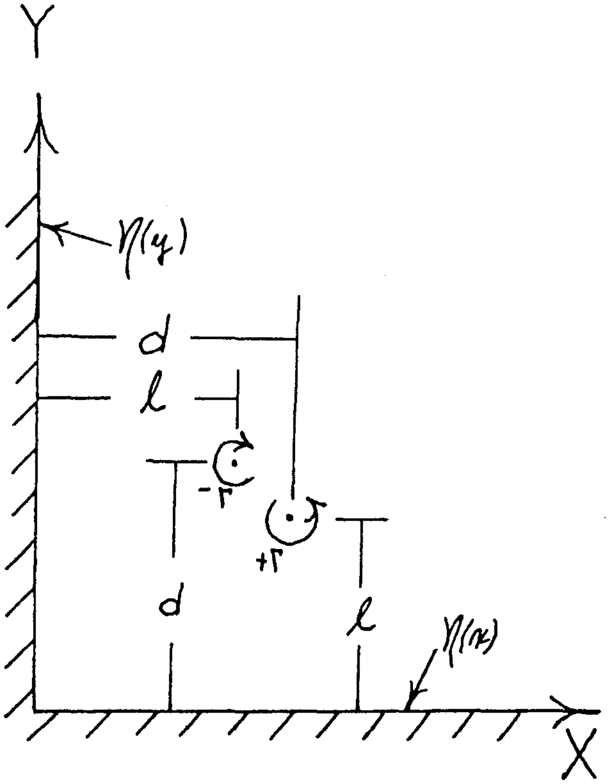

the boundary condition expressed mathematically is,

$$0 = \bar{V}\cdot\bar{n} = \frac{\eta(y)}{2} + \frac{\partial\varphi_v(y)}{\partial x} - \frac{1}{2\pi}\int_0^\infty \frac{\eta(\xi)\,\xi\, d\xi}{\xi^2+y^2}$$

$$0 = \frac{\eta(x)}{2} + \frac{\partial\varphi_v(x)}{\partial y} - \frac{1}{2\pi}\int_0^\infty \frac{\eta(\mu)\,\mu\, d\mu}{\mu^2+x^2}$$

For simplicity, we have chosen to consider a symmetric situation, so that $\eta(x)=\eta(y)$. Then, the two equations defining the boundary condition are identical. Both of these equations are linear Fredholm integral equations of the second kind with a singular kernel. This type of equation has not been solved in closed form. However, iteration procedures have been applied to these problems with some success. That is, an approximate solution can be written as,

$$\eta_n(y) = -2\frac{\partial\varphi_v(y)}{\partial x} + \lambda\int_0^\infty \frac{\eta_{n-1}(\xi)\,\xi\, d\xi}{\xi^2+y^2}$$

where $\eta_0(y) = -2\dfrac{\partial\varphi_v(y)}{\partial x}$

and $\lambda = \dfrac{1}{\pi}$

As $n\to\infty$, the approximate solution converges to the correct solution for sufficiently small λ.

Using this procedure, an attempt was made to develop an approximate solution for $\eta(y)$ and thus examine the behavior of $\eta(y)$ as $y\to 0$. However, due to the complexity of the integrals in the higher order terms, only a first approximation to $\eta(y)$ could be obtained. This approximate solution was rather lengthy so it will not be presented here. However, $\eta(0)$ was determined to be

$$\gamma_1(0) = -2\frac{\partial \varphi_v(0)}{\partial x} + \frac{1}{\pi}\left[\tan^{-1}\left(\frac{\ell}{d}\right) - \tan^{-1}\left(\frac{d}{\ell}\right)\right]$$

Hence, $\gamma_1(0)$ does not $\rightarrow \infty$ as $y \rightarrow 0$ at least to this approximation. However, higher order terms in $\gamma_n(y)$ may $\rightarrow \infty$ as $y \rightarrow 0$. Even if $\gamma(y) \rightarrow \infty$ as $y \rightarrow 0$, this singularity should not adversely affect the flow field anywhere except very near the corner. This conclusion is based on the fact that corners and steps occur quite often in two-dimensional subsonic potential flow problems. The flow is usually affected only in regions very near the corner or step. Hence, although $\gamma(0)$ may $\rightarrow \infty$, the over-all contribution of the corner to the flow field is expected to be small.

An independent method of solving the problem of the point vortices in the presence of a corner is the method of multiple images. That is, three images of the point vortices would be placed in each of the other three quadrants of the x-y plane. The ground boundary condition would be automatically satisfied. Therefore, the flow field is determined merely by summing the velocities induced by all the point vortices in the x-y plane. However, using this method to determine the flow field does not provide any information in examining the ground boundary condition at the corner.

Now, let us consider the same problem in three dimensions.

Boundary Condition at a Corner in 3 Dimensions:

Consider a horseshoe vortex in the presence of an infinite wall in both the X, Y and Z directions. We want to examine the source strength distribution at a corner in the Y, Z -direction. The figure below illustrates the problem: Let us represent the presence of the wall by a distribution of sources and sinks all along the wall. Assume we know the strength of the vortex Γ. Then the only unknown is the source-sink strength distribution along the wall.

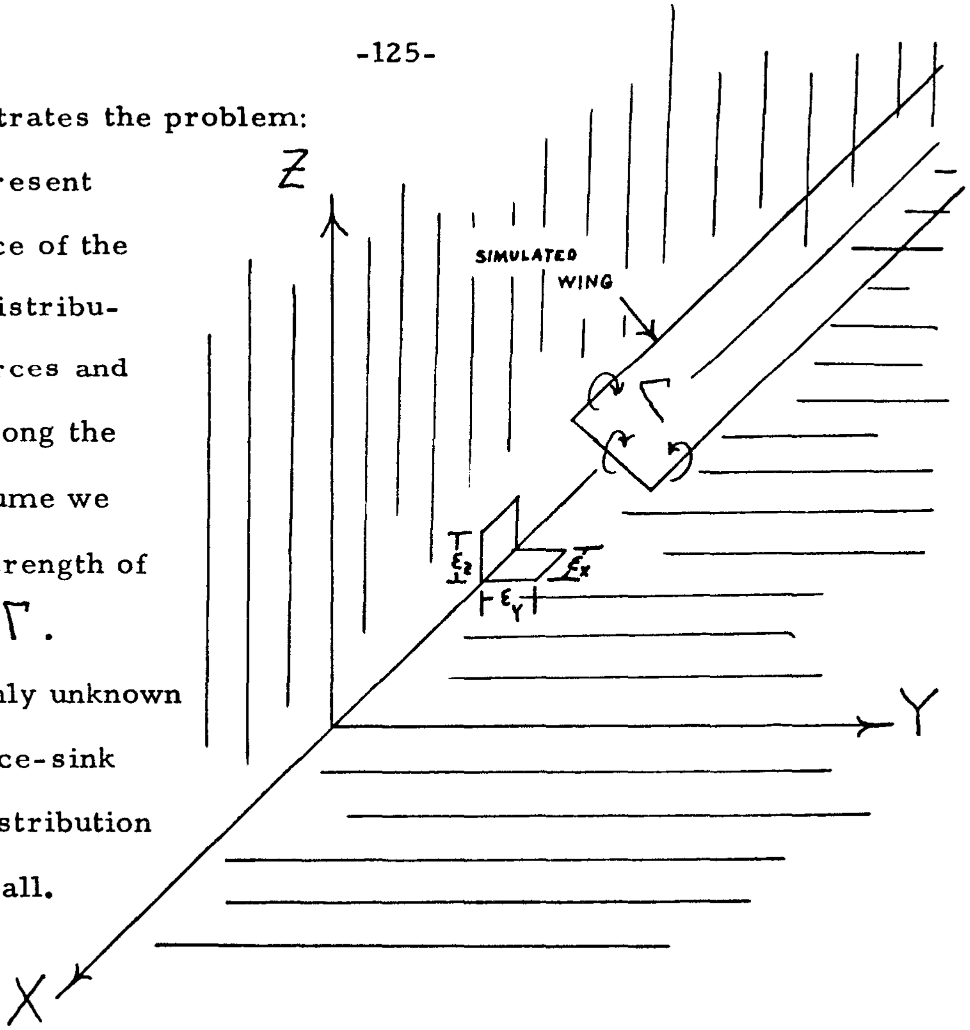

To determine this distribution we must satisfy the boundary condition at the wall that there can be no normal flow through the wall. Let $\eta(x,y)$ and $\eta(x,z)$ be the source-sink strength along the x-y and x-z planes, then the boundary condition expressed mathematically is,

$$0 = \bar{V}\cdot\bar{n} = \frac{\eta(x,z)}{2} + \frac{\partial\varphi_{H.V.}(x,z)}{\partial y} - \frac{1}{4\pi}\int_{-\infty}^{\infty}\int_{0}^{\infty}\frac{\eta(\xi,\mu)\,\mu\,d\mu\,d\xi}{\left[(x-\xi)^2+\mu^2+(z-\rho)^2\right]^{3/2}}$$

$$0 = \frac{\eta(x,y)}{2} + \frac{\partial\varphi_{H.V.}(x,y)}{\partial z} - \frac{1}{4\pi}\int_{-\infty}^{\infty}\int_{0}^{\infty}\frac{\eta(\xi,\rho)\,\rho\,d\rho\,d\xi}{\left[(x-\xi)^2+\rho^2+(y-\mu)^2\right]^{3/2}}$$

In general, it is very difficult, if not impossible, to solve these equations. They are a coupled set of linear singular integral equations of the second kind. An attempt to develop an approximate analytical solution by iteration procedures would also be exceedingly complex because the initial guess at the solution would necessarily be $\frac{\partial \varphi_{H.V.}(x,z)}{\partial y}$ and $\frac{\partial \varphi_{H.V.}(x,y)}{\partial z}$. However, the equations for these functions, as shown in Appendix C, are very long and complex. Even the integrals involved in the first iteration,

$$\int_{-\infty}^{\infty}\int_{0}^{\infty} \frac{\partial \varphi_{H.V.}(\xi,\mu)}{\partial y}\left[\frac{\mu\, d\mu\, d\xi}{[(x-\xi)^2+\mu^2+(z-\rho)^2]^{3/2}}\right]$$

and

$$\int_{-\infty}^{\infty}\int_{0}^{\infty} \frac{\partial \varphi_{H.V.}(\xi,\rho)}{\partial z}\left[\frac{\rho\, d\rho\, d\xi}{[(x-\xi)^2+\rho^2+(y-\mu)^2]^{3/2}}\right]$$

would be impossible to evaluate analytically.

Therefore, a numerical investigation was conducted to determine the behavior of the source strength distribution near a corner. Numerical calculations were performed on the same problem described on p. 120; that is, a thin wing represented by 2 horseshoe vortices, aspect ratio 4, dihedral angle 45°, angle of attack 5°, flying in the presence of two semi-infinite ground planes intersecting at a 90° angle. The 1/4 chord of the vertex of the wing was placed .5 chords above the intersection of the ground planes. The figures below illustrate the situation.

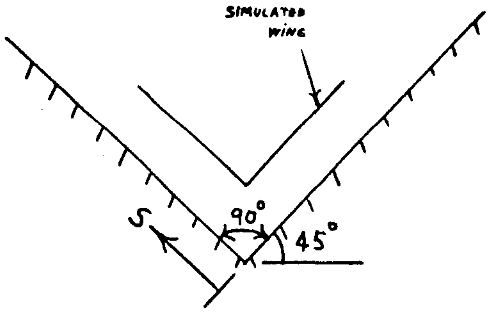

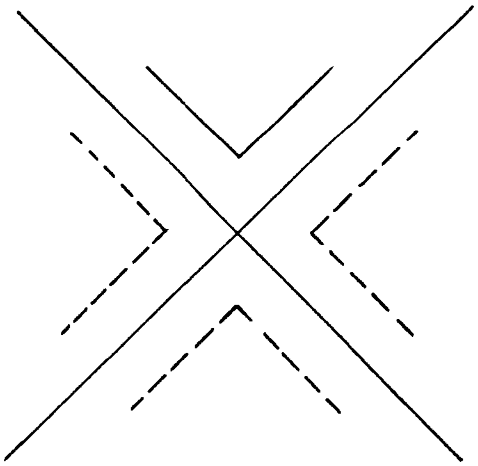

The problem was solved by both the source distribution method and the multiple image method. The agreement between the answers calculated by the two methods was excellent. The source strength distribution as developed by the source distribution method tended to become very large in the region near the corner. To determine the effect of the source strength at the corner on the rest of the source strength distribution and the rest of the flow field, the previously mentioned problem was solved using different pre-set values for the source strength at the corner. These pre-set values at the corner ranged from zero to about twice the source strength of any other point in the distribution. The results showed that the source strength became large near the corner regardless of the value of the source strength at the corner. In fact, the value of the source strength at the corner affected only a small neighborhood near the corner. Some illustrations of the variations in the source strength distribution in the y-z plane with a variation in the value of the source strength at the corner are shown in the figures below.

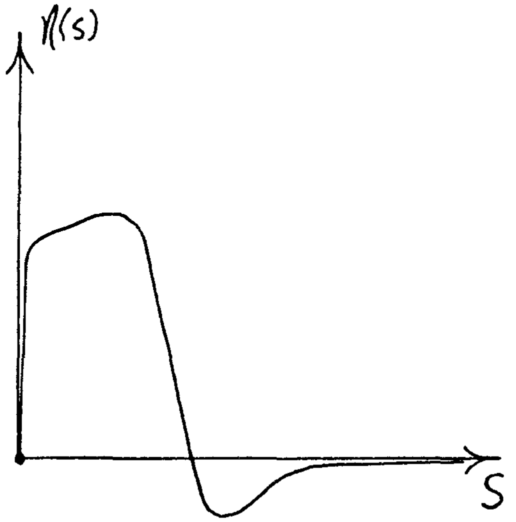

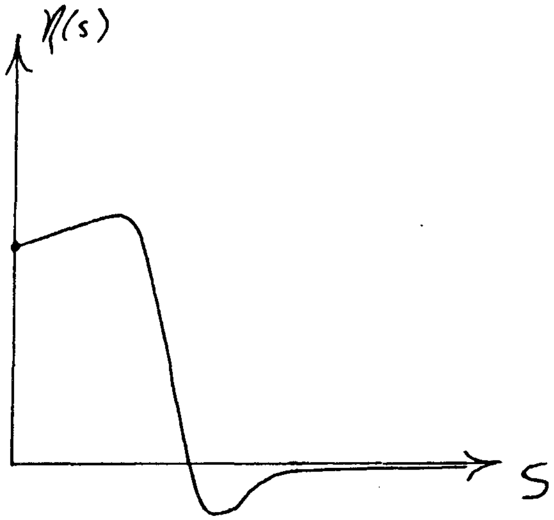

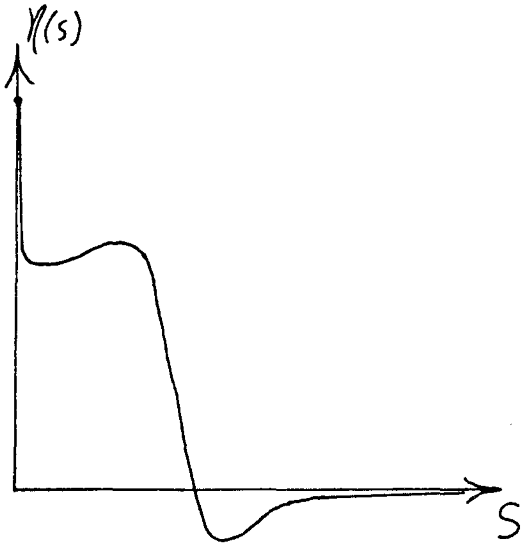

Furthermore, variation in the value of the source strength at the corner caused negligible changes in the calculated lift, drag, and moment coefficients of the wing flying above the corner. However, as the accuracy in the natural representation of the corner was increased, the source strength at the corner tended to grow larger. Therefore, it is probable that the exact source strength at the corner is $\gamma(0) = \infty$. However, this singularity in the source strength at the corner is apparently integrable, and its contribution to the integral over the entire plane is also apparently quite small.

Therefore, a simple method of representing the boundary condition at a corner was incorporated. This method is illustrated in the figure below.

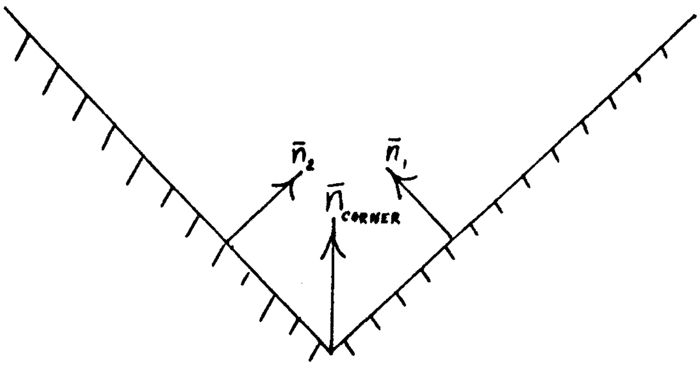

$$\bar{n}_{CORNER} = \frac{\bar{n}_1 + \bar{n}_2}{|\bar{n}_1 + \bar{n}_2|}$$

As the figure illustrates, we assume the direction of the normal at the corner to be the average of the two normal directions of the intersecting segments in the region near the corner. Since the infinite source strength at the corner is caused by the source distribution infinitely near the corner, we now can eliminate the possibility of a numerically computed infinite source strength at the corner by placing the next ground point a finite distance from the ground point at the corner. Although the source strength distribution will be in error near the corner, it will not affect appreciably the overall solution anywhere else as shown by the foregoing analysis.

Integral Arising From Calculation of Horizontal Velocity at 1/4 Chord:

In order to calculate the lift on a non-planar wing in non-planar ground effect, we must evaluate the formula,

$$L = \sum_i 2 t_i \rho U(x_i, y_i, z_i) \Gamma_i n_{w_3}$$

where we have represented the wing by a discrete set of horseshoe vortices, and the ground by a set of sources and sinks. If we know the circulation distribution on the wing and the source-sink strength distribution on the ground, then we need only numerically evaluate the quantity $U(x_i, y_i, z_i)$ at the 1/4 chord of each vortex patch on the wing. Expressing $U(x_i, y_i, z_i)$ mathematically, we have

$$U(x_i, y_i, z_i) = \sum_j u_{v_j}(x_i, y_i, z_i) + \frac{1}{4\pi} \int_{-\infty}^{\infty} \int_{-\infty}^{\infty} \frac{\gamma(\xi, \mu, \zeta)(x_i - \xi)\, d\mu\, d\xi\, d\zeta}{[(x_i - \xi)^2 + (y_i - \mu)^2 + (z_i - \zeta)^2]^{3/2}} + U_\infty$$

where $U_{v_j}(x_i, y_i, z_i)$ = Horizontal velocity induced by the jth horseshoe vortex on the wing

and the integral represents the horizontal velocity induced by the source-sink distribution on the ground. In fact, the purpose of this investigation is to study the behavior of the integral and determine where any difficulties would arise in evaluating it.

We see that the integrand is the product of $\gamma(\xi,\mu,\zeta)$ and a kernel function. As $(\xi,\mu,\zeta)\rightarrow(x_i,y_i,z_i)$ the kernel function $\rightarrow\infty$. Therefore, we can expect a peak in the kernel function near where $\|(x_i-\xi),(y_i-\mu),(z_i-\zeta)\|$ is a minimum. Also, note that when $x_i=\xi$, the kernel function is zero for $y_i\neq\mu$ and/or $z_i\neq\zeta$. So the distribution of this kernel function should be peculiar. One would expect that γ distribution is much more smooth, and that the integrand should vary like the kernel function varies.

To verify these hypotheses, some simple numerical calculations were made with a single horseshoe vortex in flat ground effect at $h/c = 0.2$ above the ground. The other parameters were $AR = 4$, $\alpha = 5°$, $\beta = 0$. All length parameters were non-dimensionalized with respect to the chord. The graphs on the following pages represent the results obtained (see figures 81 through 84).

It is seen that the kernel function has two peaks, one on either side of the minimal distance point on the ground. The sharpness of the peak varies with y and the integrand dies out a lot more slowly than the other integral equations involved in this problem. In fact, a detailed investigation was made to determine the accuracy of the numerical calculation as a function of the integration limits used to calculate the integral. It was found that for reasonable accuracy (25%) we needed to have integration limits greater than 5 times h/c in all directions away from the minimum distance on the ground from (x_i,y_i,z_i). This is illustrated in the figure below.

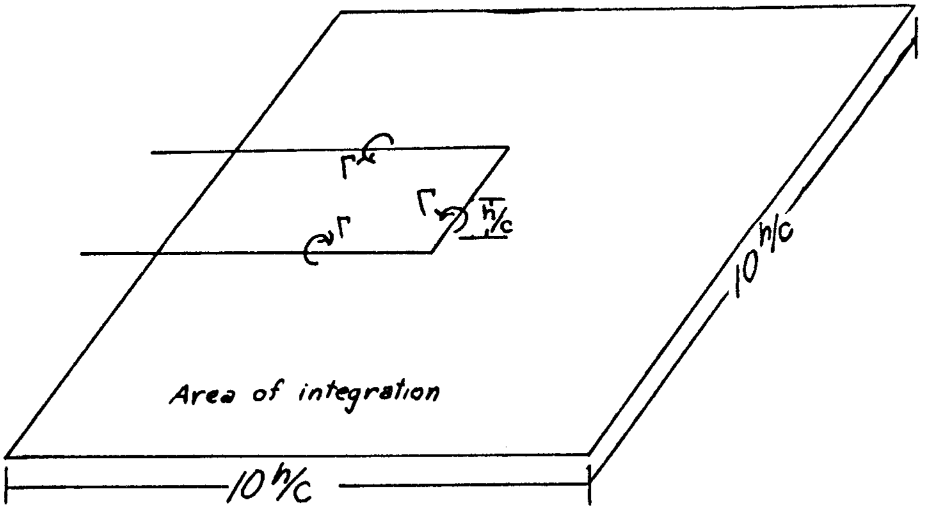

It was also found that the peaks in the kernel function occurred on the ground at a distance of $\sim h/c$ in all directions from the minimum distance from (x_i, y_i, z_i).

Summary of Appendix D

An investigation of the various integrals involved in the source sheet distribution method shows that excellent results can be obtained using this method if certain fundamental restrictions are kept in mind. In general, these restrictions dictate that discrete ground points must be placed in accordance with the peaks of the integrands of the various integrals. These peaks exist due to the nature of the kernel functions which are multiplied by the source strength to comprise the integrand of the various integrals. Figures 85 and 86 are a series of plots of the universal curves representing the normalized value of these kernel functions in terms of the distance away from the point at which the velocity is evaluated. The placement of ground points as well as the spacing between them must be done in accordance with the variation in these curves.

Furthermore, ground points may be placed at corners in the ground plane, so long as the next nearest ground point to the corner is any "finite" distance away from the corner. The source strength distribution at the corner and very near the corner must be in error, but this error does not appreciably affect the flow field anywhere else.

APPENDIX E

NUMERICAL CALCULATIONS OF THE DOWNWASH DISTRIBUTION OF AN ELLIPTICAL PLANFORM WING IN AN UNBOUNDED WING

Calculations were performed to numerically determine the downwash induced by a thin, flat, elliptical planform wing of aspect ratio 8 at an angle of attack of 2.5°. The vortex-lattice method was used to solve the problem. The downwash distribution was determined 100 chords downstream and compared with the theoretically predicted downwash distribution. These results are shown in figure 87. The agreement is very good except near the tips where the numerical solution would be expected to break down. In addition, the numerically computed circulation distribution on the wing was compared to the theoretically predicted circulation distribution and was found to agree excellently. The theoretical distribution was slightly lower near the tips.

The discrepancies near the wing tips resulted from difficulties in representing the geometry accurately near the tips. If a larger number of vortices were placed in the region near the wing tips, the solution would have been more accurate there.

APPENDIX F

PARASITIC DRAG APPROXIMATIONS

Parasitic Drag of a Lifting Flat Plate (Ref. 25)

To take into account the difference in parasitic drag due to lift we take into account the extra drag due to the change in dynamic pressure. That is, the total parasitic drag is the sum of the parasitic drags on the bottom of the wing and the top of the wing.

$$D_p = D_t + D_b = \frac{C_f}{2}\left(\tfrac{1}{2}\rho\right)(q_tS_t+q_bS_b) = \frac{C_f}{2}\tfrac{1}{2}\rho S(q_t+q_b)$$

$$C_{D_p} = \frac{C_f}{4\rho}\frac{(q_tS_t+q_bS_b)}{\frac{1}{2}\rho qS} = C_f\left(\frac{q_t}{q}+\frac{q_b}{q}\right) = C_f\left(2+\frac{q_t-q}{q}+\frac{q_b-q}{q}\right)$$

where $C_f \frac{D}{\frac{1}{2}\rho U^2 2S}$ where S = planform area of wing

Now, as a first approximation assume

$$L = \text{lift} = \rho\,\mathcal{U}\,\Gamma_{avg.}\,b = C_L\tfrac{1}{2}\rho U^2 bc$$

where

$$\Gamma(y) = \int \bar{u}\cdot d\bar{S} = 2u_{avg_x}(y)C$$

$$\Rightarrow \quad \Gamma_{avg} = 2u_{avg}C$$

$$\Rightarrow \quad 2u_{avg} = C_L\tfrac{1}{2}$$

$$\Rightarrow \quad \frac{u_{avg}}{U} = \pm\frac{C_L}{4}$$ where + for top side (suction side) of plate

\- for bottom side (press. side) of plate

$$\Rightarrow \quad q_t-q = \tfrac{1}{2}\rho(U+u)^2-\tfrac{1}{2}\rho U^2 = \tfrac{1}{2}\rho U^2\left(+\frac{\partial u}{U}+\frac{u^2}{U^2}\right)$$

$$q_t-q \approx q\left(\frac{C_L}{2}+\frac{C_L^2}{16}\right)$$

$$q_b - q = \tfrac{1}{2}\rho(U-u)^2 - \tfrac{1}{2}\rho U^2 = \tfrac{1}{2}\rho U^2\left(-\frac{2u}{U} + \frac{u^2}{U^2}\right)$$

$$q_b - q \approx q\left(-\frac{C_L}{2} + \frac{C_L^2}{16}\right)$$

$$\Rightarrow \quad C_{D_p} \approx C_f\left(2 + \frac{C_L}{2} + \frac{C_L^2}{16} - \frac{C_L}{2} + \frac{C_L{}^2}{16}\right) \approx C_f\left(2 + \frac{C_L^2}{8}\right)$$

For the wing used for the dynamic stability study of planar wings in planar ground effect, we have

$U = 200$ ft/sec.

$C = 5$ ft.

$\nu = .15 \times 10^{-3}$ ft^2/sec.

$\Rightarrow$ from skin-friction curves for flat smooth plates,

$C_f \approx .0032$

$$\Rightarrow \quad C_{D_p} \approx 3.2 \times 10^{-3}\left(2 + \frac{C_L^2}{8}\right)$$

$$\Rightarrow \quad \frac{\partial C_{D_p}}{\partial \alpha} \approx C_f\left(\frac{2C_L \frac{\partial C_L}{\partial \alpha}}{8}\right) = \frac{1}{4} C_f C_L \frac{\partial C_L}{\partial \alpha}$$

$$\frac{\partial C_{D_p}}{\partial h} \approx C_f\left(\frac{2C_L \frac{\partial C_L}{\partial h}}{8}\right) = \frac{1}{4} C_f C_L \frac{\partial C_L}{\partial h}$$

$\Rightarrow$ For our problem

$$\frac{\partial C_{D_p}}{\partial \alpha} \approx 8 \times 10^{-4}\, C_L \frac{\partial C_L}{\partial \alpha}$$

$$\frac{\partial C_{D_p}}{\partial h} \approx 8 \times 10^{-4}\, C_L \frac{\partial C_L}{\partial h}$$

Now, we are in a position to calculate total drag derivatives. That is,

$$C_D = C_{D_i} + C_{D_p}$$

$$\Rightarrow \quad \frac{\partial C_p}{\partial \alpha} = \frac{\partial C_{D_i}}{\partial \alpha} + \frac{\partial C_{D_p}}{\partial \alpha}$$

$$\frac{\partial C_D}{\partial h} = \frac{\partial C_{D_i}}{\partial h} + \frac{\partial C_{D_p}}{\partial h}$$

PARASITIC DRAG DUE TO END PLATES (Ref. 25)

End plates cause extra skin-friction drag and interference drag (at the corners).

The extra skin friction drag is just

$$C_{D_{E.P._{\text{Frict.}}}} = 2(2C_f)\frac{S_E}{S}$$

where S_E = planform area of each end plate

S = planform area of wing

The interference drag is accounted for empirically by the following formula:

$$C_{D_{E.P._{\text{inter.}}}} = \frac{2}{\mathit{AR}}\left(.8\left(\frac{t}{c}\right)^3 - .0005\right)$$

where $\frac{t}{c}$ = thickness ratio of wing

Hence the total contribution to the parasitic drag due to the presence of the end plates is

$$C_{D_{E.P.}} = C_{D_{E.P._{\text{frict.}}}} + C_{D_{E.P._{\text{inter.}}}} \doteq 4C_f\frac{S_E}{S} + \frac{2}{\mathit{AR}}\left(.8\left(\frac{t}{c}\right)^3 - .0005\right)$$

For a flat plate of chord length 15 feet, $U_\infty = 100$ ft/sec

$C_f = .003$

$$\Rightarrow \quad C_{D_{E.P.}} = .012\frac{S_E}{S} - \frac{.001}{\mathit{AR}}$$

PARASITIC DRAG FOR NON-PLANAR SINGLE WING

$U = 200$ ft/sec.

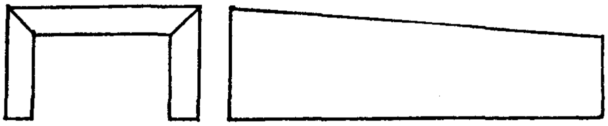

$C = 100$ ft.

$\nu = .15 \times 10^{-3}$ ft^2/sec.

$$Re = \frac{2\text{x}10^2\text{x}10^2}{.15\text{x}10^{-3}} = 1.33\text{x}\ 10^4 \text{ x } 10^3 = 1.33\text{x}10^8$$

from skin-friction curves for flat smooth plates (Hoerner, "Fluid Dynamic Drag" p. 2-6, 1965).

$$C_f \approx .002$$

$$\Rightarrow \quad C_{D_p} = C_f\left(2 + \frac{C_L^2}{8}\right) + 4C_f\frac{S_E}{S} - \frac{.0005}{AR}$$

$$S_E = \tfrac{1}{2}\sin(\theta_{NCT})C^2 + \left(\frac{\ell}{c}\right)c^2$$

$$S = C^2\ AR$$

We have neglected extra skin friction drag due to the lift of the side plates.

$$\Rightarrow \quad \frac{S_E}{S} = \left(\tfrac{1}{2}\sin(\theta_{NCT}) + \frac{\ell}{c}\right)\frac{1}{AR}$$

$$= \quad C_{D_p} \approx .002\left(2 + \frac{C_L^2}{8}\right) + .008\left(\tfrac{1}{2}\sin(\theta_{NCT}) + \frac{\ell}{c}\right)\frac{1}{AR} - \frac{.0005}{AR}$$

REFERENCES

1. Harris, G. L. and Seemann, G. R., "The Terrafoil - A New Concept in High Speed Ground Transportation," High Speed Ground Transportation Journal, Vol. IV, No. 2, May 1970.

2. S. Tomotika, et al., "The Lift on a Flat Plate Near a Plane Wall with Special Reference to the Effect of the Ground on the Lift of a Monoplane Aerofoil." Report of Aeronautics Research Institute, Tokyo Imperial Univ., No. 97 (1933).

3. Bairstow, "Applied Aerodynamics," 1939.

4. C. E. Watkins, et al., "A Systematic Kernel Function Procedure for Determining Aerodynamic Forces on Oscillating or Steady Finite Wings at Subsonic Speeds," NASA Technical Report R-48, 1959.

5. Saunders, G. H., "Aerodynamic Characteristics of Wings in Ground Proximity," Master's Thesis, Massachusetts Institute of Technology, 1963.

6. Ashley, H., Widnall, S., Landahl, M. T., New Directions in Lifting Surface Theory," AIAA Journal 3, No. 1, pp. 3-16, 1965.

7. Shames, "Mechanics of Fluids," McGraw-Hill Publishing Co., 1962.

8. Robinson & Laurmann, "Wing Theory."

9. Perkins & Hage, "Airplane Performance, Stability and Control," Wiley & Sons Publishing Co., 1949.

10. Owen, P. R., Hogg, H., "Ground Effect on Downwash with Slipstream," Aeronautical Research Council Reports and Memoranda No. 2449, 1952.

11. Bernard Etkin, "Dynamics of Flight, Stability and Control," Wiley & Sons Publishing Co., 1959.

12. Ashley & Landahl, "Aerodynamics of Wings and Bodies," Addison-Wesley Publishing Co., 1965.

13. Kumar, P. E., "On the Longitudinal Stability of a Ground Effect Wing," College of Aeronautics, Cranfield, Report No. 202.

14. Barrows, T. M., Widnall, S. E., Richardson, H. H., "The Use of Aerodynamic Lift for Application to High Speed Ground Transportation," Office of High Speed Ground Transportation, Dept. of Transportation, Report FRE-RT-71-56, June 1970.

15. Silverstein, Abe, and Katzoff, S., "Design Charts for Predicting Downwash Angles and Wake Characteristics Behind Plain and Flapped Wings," NACA Report No. 648, 1939.

16. Elder, "The Flow Past a Flat Plate of Finite Width," JFM, Vol. 9, 1960, p. 133.

17. Davis, Joseph, "Longitudinal Stability of Tandem Planar Wings in Ground Effect," Aerospace Technology, Inc., Report No. 71-07, Feb. 1971.

18. Davis, Joseph, "Dynamic Stability of End-Plated Ram Wings in Planar Ground Effect," Aerospace Technology, Inc., Report No. 71-15, April 1971.

19. Widnall, S. E., and Barrows, T. M., "An Analytic Solution for Two and Three Dimensional Wings in Ground Effect," Massachusetts Institute of Technology Fluid Dynamics Research Laboratory, Report No. 69-1, June 1969.

20. Falkner, V. M., "The Calculation of Aerodynamic Loading on Surfaces of Any Shape," R & M 1910, 1943, British Aeronautical Research Council.

21. Giesing, Joseph P., "Lifting Surface Theory for Wing-Fuselage Combinations," McDonnell-Douglas Corp., Report DAC-67212, Vol. I-II, August 1, 1968.

22. James, R. M., "On the Remarkable Accuracy of the Vortex Lattice Discretization in Thin Wing Theory," McDonnell-Douglas Corp., Report No. DAC-67211, Feb. 1969.

23. Kalman, T. P., et al., "Application of the Doublet-Lattice Method of Nonplanar Configurations in Subsonic Flow," AIAA Atmospheric Flight Mechanics Conference Paper No. 70-539, May 1970.

24. Kohlman, D., "A Theoretical Method of Determining the Ground Effect on Lift and Pitching Moment for Wings of Arbitrary Planform," Boeing Document D3-1861, October 1958.

25. Hoerner, "Fluid Dynamic Drag," 1964.

26. Katzoff, S., and Sweberg, Harold H., "Ground Effect on Downwash Angles and Wake Location," NACA Report No. 738, 1943.

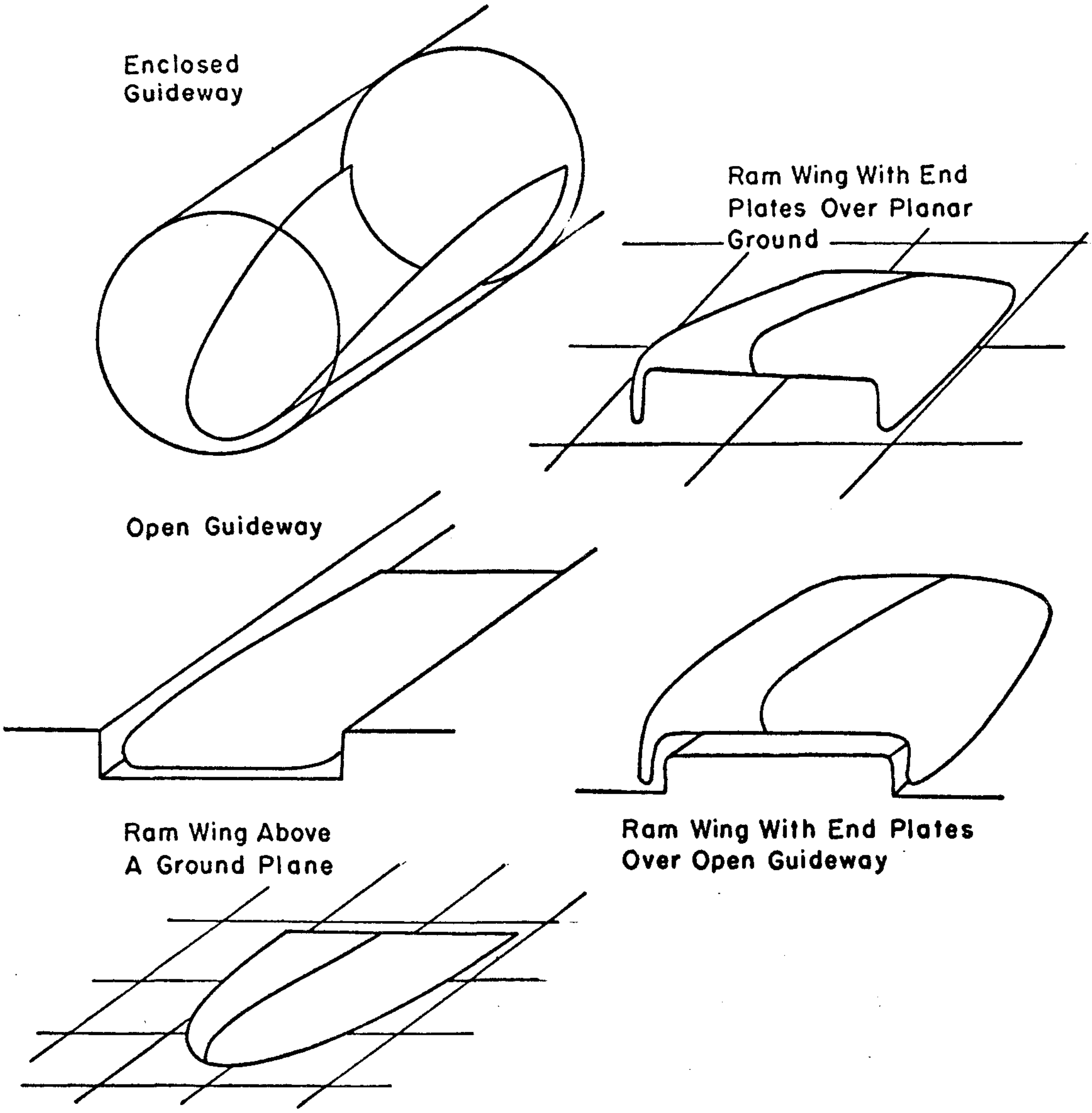

Fig. No. 1 HIGH SPEED GROUND TRANSPORTATION VEHICLES IN CLOSE PROXIMITY TO SOLID BOUNDARIES

Fig. 2 TERRAFOIL CONFIGURATIONS

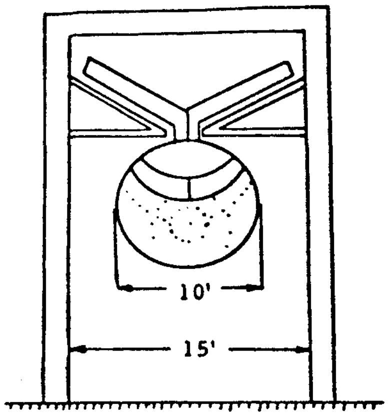

Front View of TV-Guideway

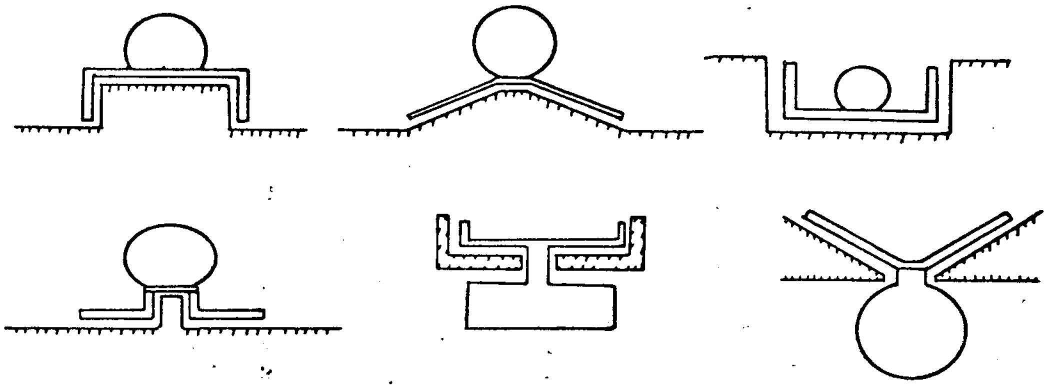

Possible Terrafoil Configurations

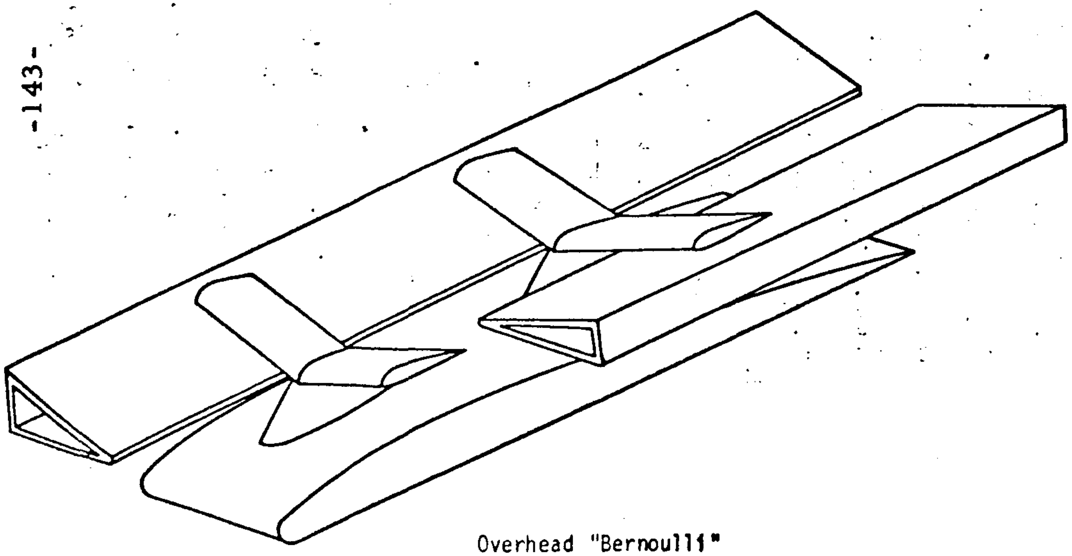

Overhead "Bernoulli" Terrafoil Vehicle

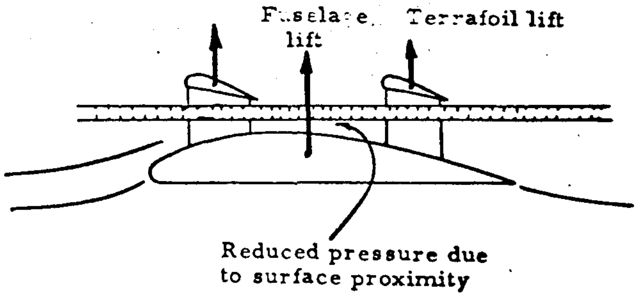

Force Schematic

2-d VORTEX DISTRIBUTION IN GROUND PROXIMITY SOURCE DISTRIBUTION METHOD

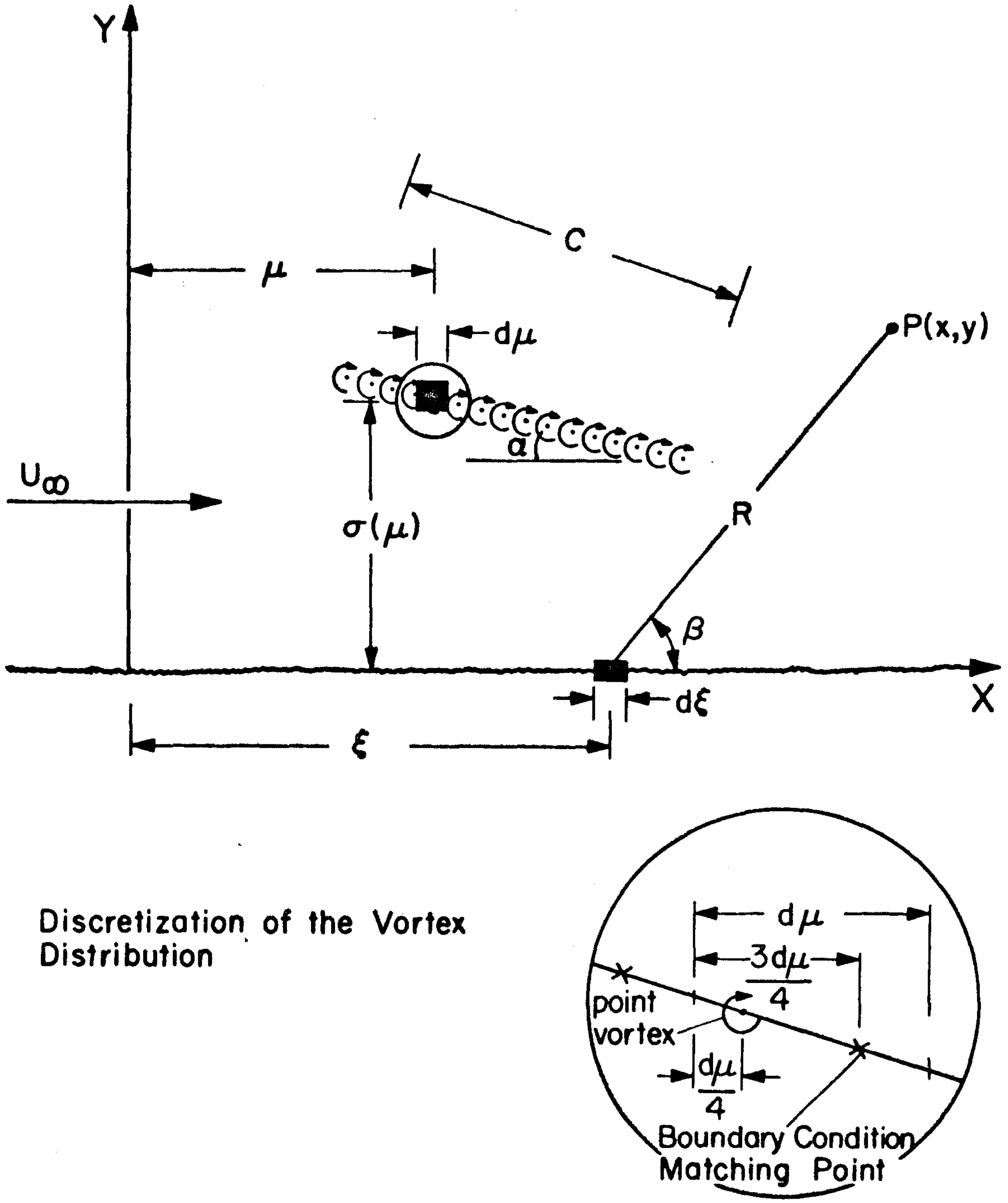

Fig. 3

3-d NON-PLANAR THIN WINGS
IN
NON-PLANAR GROUND EFFECT

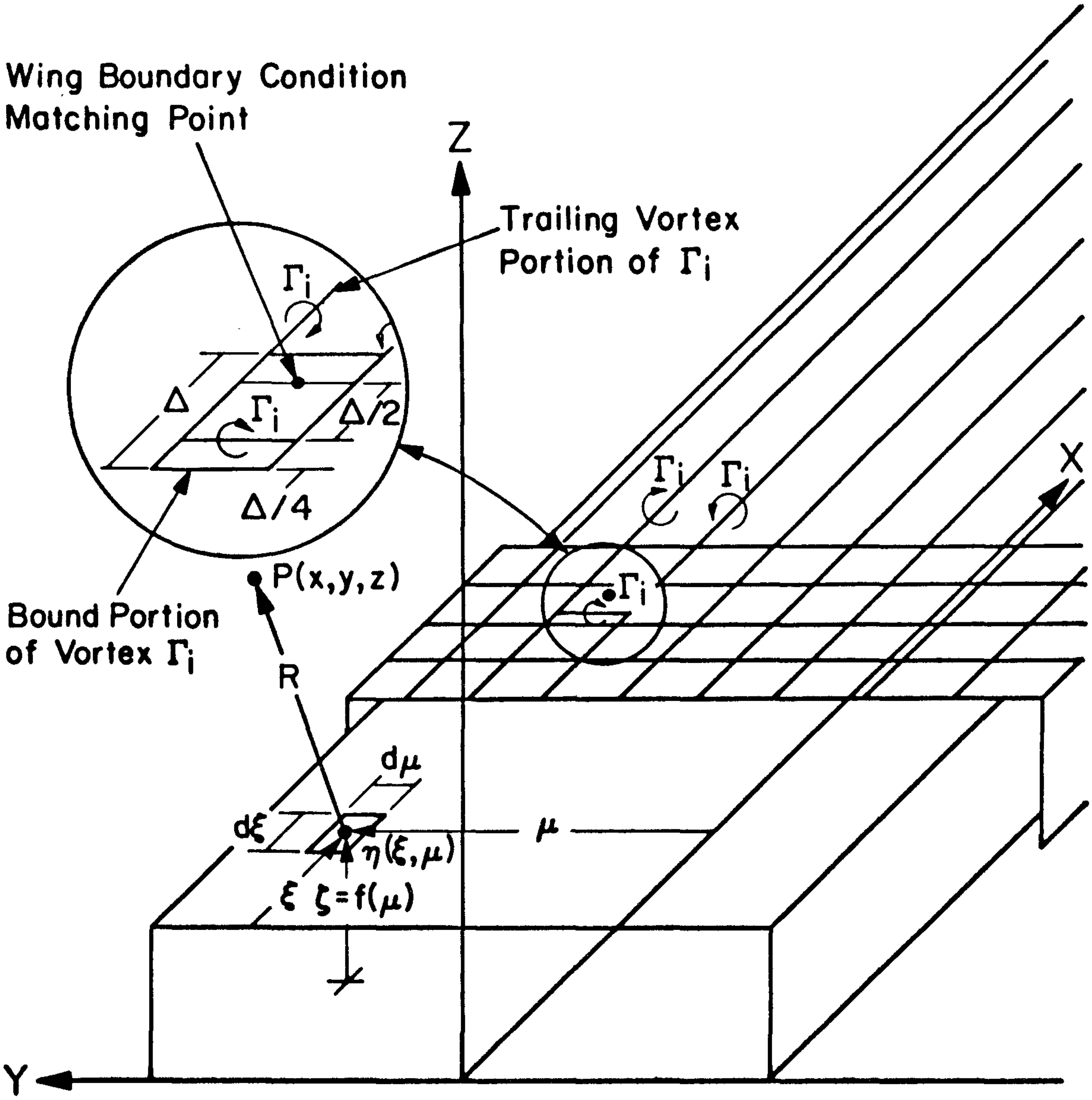

Fig. 4

VORTEX-LATTICE
SEGMENT SHAPES

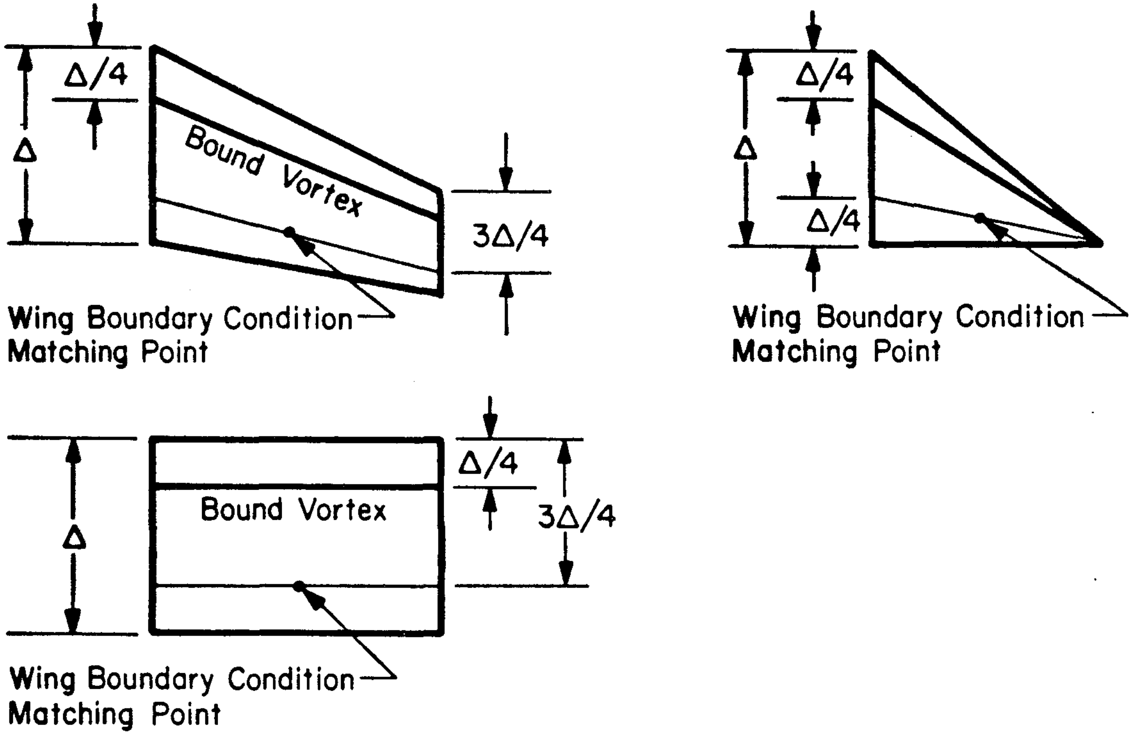

Fig. 5

MULTIPLE IMAGE METHOD

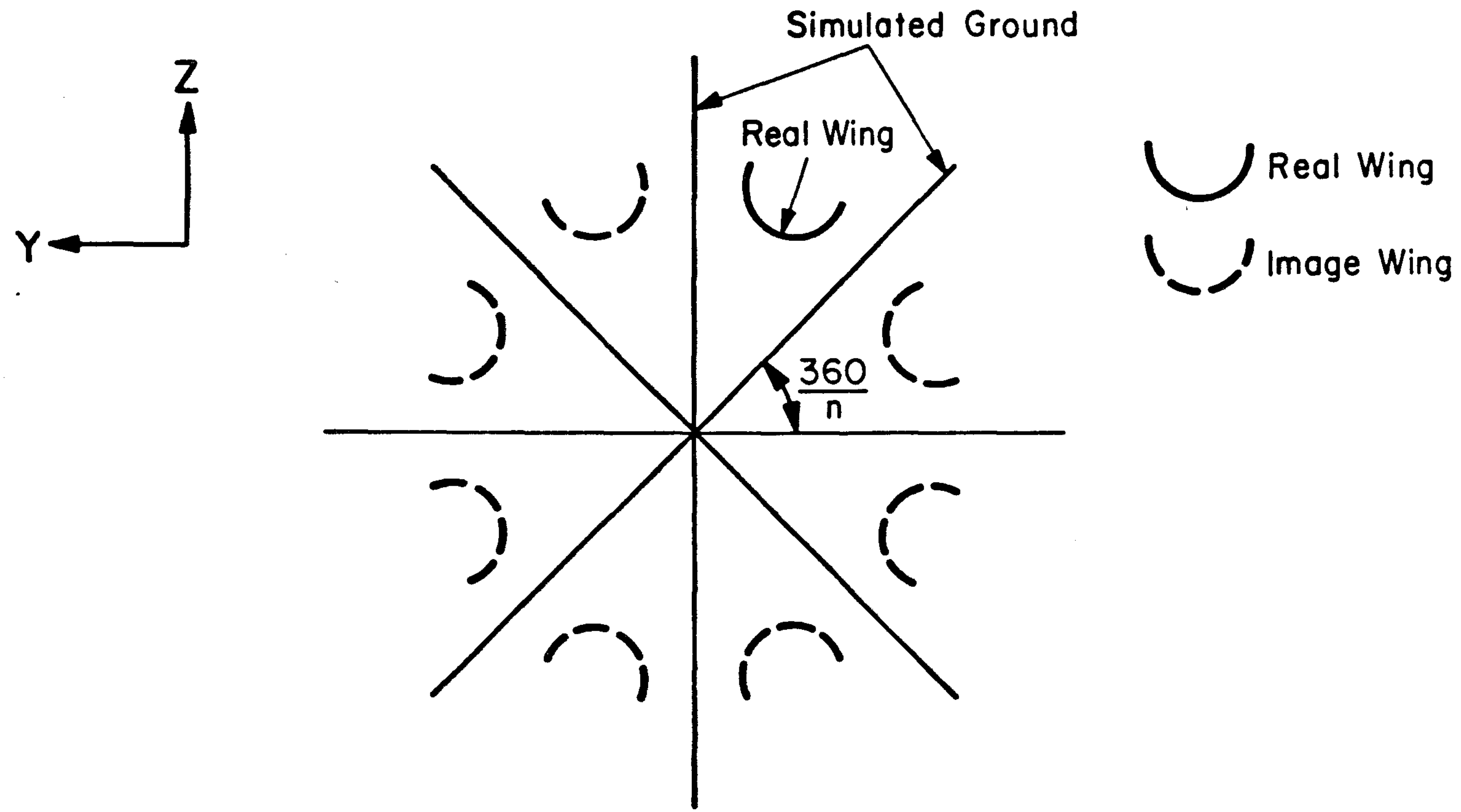

FRONT VIEW OF REAL WING AND n-1 IMAGE WINGS .

Fig. 6

L/L$_0$ vs h/c

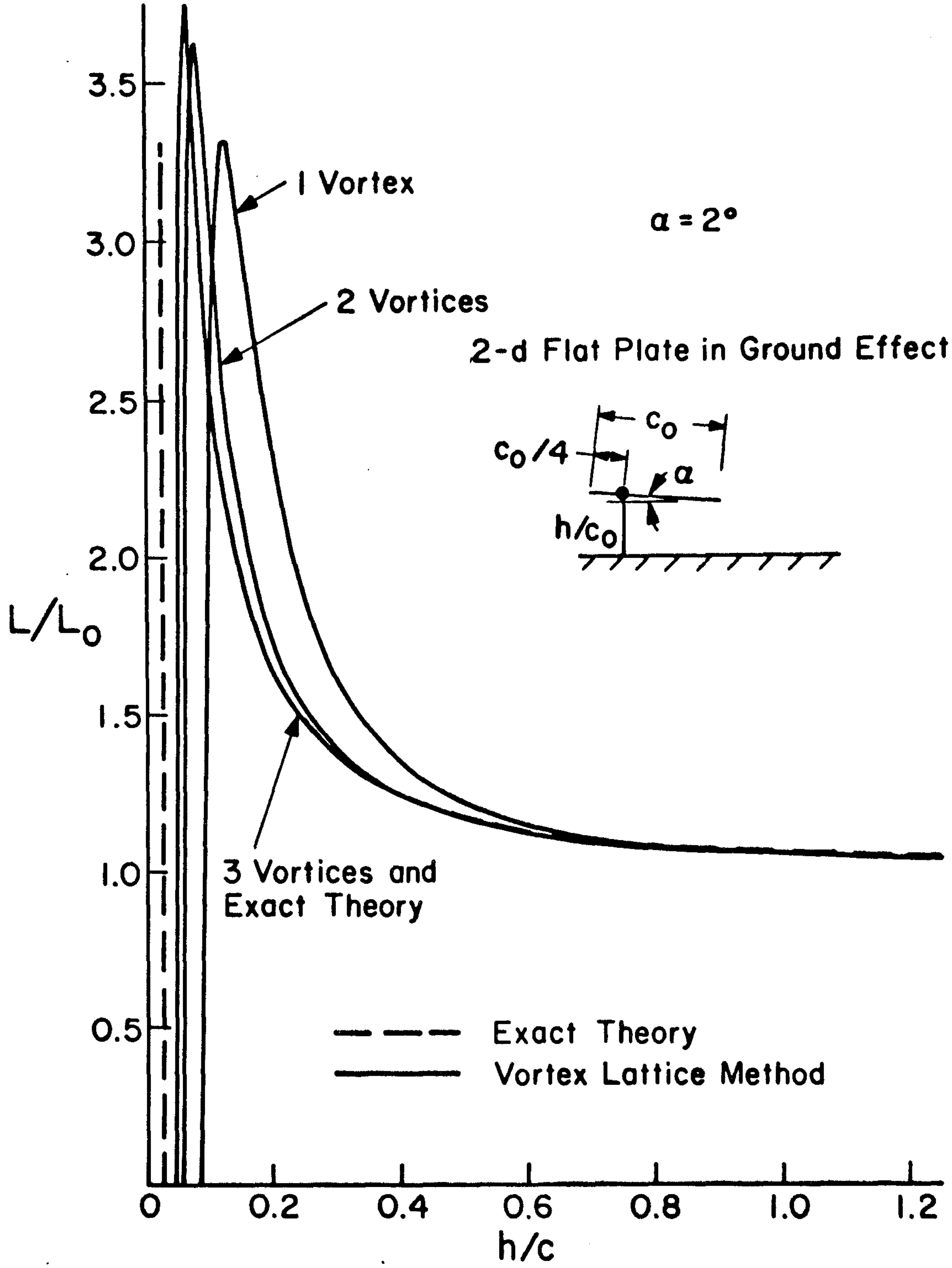

Fig. 7

L/L_0 vs h/c

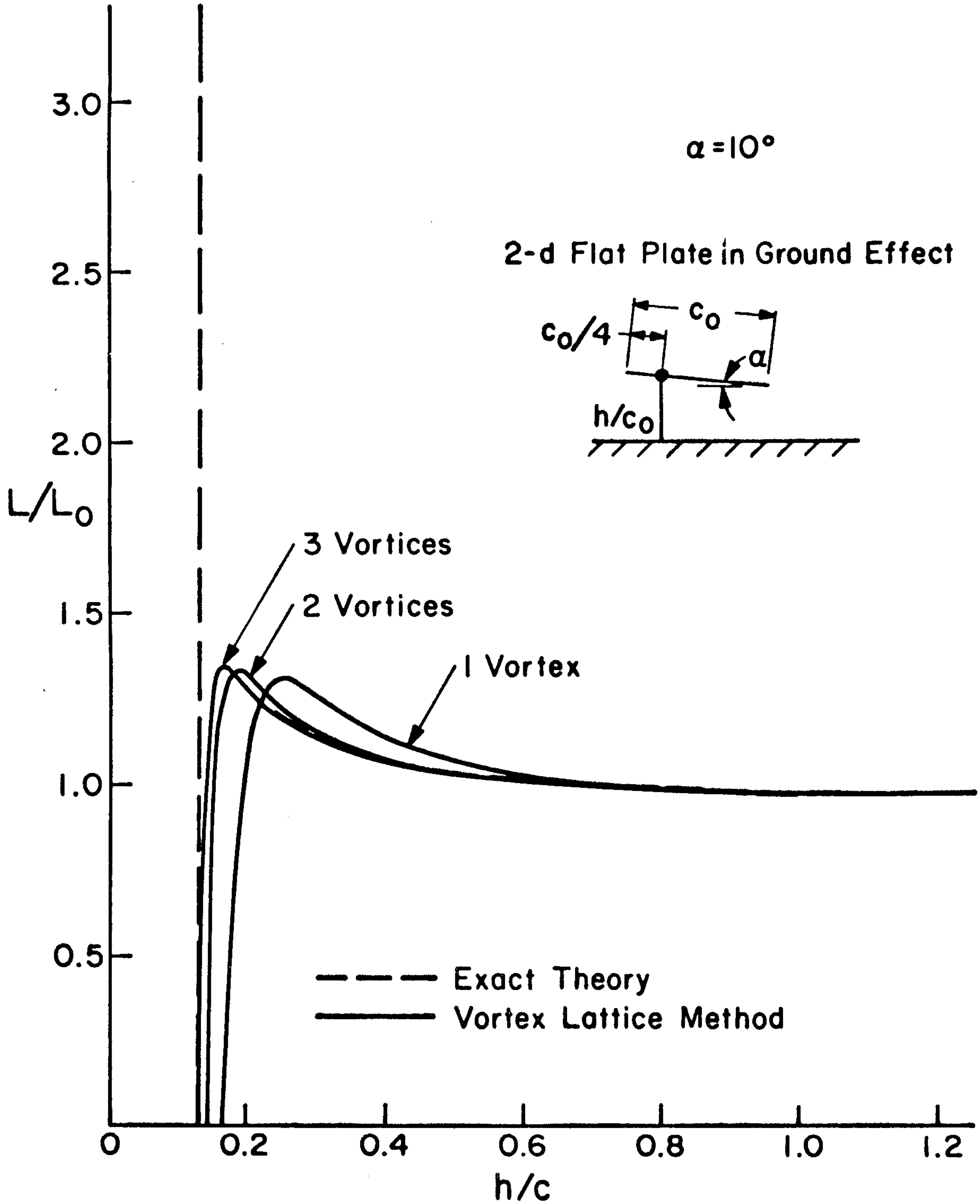

Fig. 8

L/L$_0$ vs h/c

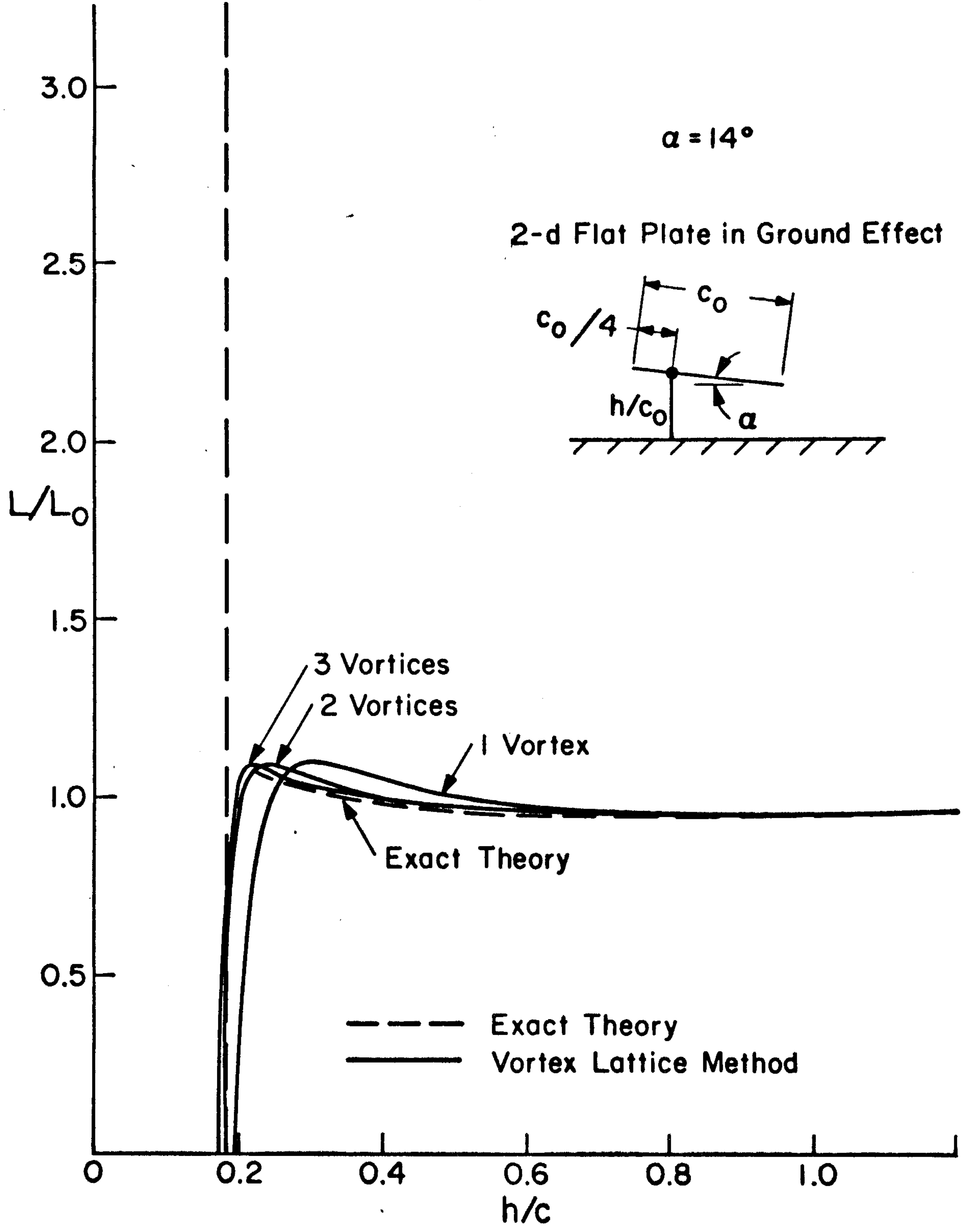

Fig. 9

LIFT CURVE SLOPE vs ASPECT RATIO

FLAT RECTANGULAR WINGS AT H = ∞

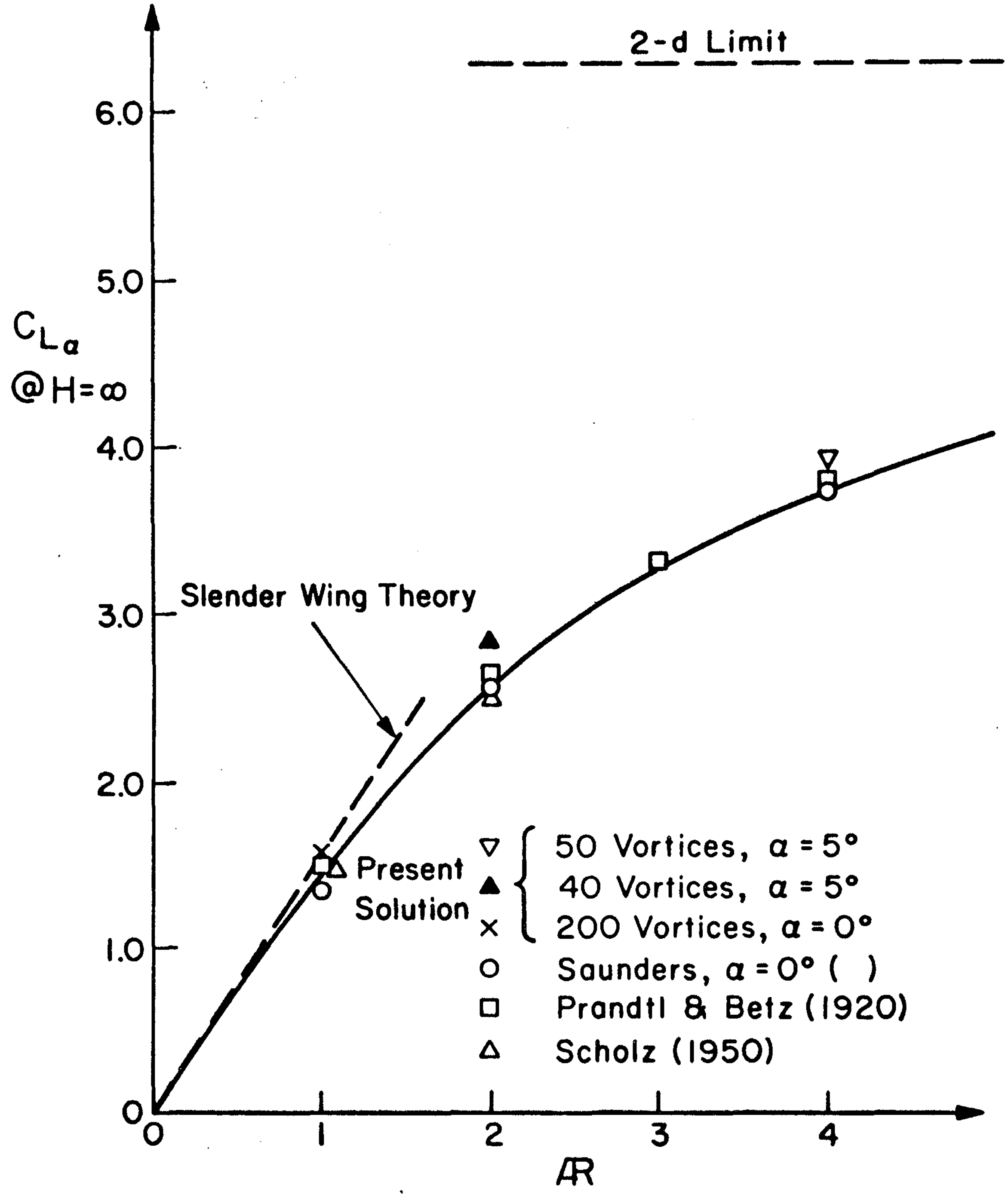

Fig. 10

LIFT CURVE SLOPE vs h/c

THIN FLAT RECTANGULAR WINGS IN GROUND EFFECT

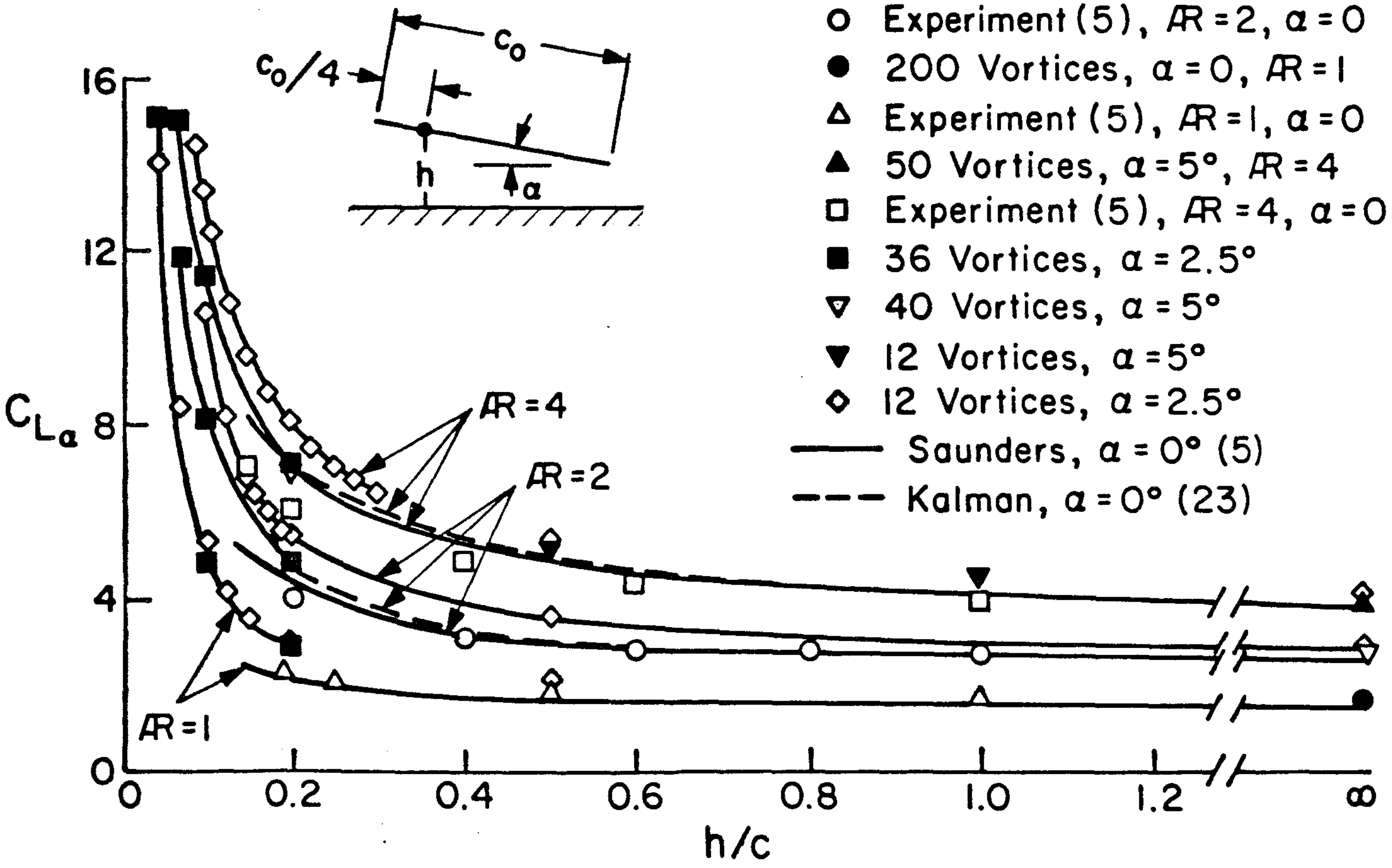

Fig. 11

LIFT CURVE SLOPE vs α
THIN FLAT RECTANGULAR WING

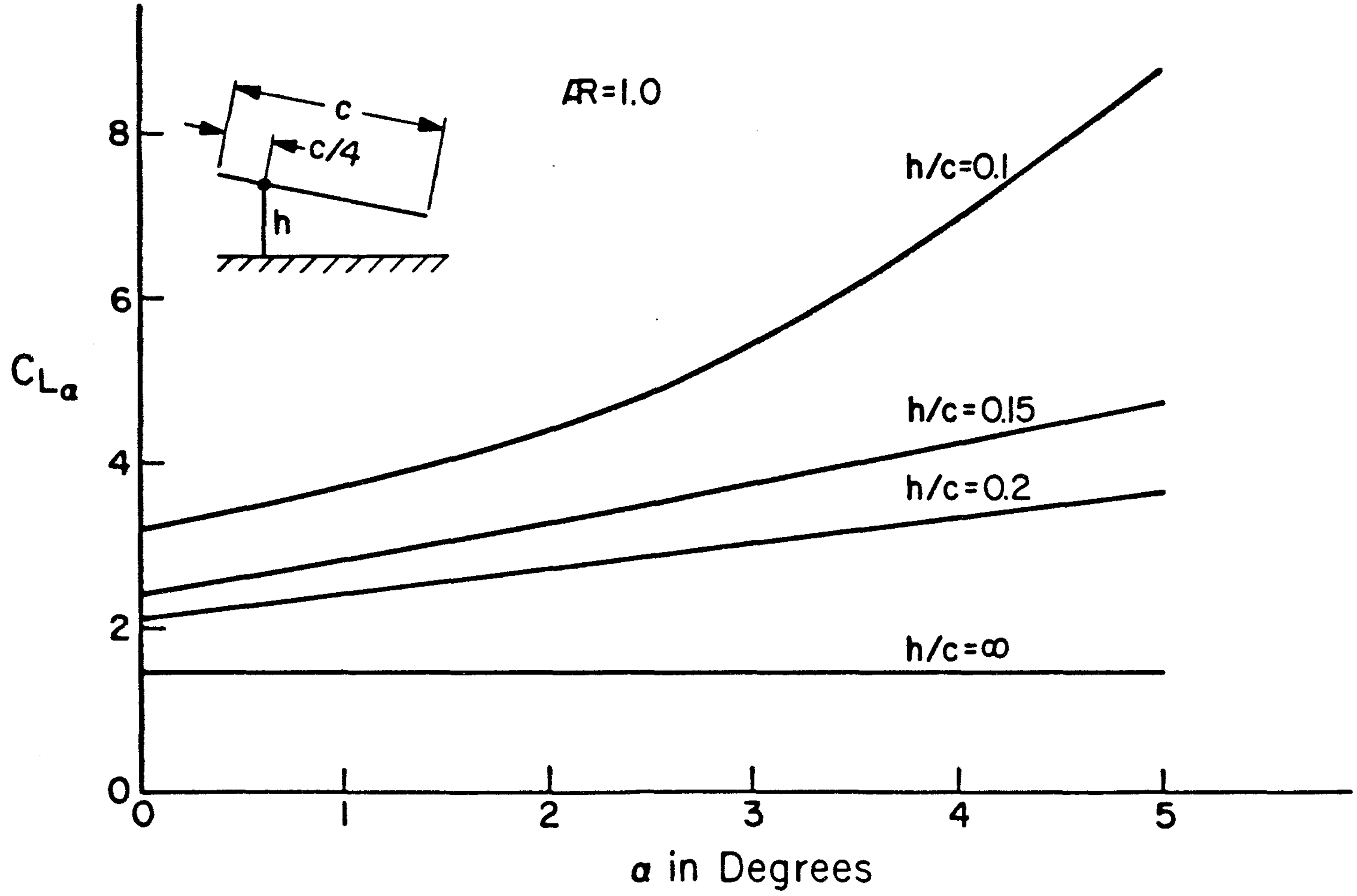

Fig. 12

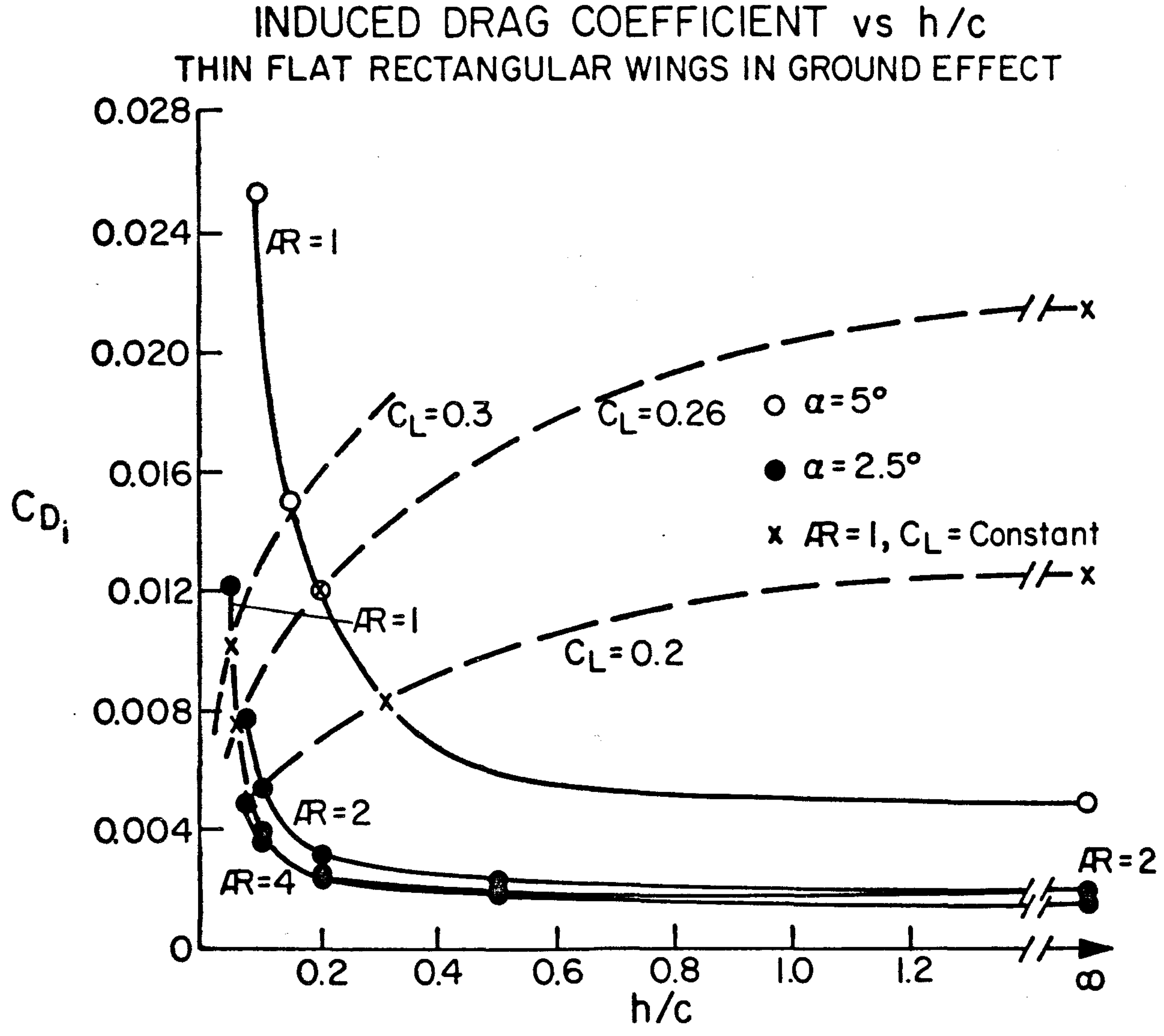
INDUCED DRAG COEFFICIENT vs h/c
THIN FLAT RECTANGULAR WINGS IN GROUND EFFECT
C_{D_i}
0.028
0.024
0.020
0.016
0.012
0.008
0.004
0
0.2
0.4
0.6
0.8
1.0
1.2
∞
h/c
AR = 1
AR = 1
AR = 2
AR = 4
AR = 2
$C_L = 0.3$
$C_L = 0.26$
$C_L = 0.2$
○ $\alpha = 5°$
● $\alpha = 2.5°$
x AR = 1, C_L = Constant

Fig. 13

MOMENT CURVE SLOPE vs h/c
THIN FLAT RECTANGULAR WINGS IN GROUND EFFECT

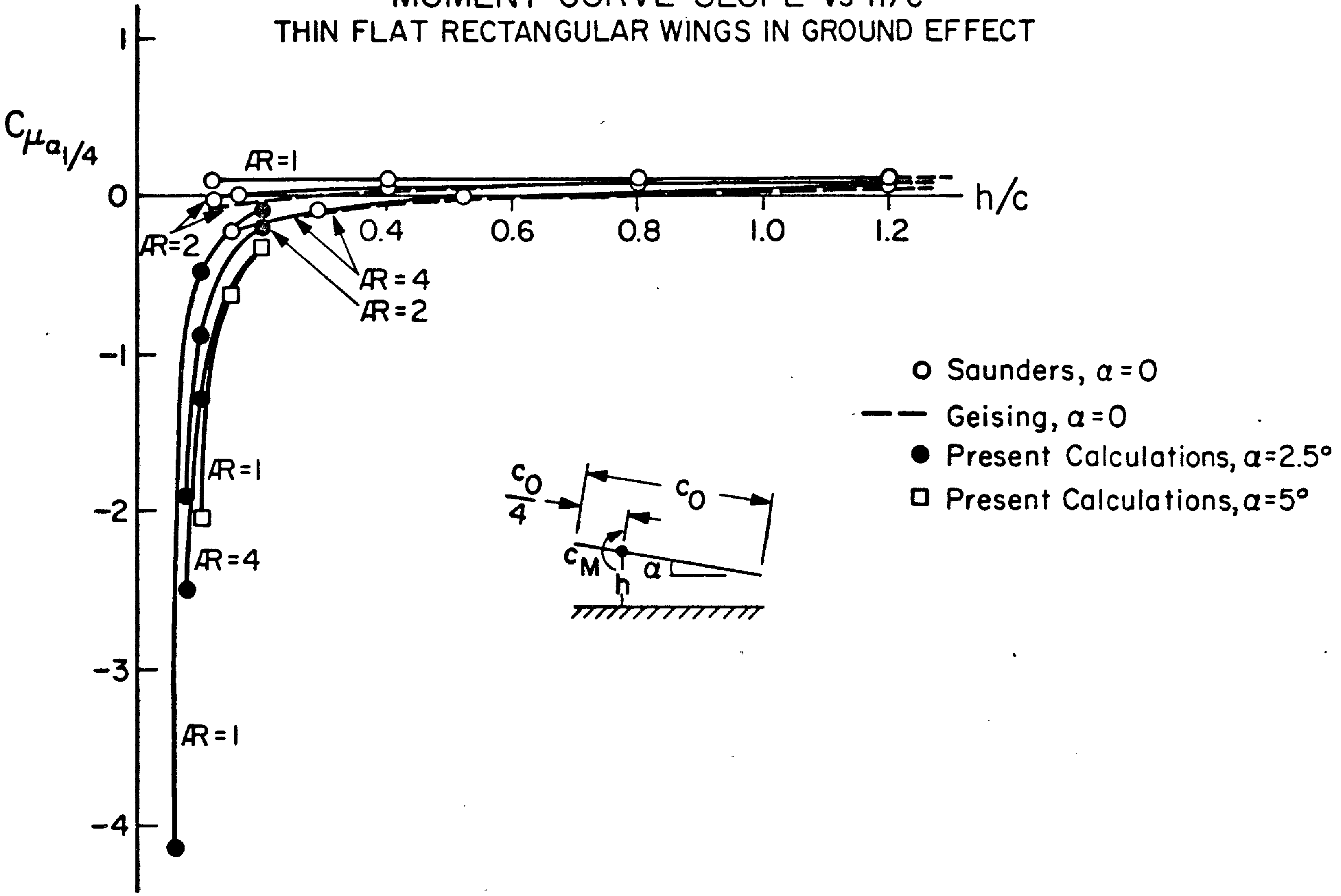

Fig. 14

LIFT CURVE SLOPE vs DIHEDRAL
THIN RECTANGLAR WING IN GROUND EFFECT

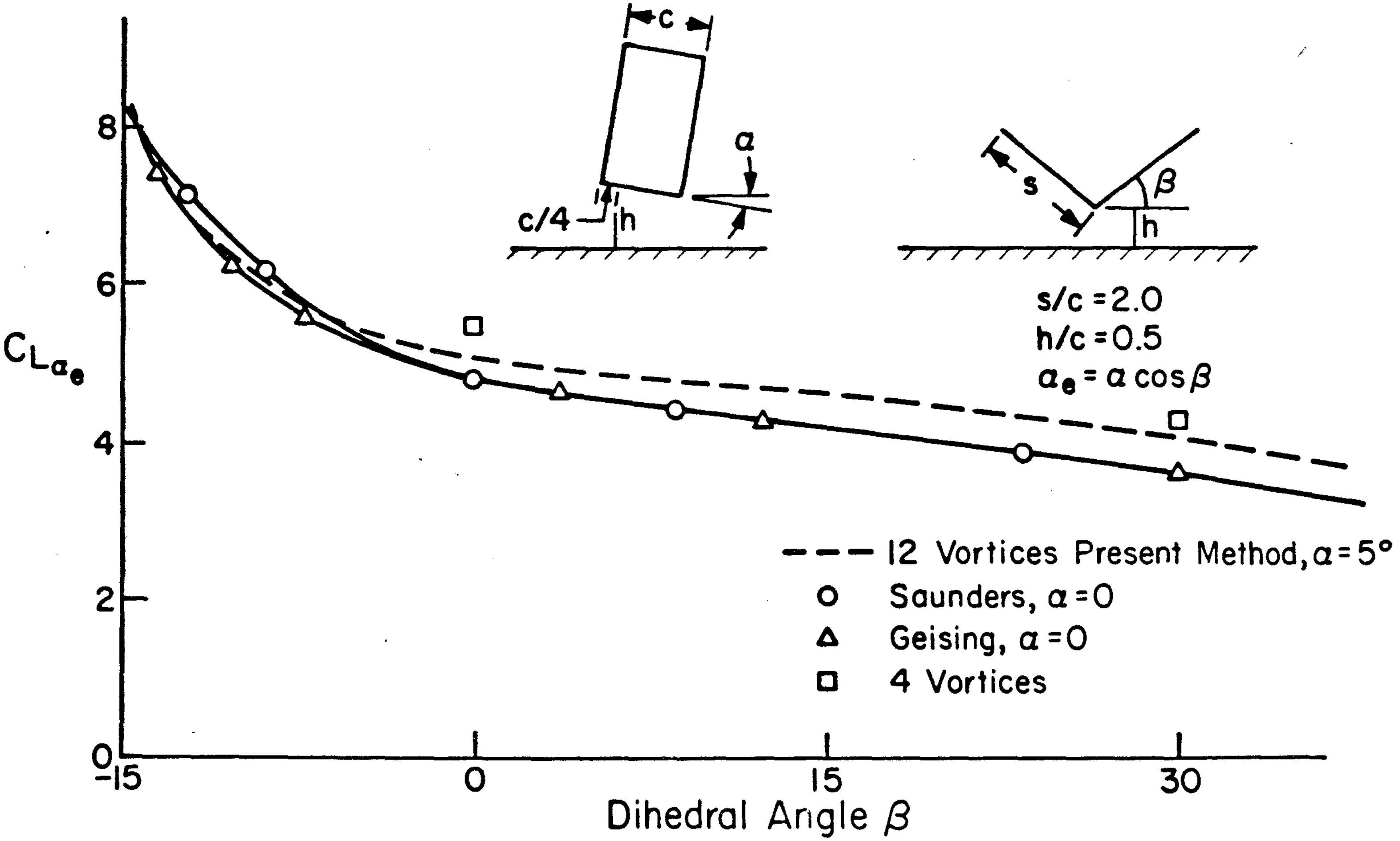

- – – 12 Vortices Present Method, α = 5°
- ○ Saunders, α = 0
- △ Geising, α = 0
- □ 4 Vortices

Fig. 15

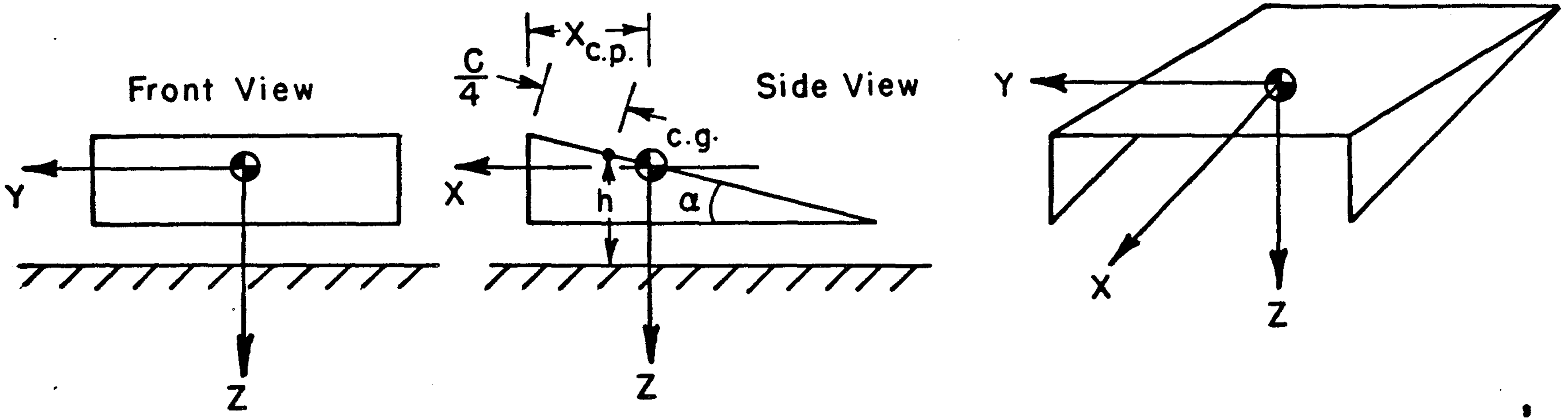

Fig.16 (a) Thin Flat Rectangular Wing With Triangular End Plates

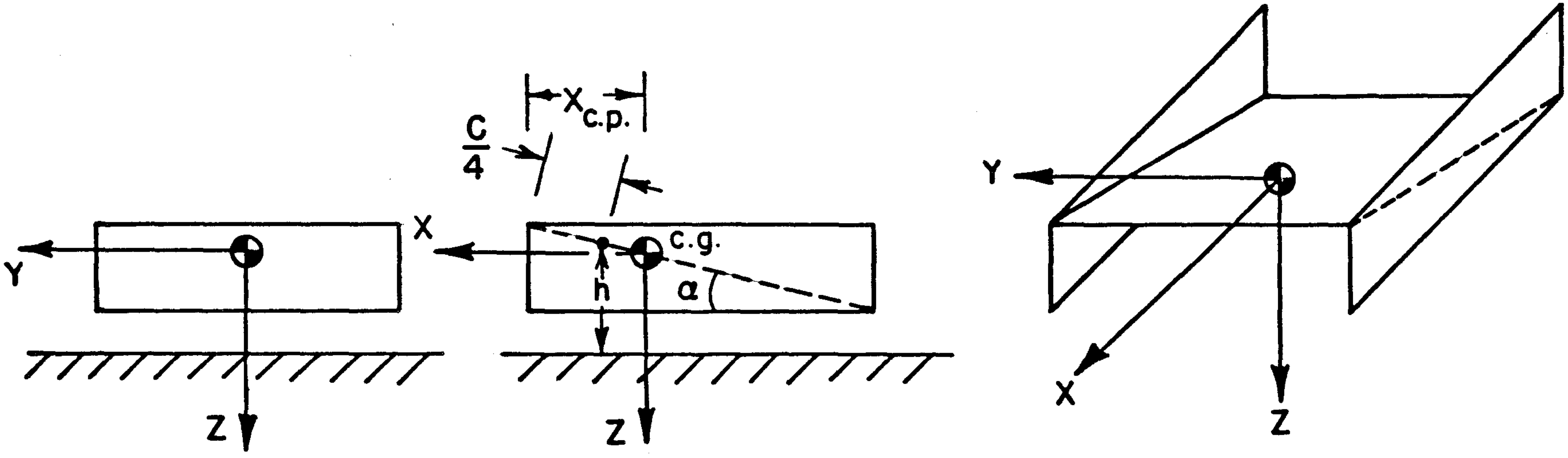

Fig. 16 (b) Thin Flat Rectangular Wing With Rectangular End Plates

C_L and C_{L_α} vs h/c

WINGS WITH END PLATES IN GROUND EFFECT

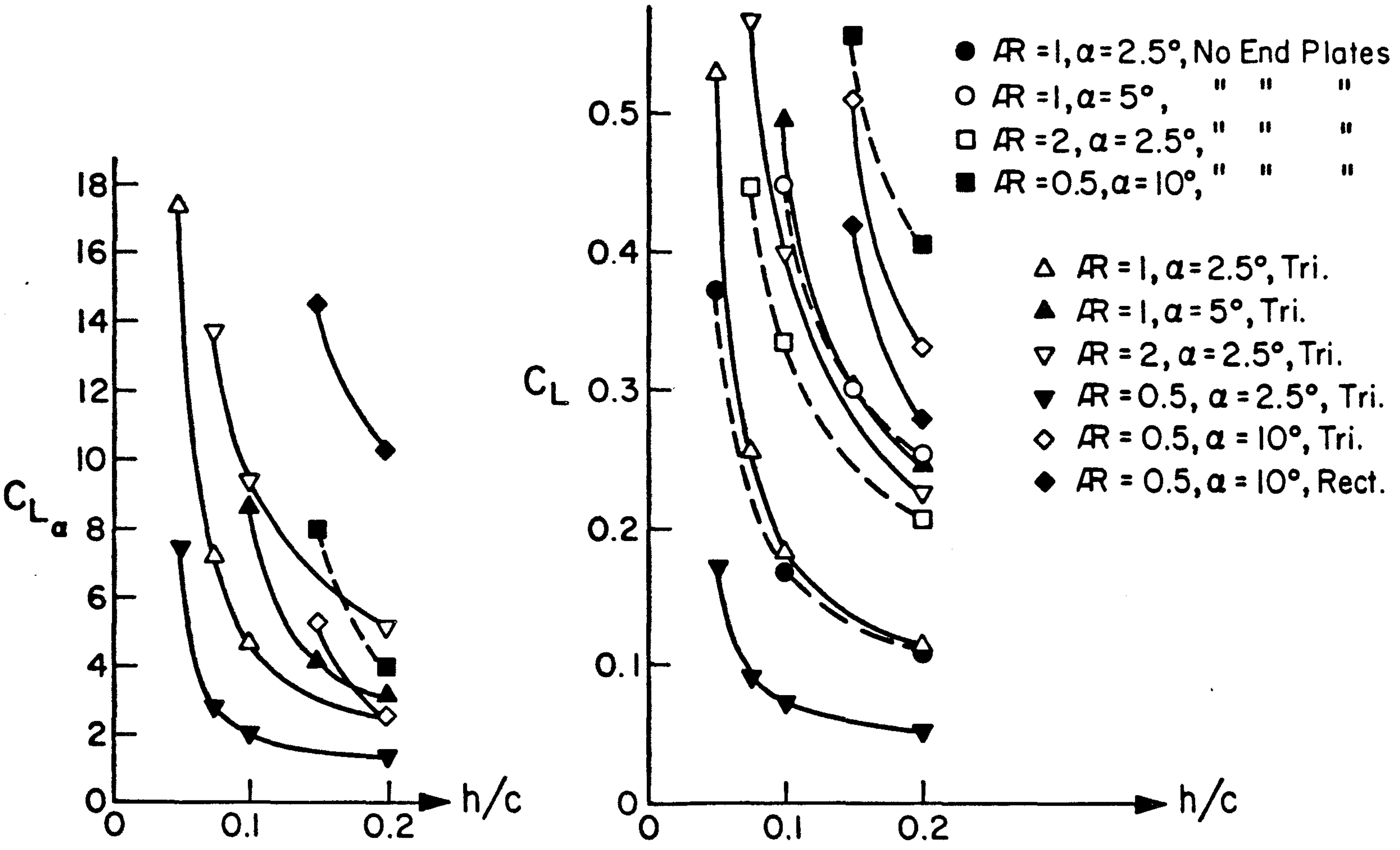

Fig. 17

LEADING EDGE MOMENT AND INDUCED DRAG COEFFICIENTS
WINGS WITH END PLATES IN GROUND EFFECT

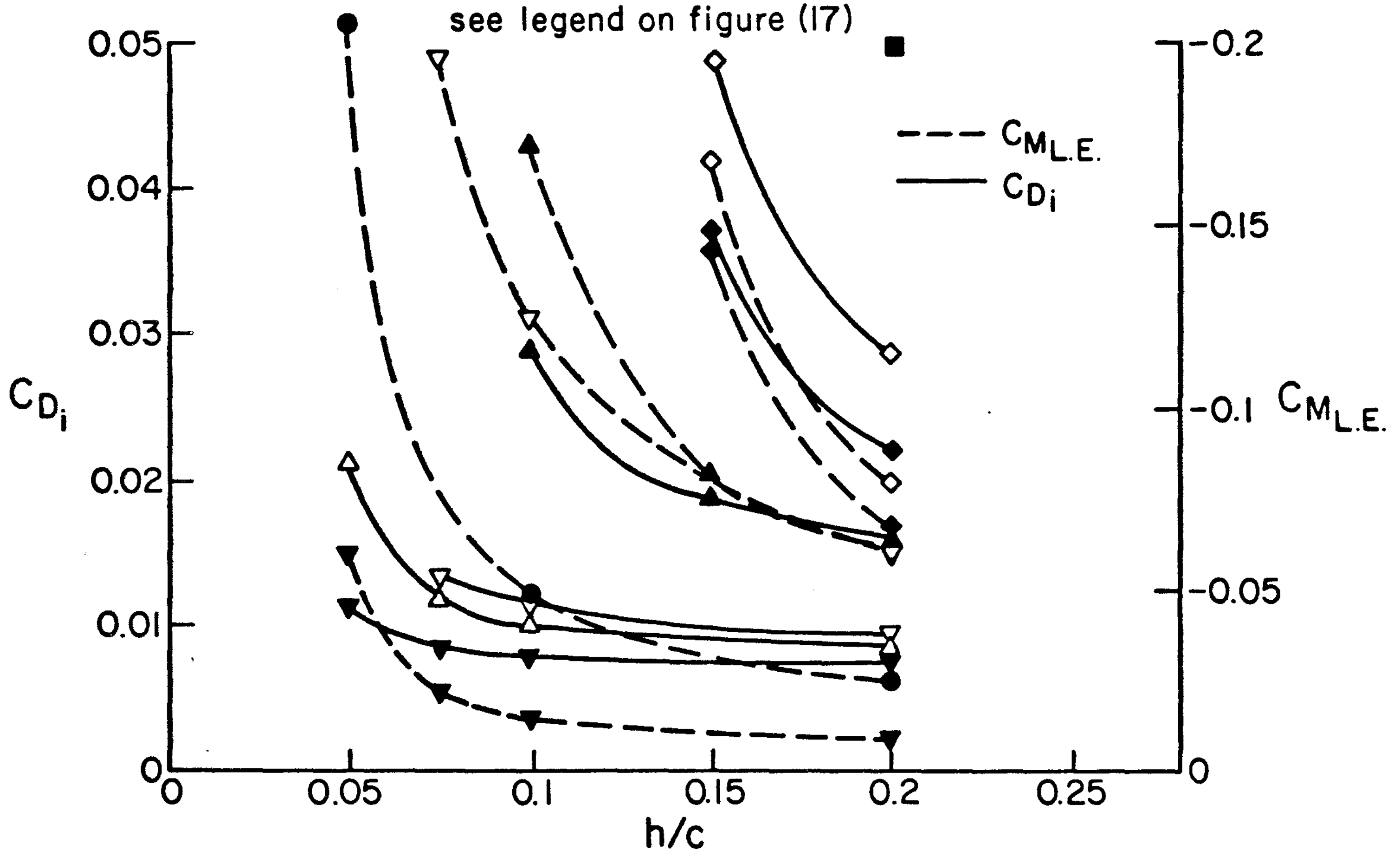

Fig. 18

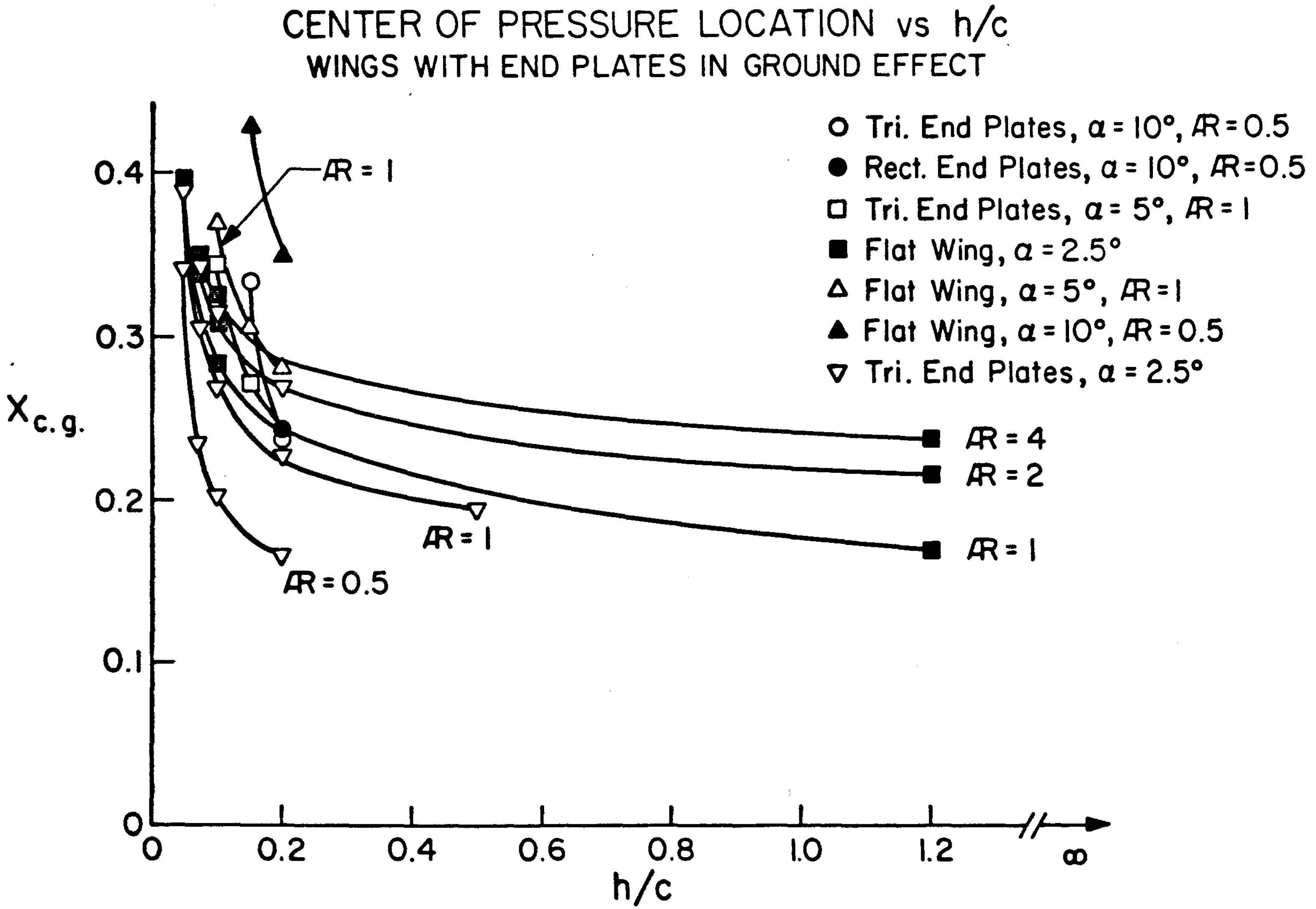
CENTER OF PRESSURE LOCATION vs h/c
WINGS WITH END PLATES IN GROUND EFFECT
○ Tri. End Plates, α = 10°, Æ = 0.5
● Rect. End Plates, α = 10°, Æ = 0.5
☐ Tri. End Plates, α = 5°, Æ = 1
■ Flat Wing, α = 2.5°
△ Flat Wing, α = 5°, Æ = 1
▲ Flat Wing, α = 10°, Æ = 0.5
▽ Tri. End Plates, α = 2.5°
Æ = 1
Æ = 4
Æ = 2
Æ = 1
Æ = 1
Æ = 0.5
Xc.g.
0.4
0.3
0.2
0.1
0
0
0.2
0.4
0.6
0.8
1.0
1.2
∞
h/c

Fig. 19

LIFT COEFFICIENT vs h/c

WINGS WITH END PLATES AT ANGLE OF ATTACK

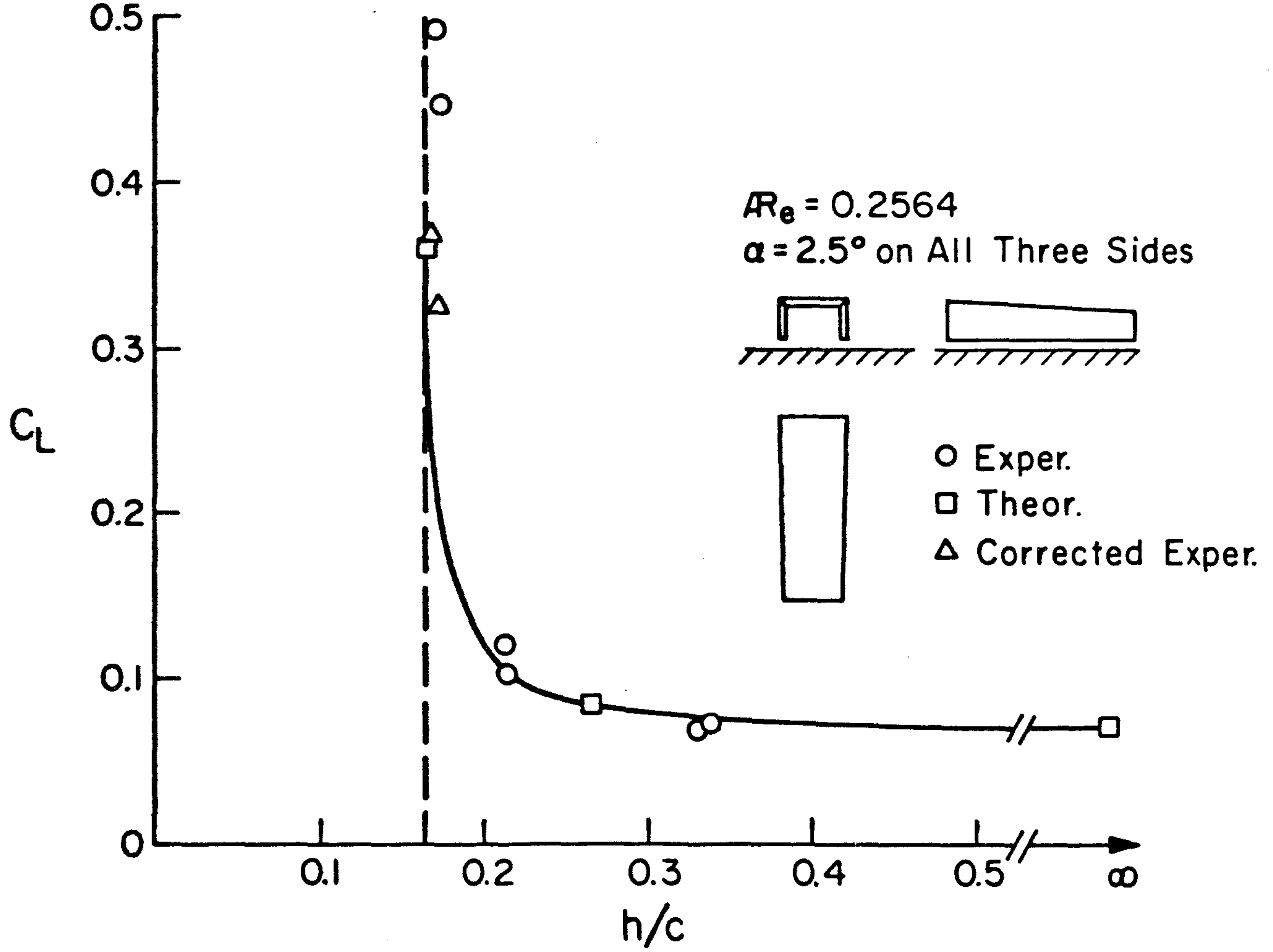

Fig. 20

LIFT COEFFICIENT vs ANGLE OF ATTACK
WINGS WITH END PLATES AT ANGLE OF ATTACK

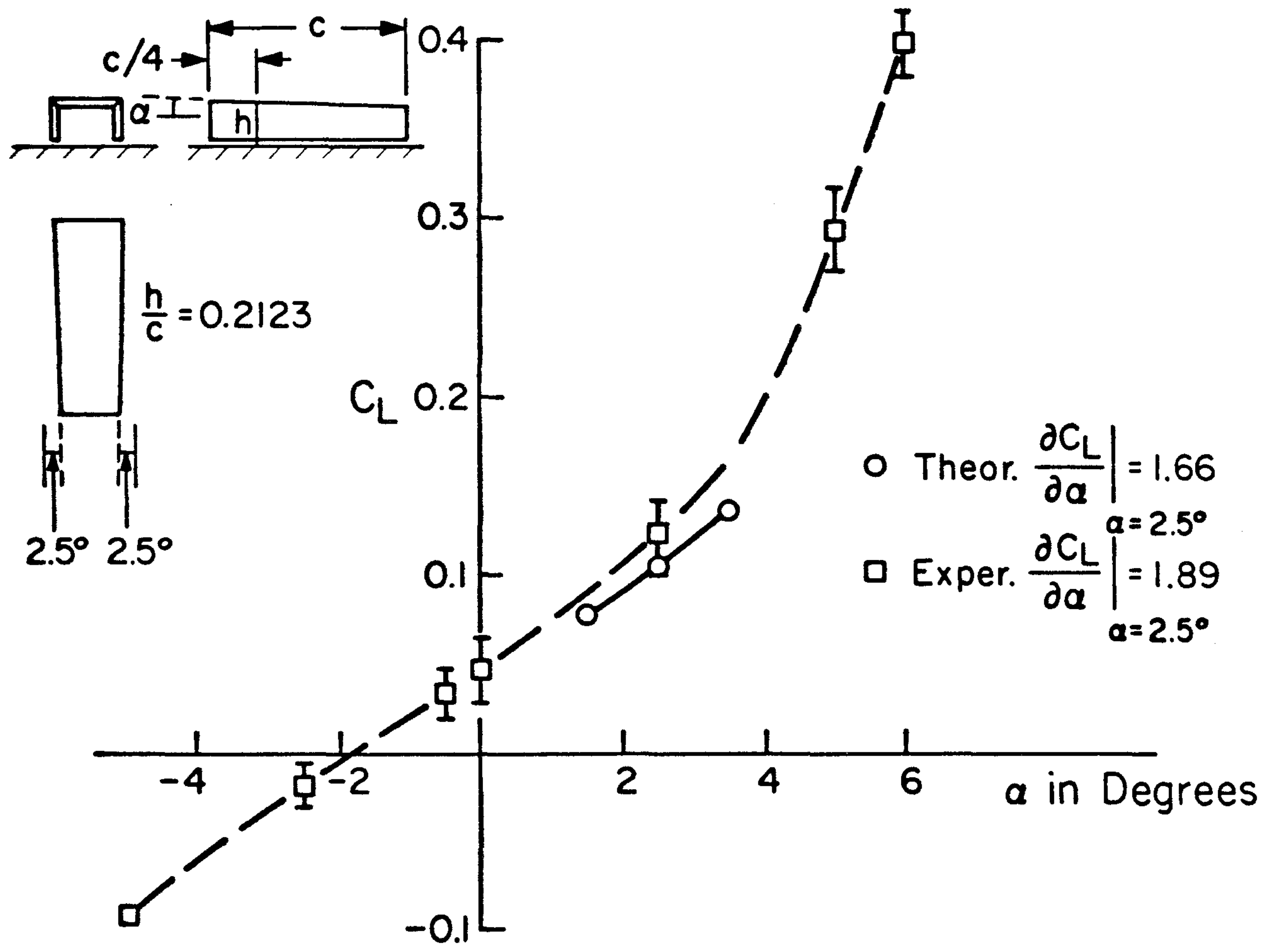

Fig. 21

LIFT CURVE SLOPE vs h/c
TANDEM FLAT RECTANGULAR WINGS IN GROUND EFFECT

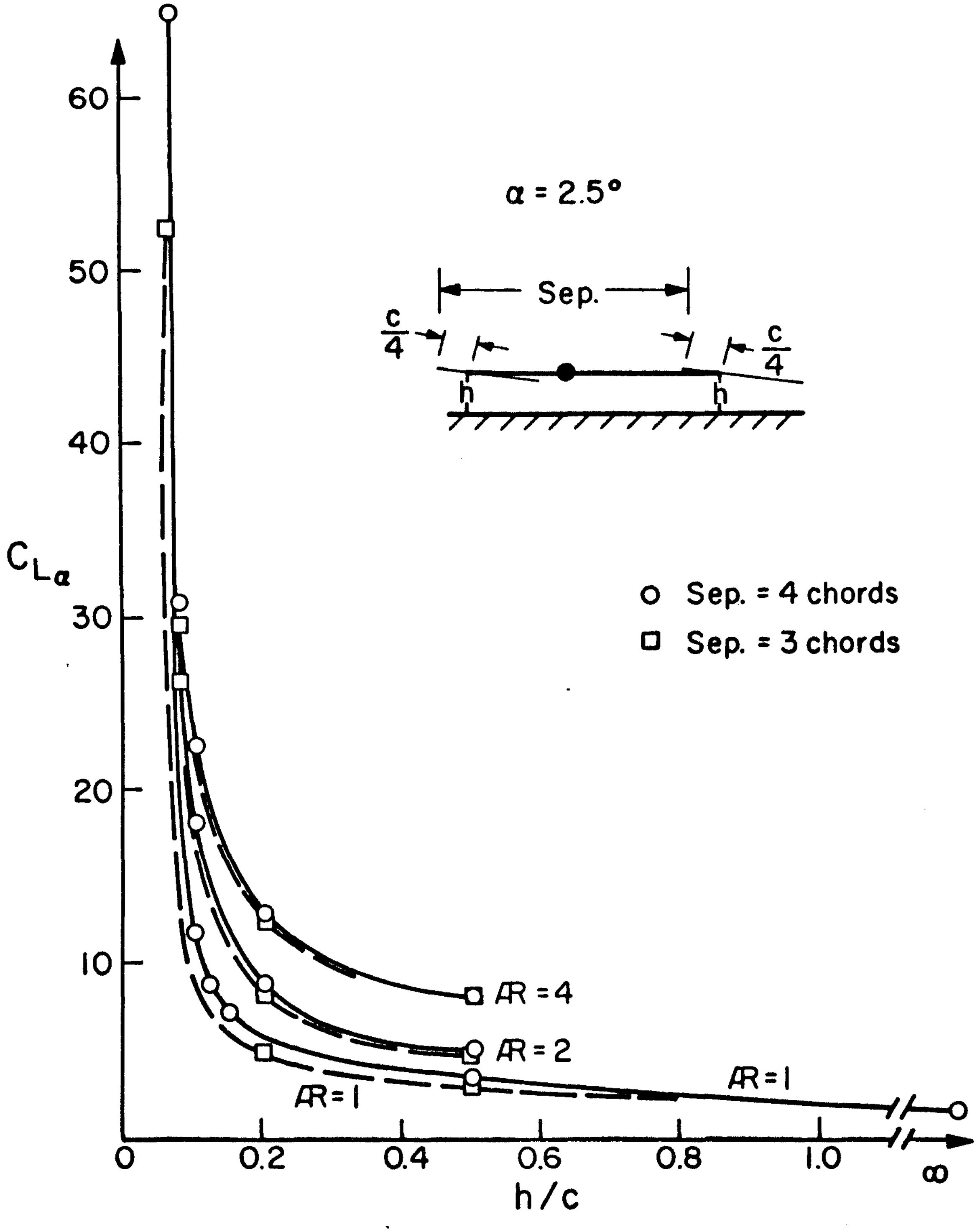

Fig. 22

INDUCED DRAG AND MOMENT COEFFICIENTS vs h/c
TANDEM FLAT RECTANGULAR WINGS IN GROUND EFFECT

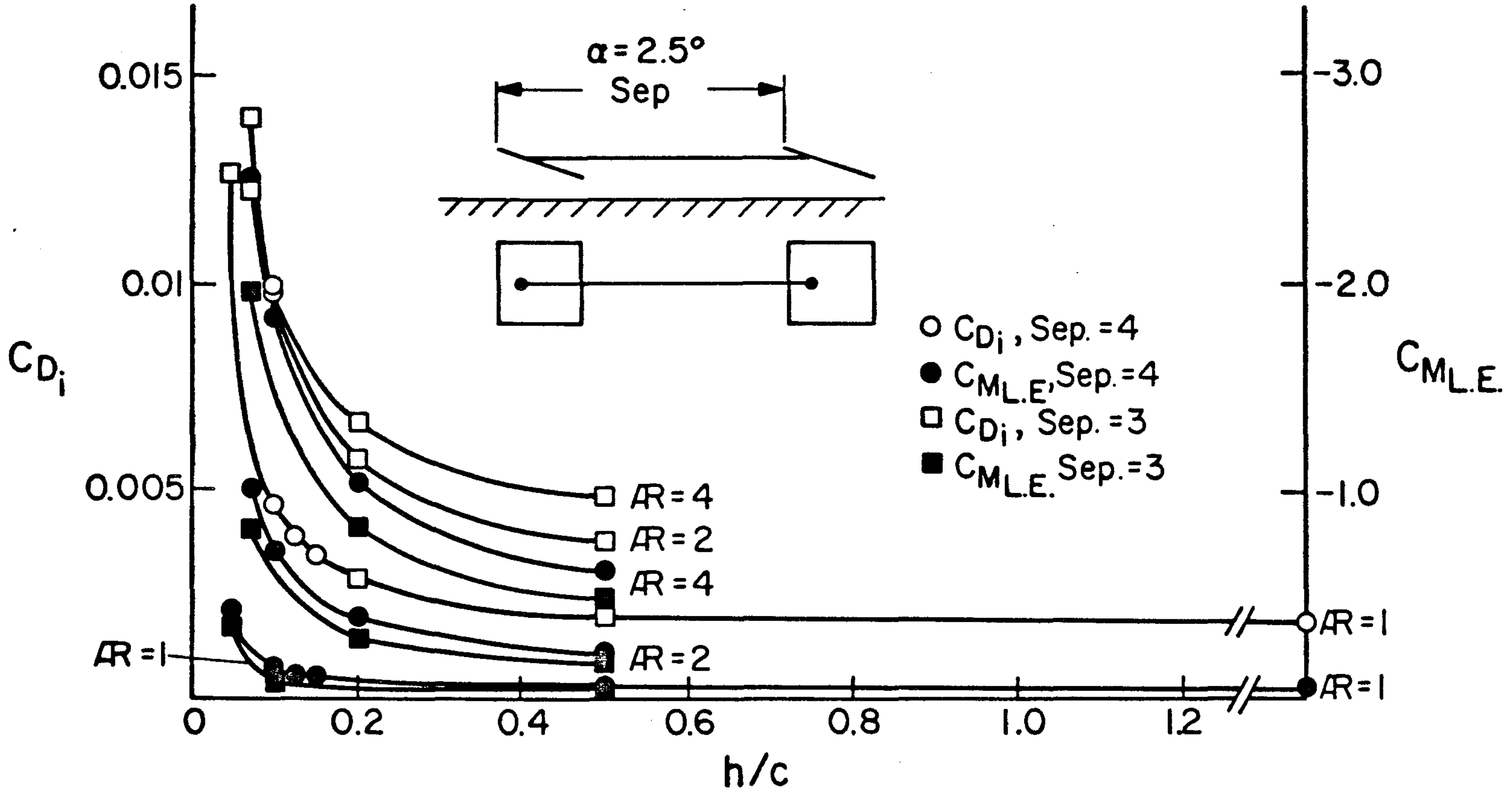

Fig. 23

CENTER OF PRESSURE LOCATION vs h/c
TANDEM FLAT RECTANGULAR WINGS IN GROUND EFFECT

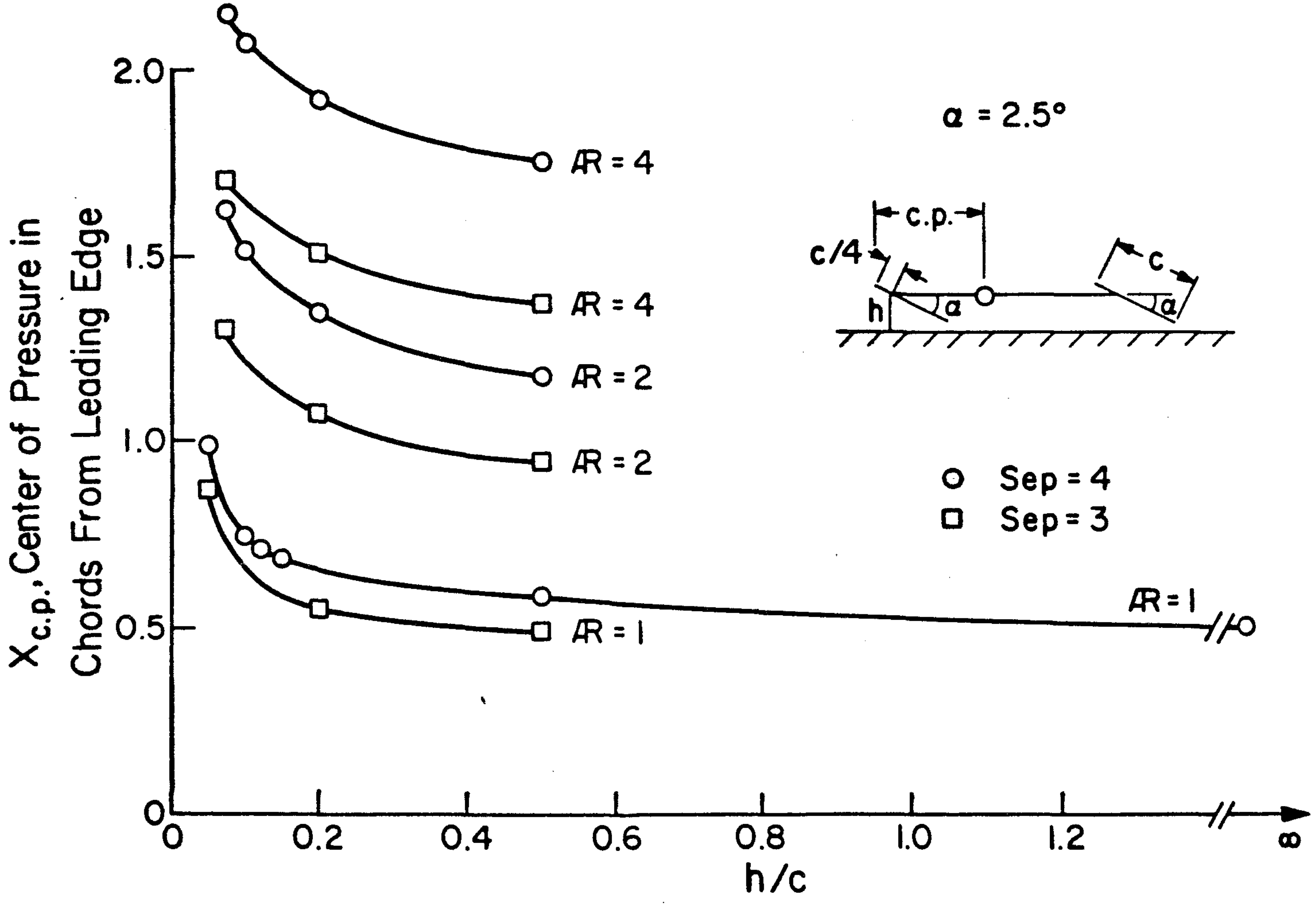

Fig. 24

NON-PLANAR GROUND EFFECT CONFIGURATIONS

FRONT SIDE TOP

b) Slanted Channel – Wing with Dihedral

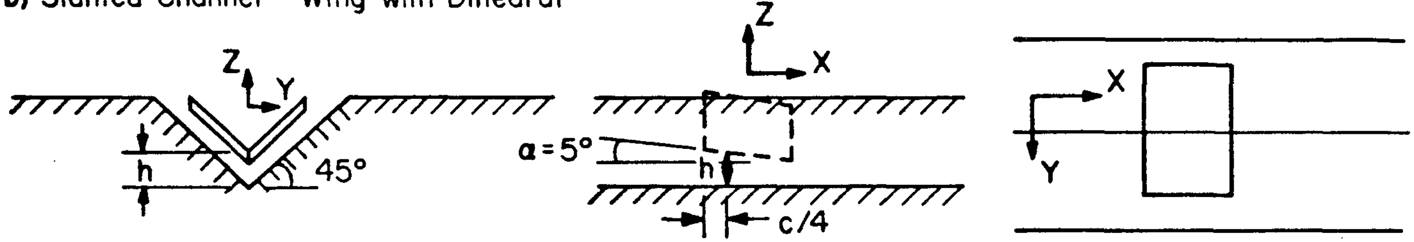

c) Rectangular Railing - Wing with End Plates at Angle of Attack Extending Beneath the Wing

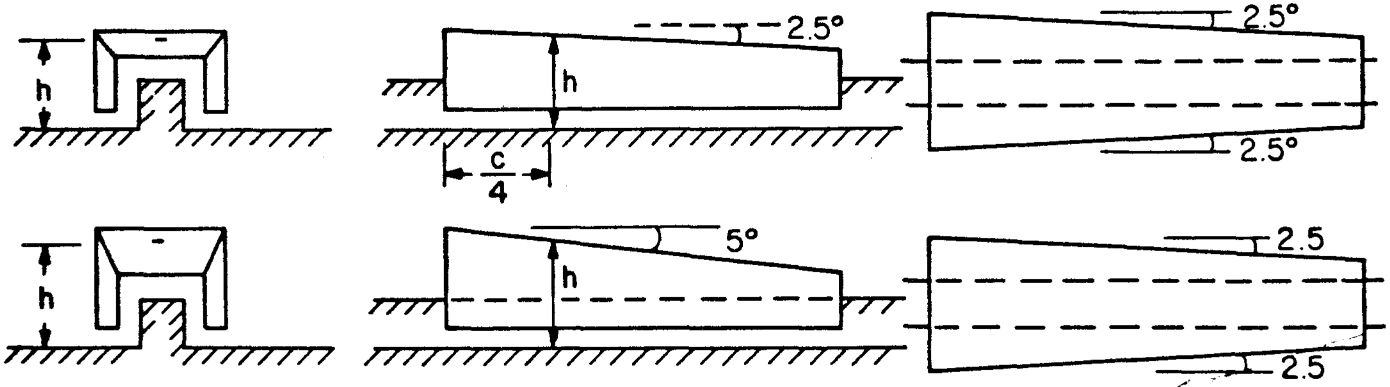

d) Rectangular Channel - Wing with End Plates at Angle of Attack Extending Above the Wing

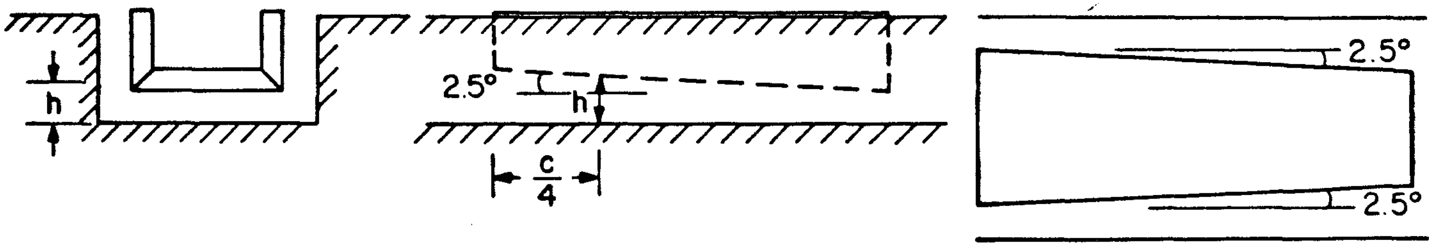

Fig. 25

SIMULATION OF NON-PLANAR GROUND BY MULTIPLE IMAGE METHOD

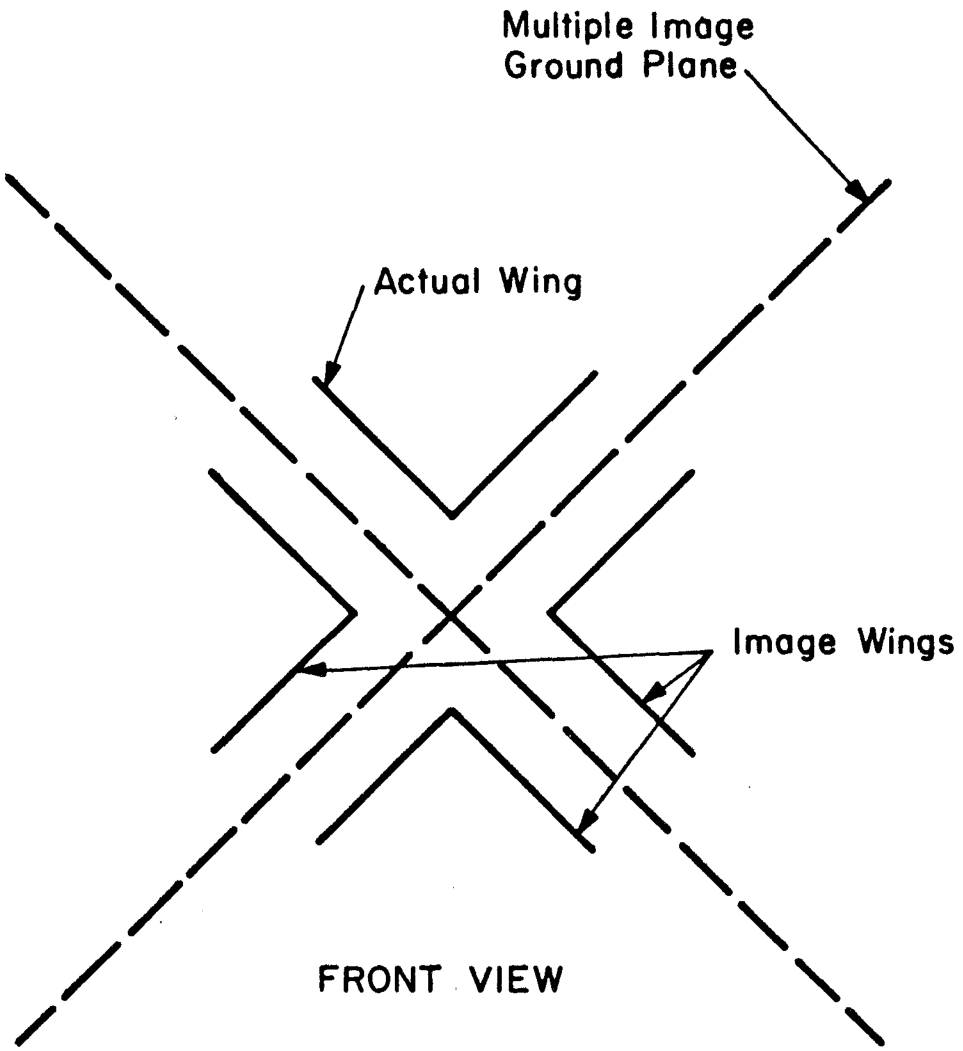

Fig. 26

SIMULATION OF NON-PLANAR GROUND BY SOURCE SHEET DISTRIBUTION METHOD

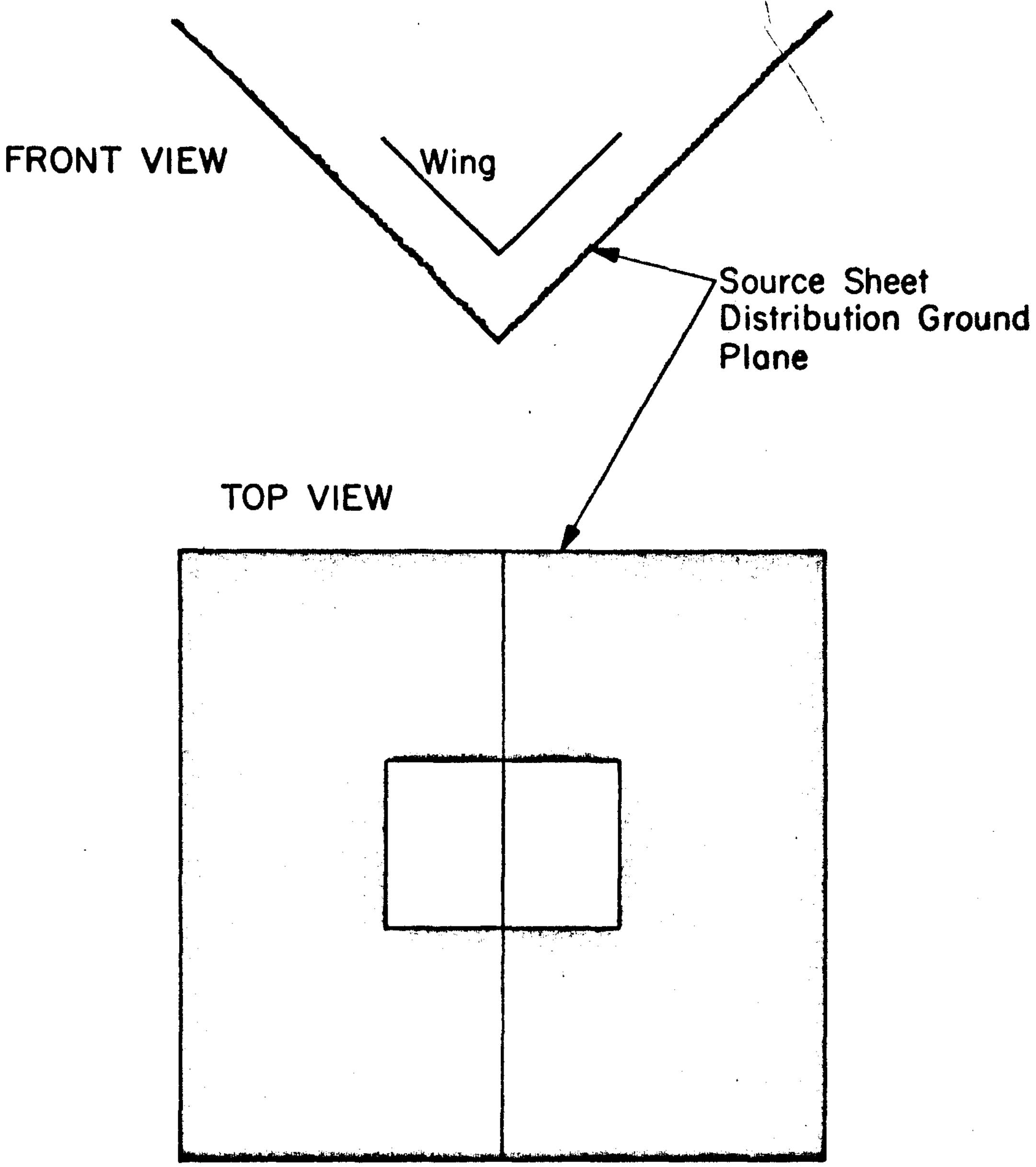

Fig. 27

SPANWISE LOAD DISTRIBUTION

CHECK CASE INFINITE CHANNEL--WING WITH DIHEDRAL

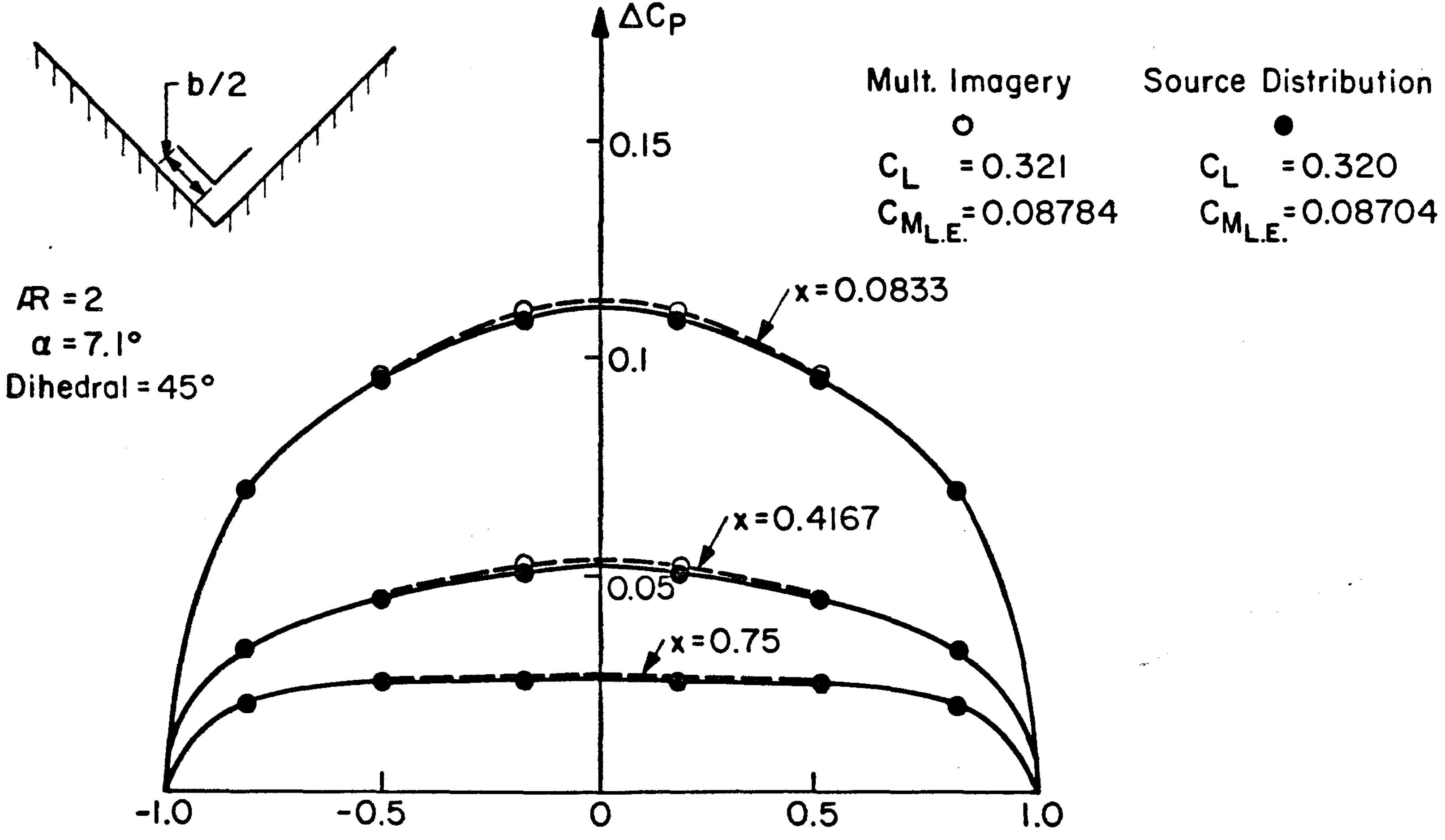

Fig. 28

SLANTED CHANNEL

C_L, $C_{M_{L.E.}}$, C_{D_i}, C_Y, C_R vs ROLL ANGLE FROM EQUILIBRIUM

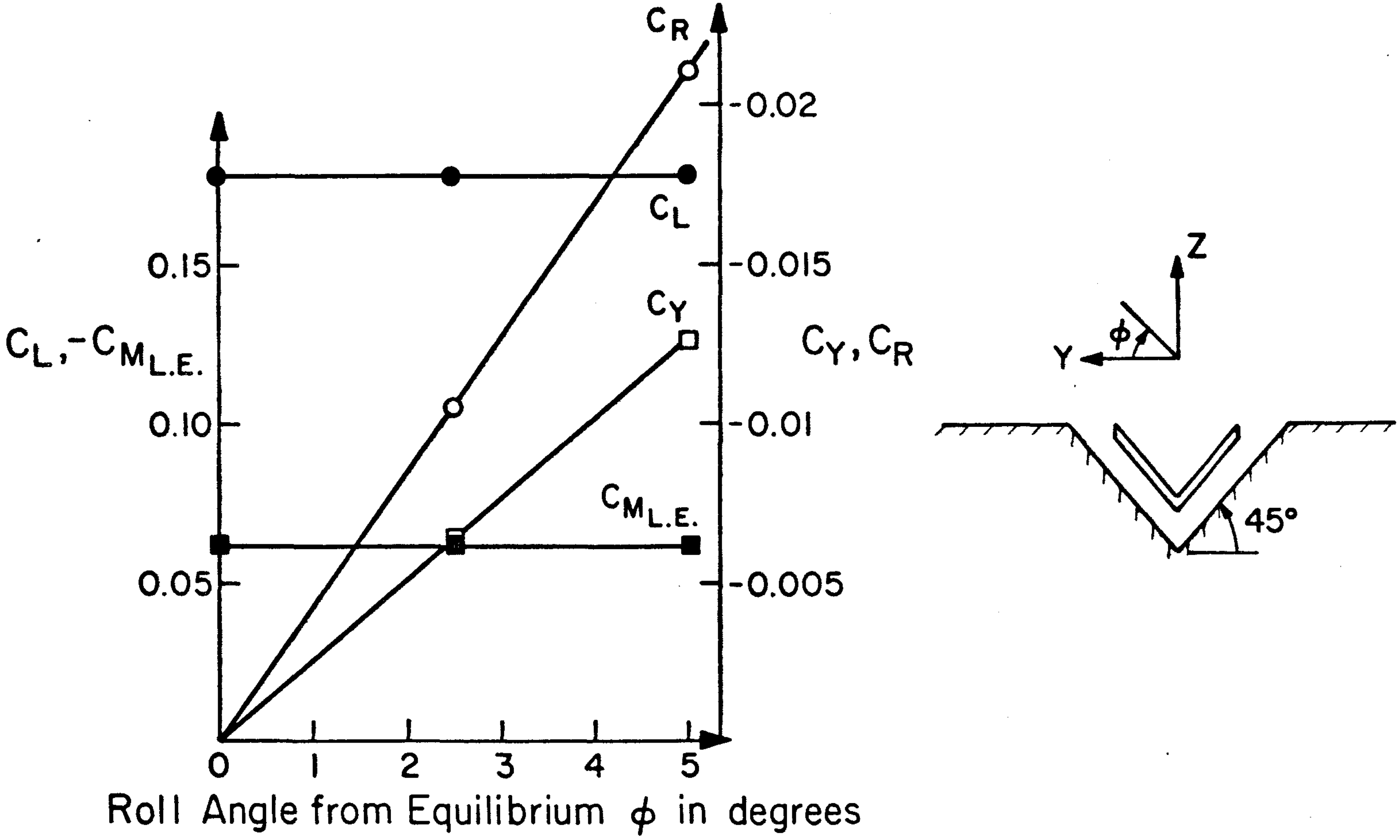

Fig. 29

SLANTED CHANNEL WING WITH DIHEDRAL

C_L, $C_{M_{L.E.}}$, C_{D_i}, C_Y, C_R vs

ANGLE OF ATTACK AND LATERAL SHIFT

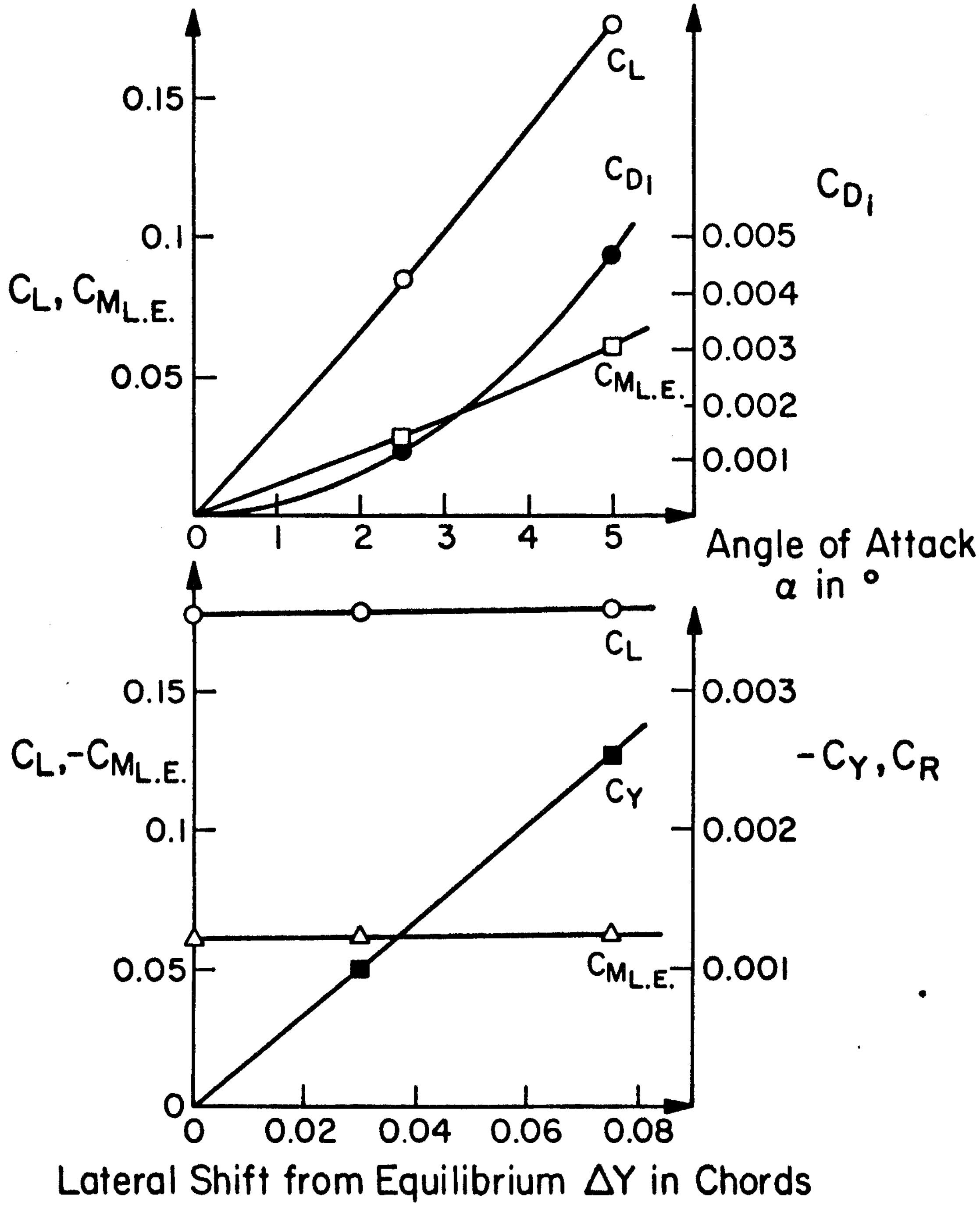

Fig. 30

CHORDWISE SOURCE STRENGTH DISTRIBUTION ON THE GROUND

SLANTED GROUND WING WITH DIHEDRAL

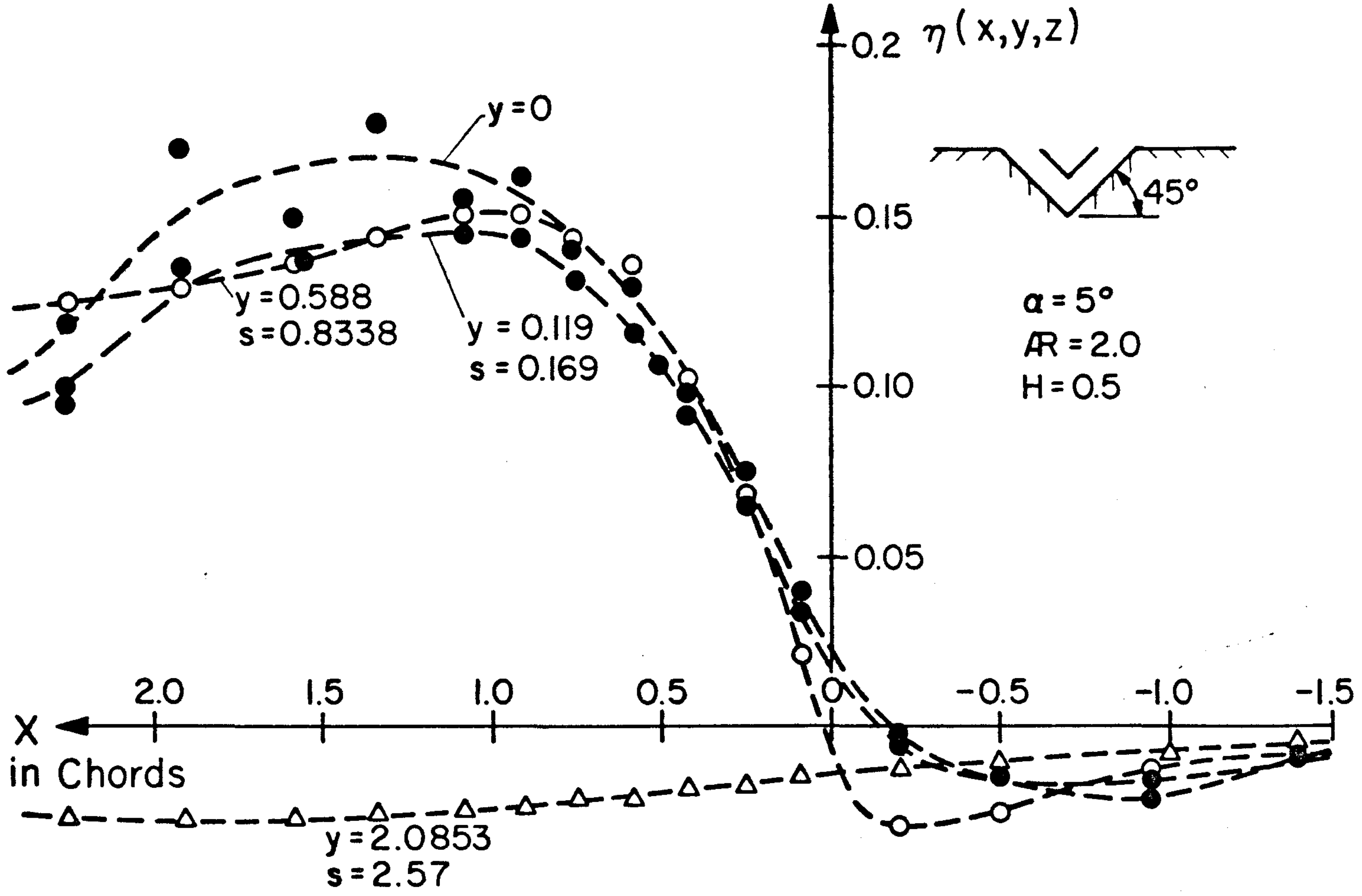

Fig. 31

SPANWISE SOURCE STRENGTH DISTRIBUTION ON THE GROUND

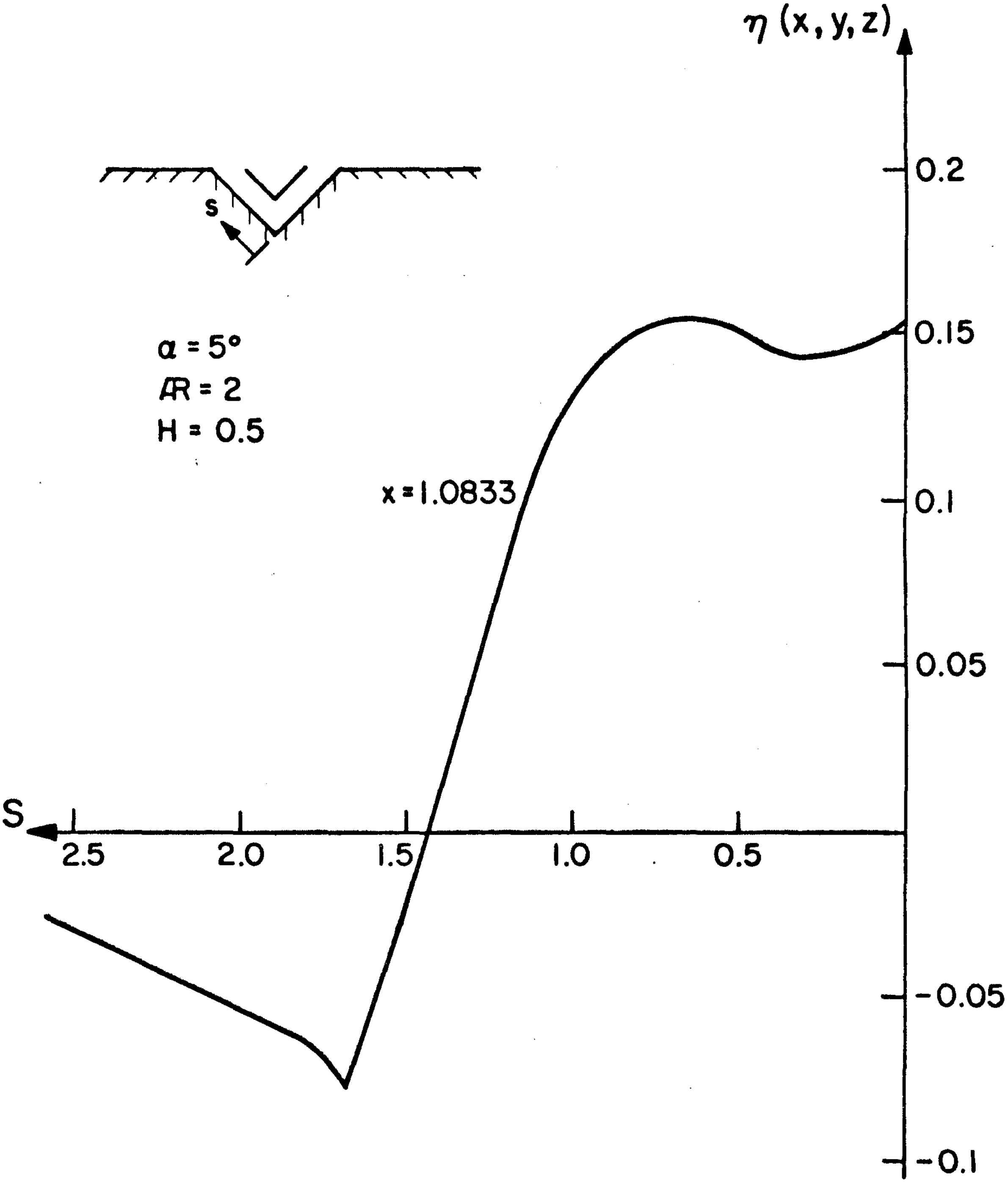

Fig. 32

AERODYNAMIC COEFFICIENTS vs h/c
RECTANGULAR RAIL - WING WITH END PLATES AT ANGLE OF ATTACK

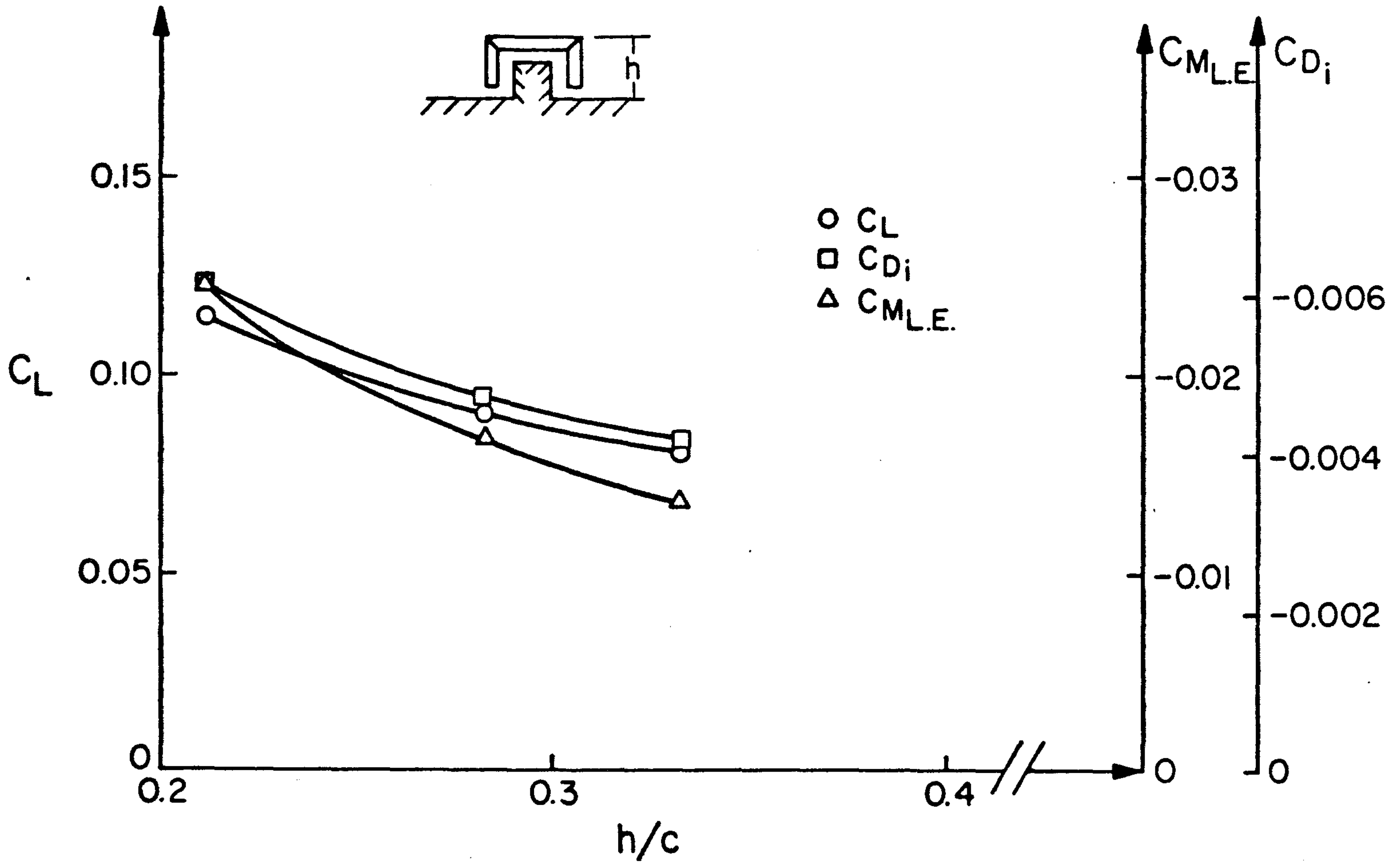

Fig. 33

LONGITUDINAL COORDINATE SYSTEM
IN
PERTURBED STATE

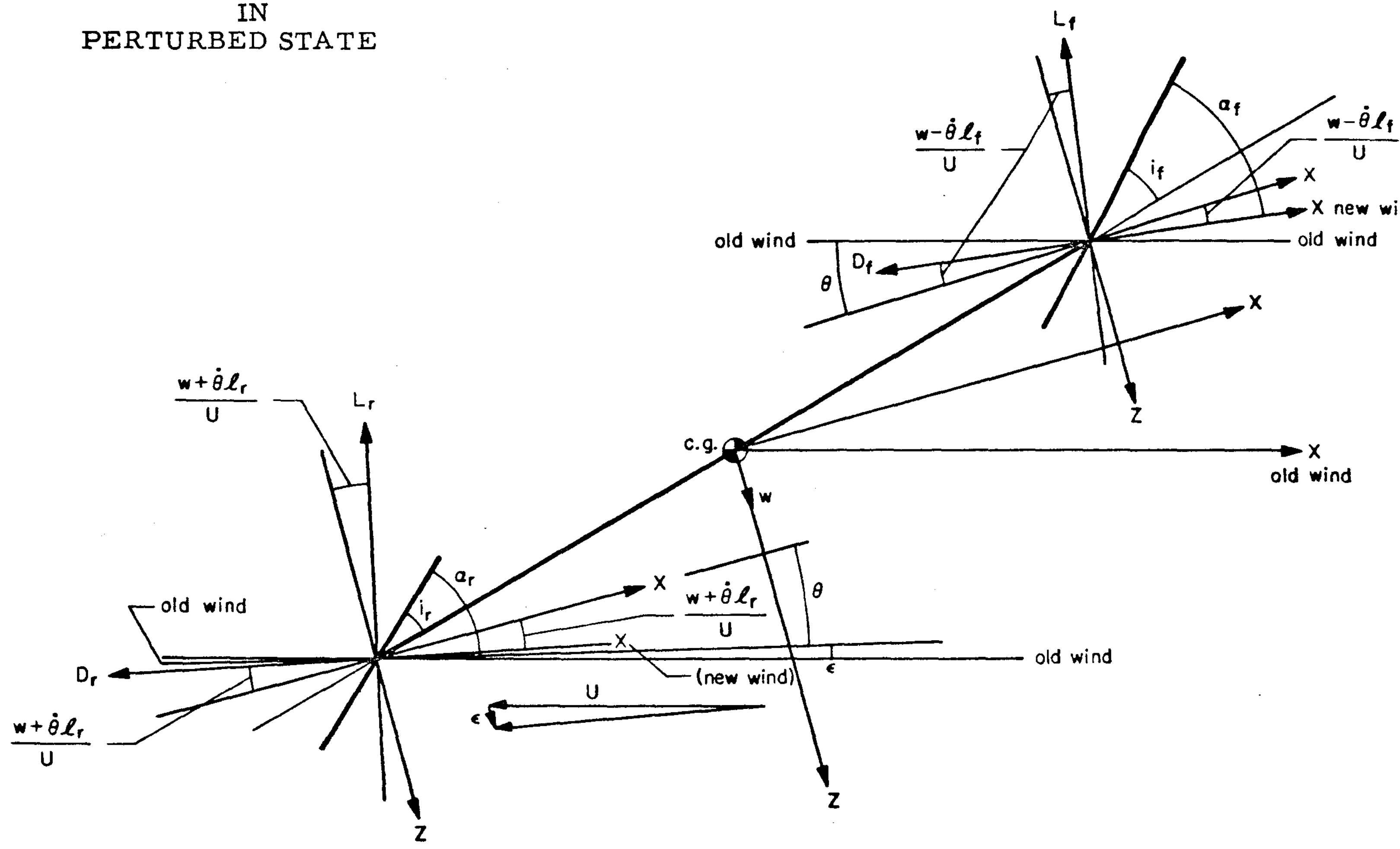

Fig. 34

LATERAL COORDINATE SYSTEM
IN
PERTURBED STATE

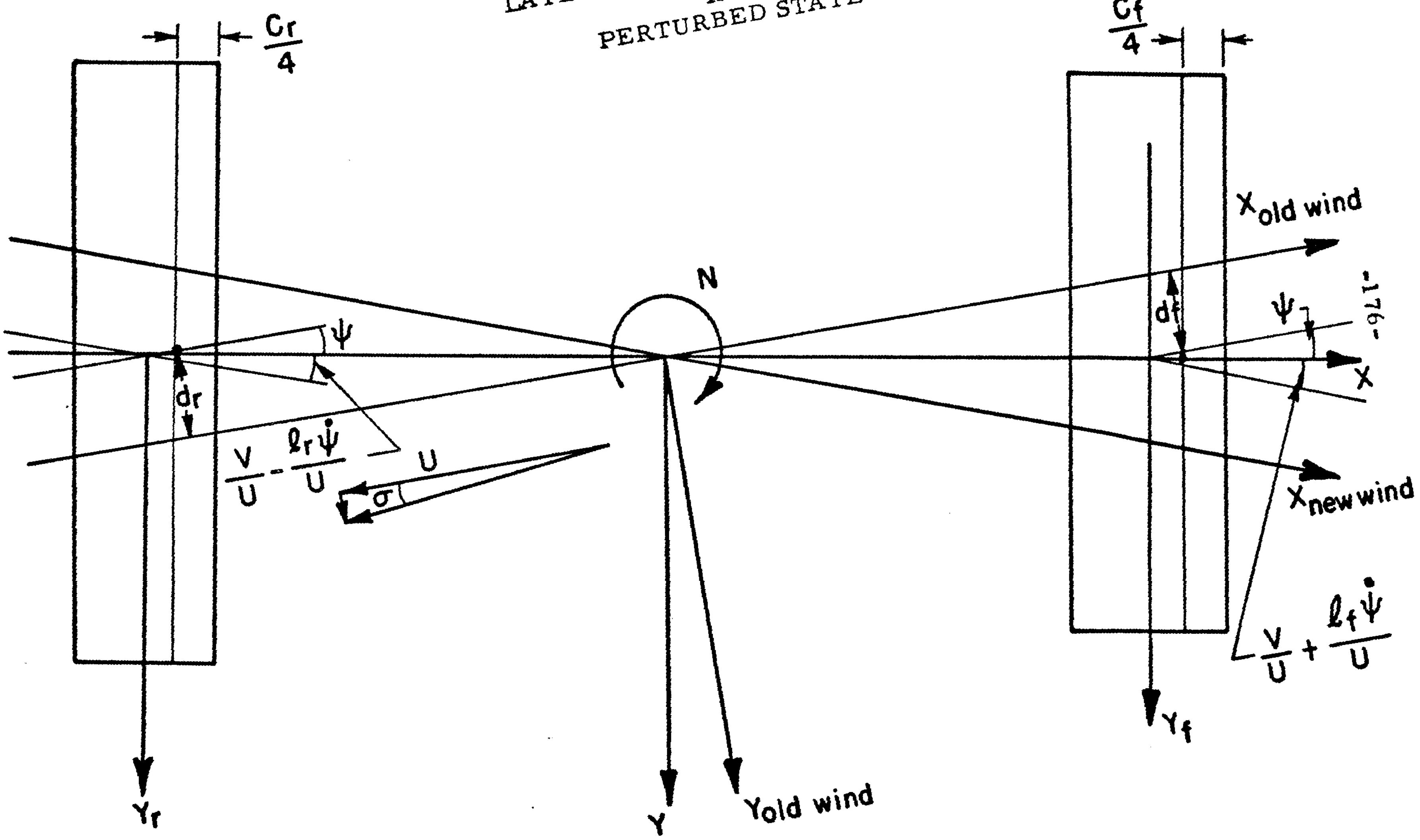

Fig. 35

LATERAL COORDINATE SYSTEM
IN
PERTURBED STATE

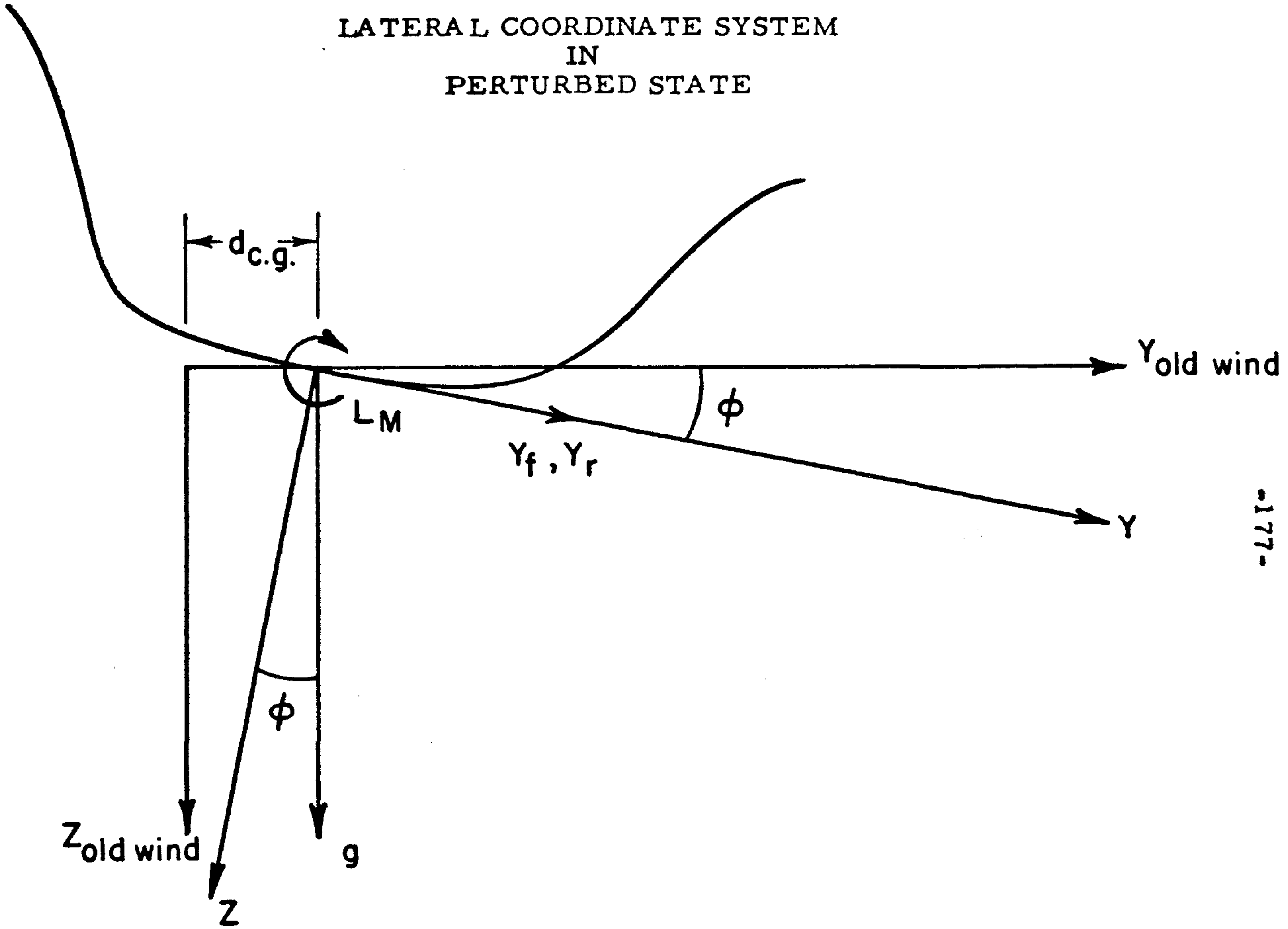

Fig. 36

ROOT LOCUS DIAGRAM LONGITUDINAL STABILITY
SINGLE FLAT WING

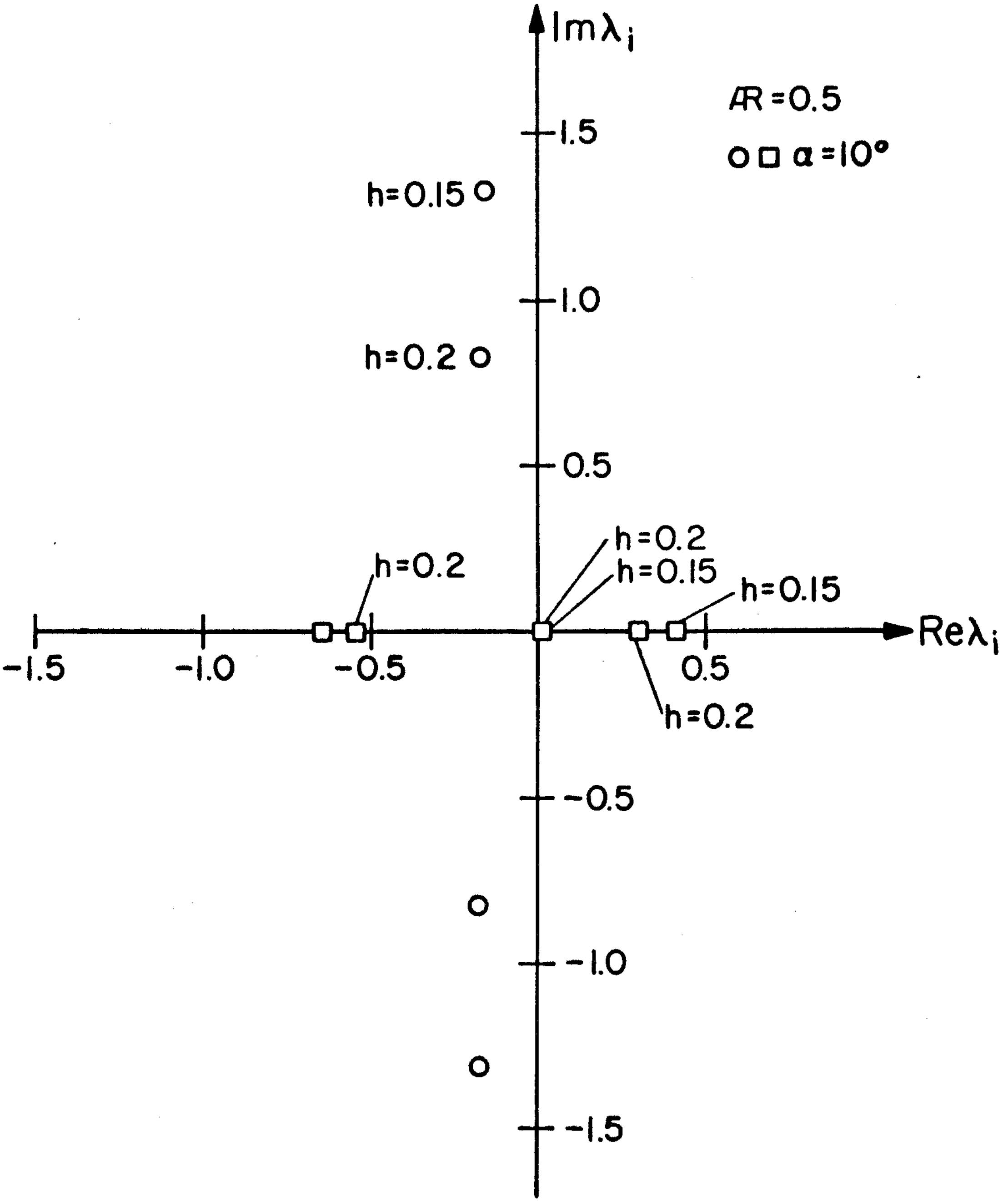

Fig. 37

ROOT LOCUS DIAGRAM LONGITUDINAL STABILITY
SINGLE FLAT WING

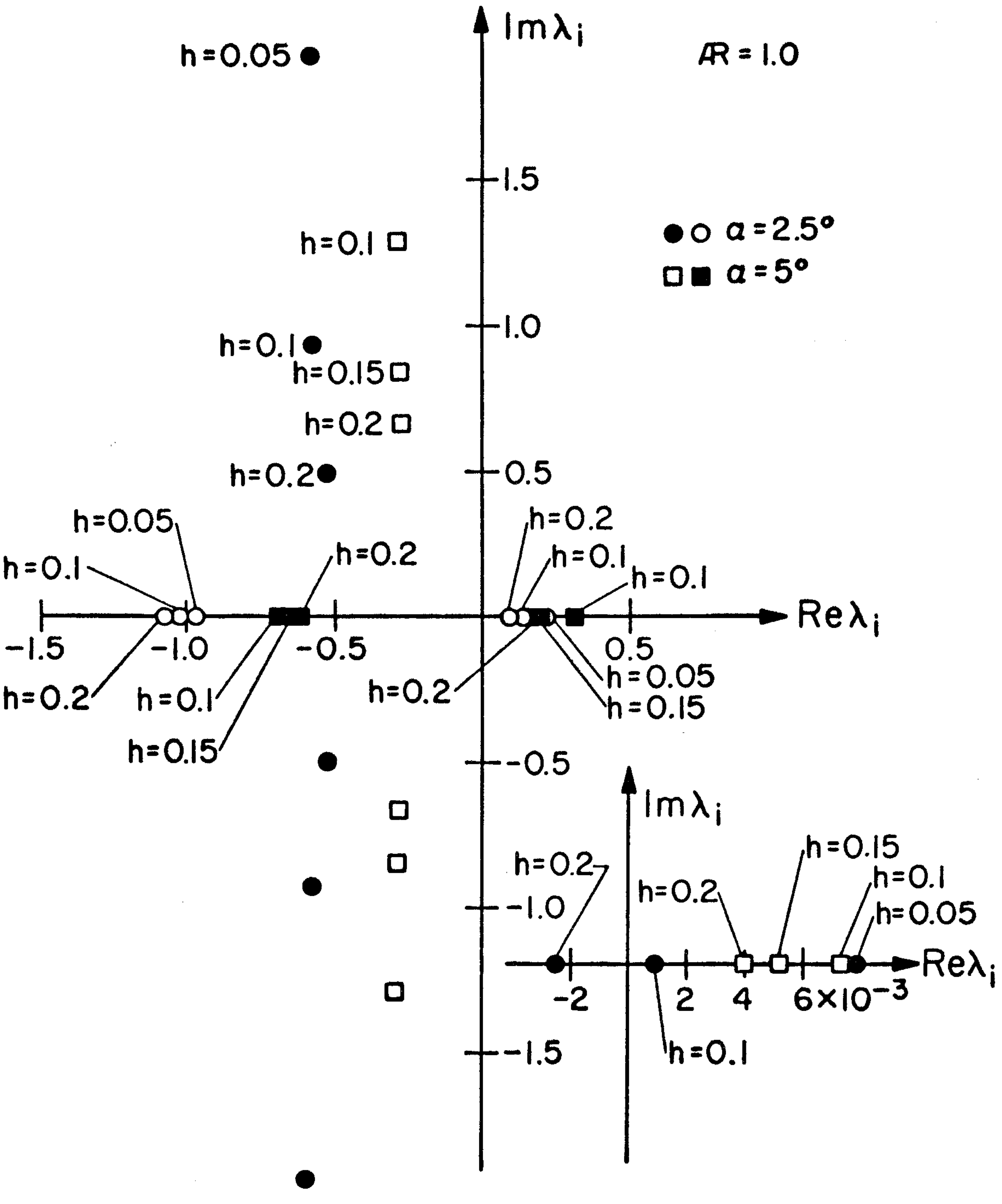

Fig. 38

ROOT LOCUS DIAGRAM LONGITUDINAL STABILITY
SINGLE FLAT WING

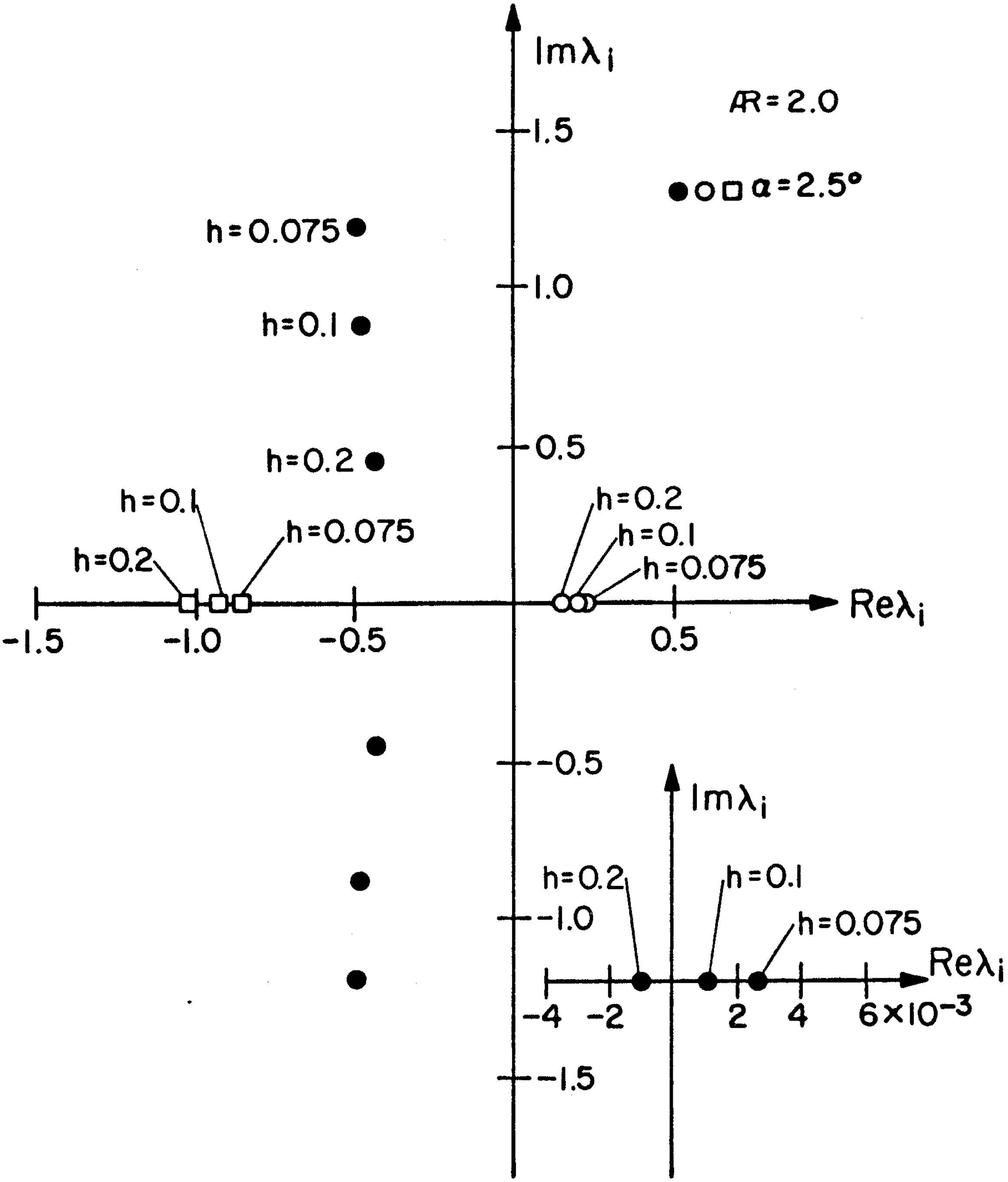

Fig. 39

ROOT LOCUS DIAGRAM LONGITUDINAL STABILITY
SINGLE FLAT WING

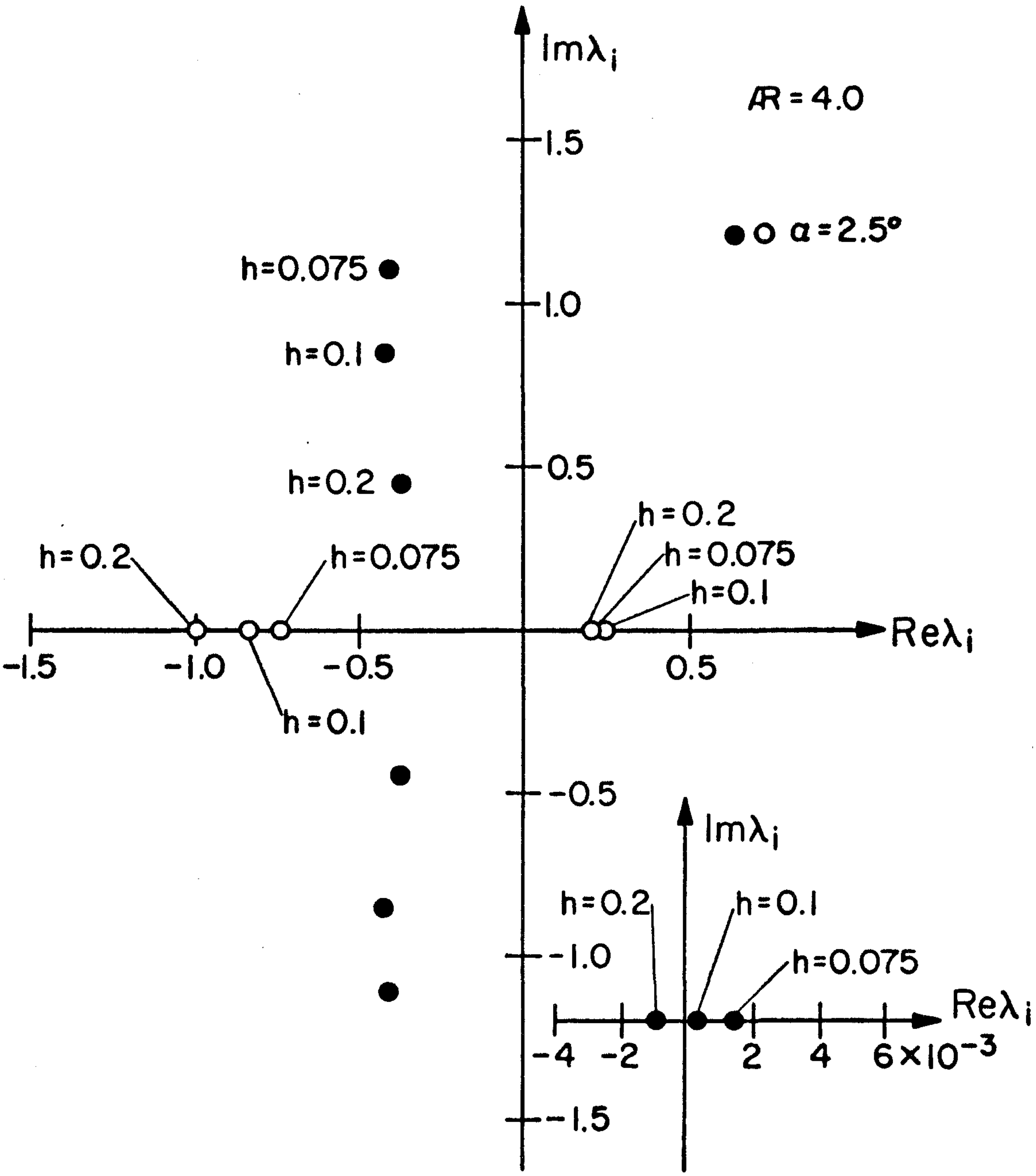

Fig. 40

ROOT LOCUS DIAGRAM LATERAL STABILITY
SINGLE FLAT WING

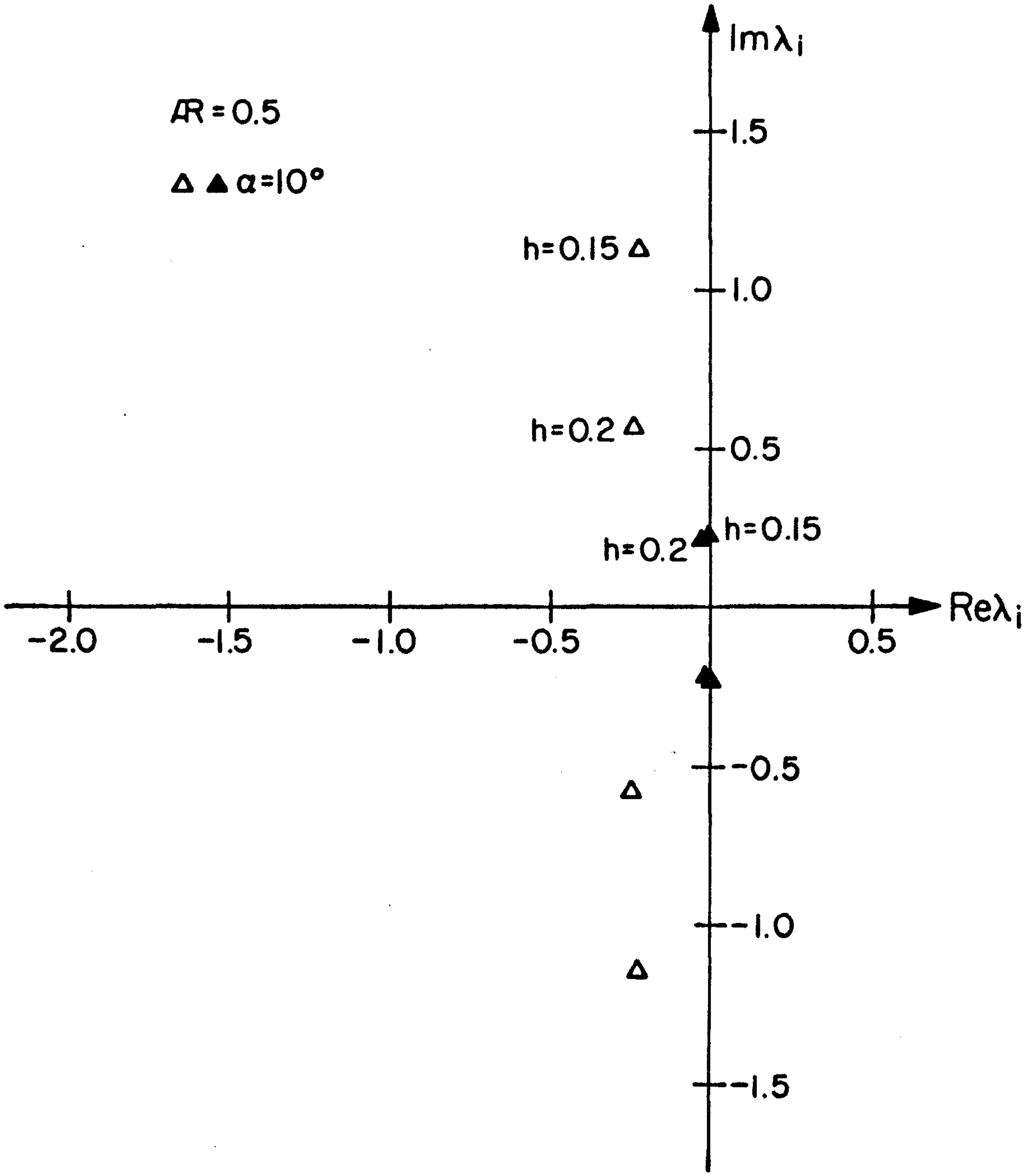

Fig. 41

ROOT LOCUS DIAGRAM LATERAL STABILITY
SINGLE FLAT WING

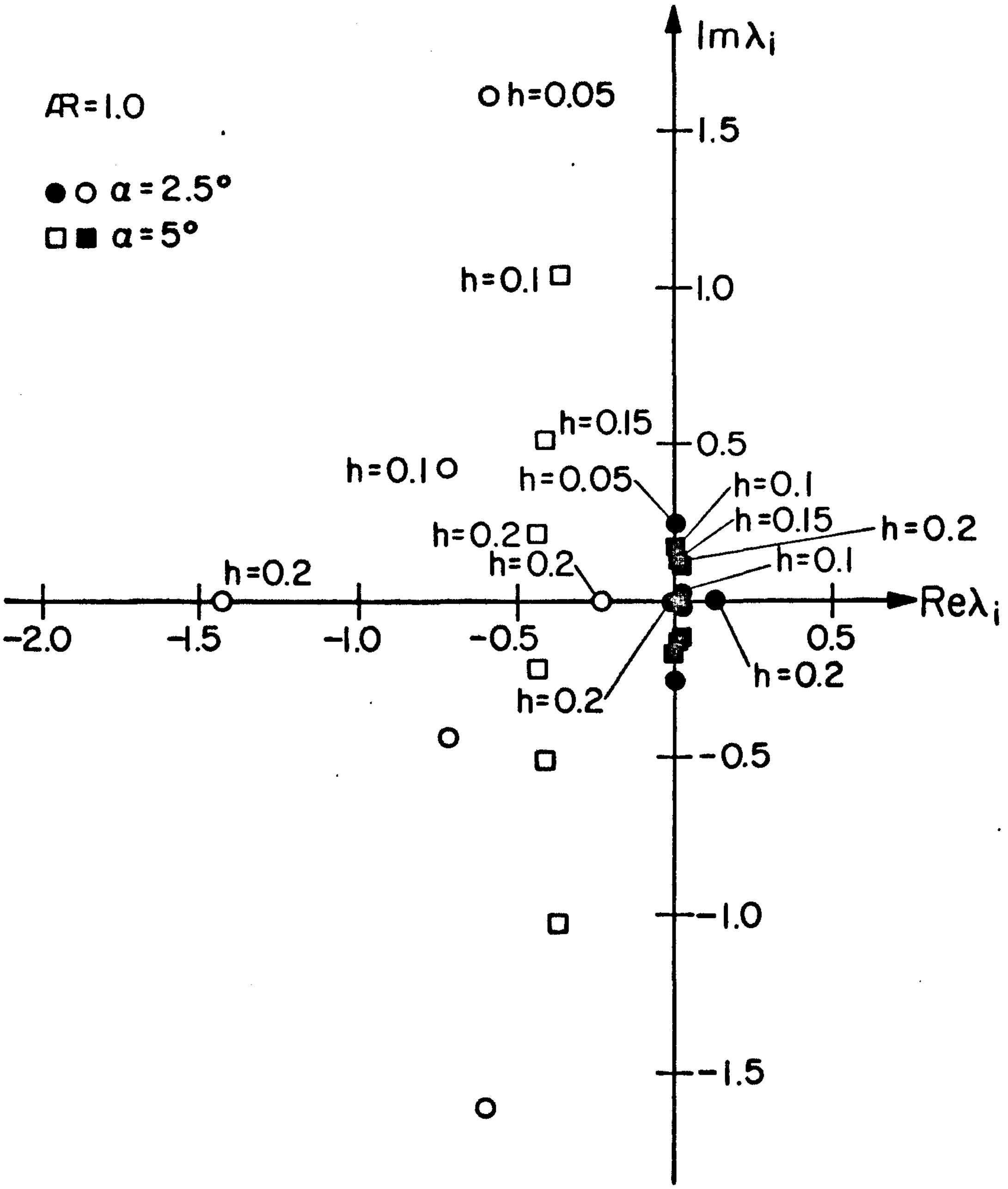

Fig. 42

ROOT LOCUS DIAGRAM LATERAL STABILITY
SINGLE FLAT WING

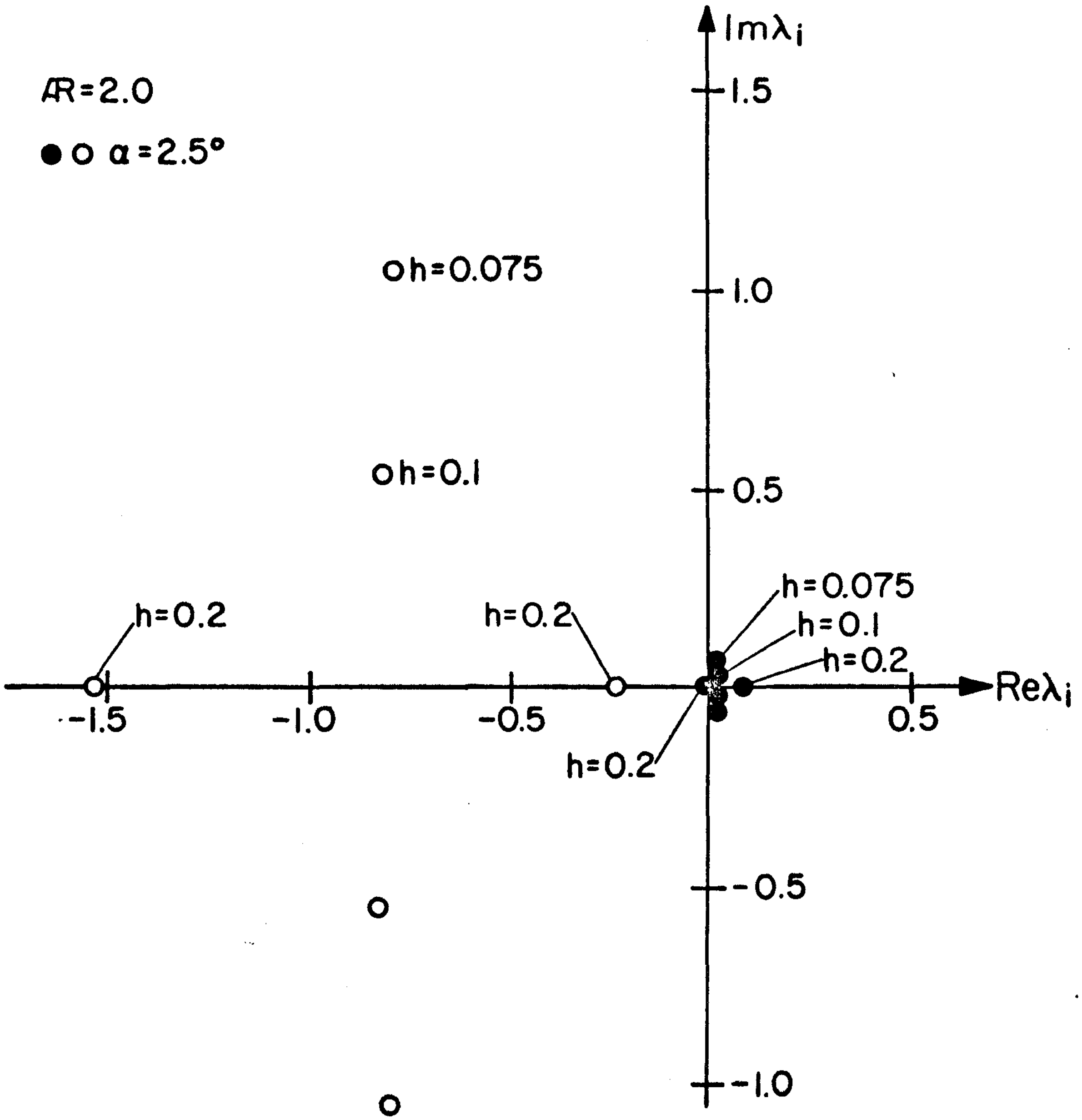

Fig. 43

ROOT LOCUS DIAGRAM LATERAL STABILITY
SINGLE FLAT WING

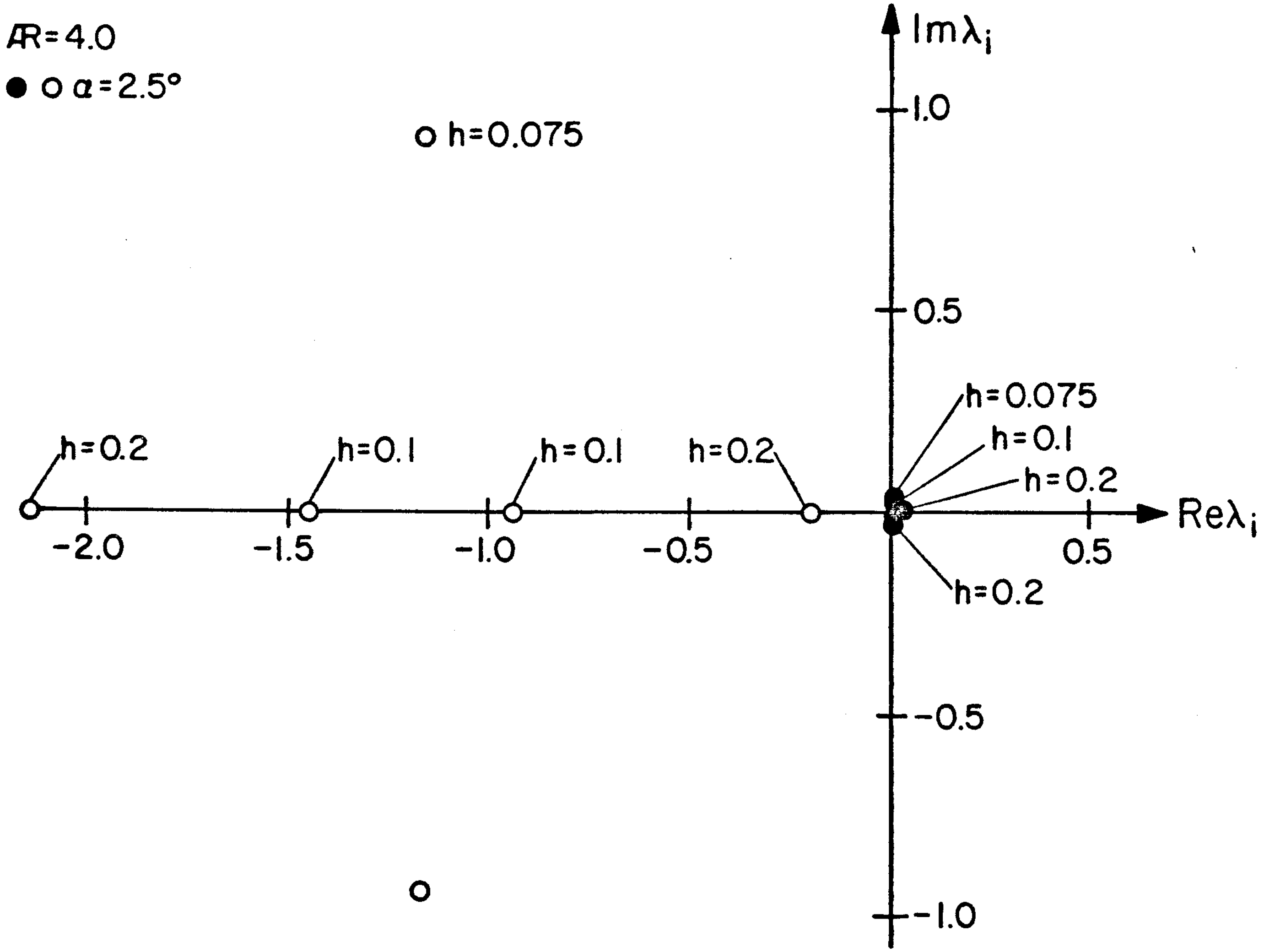

Fig. 44

ROOT LOCUS DIAGRAM

TRIANGULAR END PLATED WING IN GROUND EFFECT

(LONG. STAB)

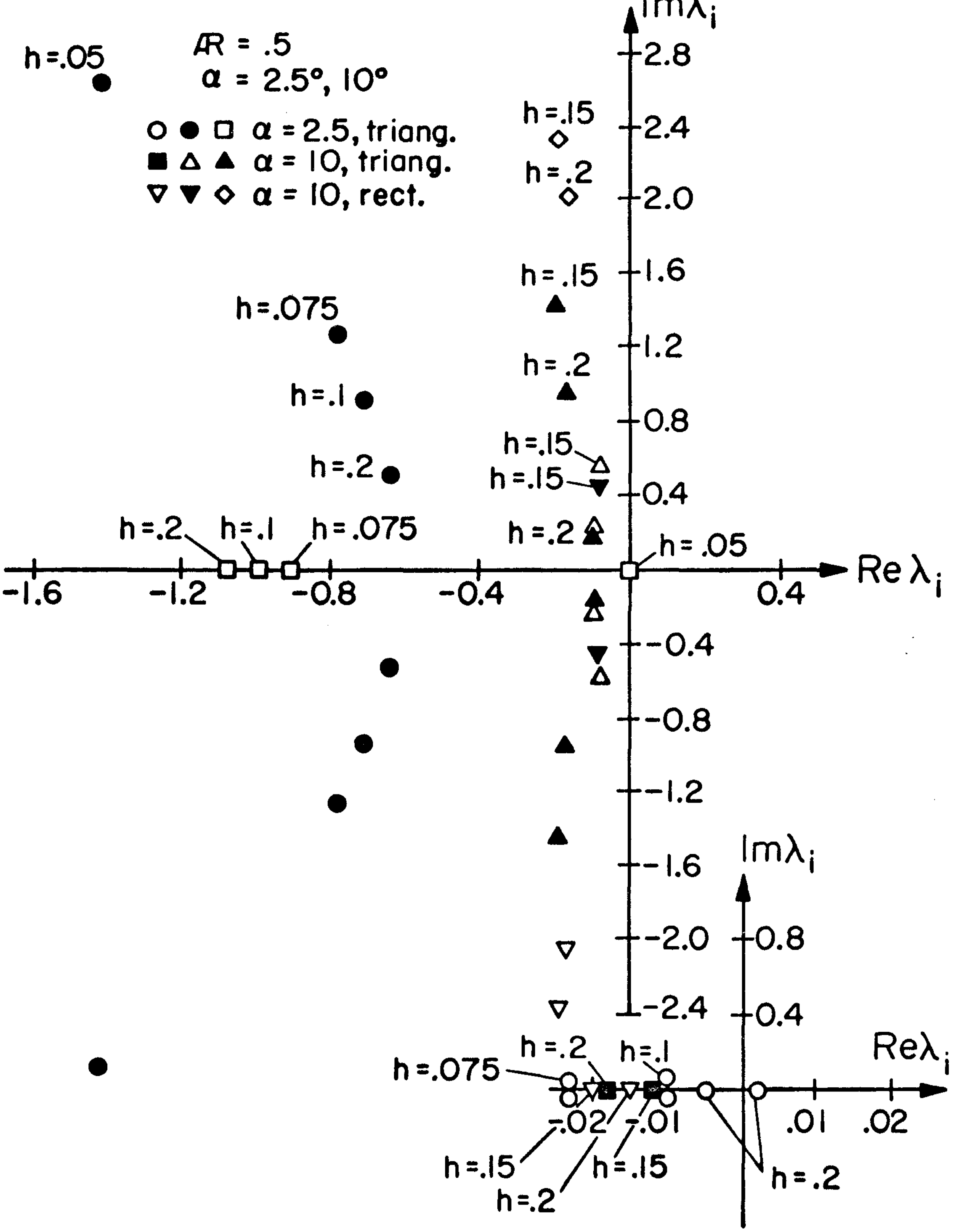

Fig. 45

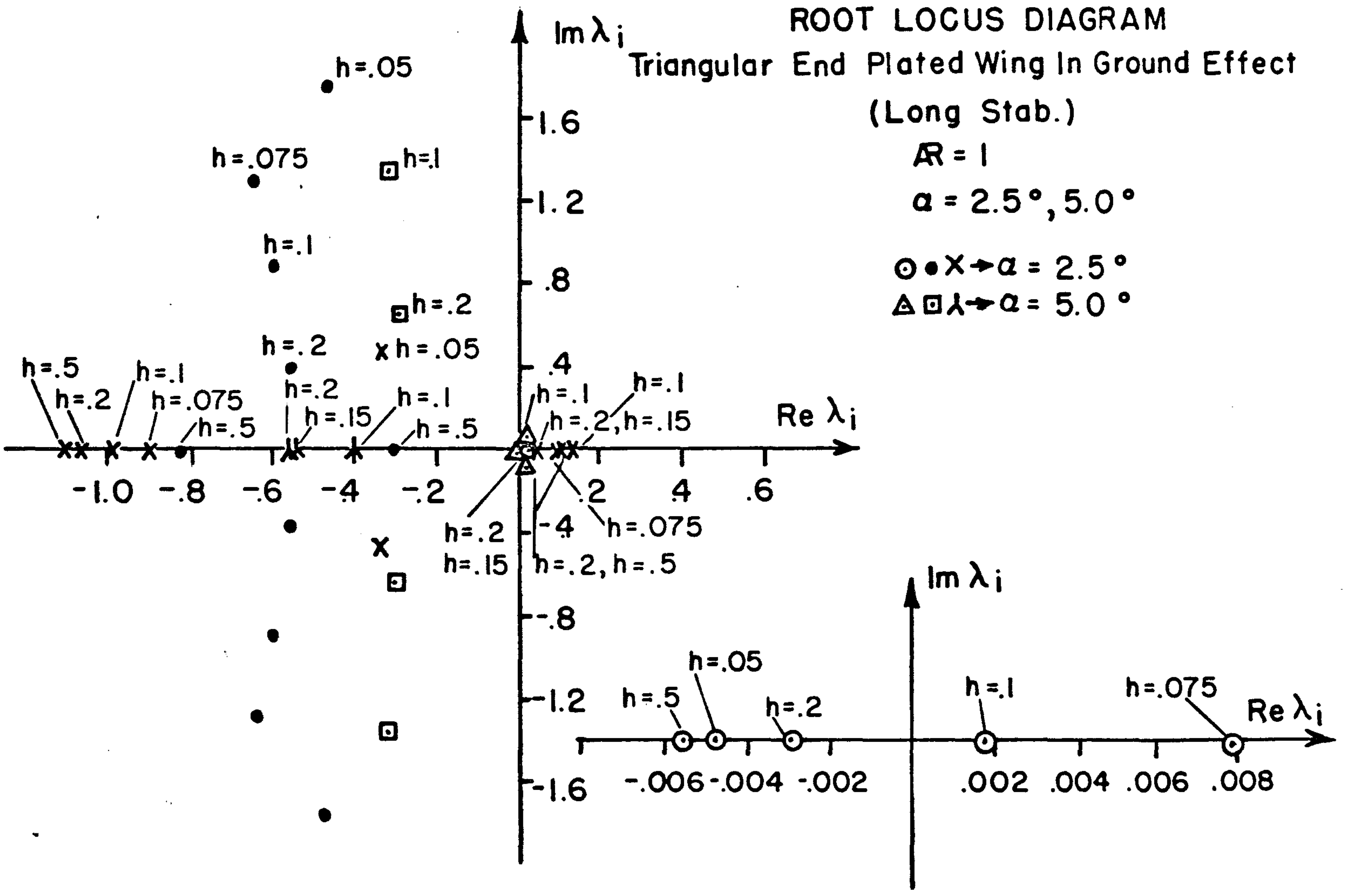
ROOT LOCUS DIAGRAM
Triangular End Plated Wing In Ground Effect
(Long Stab.)
$AR = 1$
$\alpha = 2.5°, 5.0°$
⊙ ● X → $\alpha = 2.5°$
△ ⊡ λ → $\alpha = 5.0°$
Im λ_i
Re λ_i
1.6
1.2
.8
.4
-.4
-.8
-1.2
-1.6
-1.0
-.8
-.6
-.4
-.2
.2
.4
.6
h=.05
h=.075
h=.1
h=.2
h=.1
h=.2
x h=.05
h=.5
h=.2
h=.1
h=.075
h=.5
h=.2
h=.15
h=.1
h=.5
h=.1
h=.2, h=.15
h=.1
h=.2
h=.15
h=.075
h=.2, h=.5
Im λ_i
Re λ_i
h=.5
h=.05
h=.2
h=.1
h=.075
-.006
-.004
-.002
.002
.004
.006
.008

Fig. 46

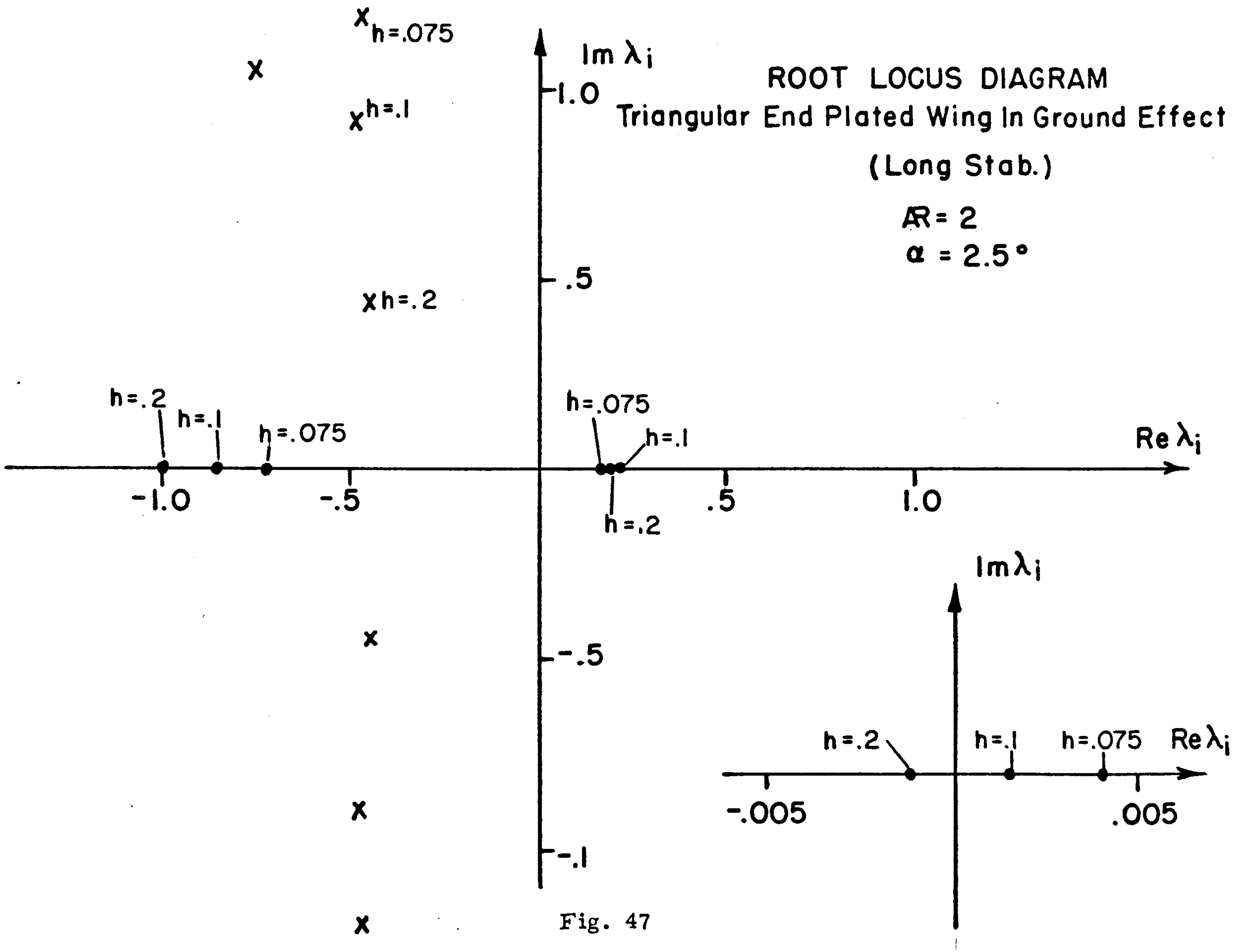
ROOT LOCUS DIAGRAM
Triangular End Plated Wing In Ground Effect
(Long Stab.)
Æ = 2
α = 2.5°
Im λ_i
Re λ_i
1.0
.5
-.5
-.1
-1.0
-.5
.5
1.0
h=.075
h=.1
h=.2
h=.2
h=.1
h=.075
h=.075
h=.1
h=.2
Im λ_i
Re λ_i
-.005
.005
h=.2
h=.1
h=.075

Fig. 47

ROOT LOCUS DIAGRAM
END PLATED WING IN GROUND EFFECT
(LAT. STAB)

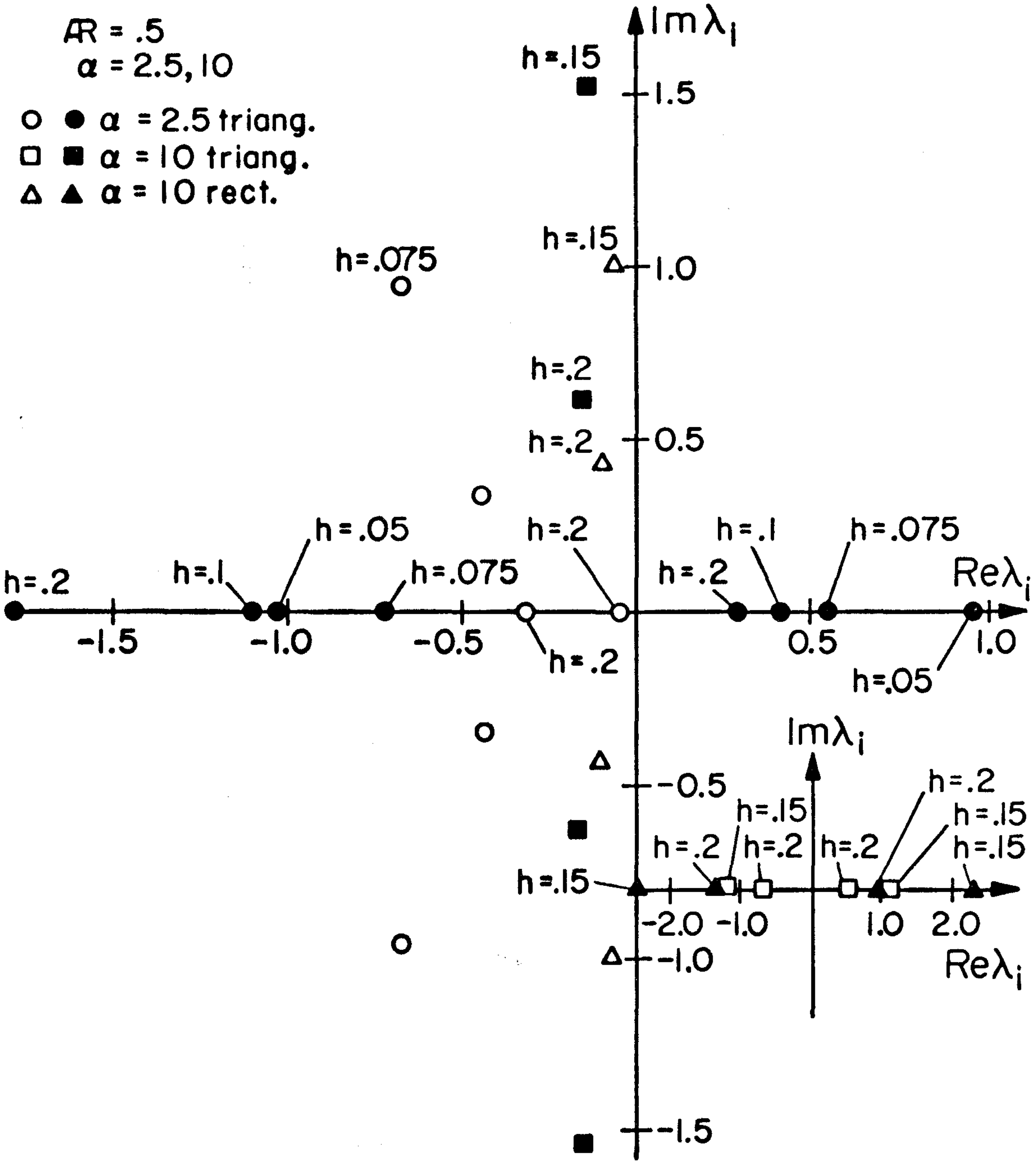

Fig. 48

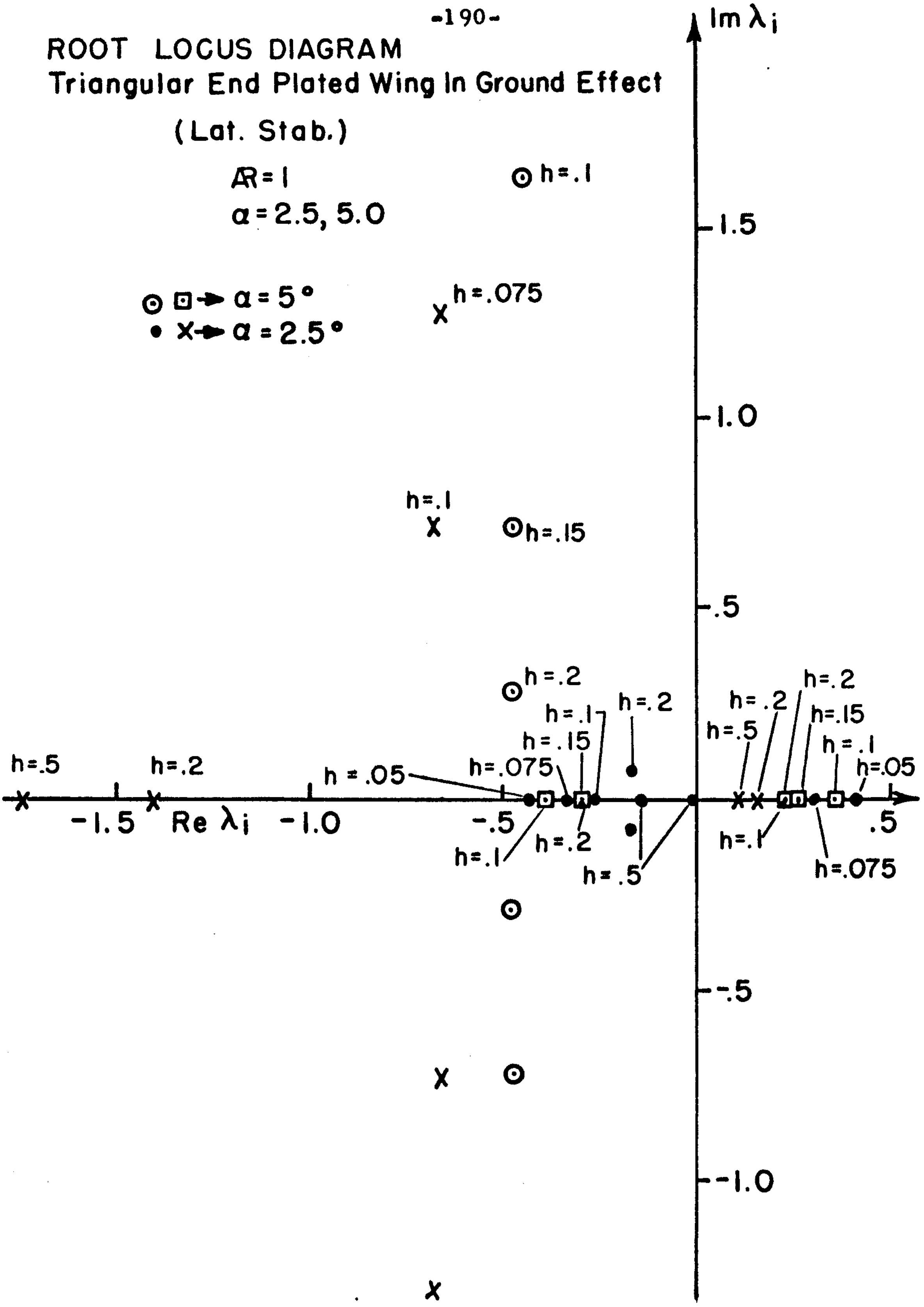
ROOT LOCUS DIAGRAM
Triangular End Plated Wing In Ground Effect
(Lat. Stab.)
Æ = 1
α = 2.5, 5.0
⊙ ⊡ → α = 5°
● X → α = 2.5°
Im λi
Re λi
1.5
1.0
.5
-.5
-1.0
-1.5
-1.0
-.5
.5
h = .1
h = .075
h = .1
h = .15
h = .2
h = .2
h = .1
h = .15
h = .05
h = .075
h = .2
h = .5
h = .2
h = .5
h = .2
h = .1
h = .5
h = .2
h = .2
h = .15
h = .1
h = .05
h = .1
h = .075

Fig. 49

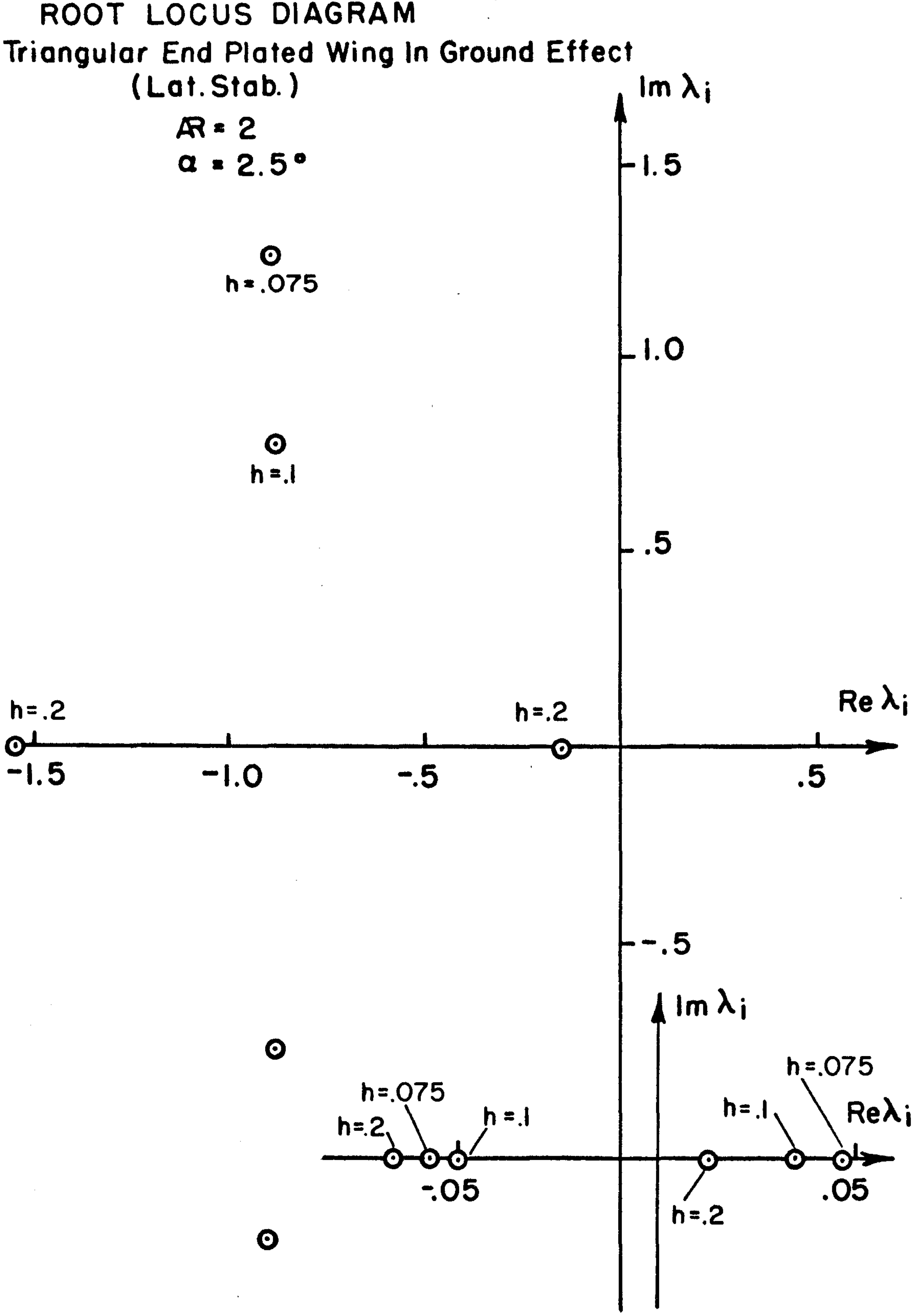
ROOT LOCUS DIAGRAM
Triangular End Plated Wing In Ground Effect
(Lat. Stab.)
Æ = 2
α = 2.5°
Im λ$_i$
1.5
1.0
.5
-.5
h=.075
h=.1
h=.2
h=.2
Re λ$_i$
-1.5
-1.0
-.5
.5
Im λ$_i$
h=.075
h=.1
Reλ$_i$
h=.075
h=.2
h=.1
-.05
.05
h=.2

Fig. 50

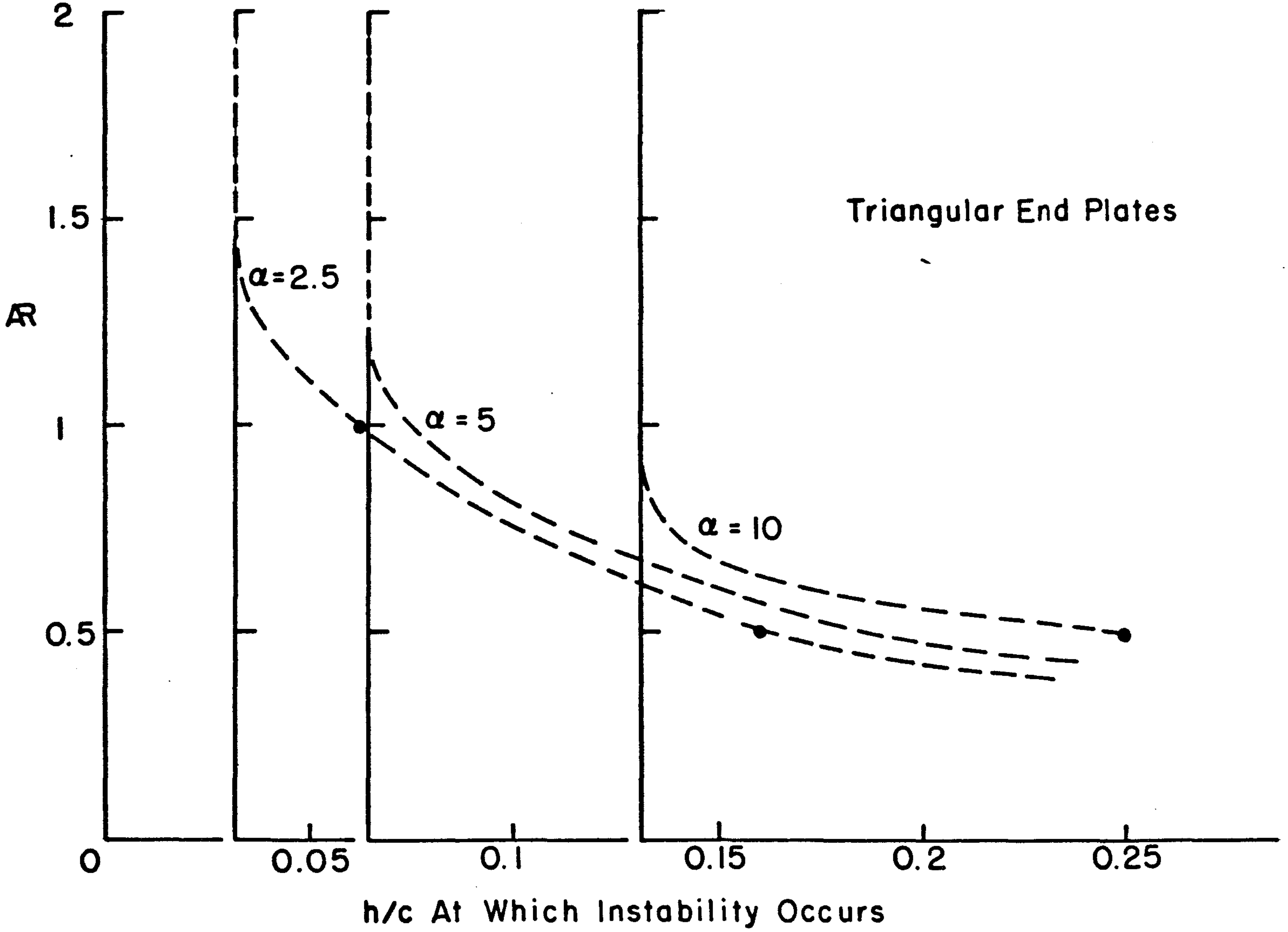
Triangular End Plates
$\alpha=2.5$
$\alpha=5$
$\alpha=10$
Æ
2
1.5
1
0.5
0
0.05
0.1
0.15
0.2
0.25
h/c At Which Instability Occurs

Fig. 51

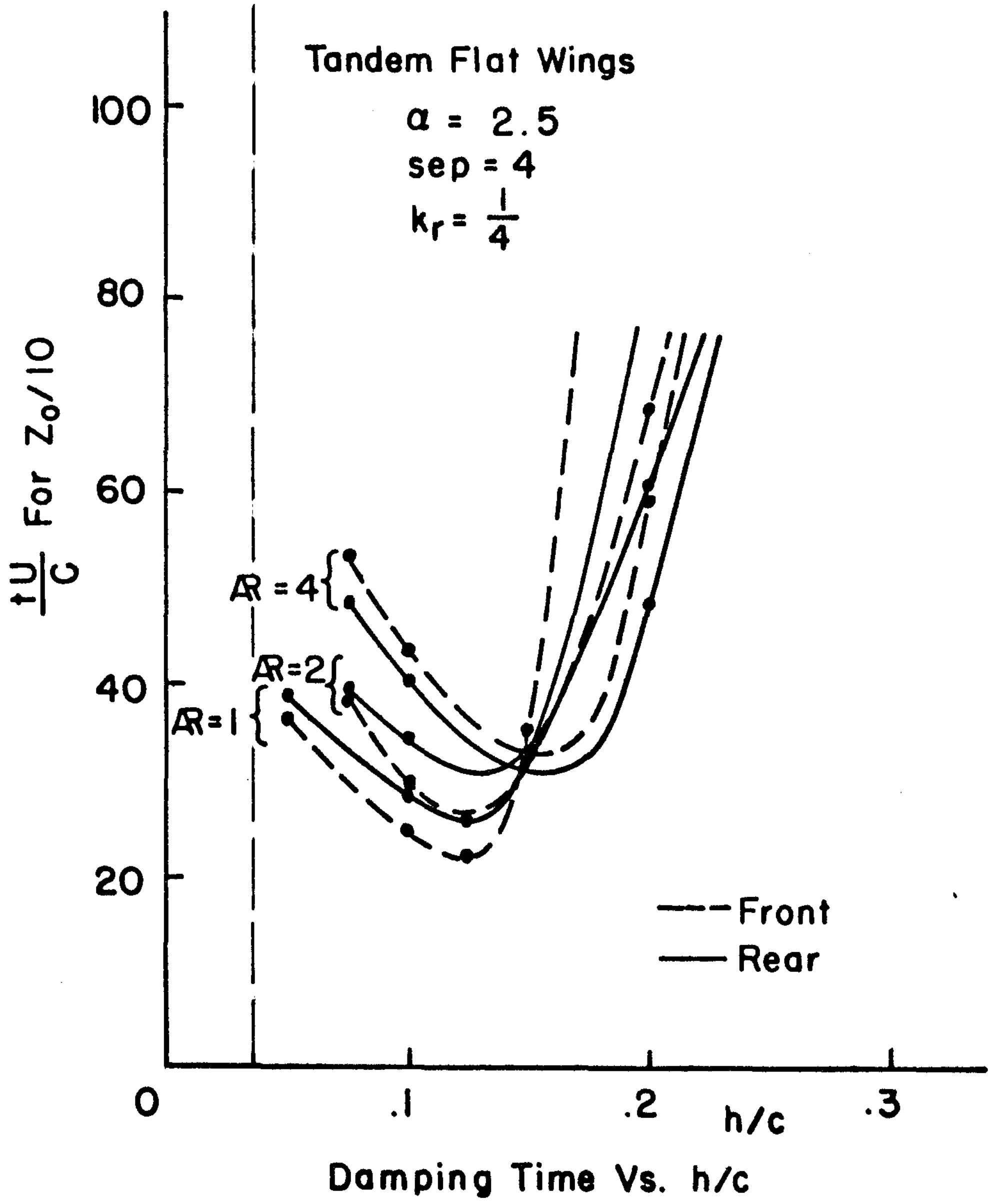
Tandem Flat Wings
α = 2.5
sep = 4
$k_r = \frac{1}{4}$
$\frac{tU}{c}$ For $Z_o/10$
100
80
60
40
20
0
.1
.2
.3
h/c
AR = 4
AR=2
AR=1
Front
Rear
Damping Time Vs. h/c

Fig. 52

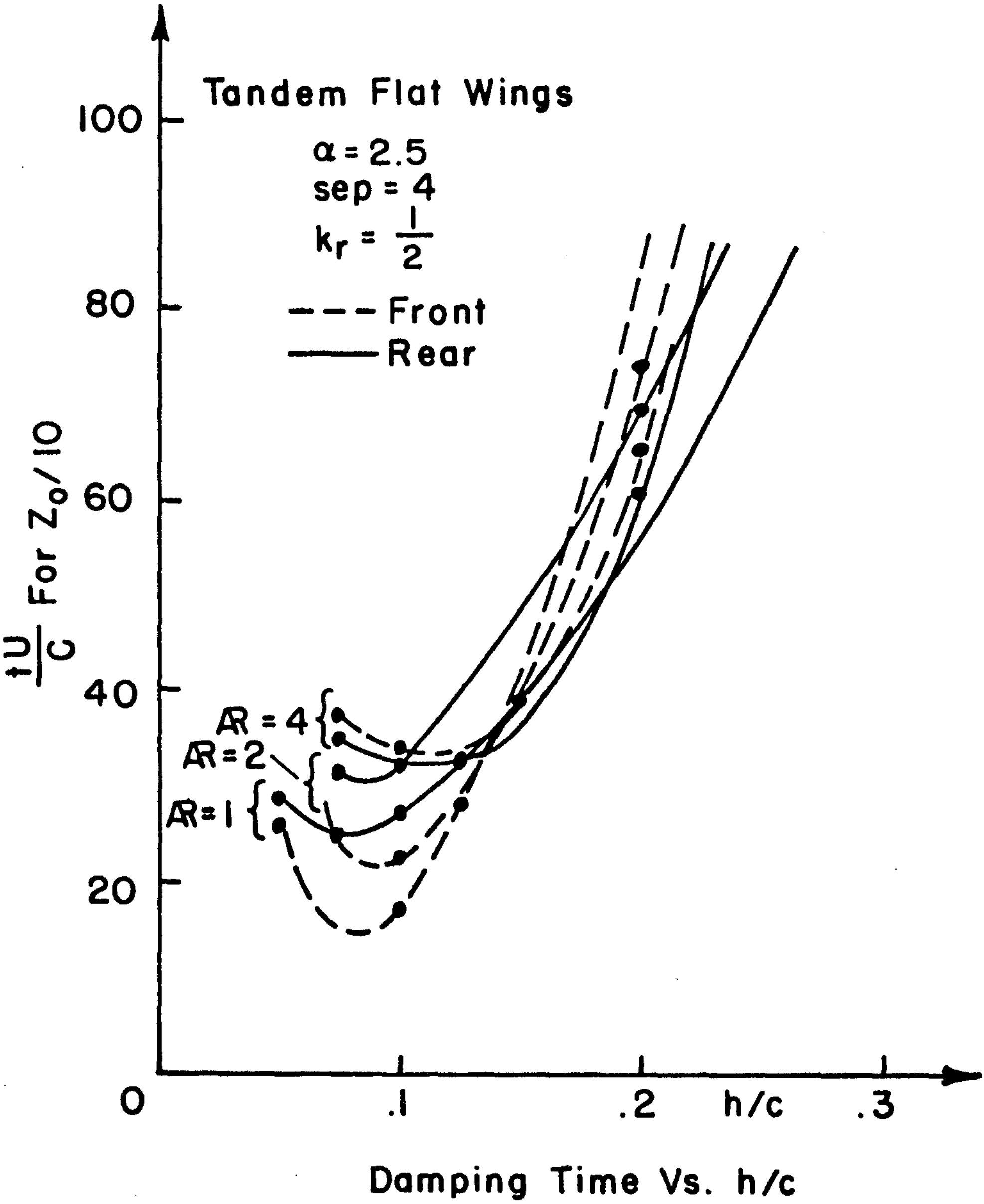
Tandem Flat Wings
α = 2.5
sep = 4
$k_r = \frac{1}{2}$
Front
Rear
Æ = 4
Æ = 2
Æ = 1
$\frac{tU}{c}$ For $Z_o/10$
100
80
60
40
20
0
.1
.2
h/c
.3
Damping Time Vs. h/c

Fig. 53

Fig. 54

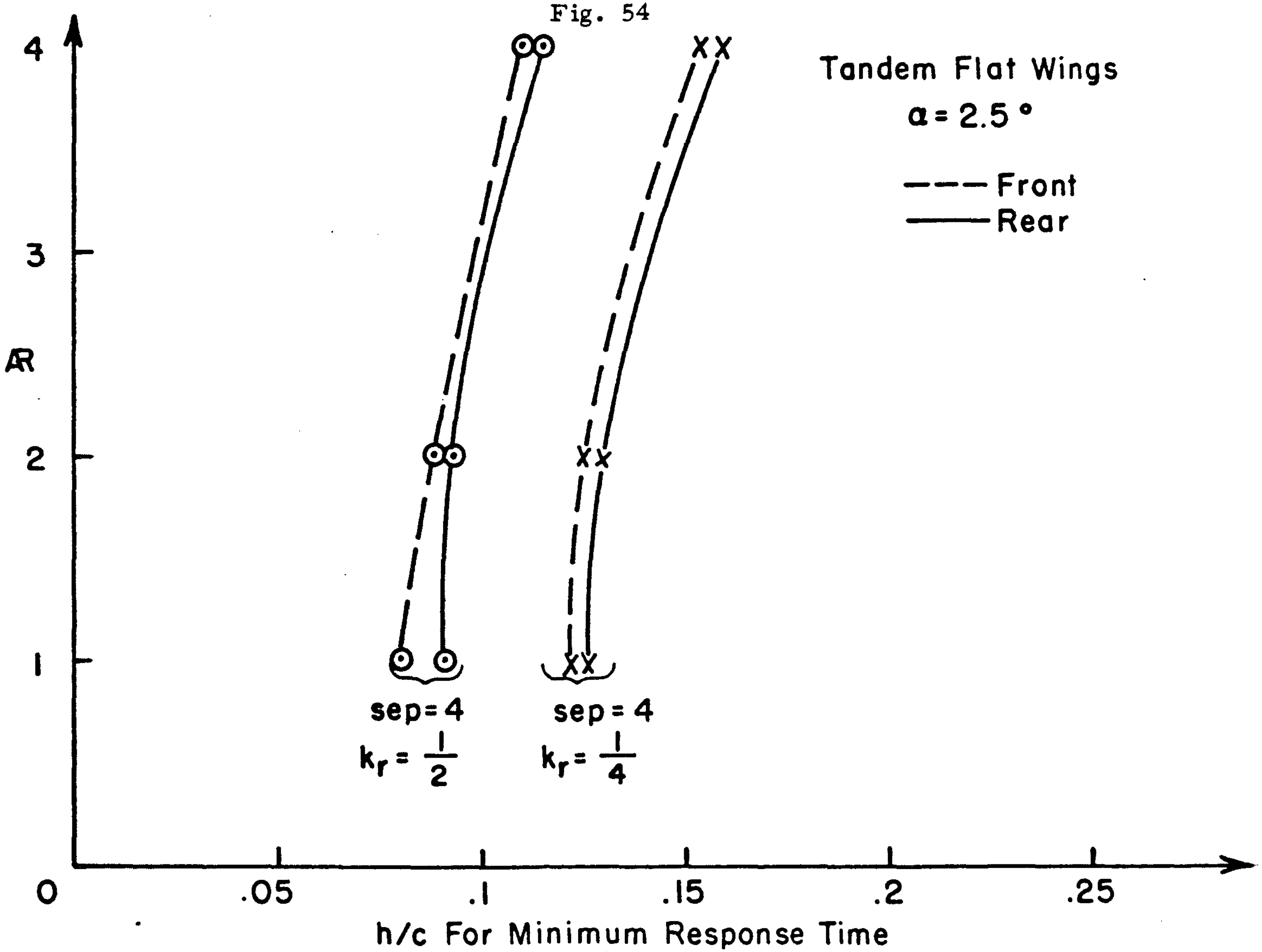

OPTIMUM HEIGHT VS. ASPECT RATIO

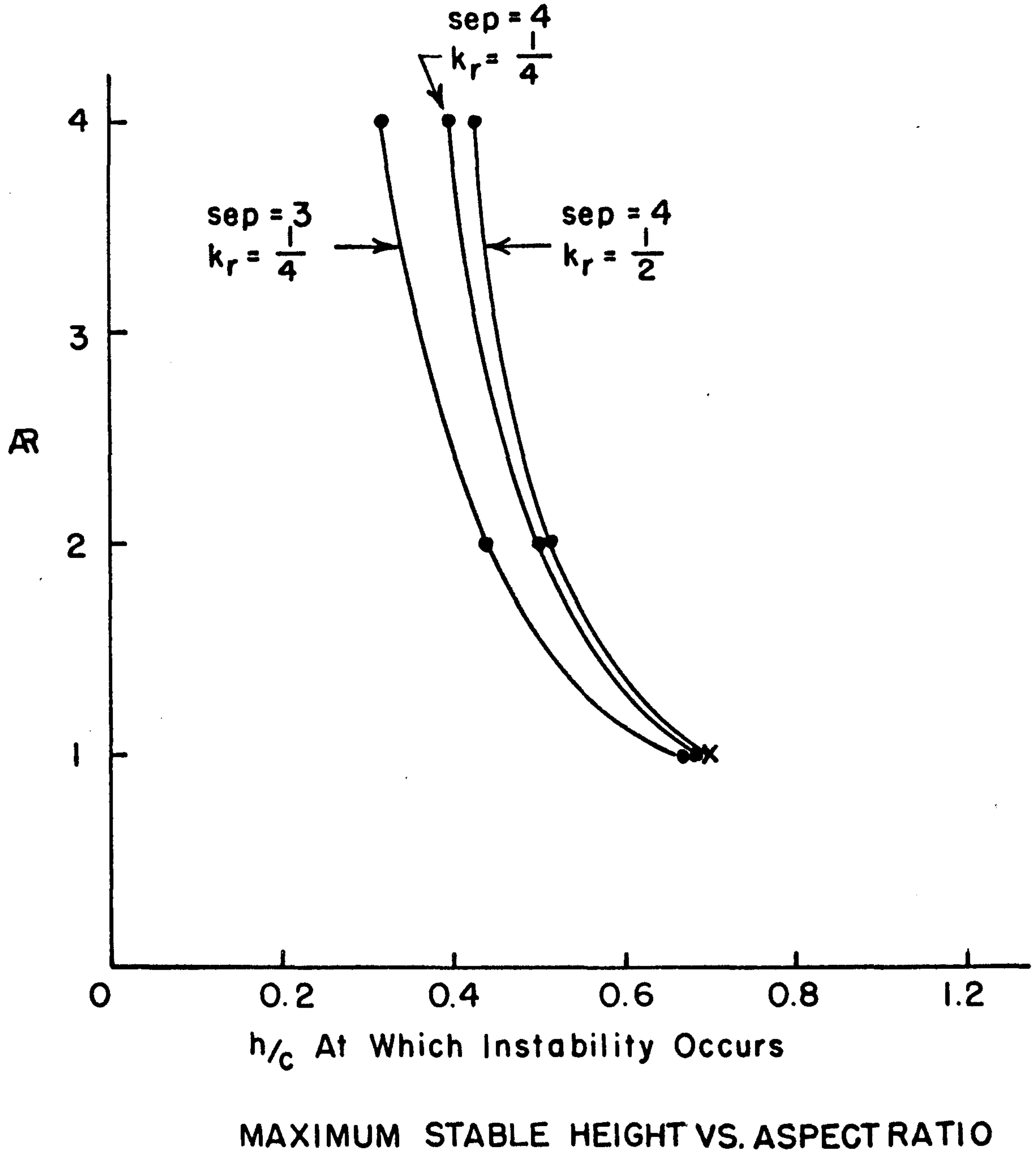

MAXIMUM STABLE HEIGHT VS. ASPECT RATIO

Fig. 55

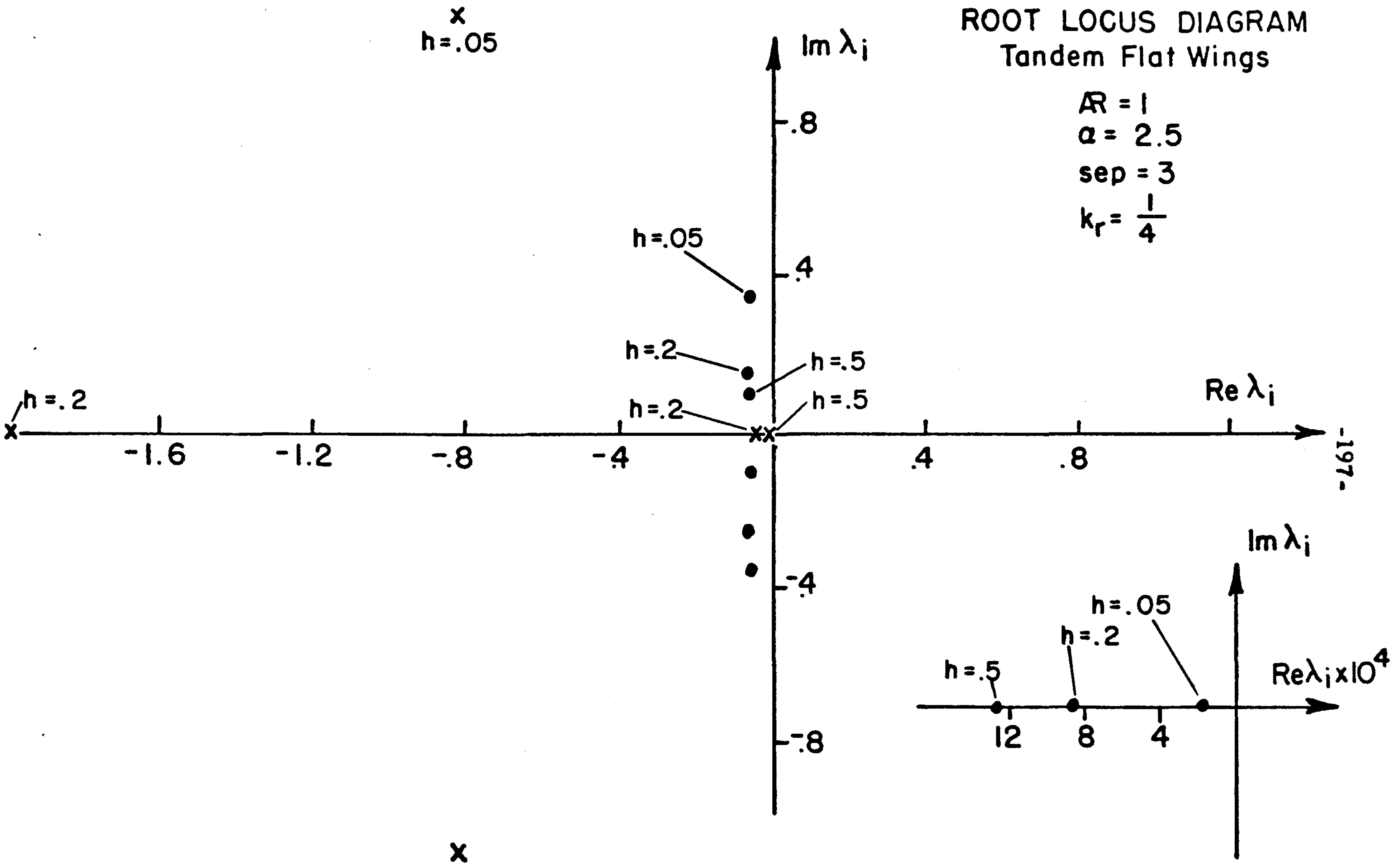
ROOT LOCUS DIAGRAM
Tandem Flat Wings
Æ = 1
a = 2.5
sep = 3
$k_r = \frac{1}{4}$
$\mathrm{Im}\,\lambda_i$
$\mathrm{Re}\,\lambda_i$
h = .05
h = .05
h = .2
h = .5
h = .2
h = .5
h = .2
-1.6
-1.2
-.8
-.4
.4
.8
.8
.4
-.4
-.8
$\mathrm{Im}\,\lambda_i$
$\mathrm{Re}\,\lambda_i \times 10^4$
h = .05
h = .2
h = .5
12
8
4

Fig. 56 a

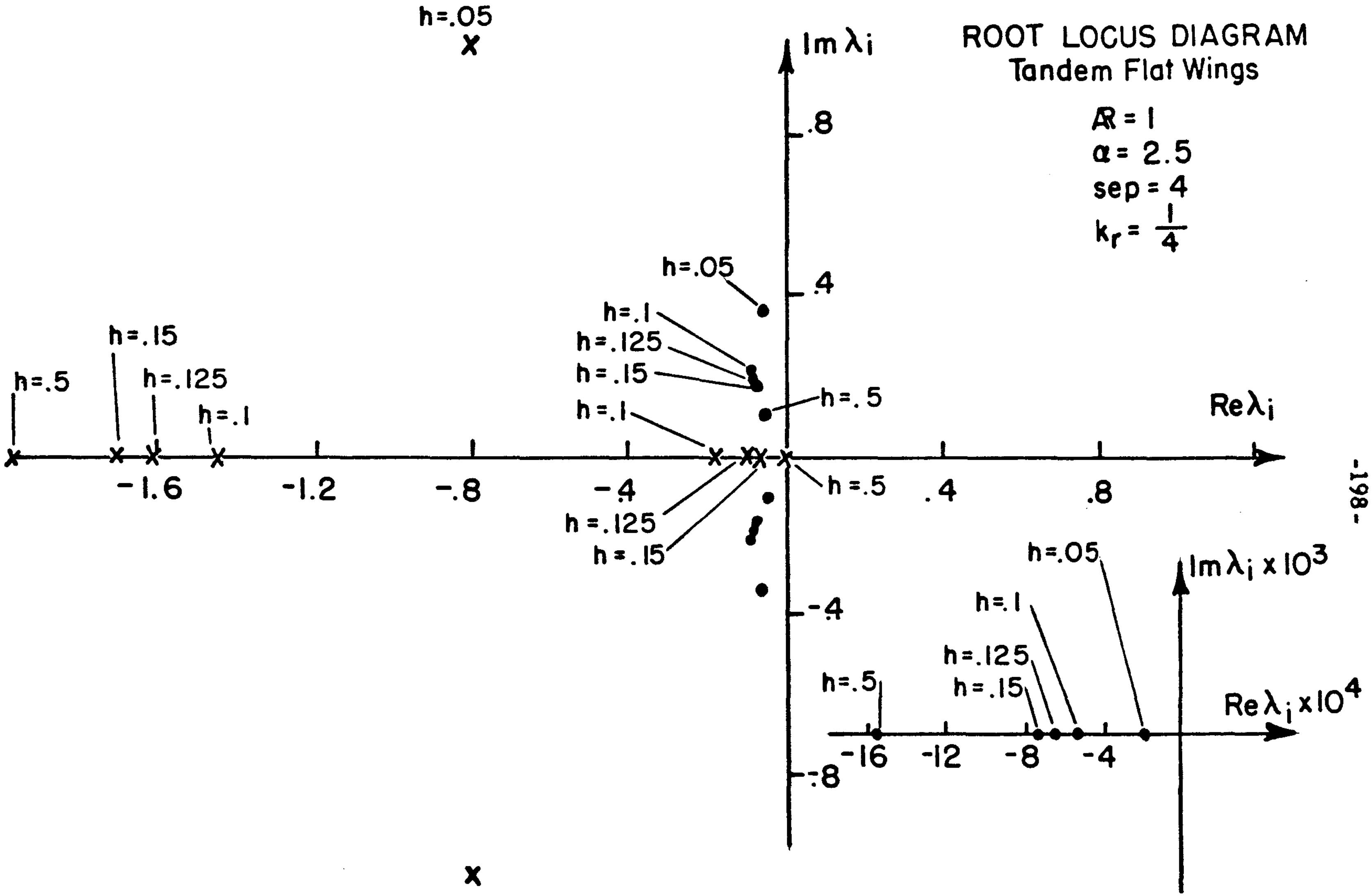

ROOT LOCUS DIAGRAM
Tandem Flat Wings

$AR = 1$
$\alpha = 2.5$
sep = 4
$k_r = \frac{1}{4}$

Fig. 56 b

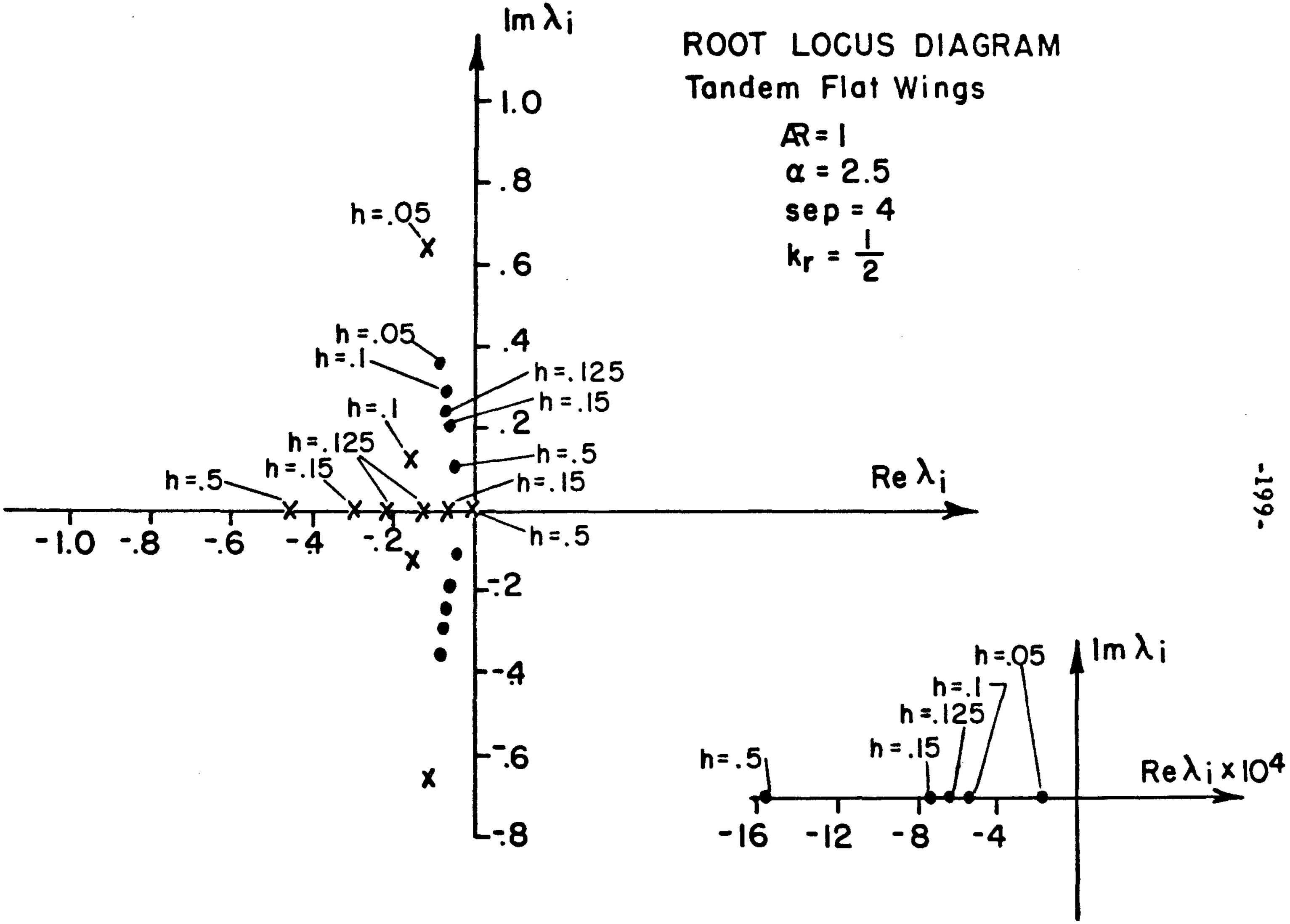
ROOT LOCUS DIAGRAM
Tandem Flat Wings
Æ = 1
α = 2.5
sep = 4
$k_r = \frac{1}{2}$
$\mathrm{Im}\,\lambda_i$
$\mathrm{Re}\,\lambda_i$
1.0
.8
.6
.4
.2
-.2
-.4
-.6
-.8
-1.0
-.8
-.6
-.4
-.2
h=.05
h=.05
h=.1
h=.125
h=.15
h=.1
h=.5
h=.125
h=.15
h=.15
h=.5
h=.5
$\mathrm{Im}\,\lambda_i$
$\mathrm{Re}\,\lambda_i \times 10^4$
h=.05
h=.1
h=.125
h=.15
h=.5
-16
-12
-8
-4

Fig. 56 c

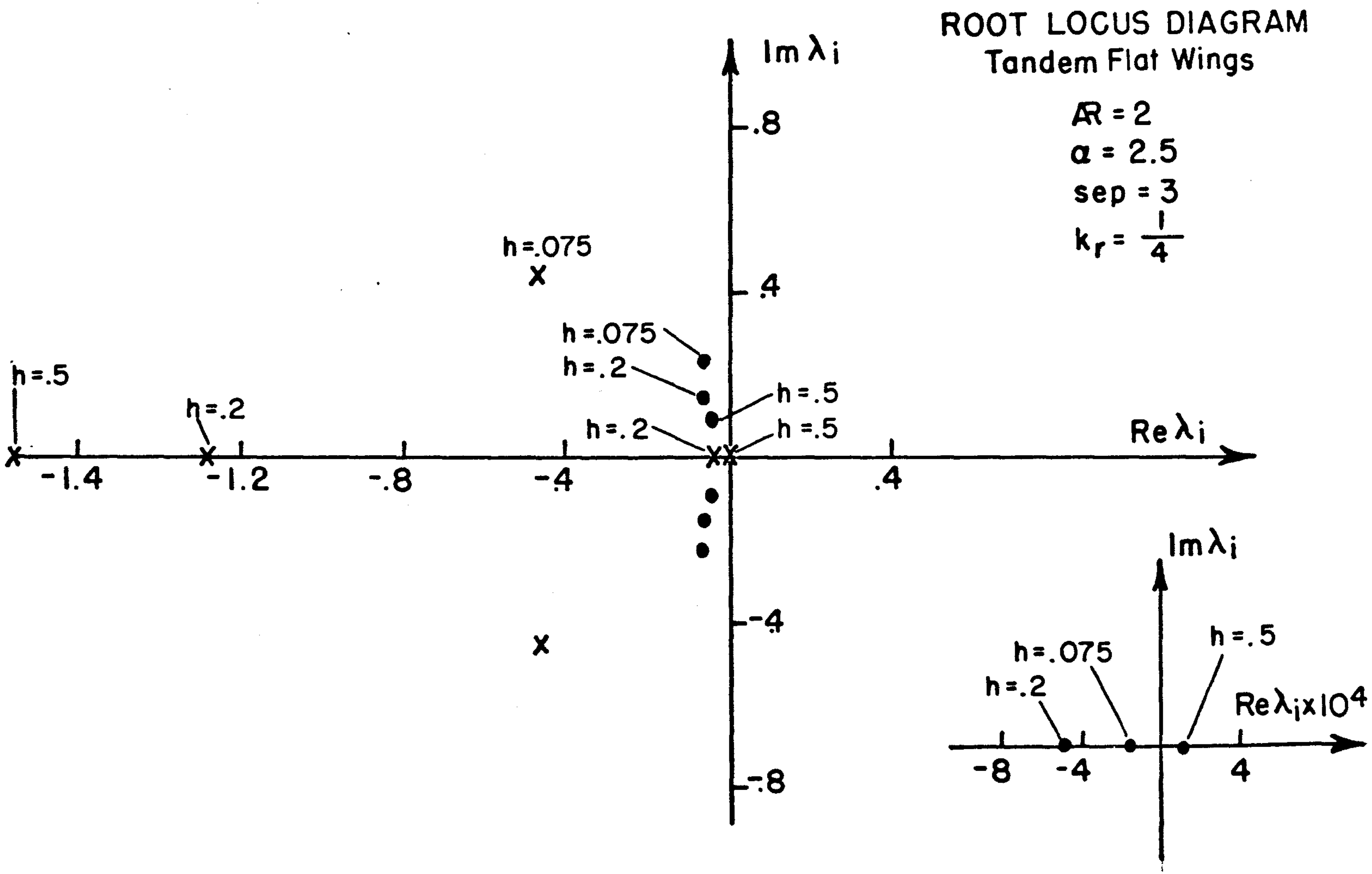
ROOT LOCUS DIAGRAM
Tandem Flat Wings
Æ = 2
α = 2.5
sep = 3
$k_r = \frac{1}{4}$
$\mathrm{Im}\,\lambda_i$
.8
.4
-4
-8
$\mathrm{Re}\,\lambda_i$
-1.4
-1.2
-.8
-.4
.4
h=.5
h=.2
h=.075
h=.075
h=.2
h=.5
h=.2
h=.5
$\mathrm{Im}\,\lambda_i$
$\mathrm{Re}\,\lambda_i \times 10^4$
h=.2
h=.075
h=.5
-8
-4
4

Fig. 57 a

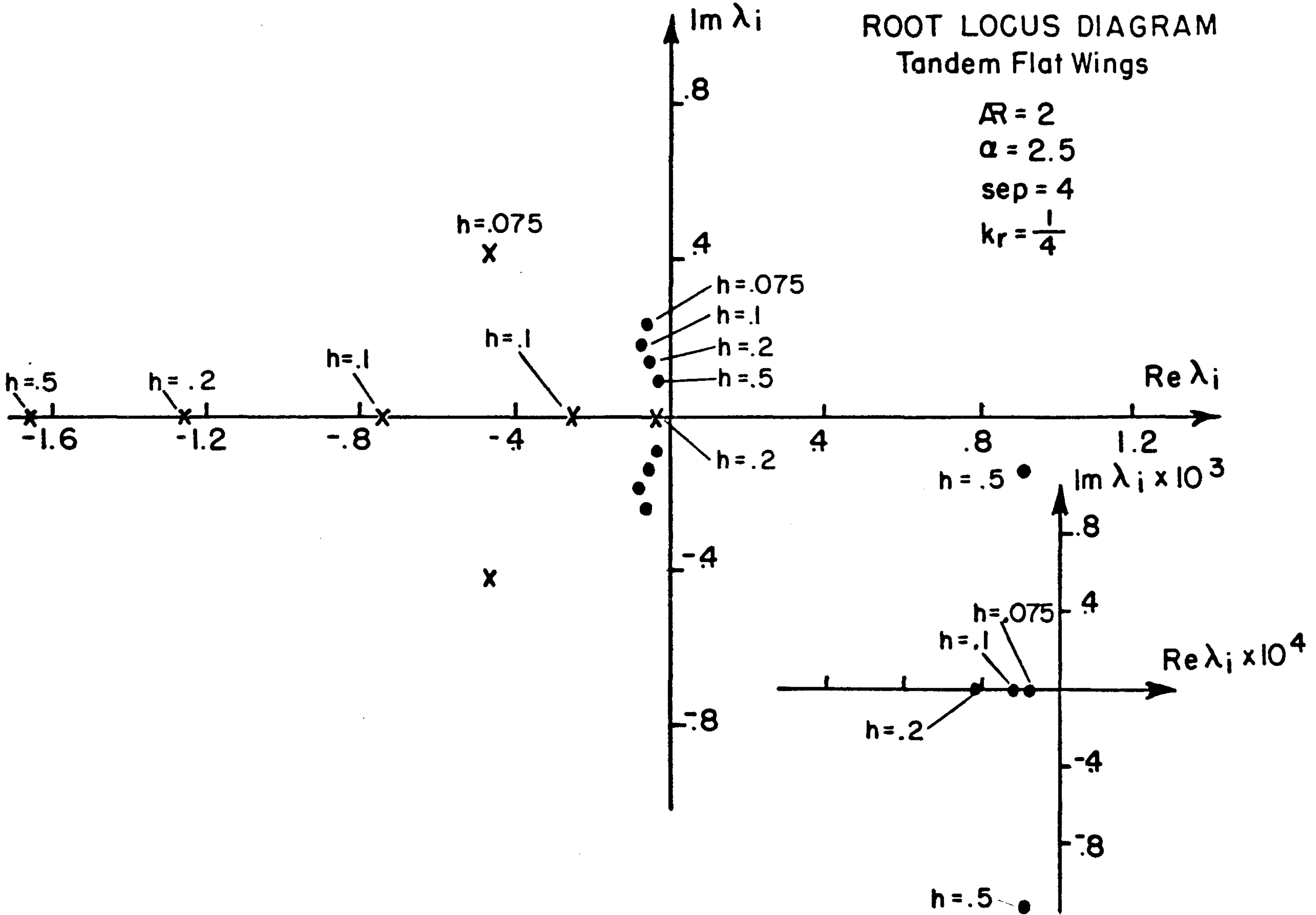
ROOT LOCUS DIAGRAM
Tandem Flat Wings
Æ = 2
α = 2.5
sep = 4
$k_r = \frac{1}{4}$
Im λ_i
Re λ_i
.8
.4
-.4
-.8
-1.6
-1.2
-.8
-.4
.4
.8
1.2
h=.5
h=.2
h=.1
h=.1
h=.075
h=.075
h=.1
h=.2
h=.5
h=.2
h=.5
Im λ_i x 10^3
Re λ_i x 10^4
.8
.4
-.4
-.8
h=.075
h=.1
h=.2
h=.5

Fig. 57 b

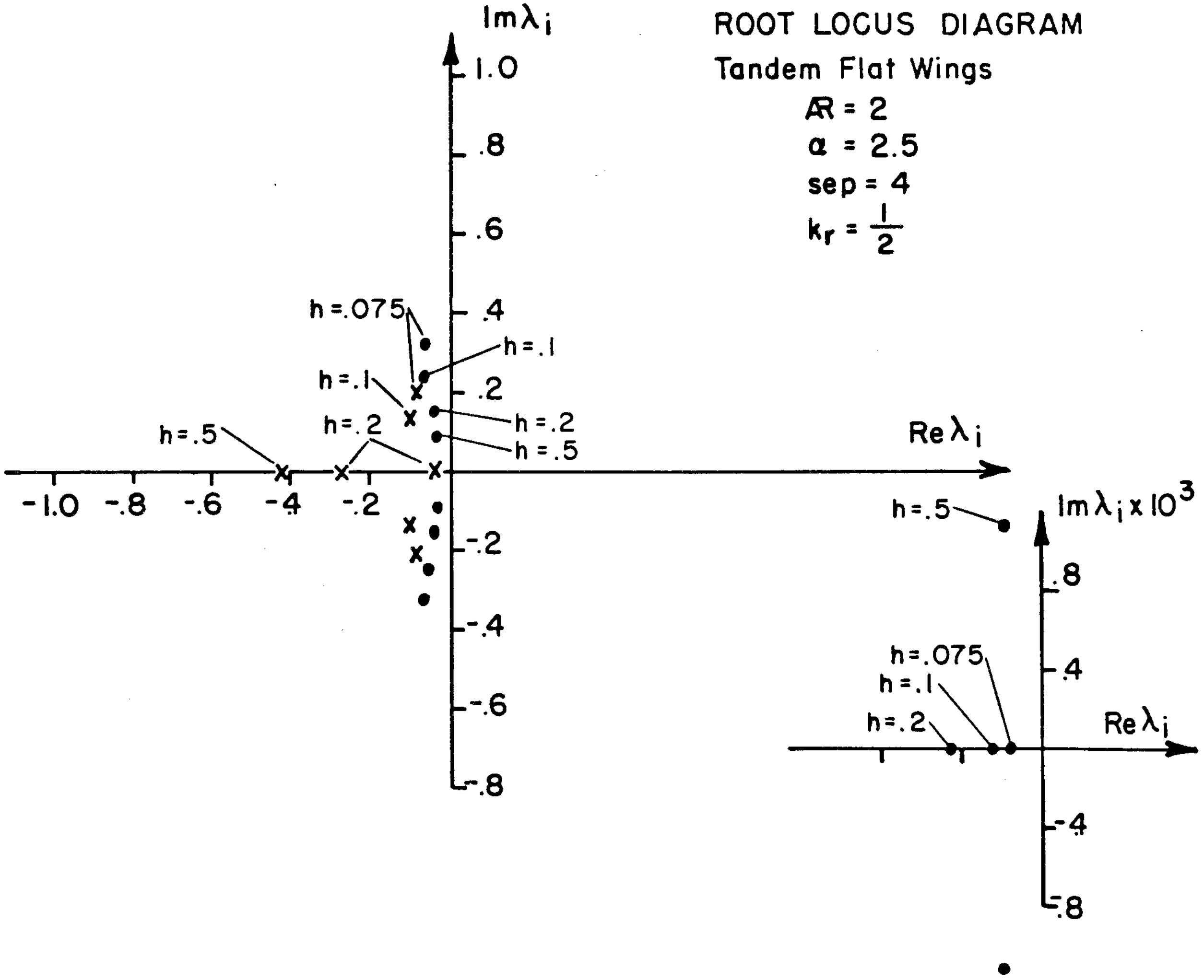
ROOT LOCUS DIAGRAM
Tandem Flat Wings
Æ = 2
α = 2.5
sep = 4
$k_r = \frac{1}{2}$
$\mathrm{Im}\lambda_i$
1.0
.8
.6
.4
.2
-.2
-.4
-.6
-.8
$\mathrm{Re}\lambda_i$
-1.0
-.8
-.6
-.4
-.2
h=.075
h=.1
h=.1
h=.2
h=.2
h=.5
h=.5
h=.5
$\mathrm{Im}\lambda_i \times 10^3$
.8
.4
-.4
-.8
$\mathrm{Re}\lambda_i$
h=.075
h=.1
h=.2

Fig. 57 c

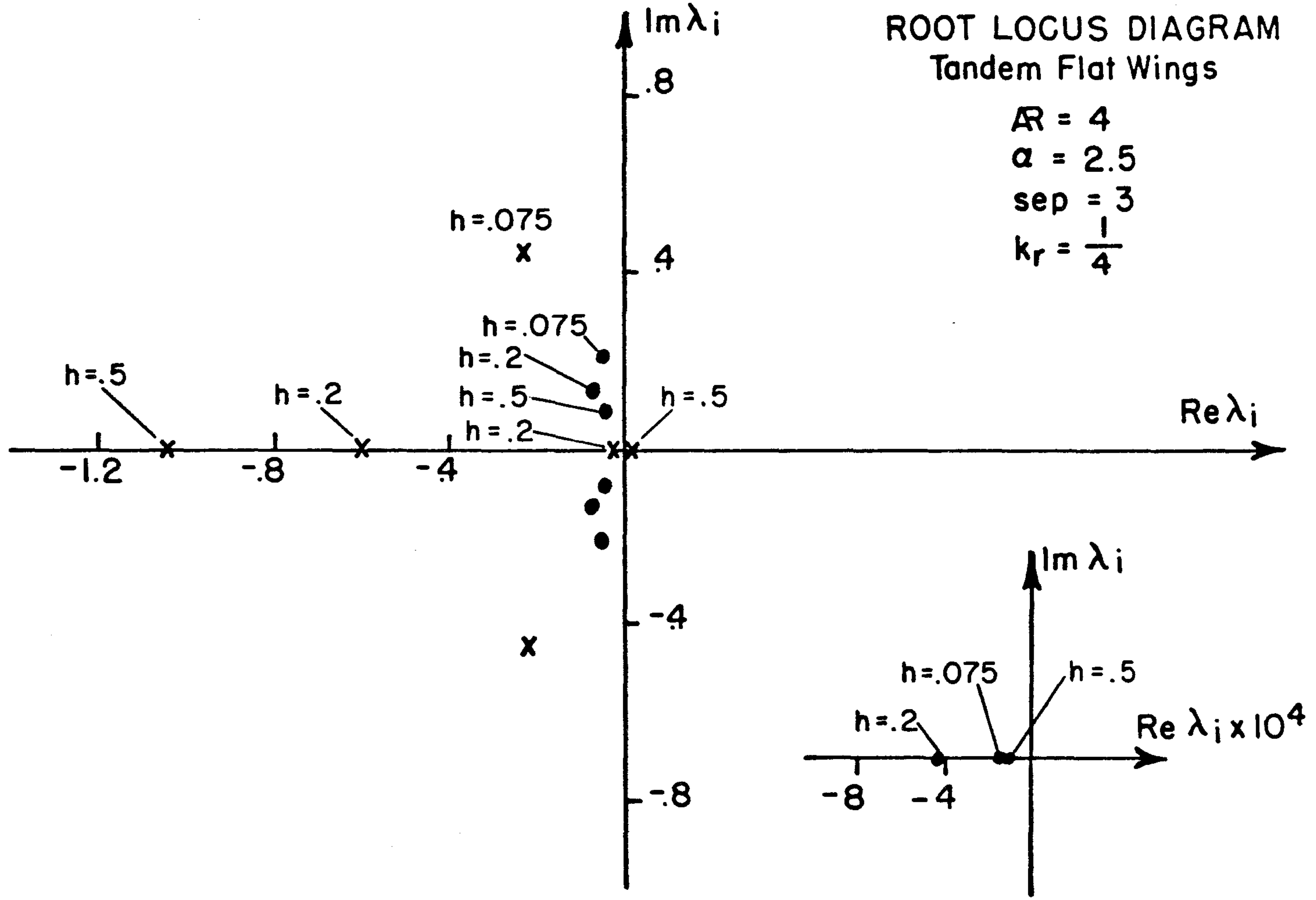
ROOT LOCUS DIAGRAM
Tandem Flat Wings
Æ = 4
α = 2.5
sep = 3
$k_r = \frac{1}{4}$
$\text{Im}\lambda_i$
.8
.4
-.4
-.8
$\text{Re}\lambda_i$
-1.2
-.8
-.4
h=.075
h=.075
h=.2
h=.5
h=.2
h=.5
h=.5
h=.2
$\text{Im}\,\lambda_i$
$\text{Re}\,\lambda_i \times 10^4$
h=.075
h=.5
h=.2
-8
-4

Fig. 58 a

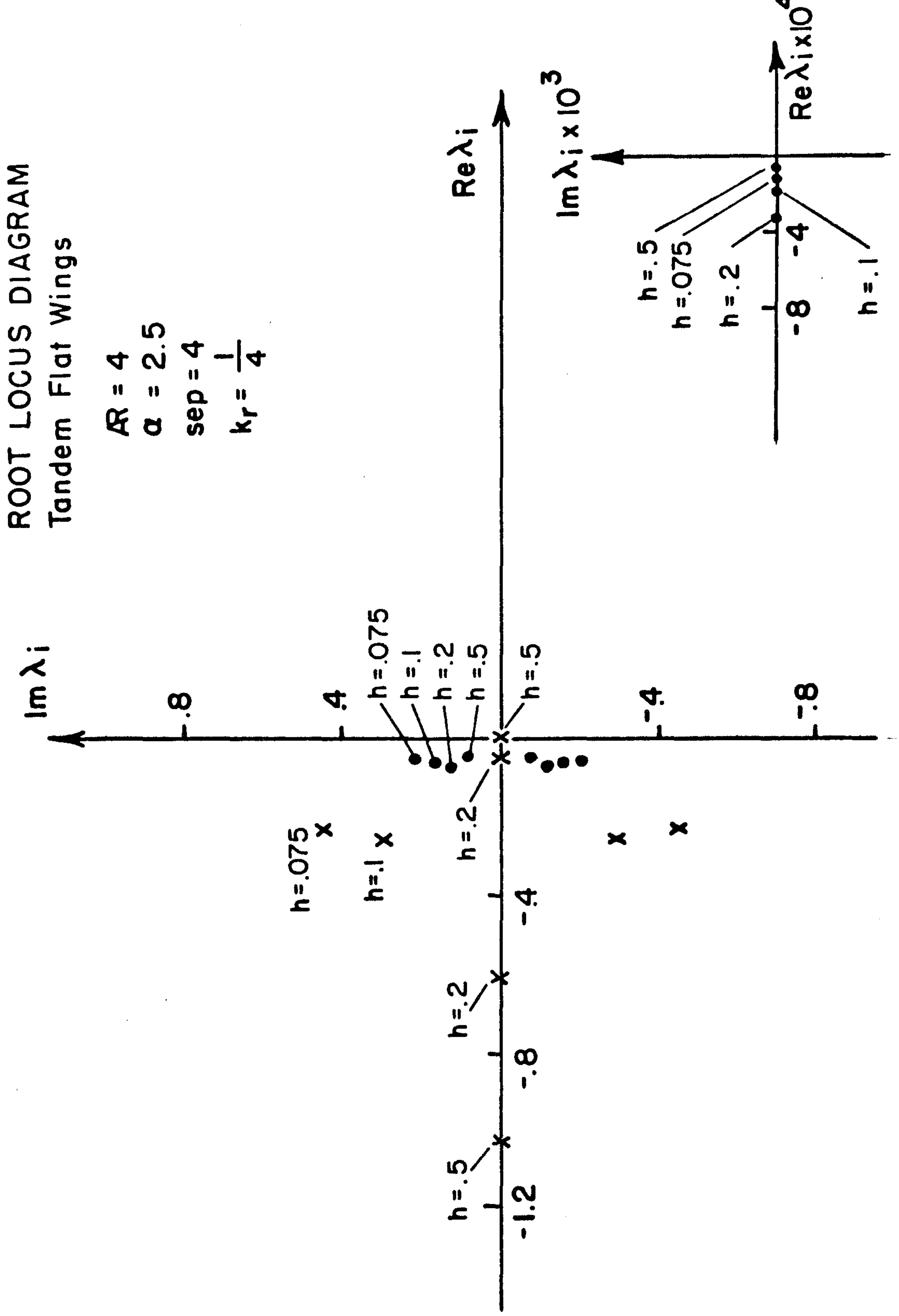
ROOT LOCUS DIAGRAM
Tandem Flat Wings
Æ = 4
α = 2.5
sep = 4
$k_r = \frac{1}{4}$
$\mathrm{Im}\,\lambda_i$
$\mathrm{Re}\,\lambda_i$
.8
.4
-.4
-.8
-.4
-.8
-1.2
h=.075
h=.1
h=.2
h=.5
h=.5
h=.2
h=.075
h=.1
h=.2
h=.5
$\mathrm{Im}\,\lambda_i \times 10^3$
$\mathrm{Re}\,\lambda_i \times 10^4$
-4
-8
h=.5
h=.075
h=.2
h=.1

Fig. 58 b

Fig.

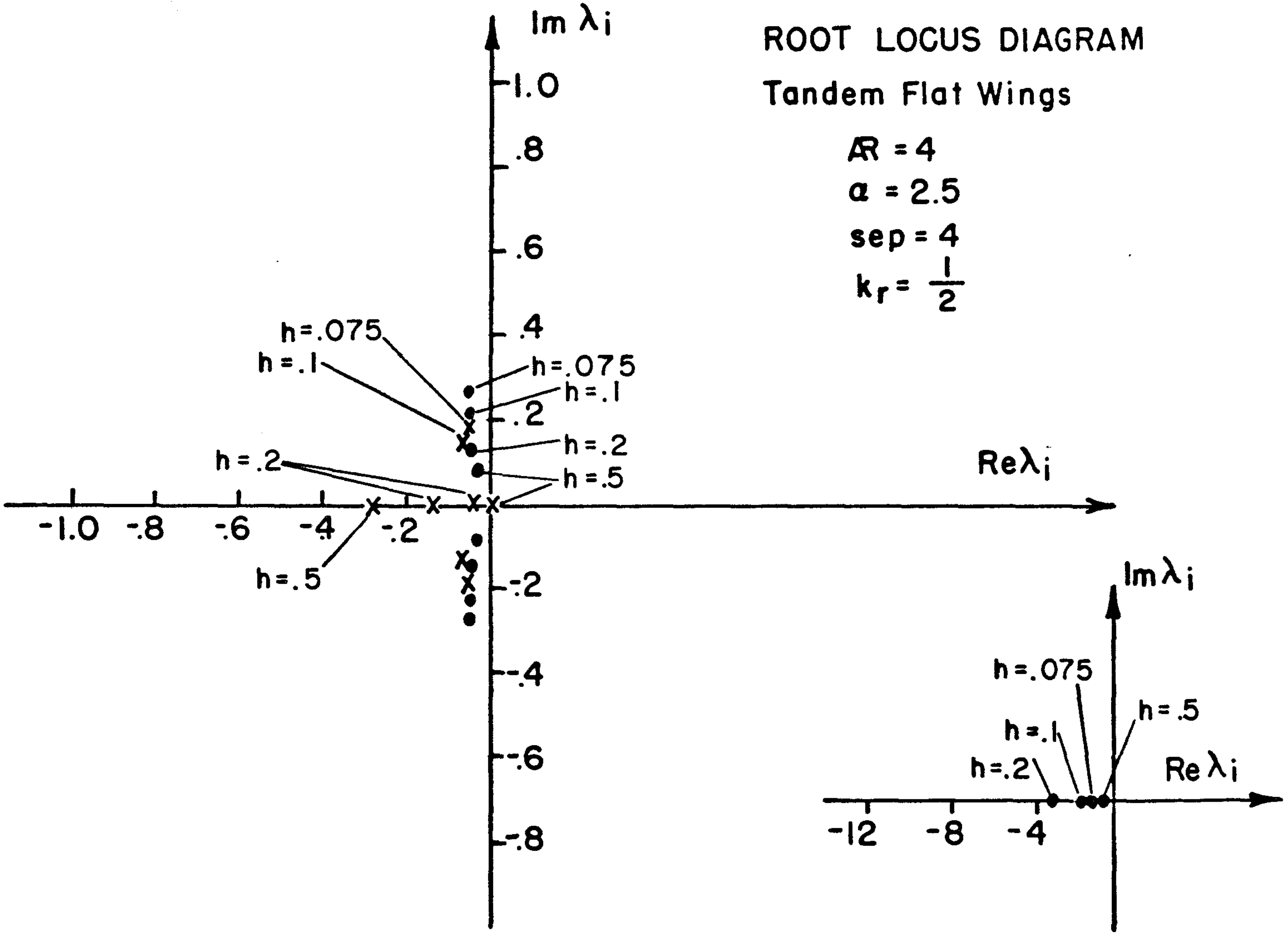
ROOT LOCUS DIAGRAM
Tandem Flat Wings
Æ = 4
a = 2.5
sep = 4
$k_r = \frac{1}{2}$
Im λ_i
Reλ_i
1.0
.8
.6
.4
.2
-.2
-.4
-.6
-.8
-1.0
-.8
-.6
-.4
-.2
h=.075
h=.1
h=.2
h=.5
h=.075
h=.1
h=.2
h=.5
Imλ_i
Re λ_i
h=.075
h=.1
h=.2
h=.5
-12
-8
-4

Fig. 58 c

ROOT LOCUS DIAGRAM LONGITUDINAL STABILITY
NON-PLANAR WINGS IN NON-PLANAR GROUND EFFECT

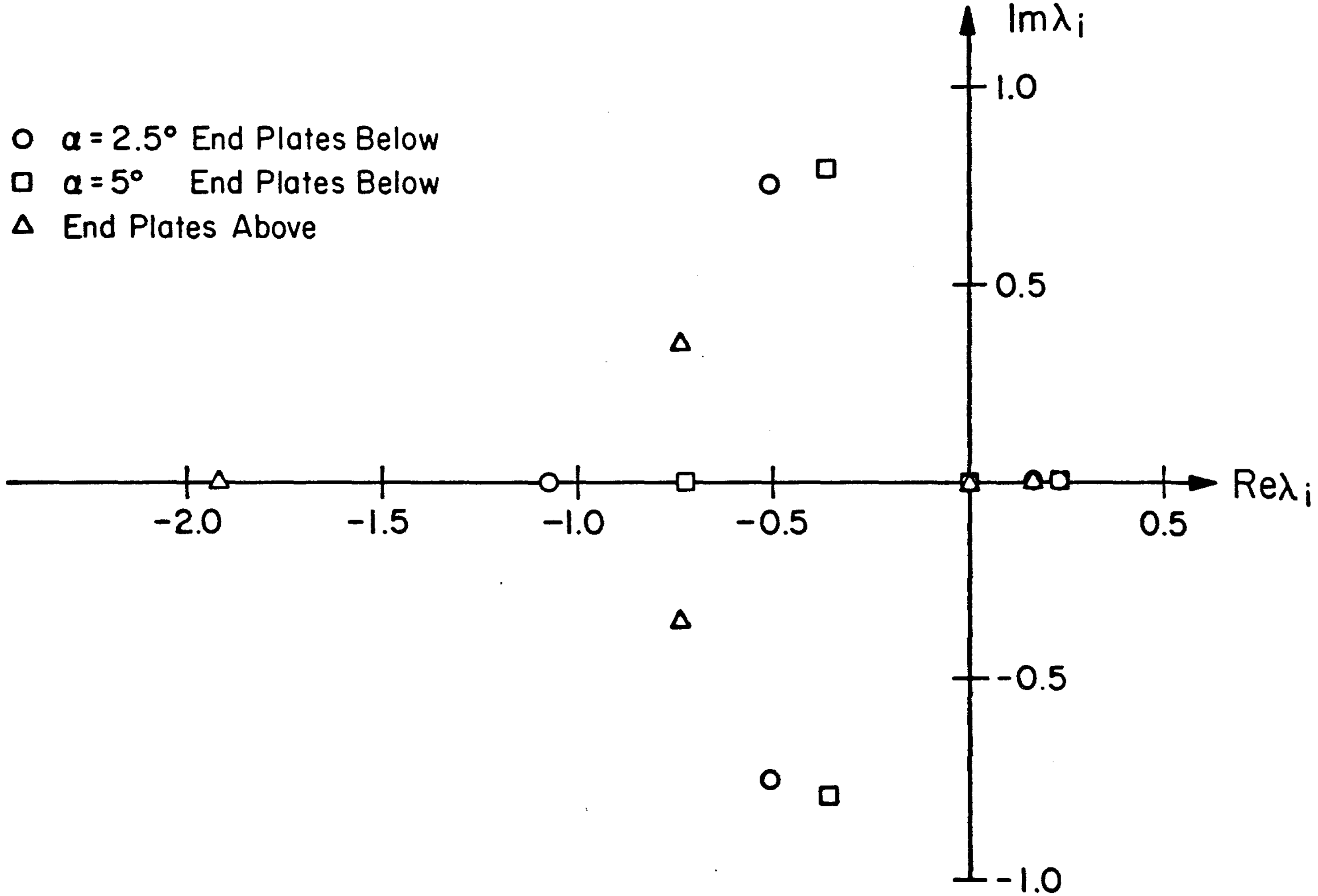

Fig. 59

ROOT LOCUS DIAGRAM LATERAL STABILITY
NON-PLANAR WINGS IN NON-PLANAR GROUND EFFECT

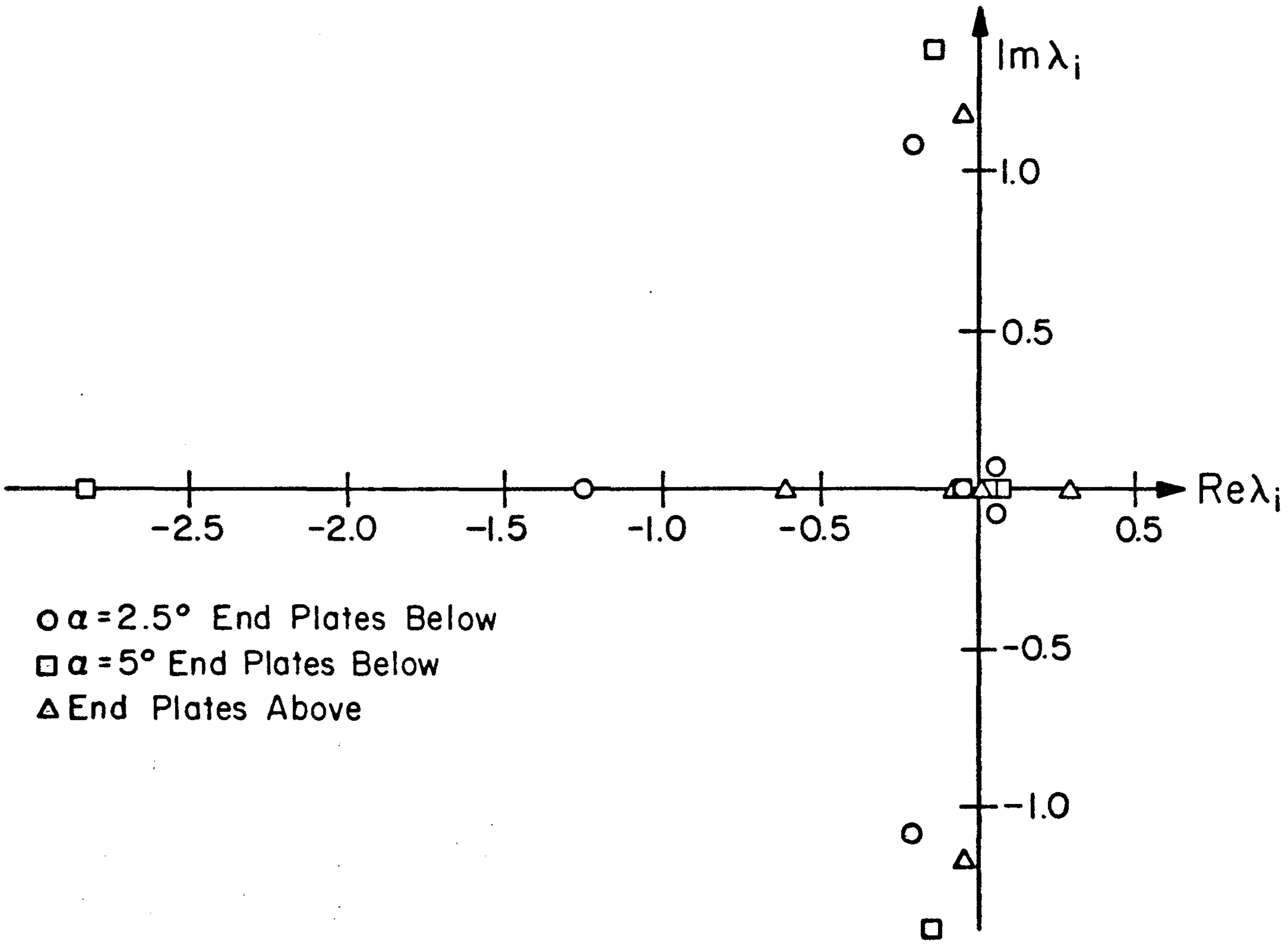

Fig. 60

EXPERIMENTAL WING MODEL

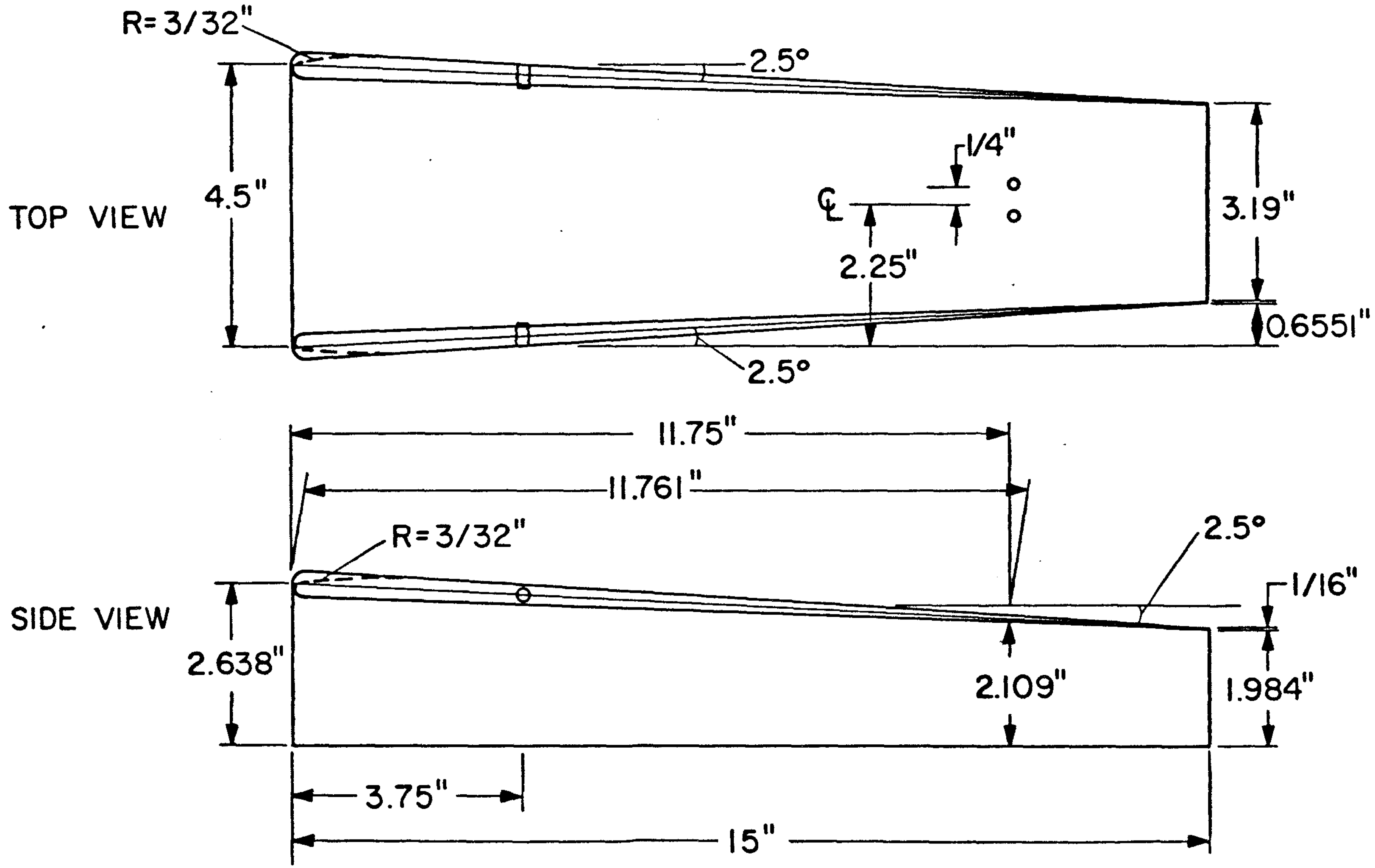

Fig. 61

EXPERIMENTAL WING MODEL

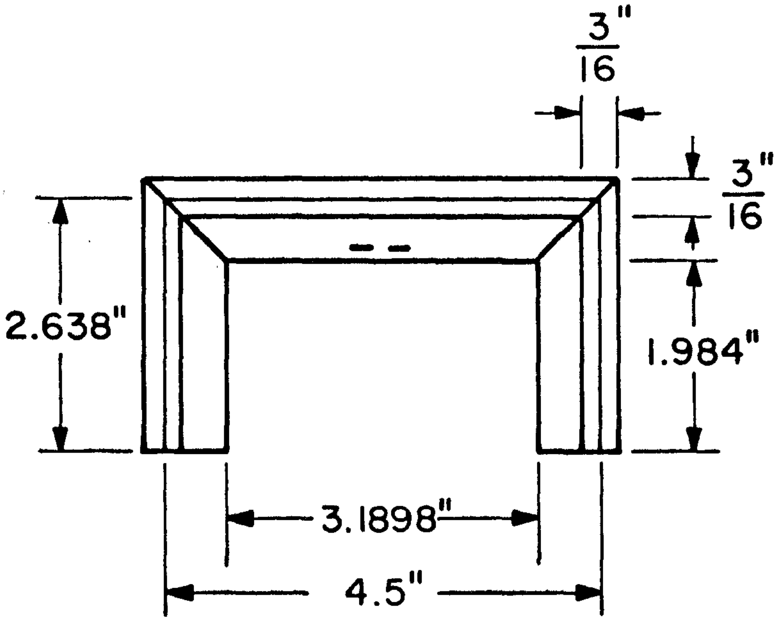

FRONT
VIEW

Fig. 62

SUPPORTS FOR WING MODEL

SIDE SUPPORTS (2)

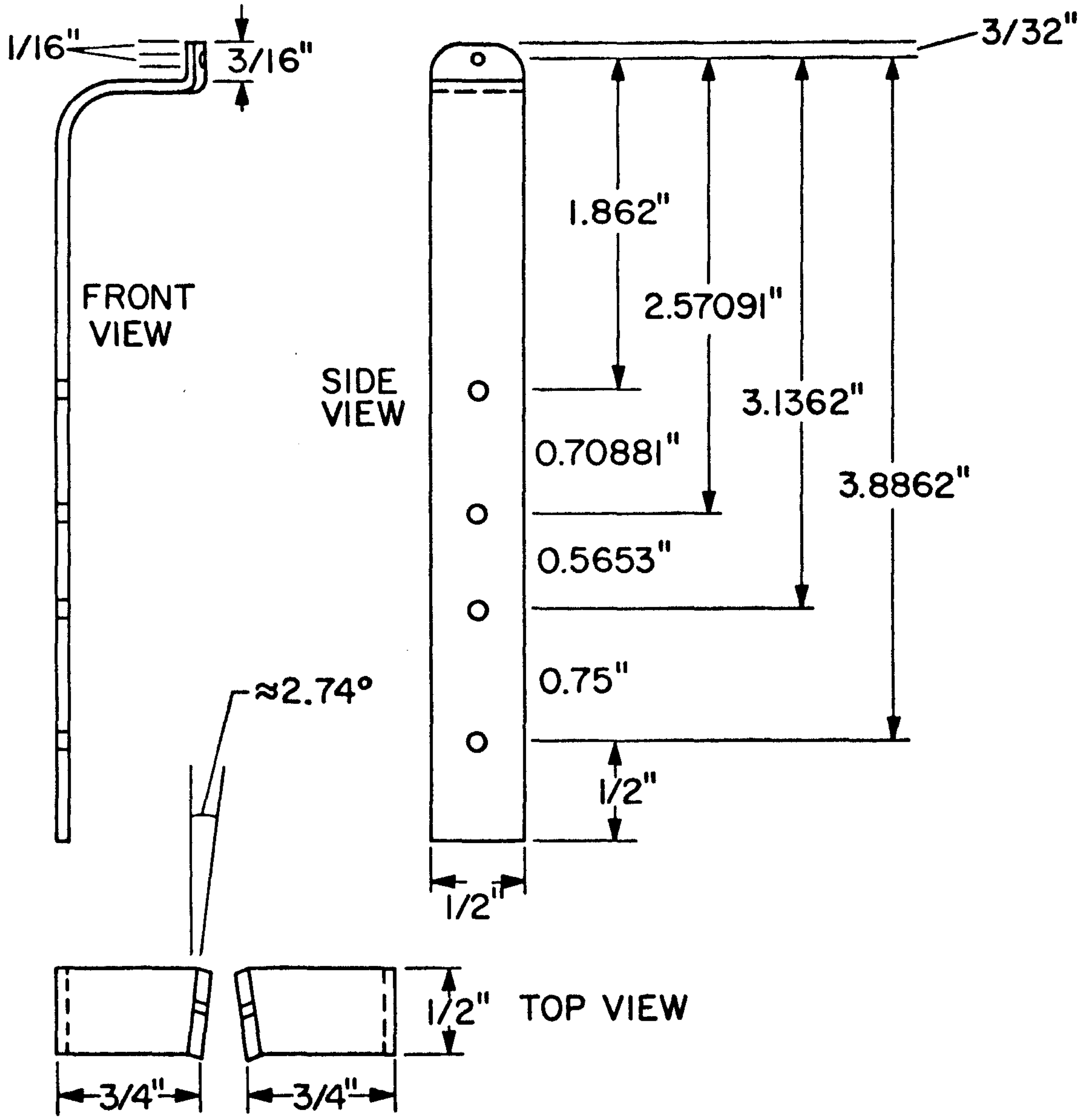

Fig. 63

SUPPORTS FOR WING MODEL
REAR SUPPORT

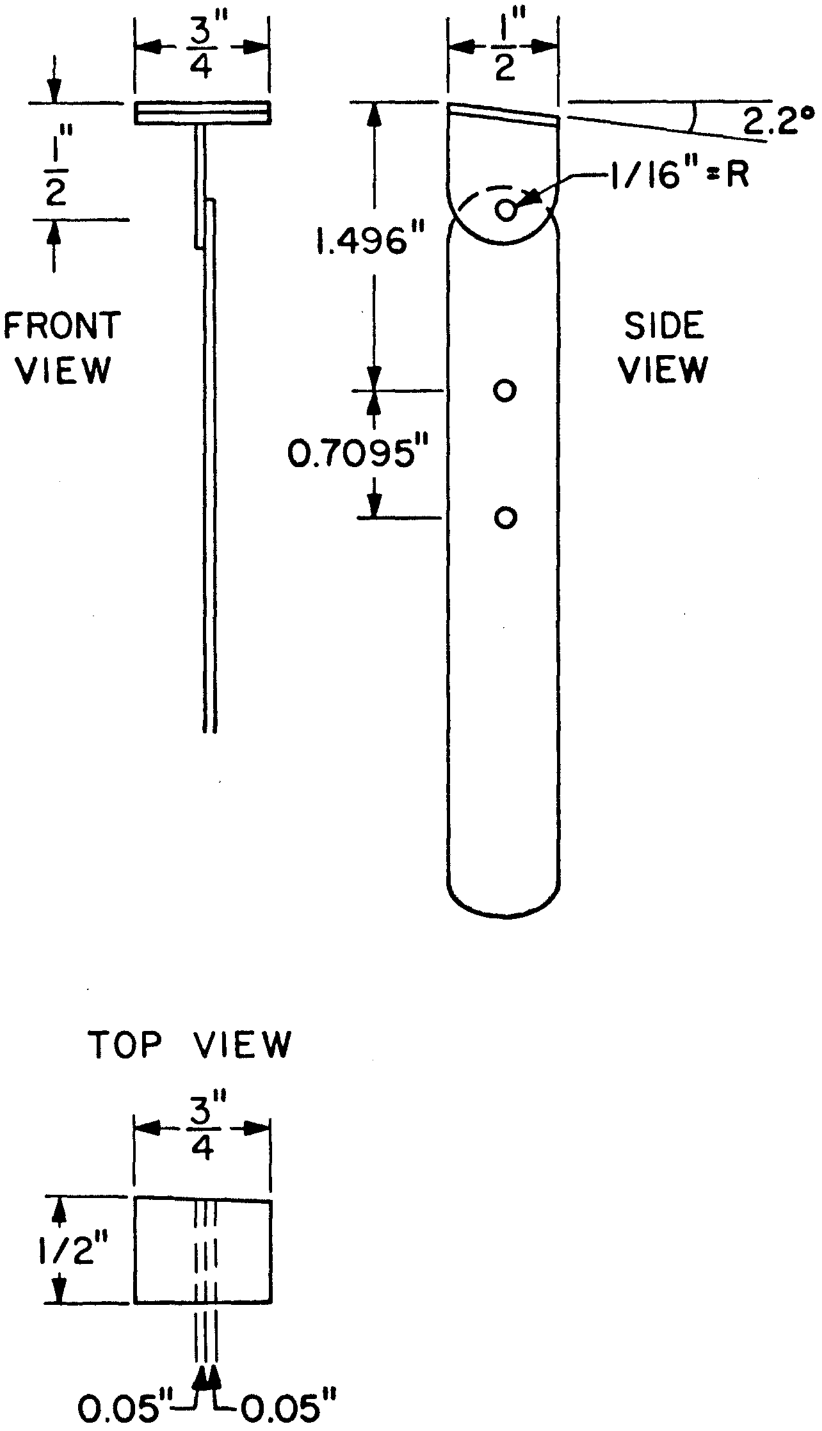

Fig. 64

PHOTOGRAPHS OF EXPERIMENTAL APPARATUS

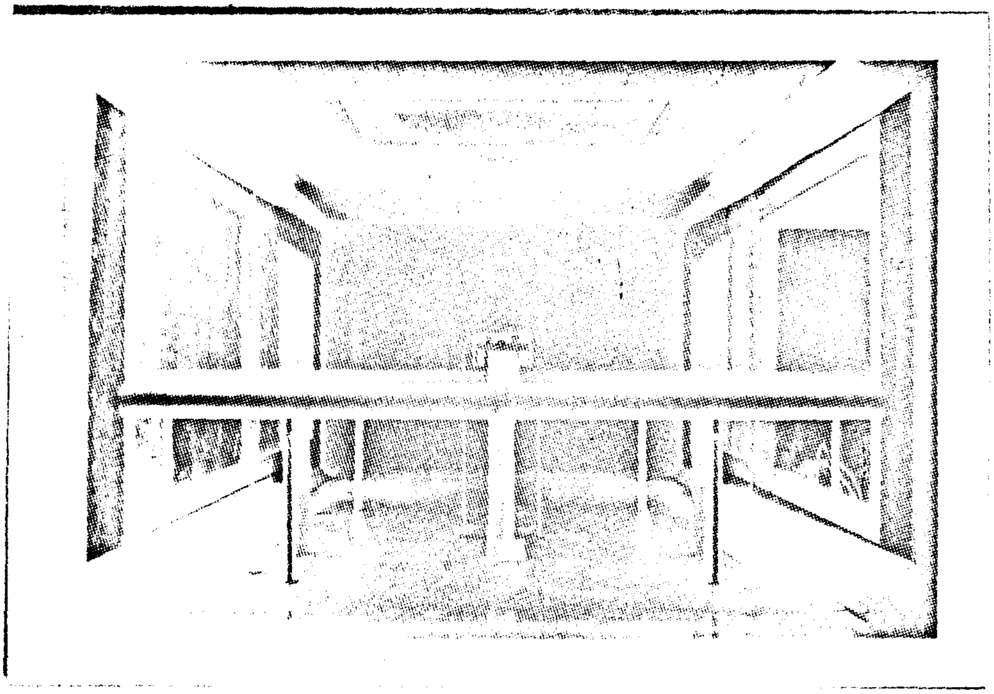

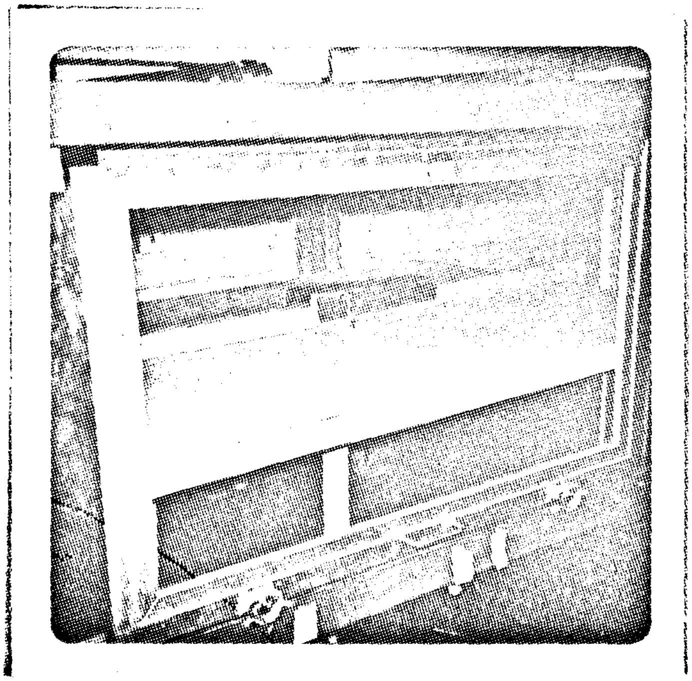

Fig. 65

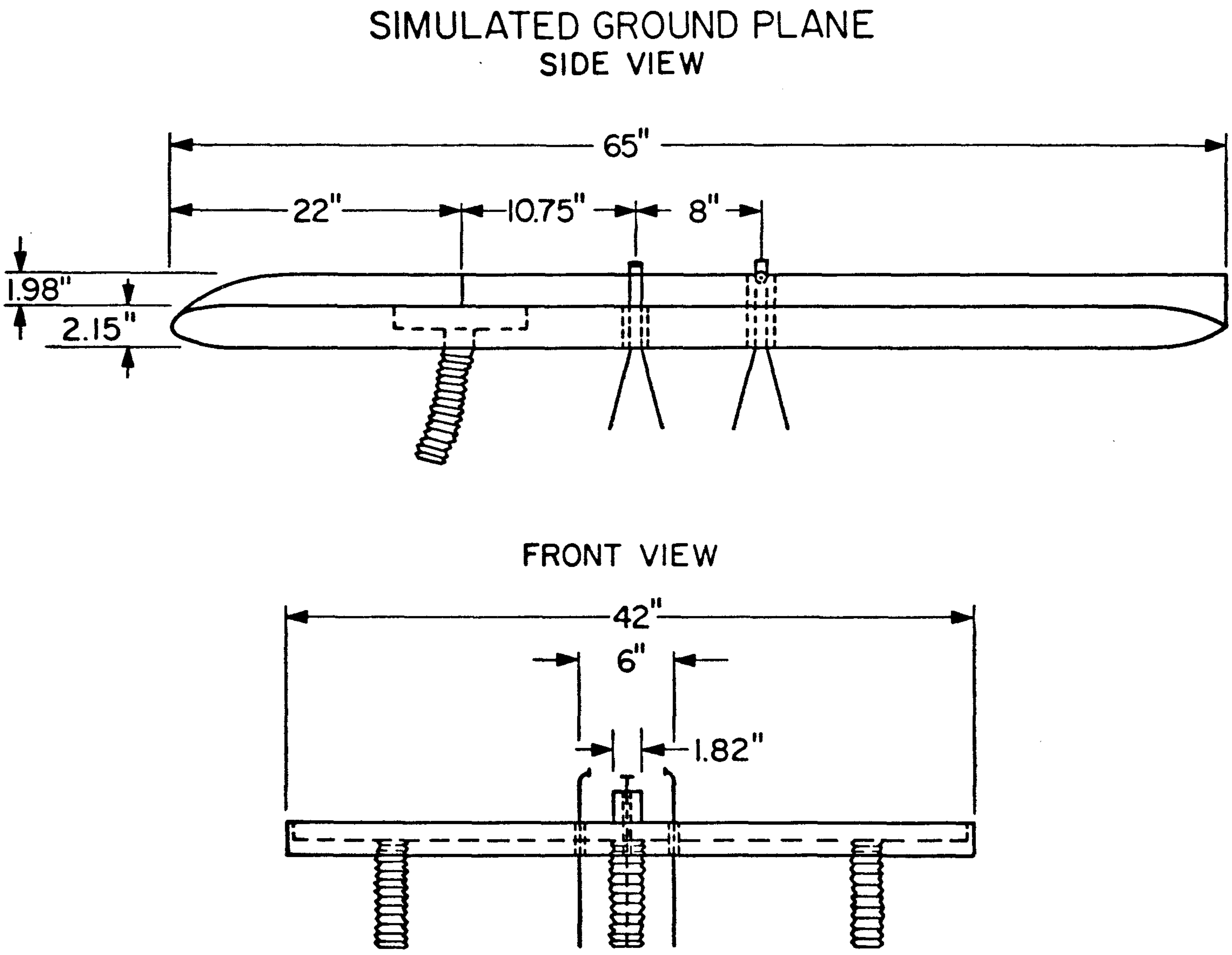

SIMULATED GROUND PLANE
SIDE VIEW

FRONT VIEW

Fig. 66

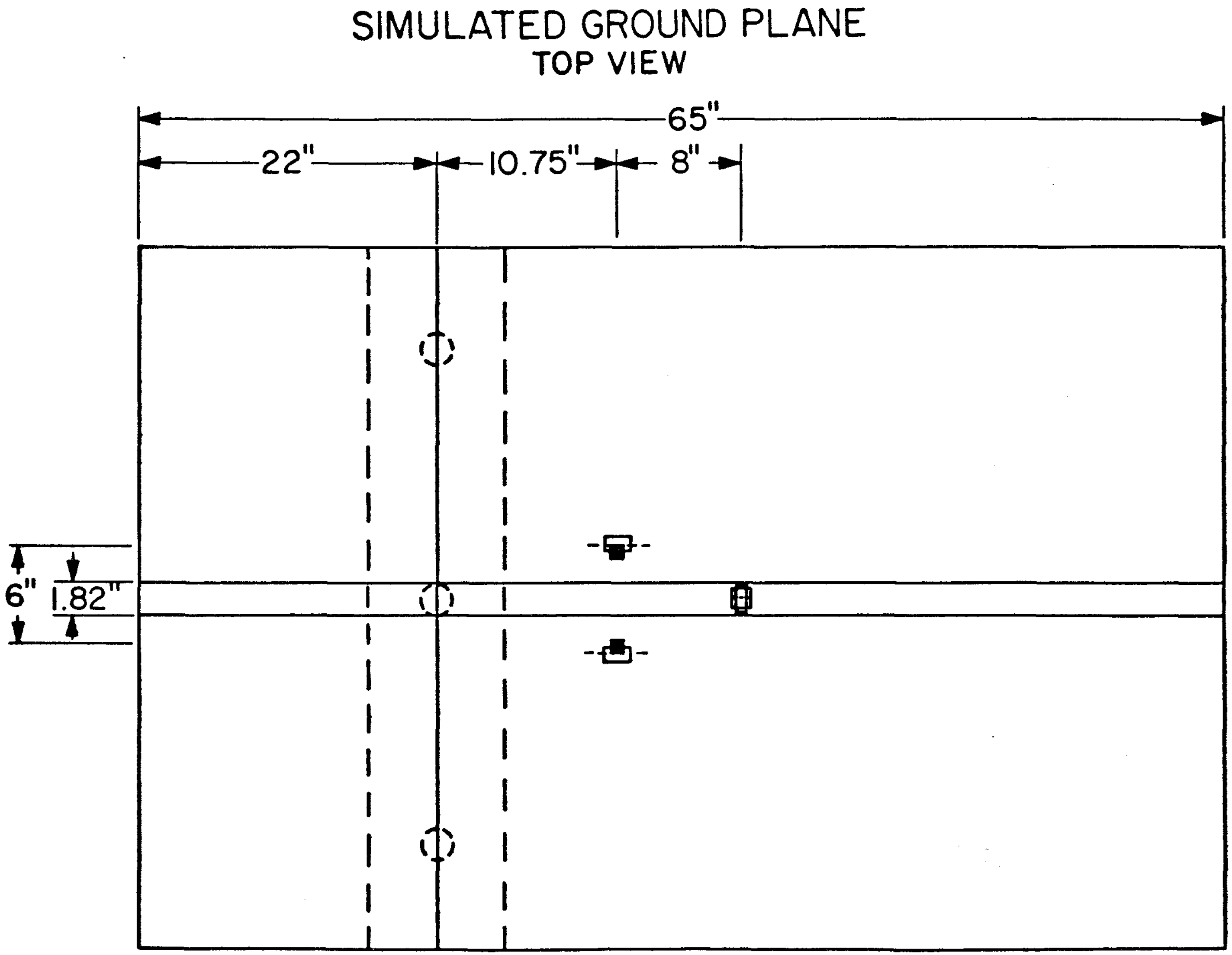

Fig. 67

LIFT COEFFICIENT vs h/c
PLANAR GROUND

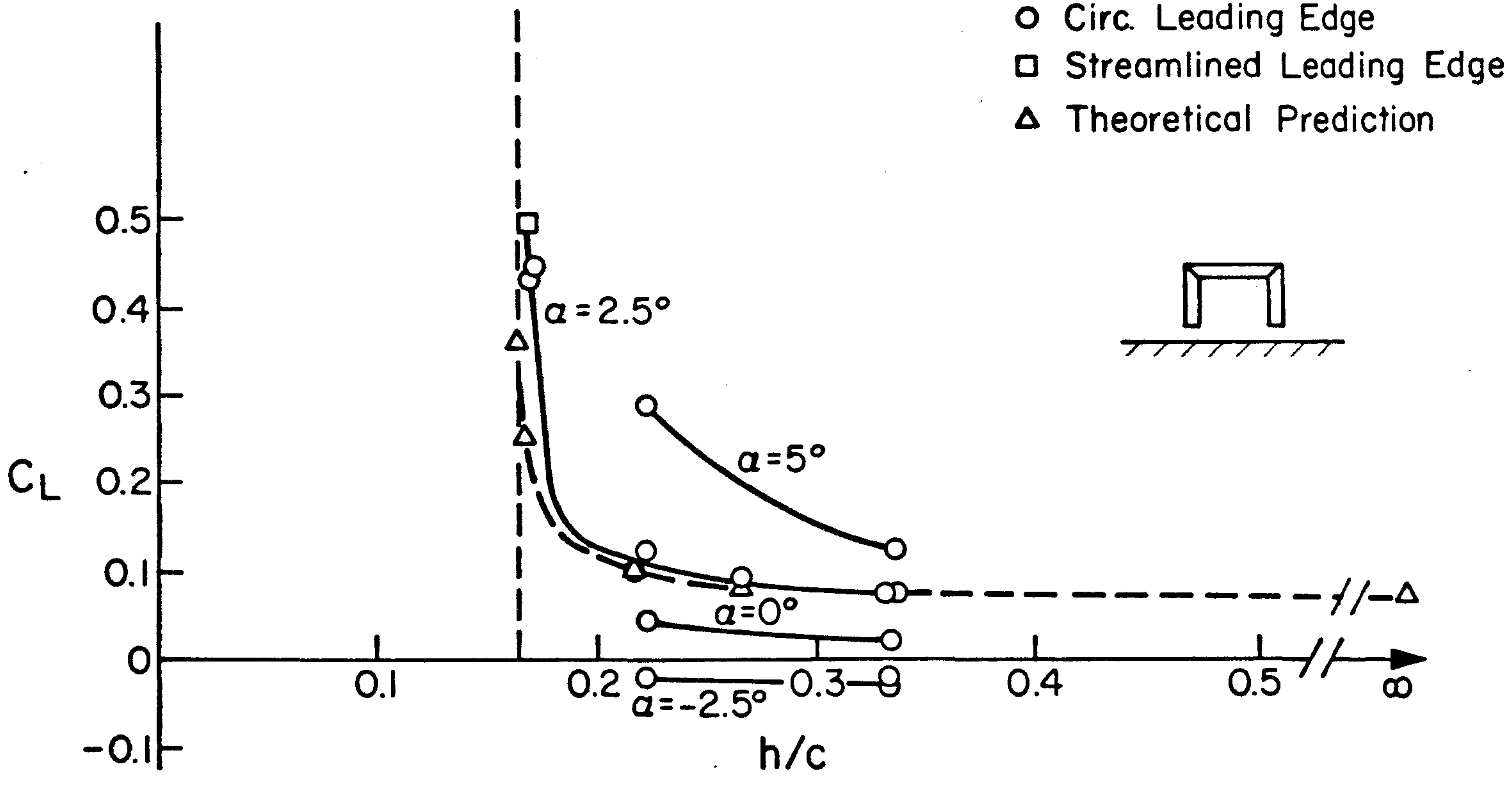

Fig. 68

LIFT COEFFICIENT vs ANGLE OF ATTACK
PLANAR GROUND

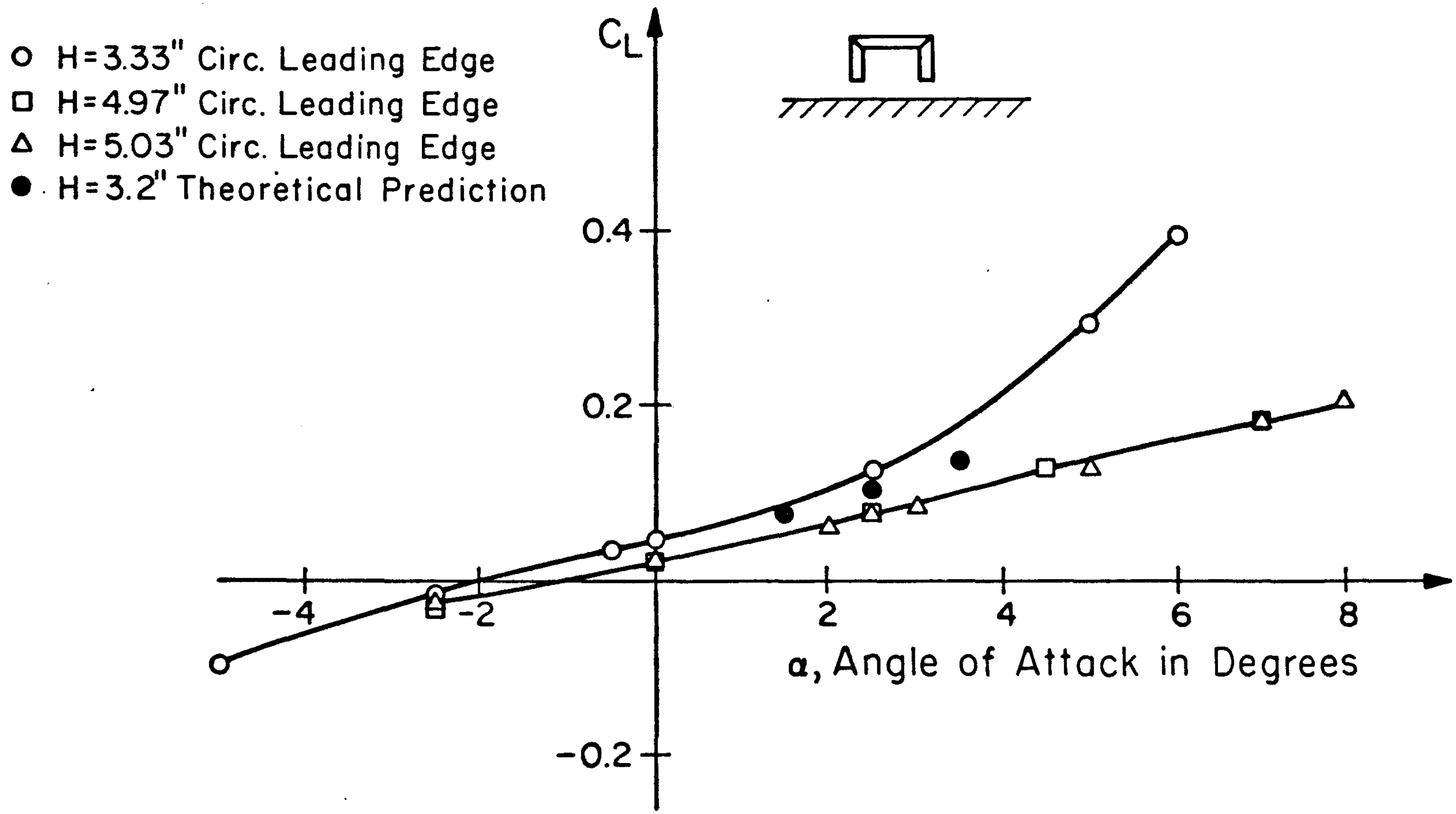

Fig. 69

LIFT COEFFICIENT vs h/c
NON-PLANAR GROUND

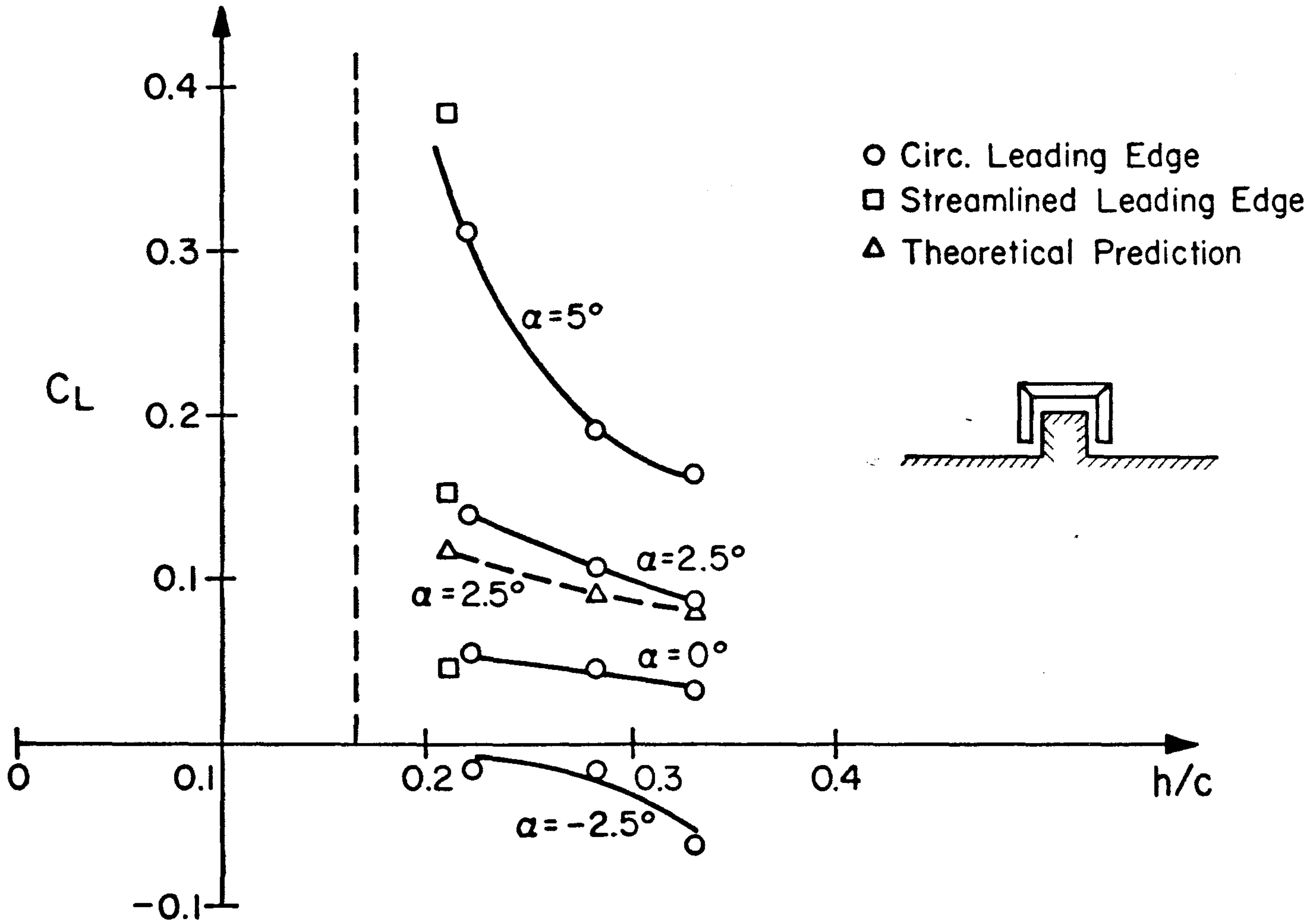

Fig. 70

LIFT COEFFICIENT vs ANGLE OF ATTACK
NON-PLANAR GROUND

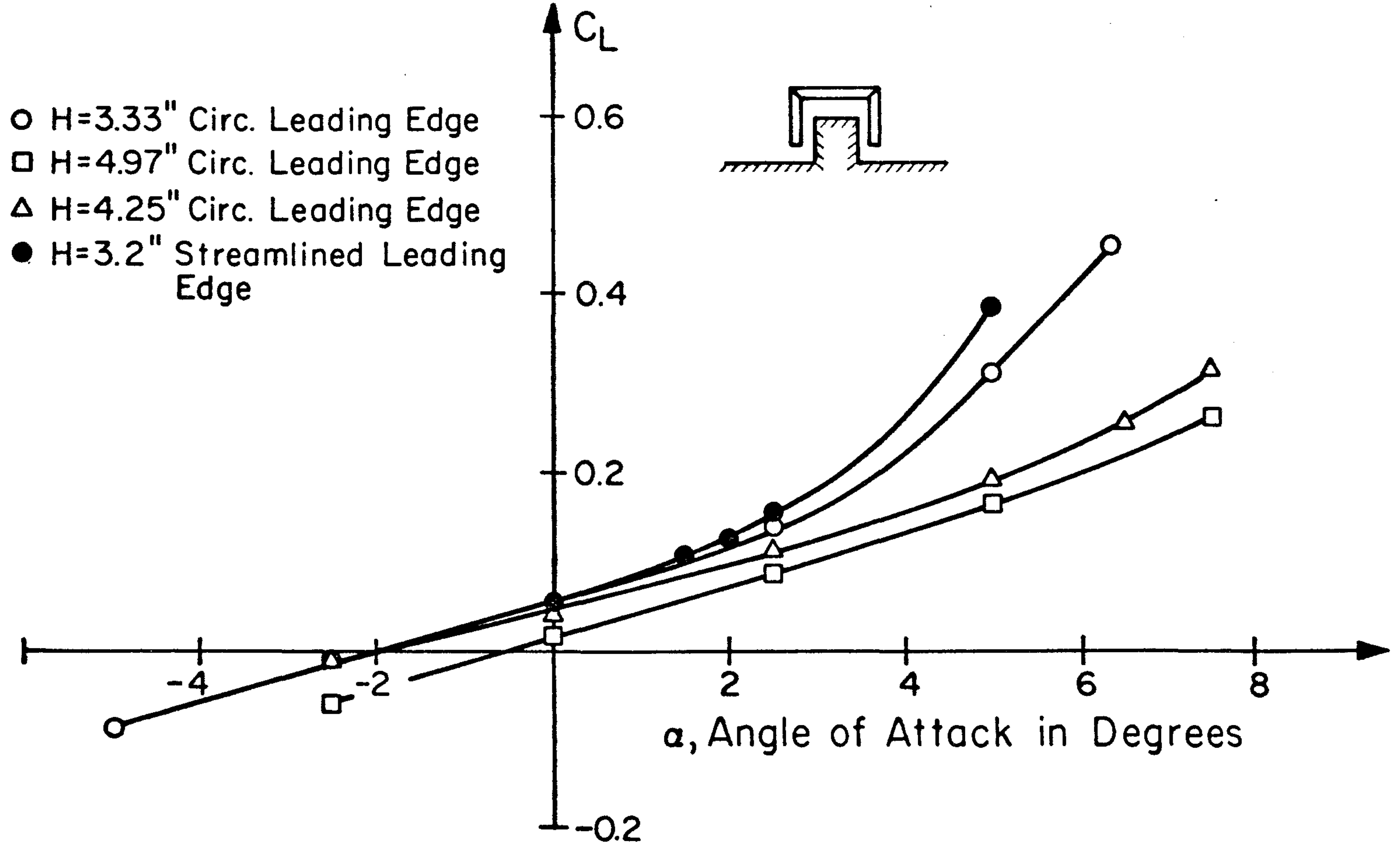

Fig. 71

PRESSURE DISTRIBUTION ALONG CENTERLINE
OF NON-PLANAR GROUND PIECE

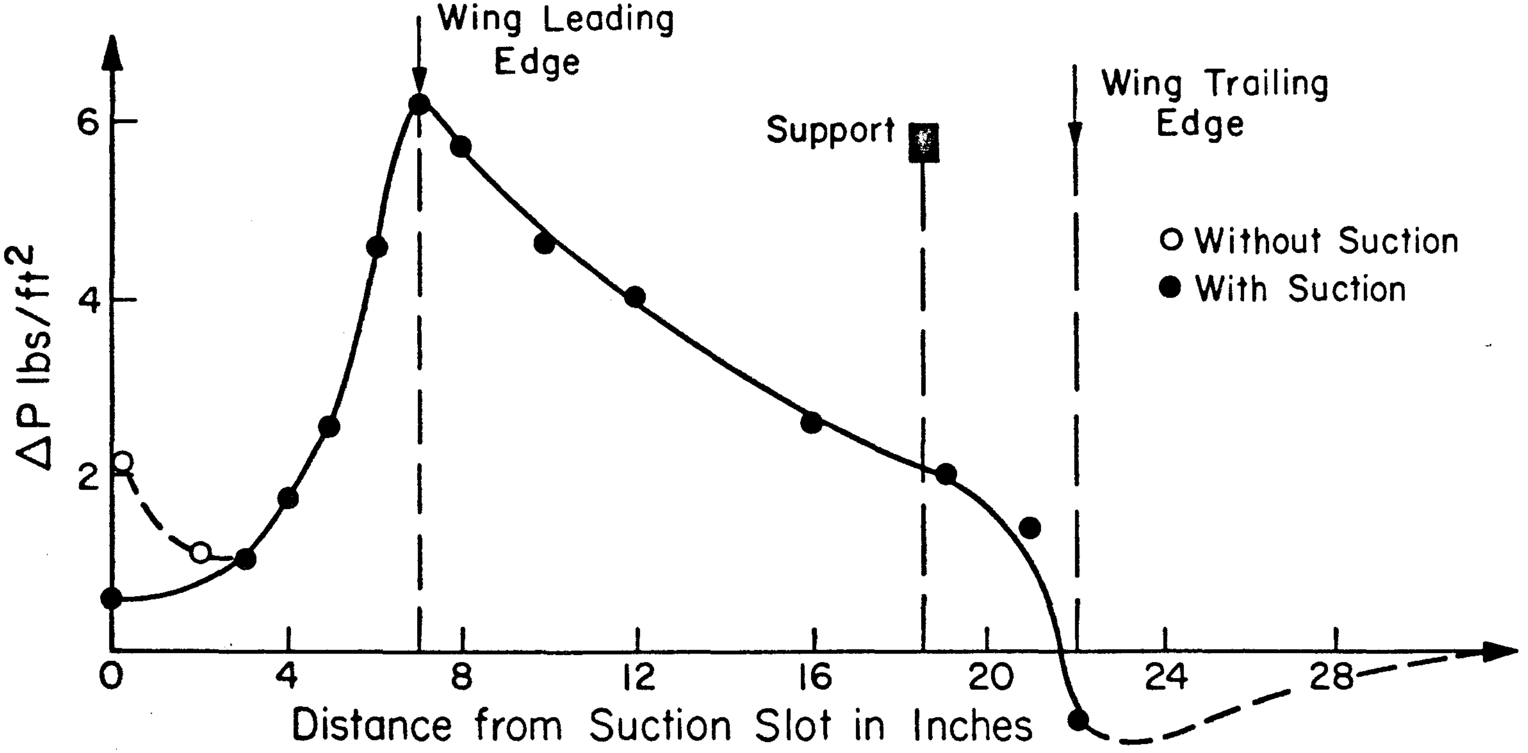

Fig. 72

LOAD DISTRIBUTION ALONG TOP CENTERLINE OF WING
NON-PLANAR GROUND

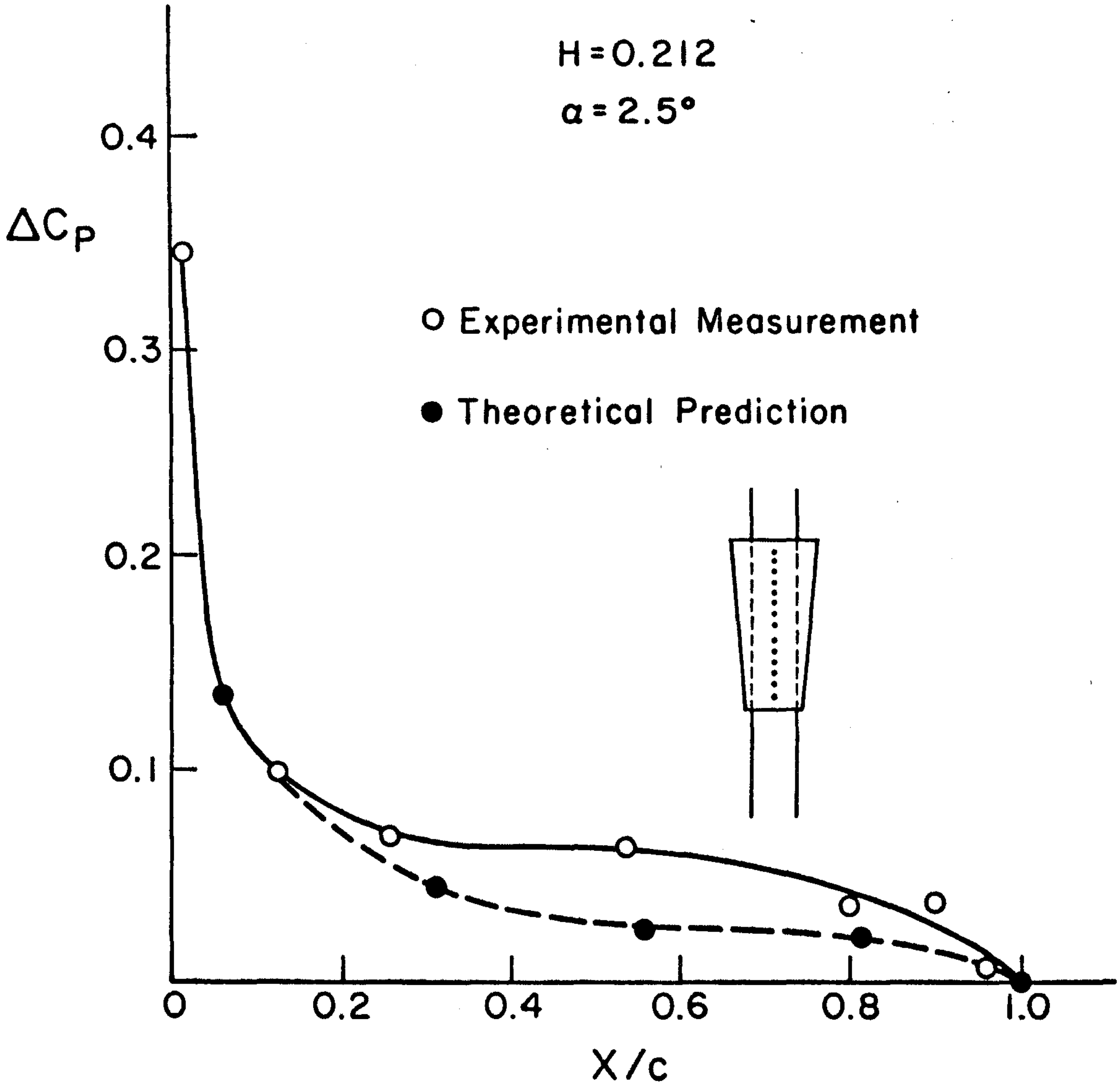

Fig. 73

2-d SOURCE DISTRIBUTION METHOD

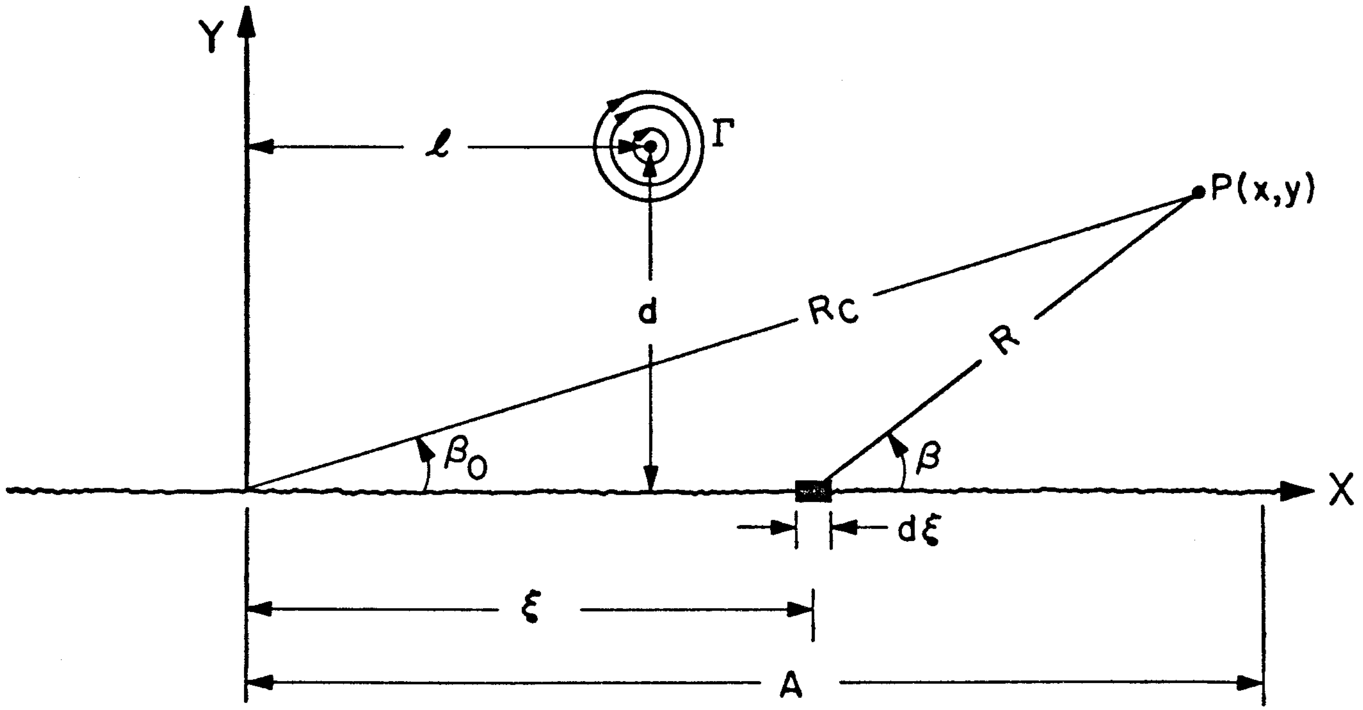

Fig. 74

2-d IMAGE METHOD

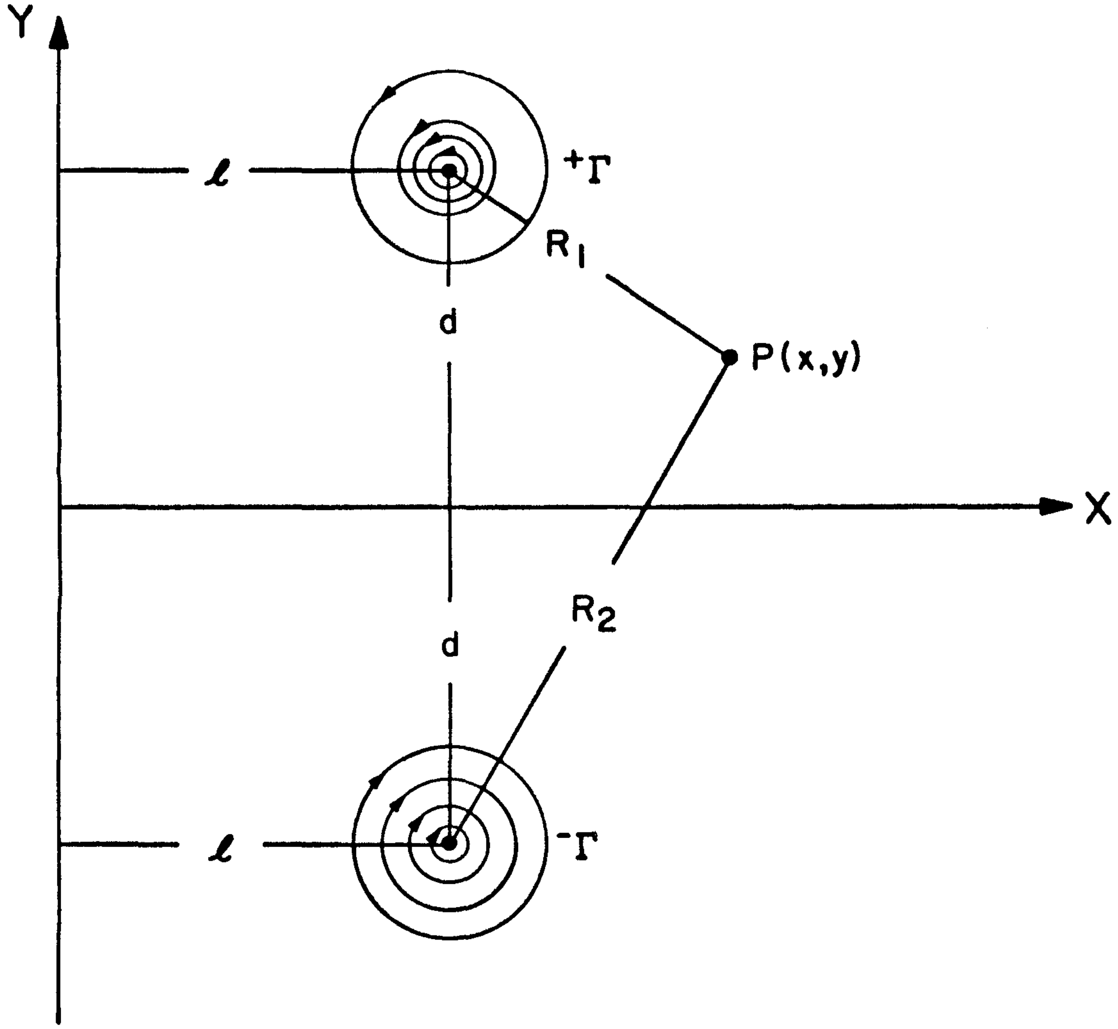

Fig. 75

FINITE LENGTH POINT VORTEX AT AN ARBITRARY ANGLE TO THE FREESTREAM DIRECTION

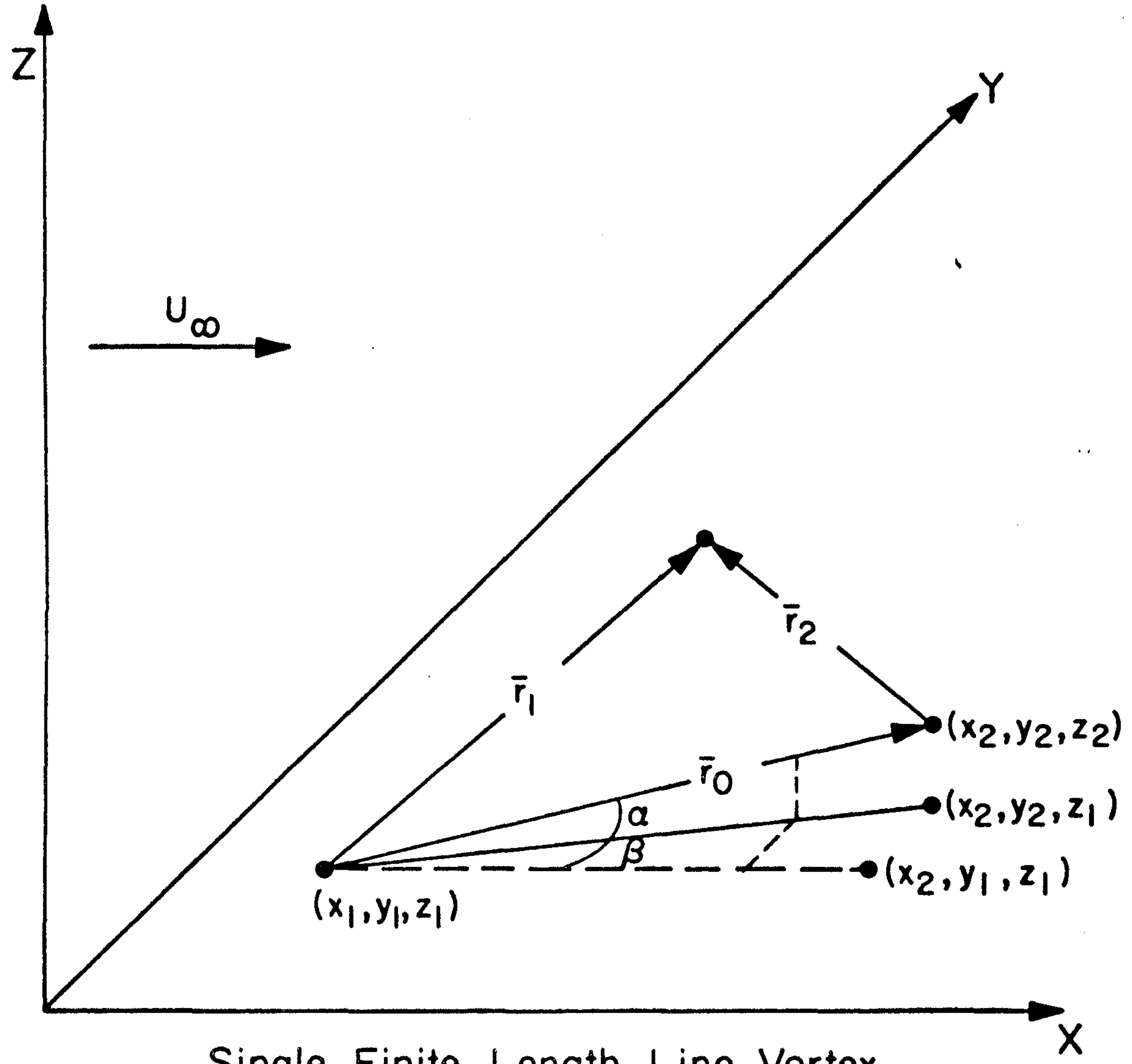

Single Finite Length Line Vortex

Fig. 76

HORSESHOE VORTEX WITH TRAILING VORTICES AT AN ARBITRARY ANGLE TO THE FREESTREAM

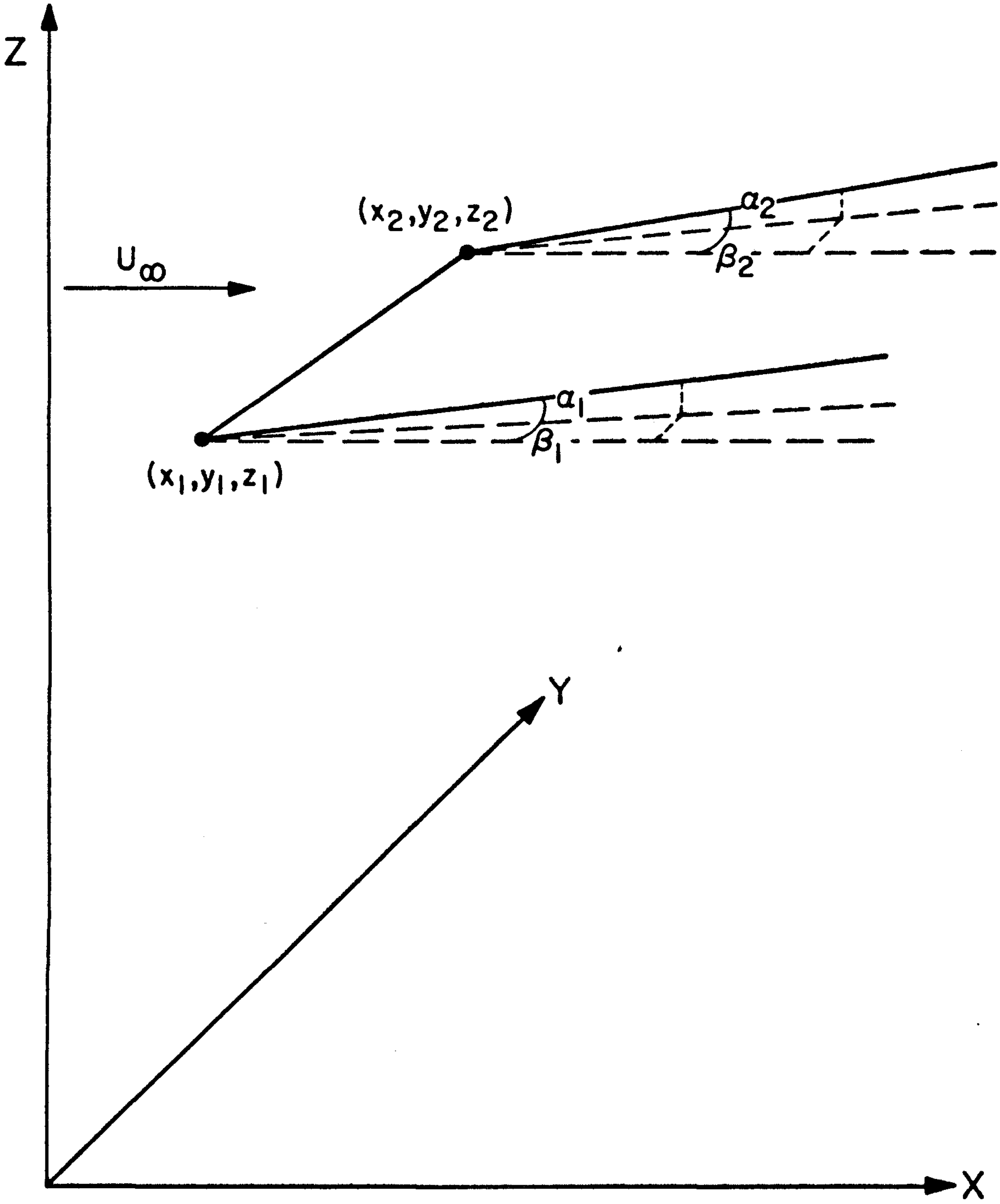

Fig. 77

COMPONENTS OF INTEGRAND OF INTEGRAL EQUATION IN WING BOUNDARY CONDITION

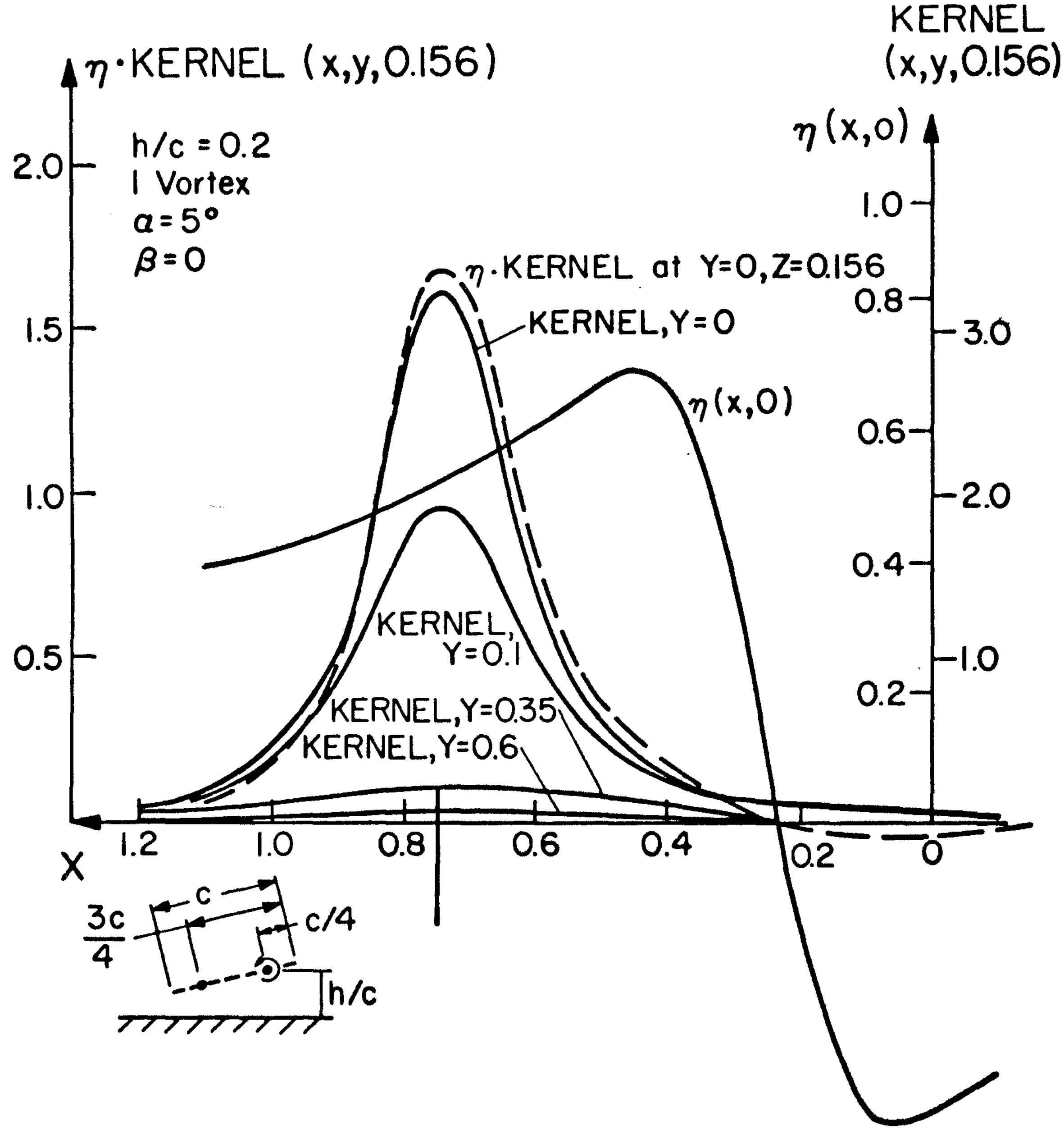

Fig. 78

COMPONENTS OF INTEGRAND OF INTEGRAL EQUATION IN WING BOUNDARY CONDITION

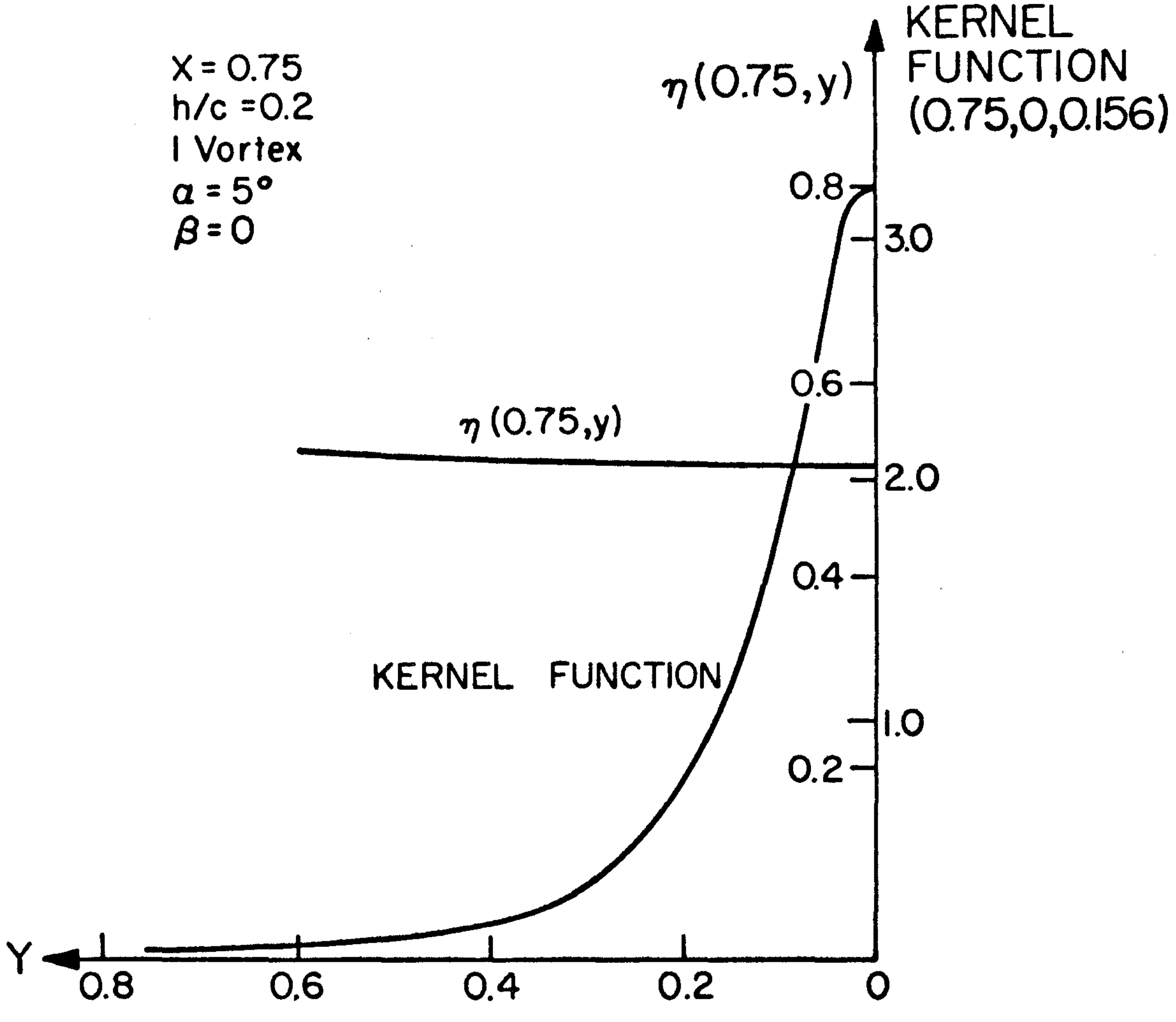

Fig. 79

ERROR IN GROUND INDUCED VERTICAL VELOCITY vs RATIO OF Y-LIMITS OF FINITE GROUND PLANE TO HEIGHT OF VERTICAL VELOCITY EVALUATION POINT

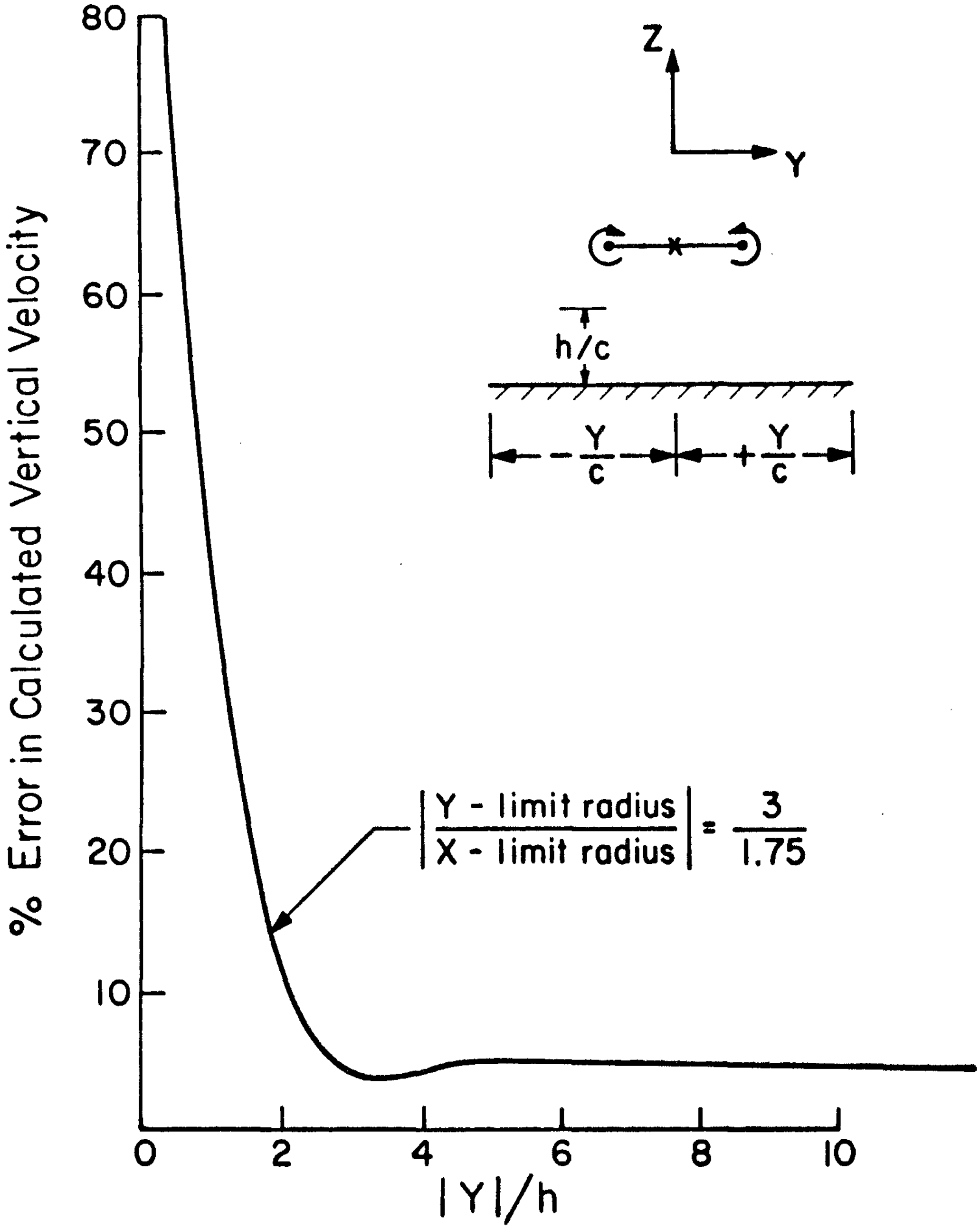

Fig. 80

INTEGRAND OF INTEGRAL EQUATION IN EVALUATION OF LIFT

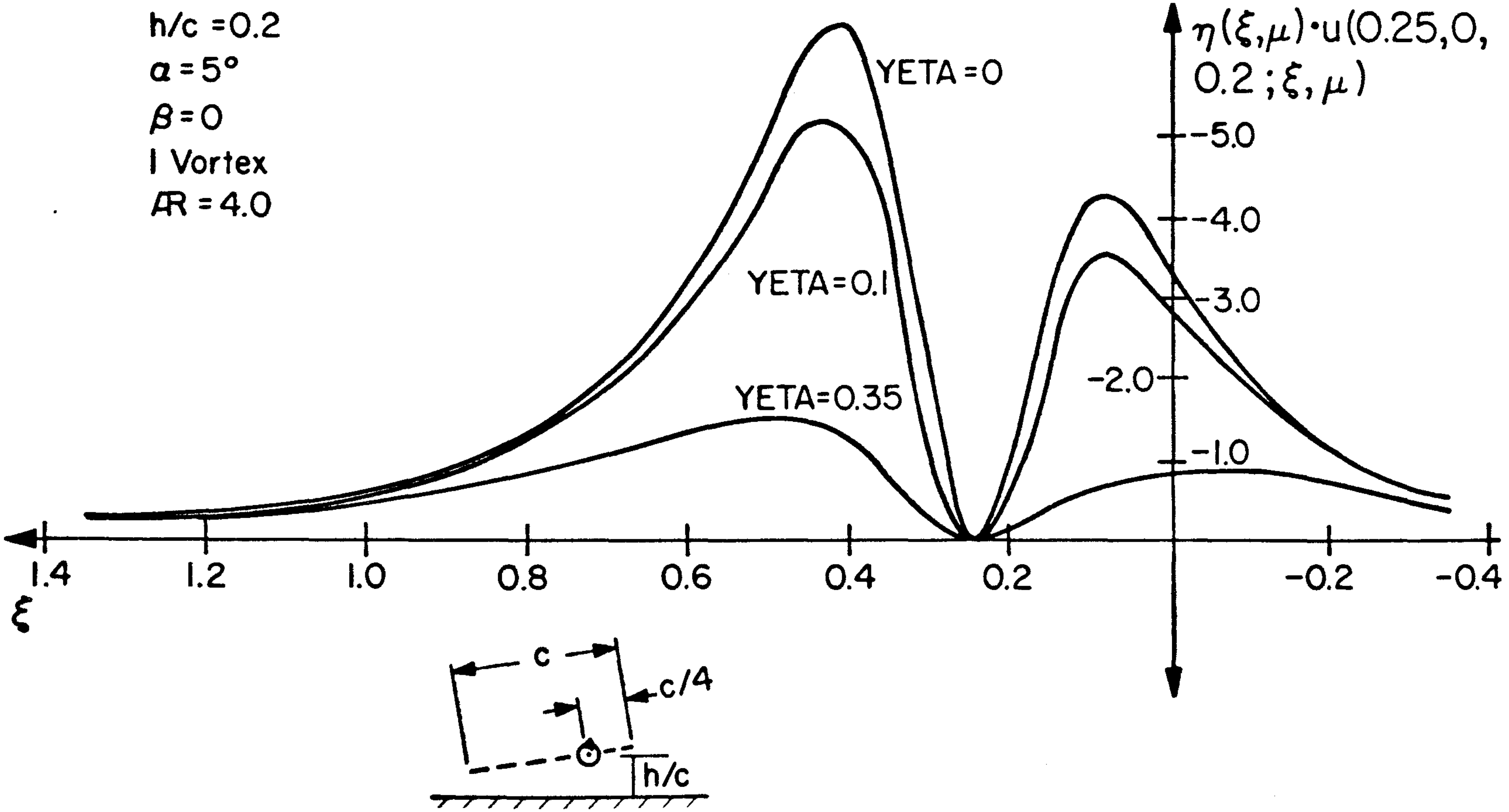

Fig. 81

INTEGRAND OF INTEGRAL EQUATION IN EVALUATION OF LIFT

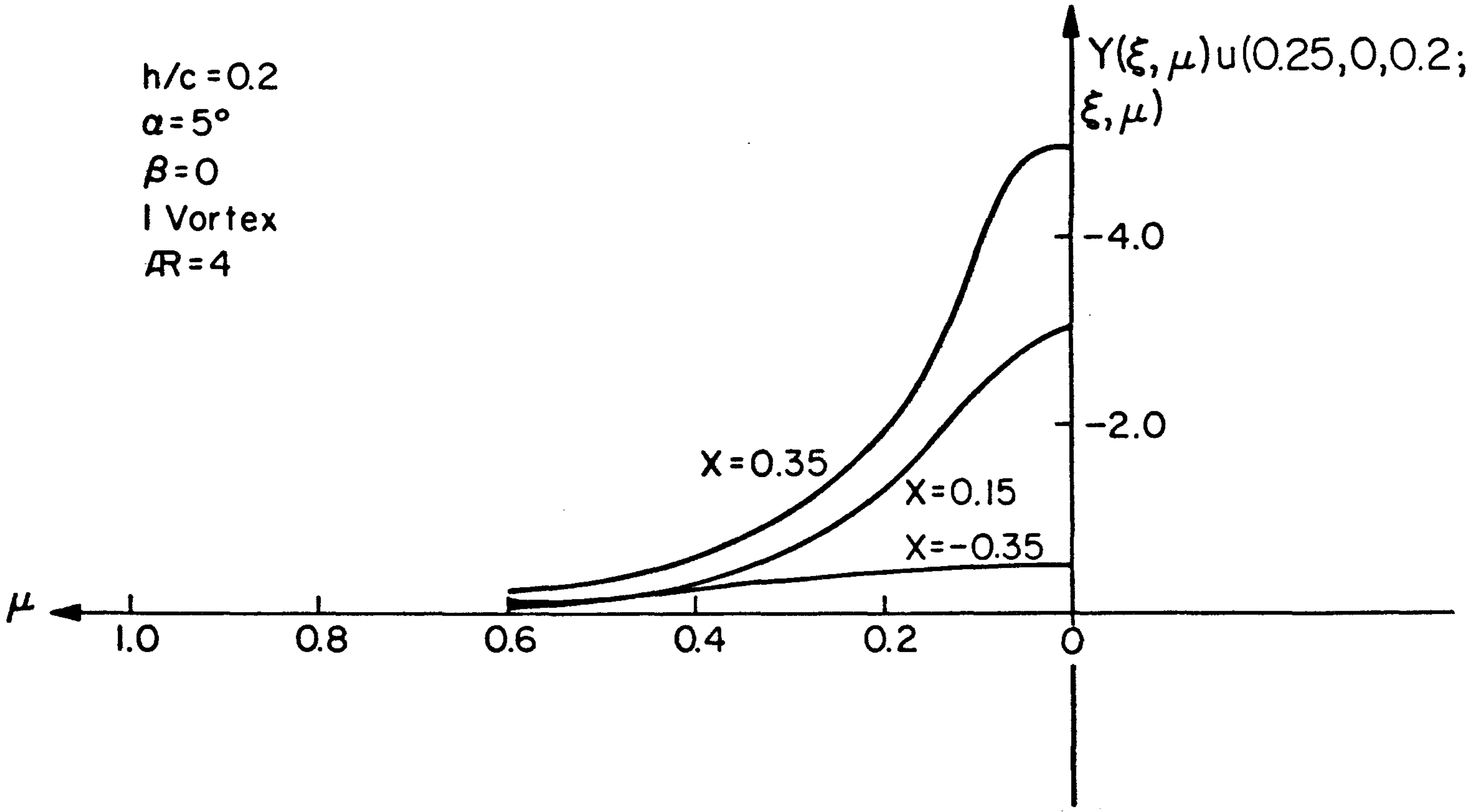

Fig. 82

ERROR IN GROUND INDUCED HORIZONTAL VELOCITY vs Y-LIMITS OF FINITE GROUND PLANE

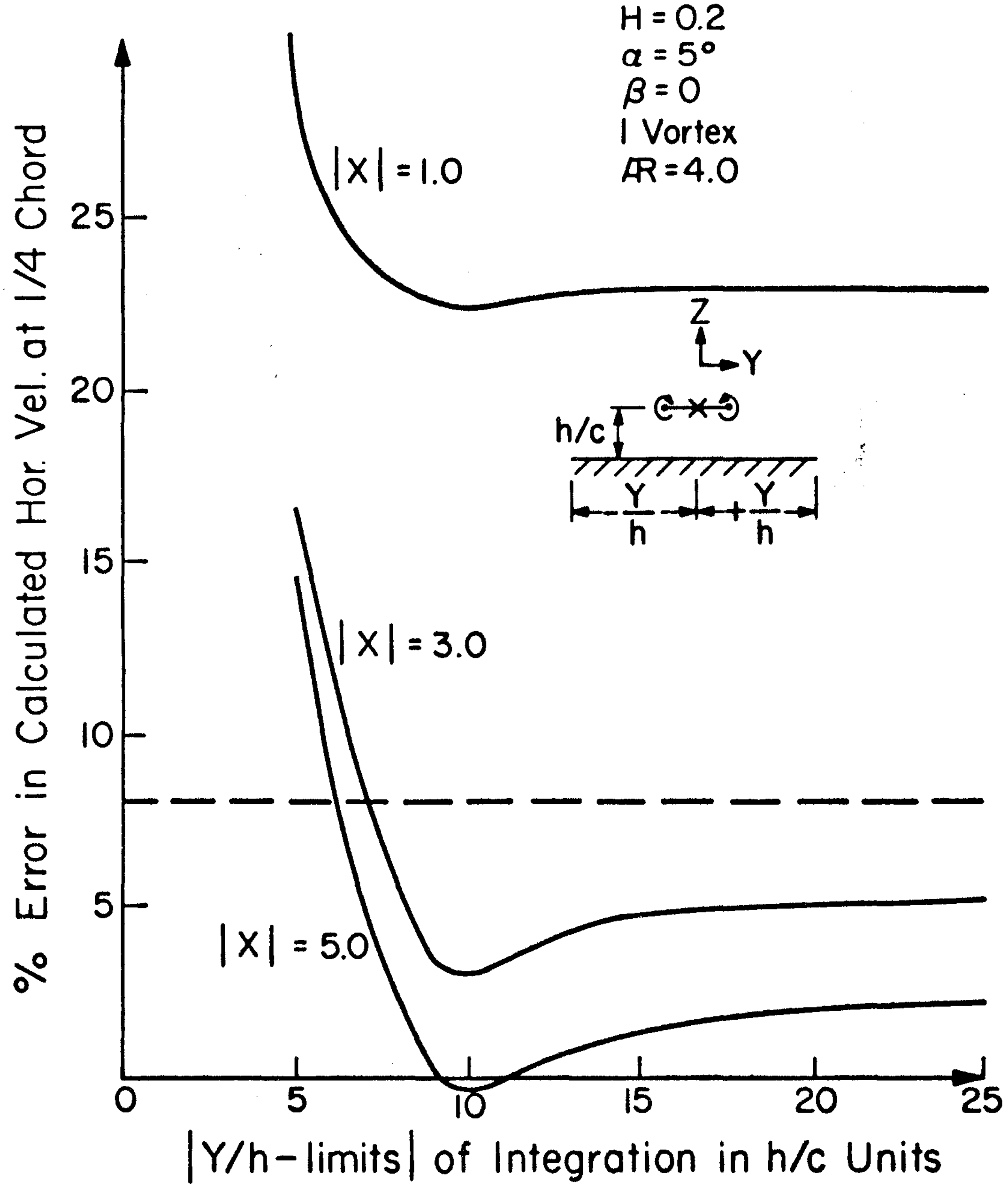

Fig. 83

ERROR IN GROUND INDUCED HORIZONTAL VELOCITY vs X-LIMITS OF FINITE GROUND PLANE

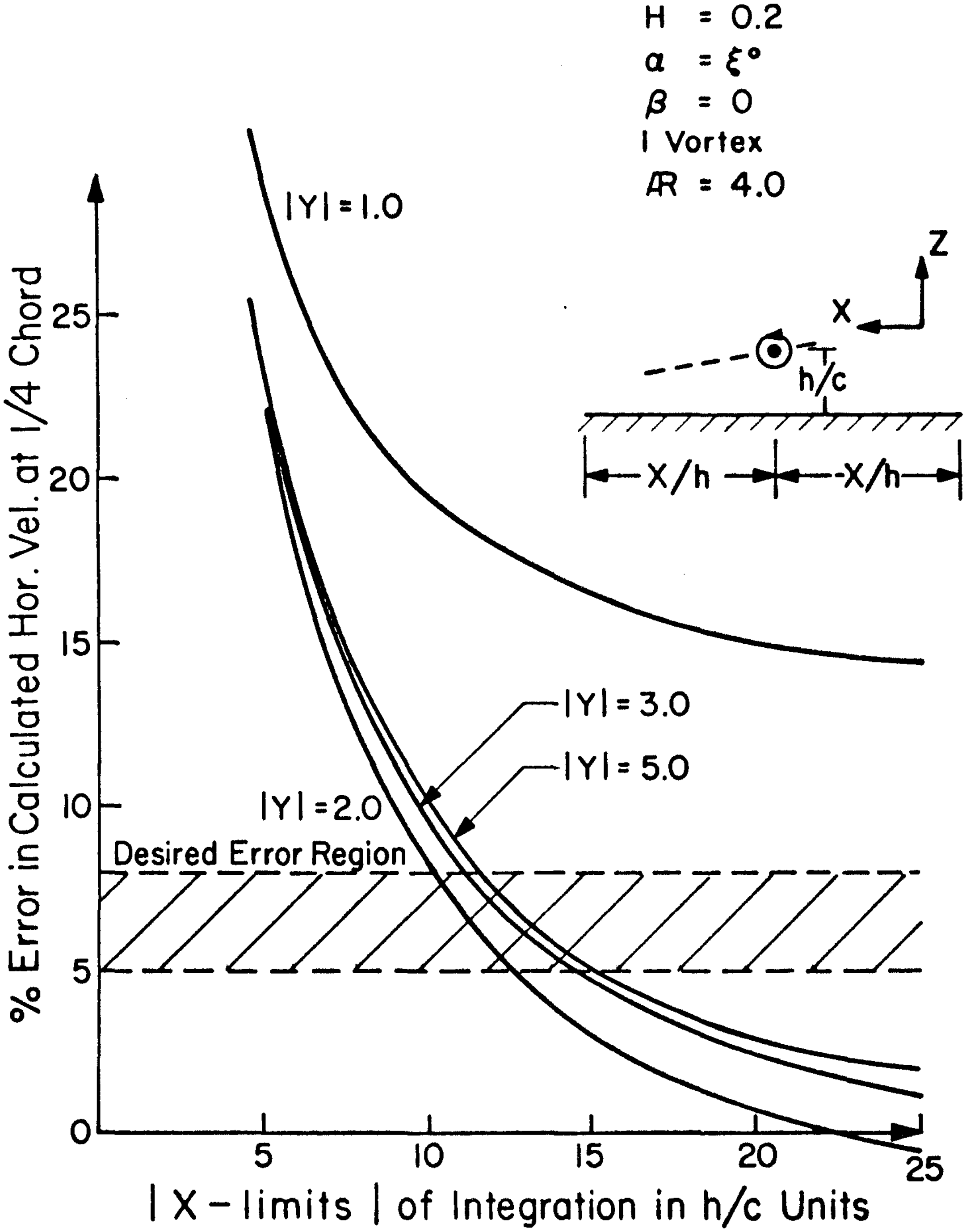

Fig. 84

COMPONENTS OF KERNEL FUNCTION IN INTEGRALS FOR EVALUATING THE VELOCITY INDUCED BY A SOURCE SHEET DISTRIBUTION

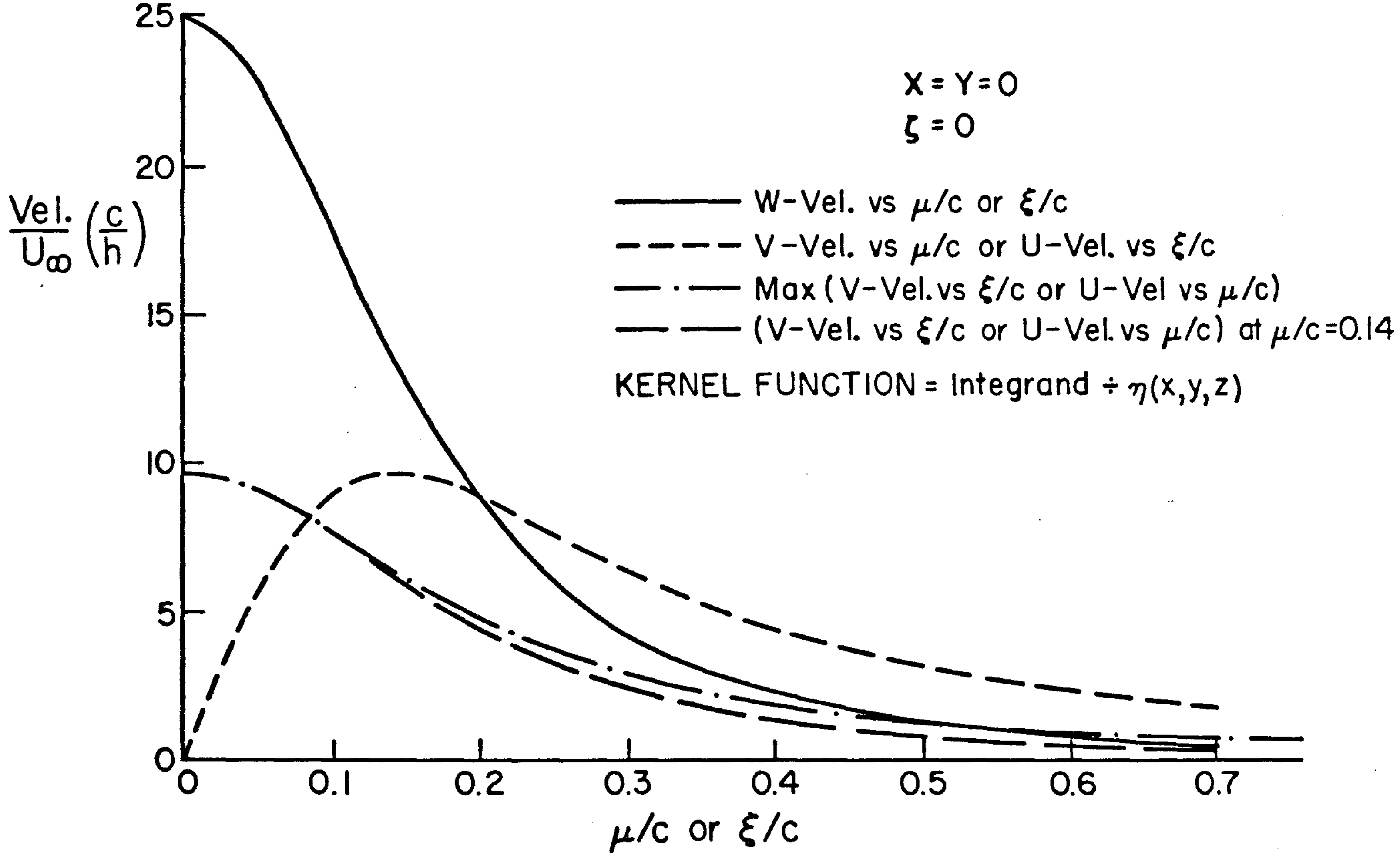

Fig. 85

POSITION OF KERNEL FUNCTION MAXIMUM FOR U-VELOCITY AND V-VELOCITY

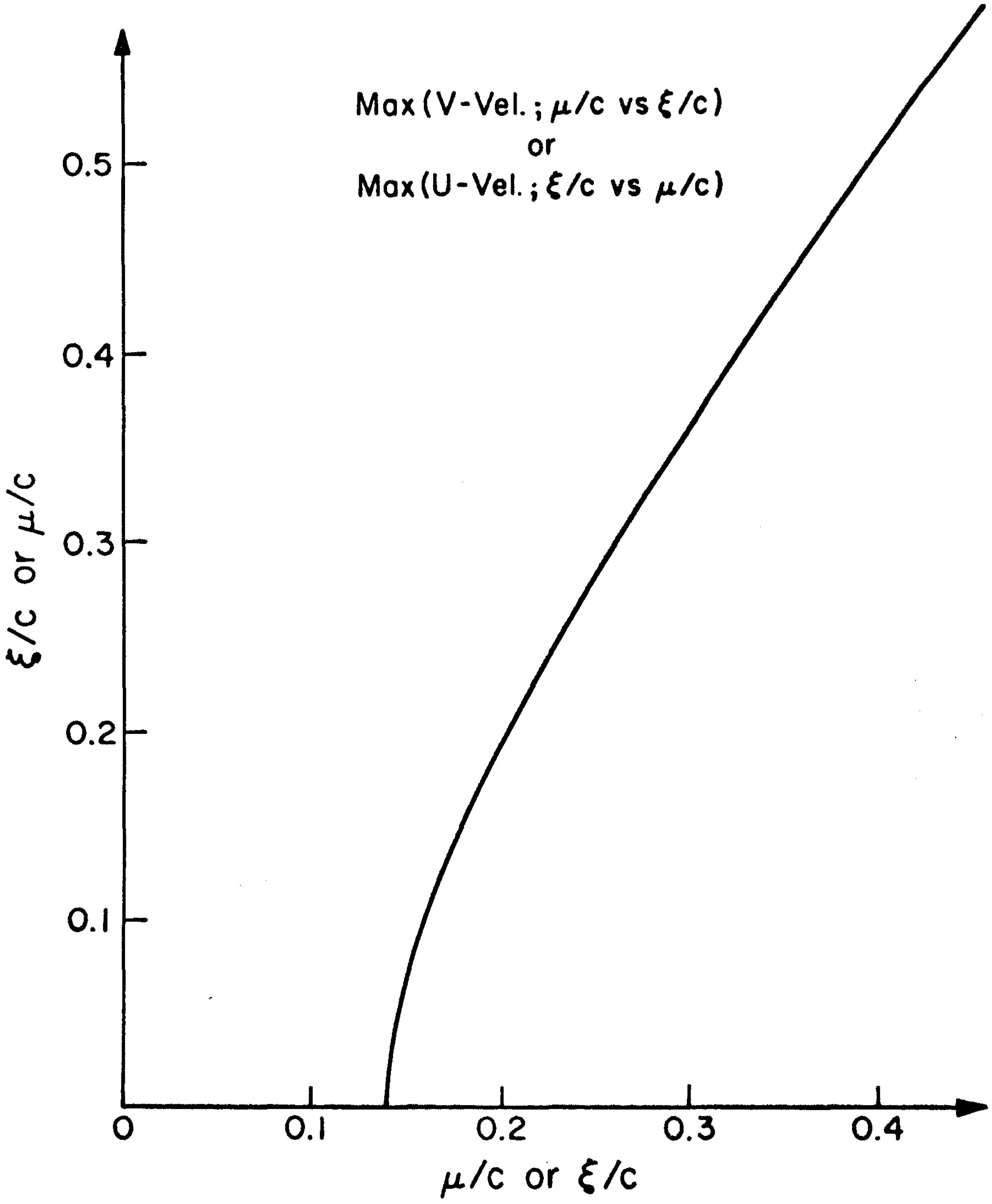

Fig. 86

NUMERICAL CALCULATIONS FOR AN ELLIPTICAL PLANFORM WING

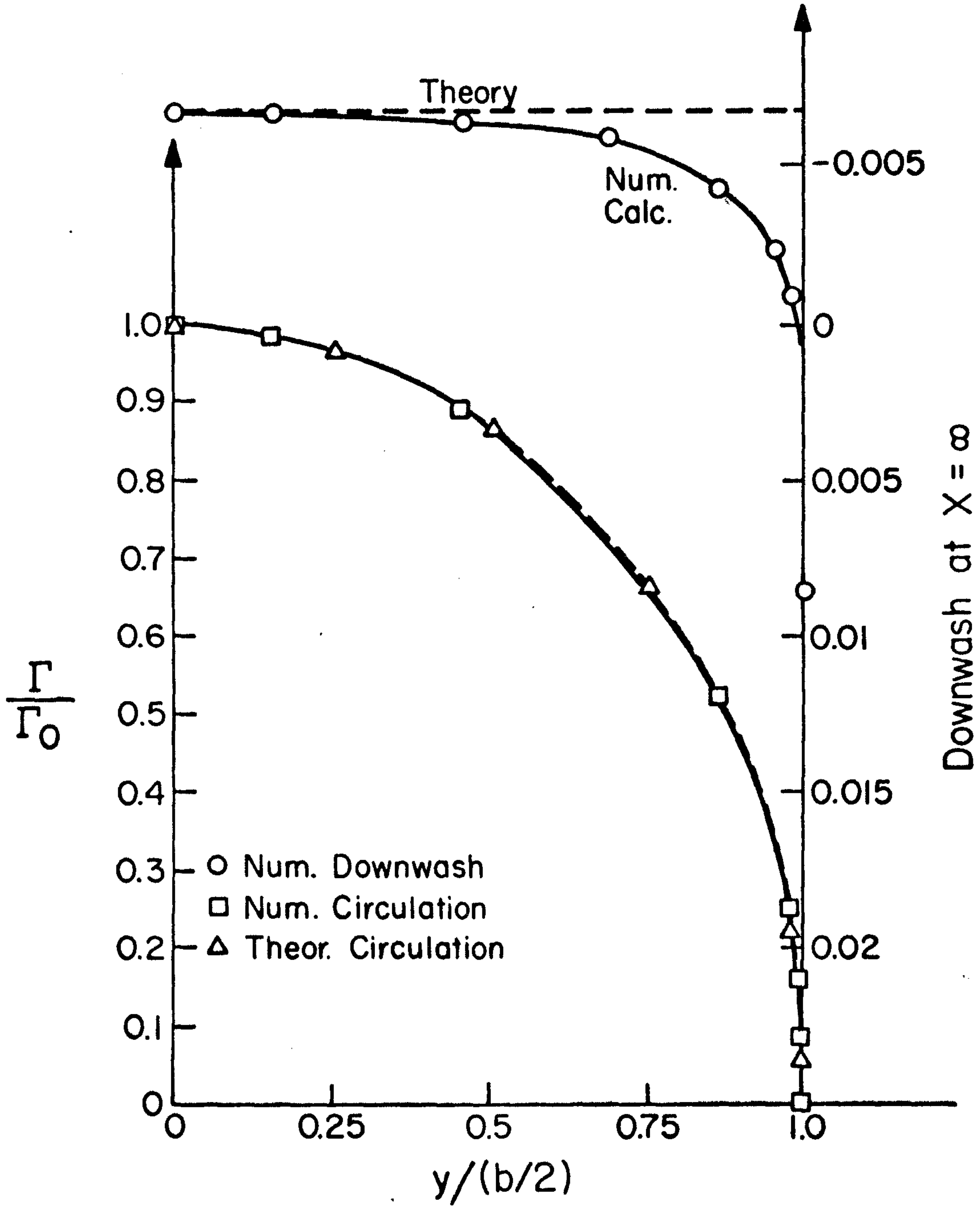

Fig. 87

Tables of Aerodynamic Coefficients And Stability Derivatives

Symbol	Description
AR	Aspect Ratio
ANGLE	Angle of Attack in Degrees of Horizontal Segment of Wing
HEIGHT	Height in Chords of 1/4 Chord of Horizontal Segment of Wing
CDI	Induced Drag Coefficient = C_{D_i}
CL	Lift Coefficient= C_L
CMLE	Leading Edge Moment Coefficient = $C_{M_{L.E.}}$
XCG	Position ofCenter of Pressure
DCDI/DH	$\frac{\partial C_{D_i}}{\partial h}$
DCL/DH	$\frac{\partial C_L}{\partial h}$
DCMLE/DH	$\frac{\partial C_{M_{L.E.}}}{\partial h}$
DCDI/DT	$\frac{\partial C_{D_i}}{\partial \theta}$
DCL/DT	$\frac{\partial C_L}{\partial \theta}$
DCMLE/DT	$\frac{\partial C_{M_{L.E.}}}{\partial \theta}$
DCDI/DW	$\frac{\partial C_{D_i}}{\partial w}$
DCL/DW	$\frac{\partial C_L}{\partial w}$
DCMLE/DW	$\frac{\partial C_{M_{L.E.}}}{\partial w}$
DCDI/DQ	$\frac{\partial C_{D_i}}{\partial q}$
DCL/DQ	$\frac{\partial C_L}{\partial q}$
DCMLE/DQ	$\frac{\partial C_{M_{L.E.}}}{\partial q}$
DCY/DY	$\frac{\partial C_Y}{\partial y}$
DCLLE/DY	$\frac{\partial C_{l_{L.E.}}}{\partial y}$
DCNLE/DY	$\frac{\partial C_{N_{L.E.}}}{\partial y}$
DCY/DPHI	$\frac{\partial C_Y}{\partial \phi}$
DCLLE/DPHI	$\frac{\partial C_{l_{L.E.}}}{\partial \phi}$
DCNLE/DPHI	$\frac{\partial C_{N_{L.E.}}}{\partial \phi}$
DCY/DPSI	$\frac{\partial C_Y}{\partial \psi}$
DCLLE/DPSI	$\frac{\partial C_{l_{L.E.}}}{\partial \psi}$
DCNLE/DPSI	$\frac{\partial C_{N_{L.E.}}}{\partial \psi}$
DCY/DV	$\frac{\partial C_Y}{\partial v}$
DCLLE/DV	$\frac{\partial C_{l_{L.E.}}}{\partial v}$

Tables of Aerodynamic Coefficients And Stability Derivatives (Cont'd)

Symbol	Description
DCNLE/DV	$\frac{\partial C_{N_{L.E.}}}{\partial V}$
DCY/DP	$\frac{\partial C_Y}{\partial p}$
DCLLE/DP	$\frac{\partial C_{\ell_{L.E.}}}{\partial p}$
DCNLE/DP	$\frac{\partial C_{N_{L.E.}}}{\partial p}$
DCY/DR	$\frac{\partial C_Y}{\partial r}$
DCLLE/DR	$\frac{\partial C_{\ell_{L.E.}}}{\partial r}$
DCNLE/DR	$\frac{\partial C_{N_{L.E.}}}{\partial r}$

TABLE 1

THIN FLAT RECTANGULAR WINGS IN GROUND EFFECT

AR	.5	.5	1.	1.	1.
ANGLE	10.	10.	2.5	2.5	2.5
HEIGHT	.15	.2	.05	.1	.2
CDI	.0798	.0525	.01217	.003891	.002359
CL	.555	.4034	.3723	.1669	.1095
CMLE	-.2457	-.1453	-.1478	-.04727	-.02649
XCG	.4318	.3521	.3695	.3049	.28
DCDI/DH	-1.325	-.2351	-.6591	-.03812	-.006102
DCL/DH	-6.46	-1.425	-11.89	-1.303	-.2501
DCMLE/DH	4.597	.8565	6.542	.5086	.08433
DCDI/DT	1.15	.3487	.5438	.05139	.01884
DCL/DT	4.979	1.704	7.855	1.096	.3996
DCMLE/DT	-3.504	-.9631	-5.119	-.6164	-.2058
DCDI/DW	.7771	.533	.4947	.1683	.104
DCL/DW	2.92	2.222	7.289	3.707	2.48
DCMLE/DW	-1.285	-.816	-2.805	-1.057	-.6016
DCDI/DQ	.2385	.1865	.2213	.08376	.05622
DCL/DQ	.8615	.8026	3.103	1.842	1.322
DCMLE/DQ	-.683	-.5564	-1.956	-.9659	-.6471
DCY/DY	0.	0.	0.	0.	0.
DCLLE/DY	0.	0.	0.	0.	0.
DCNLE/DY	0.	0.	0.	0.	0.
DCY/DPHI	0.	0.	0.	0.	0.
DCLLE/DPHI	-.08608	-.01681	-.271	-.06275	-.02676
DCNLE/DPHI	.01928	.003015	.02609	.004828	.001919
DCY/DPSI	0.	0.	0.	0.	0.
DCLLE/DPSI	0.	0.	0.	0.	0.
DCNLE/DPSI	0.	0.	0.	0.	0.
DCY/DV	.01805	.01863	.01377	.01152	.0101
DCLLE/DV	-.01267	-.03436	.3145	.1168	.06967
DCNLE/DV	.0007509	.005174	-.02514	-.007696	-.004111
DCY/DP	0.	0.	0.	0.	0.
DCLLE/DP	-.02853	-.02335	-.1511	-.1111	-.09796
DCNLE/DP	.0113	.008475	.02773	.01821	.0153
DCY/DR	0.	0.	0.	0.	0.
DCLLE/DR	.007294	.005269	.01873	.01207	.01021
DCNLE/DR	-.00238	-.001687	-.002902	-.001795	-.001476

TABLE 1

THIN FLAT RECTANGULAR WINGS IN GROUND EFFECT

AR	1.	1.	1.	2.	2.
ANGLE	5.	5.	5.	2.5	2.5
HEIGHT	.1	.15	.2	.075	.1
CDI	.02548	.01496	.01194	.007775	.005303
CL	.4487	.3027	.2525	.4471	.3341
CMLE	-.1666	-.09269	-.07098	-.151	-.103
XCG	.3963	.2829	.2417	.3375	.3082
DCDI/DH	-.4739	-.09218	-.03908	-.1664	-.05719
DCL/DH	-5.703	-1.465	-.6785	-6.764	-2.898
DCMLE/DH	3.141	.6617	.2803	3.02	1.157
DCDI/DT	.4409	.1363	.08662	.172	.07631
DCL/DT	4.074	1.39	.8811	2.913	1.209
DCMLE/DT	-2.5	-.7547	-.4405	-1.793	-.7206
DCDI/DW	.4981	.307	.2495	.2687	.1988
DCL/DW	4.679	3.324	2.814	8.978	7.098
DCMLE/DW	-1.73	-1.025	-.7963	-3.074	-2.213
DCDI/DQ	.2131	.1423	.1214	.1438	.1034
DCL/DQ	1.874	1.492	1.329	3.849	3.131
DCMLE/DQ	-1.134	-.8098	-.6928	-1.972	-1.505
DCY/DY	0.	0.	0.	0.	0.
DCLLE/DY	0.	0.	0.	0.	0.
DCNLE/DY	0.	0.	0.	0.	0.
DCY/DPHI	0.	0.	0.	0.	0.
DCLLE/DPHI	-.5637	-.05104	-.008309	-1.425	-.5725
DCNLE/DPHI	.03425	.001827	.0002468	.04905	.01634
DCY/DPSI	0.	0.	0.	0.	0.
DCLLE/DPSI	0.	0.	0.	0.	0.
DCNLE/DPSI	0.	0.	0.	0.	0.
DCY/DV	.00409	.003397	.002422	.01174	.009285
DCLLE/DV	1.093	.2566	.1085	1.639	.9969
DCNLE/DV	-.05477	-.009797	-.004004	-.05113	-.02926
DCY/DP	0.	0.	0.	0.	0.
DCLLE/DP	-.2047	-.1058	-.07876	-1.291	-.9911
DCNLE/DP	.02409	.009138	.006036	.07982	.05779
DCY/DR	0.	0.	0.	0.	0.
DCLLE/DR	.01296	.0053	.00373	.0784	.05449
DCNLE/DR	-.001226	-.000427	-.000276	-.004466	-.003028

TABLE 1

THIN FLAT RECTANGULAR WINGS IN GROUND EFFECT

AR	2.	4.	4.	4.
ANGLE	2.5	2.5	2.5	2.5
HEIGHT	.2	.075	.1	.2
CDI	.003141	.004974	.003671	.002441
CL	.2081	.6803	.5156	.3178
CMLE	-.05514	-.2386	-.1672	-.09119
XCG	.2696	.3506	.3242	.2869
DCDI/DH	-.008519	-.08931	-.03251	-.005243
DCL/DH	-.5613	-9.174	-4.486	-.8694
DCMLE/DH	.1956	4.169	1.84	.314
DCDI/DT	.02326	.2823	.1316	.0401
DCL/DT	.28	2.903	1.086	.1025
DCMLE/DT	-.1577	-1.906	-.7308	-.09562
DCDI/DW	.1284	-.01456	.05128	.07377
DCL/DW	4.639	12.12	10.33	6.942
DCMLE/DW	-1.256	-4.335	-3.4	-2.
DCDI/DQ	.0679	.08721	.06758	.04967
DCL/DQ	2.206	4.759	4.182	3.049
DCMLE/DQ	-.9847	-2.335	-1.92	-1.287
DCY/DY	0.	0.	0.	0.
DCLLE/DY	0.	0.	0.	0.
DCNLE/DY	0.	0.	0.	0.
DCY/DPHI	0.	0.	0.	0.
DCLLE/DPHI	-.09644	-11.24	-5.108	-.8614
DCNLE/DPHI	.002139	.2091	.07375	.01052
DCY/DPSI	0.	0.	0.	0.
DCLLE/DPSI	0.	0.	0.	0.
DCNLE/DPSI	0.	0.	0.	0.
DCY/DV	.005946	.02473	.01884	.01143
DCLLE/DV	.3927	1.569	1.286	.6596
DCNLE/DV	-.01129	-.01547	-.01464	-.009025
DCY/DP	0.	0.	0.	0.
DCLLE/DP	-.6582	-11.79	-9.112	-5.481
DCNLE/DP	.03648	.2166	.205	.1534
DCY/DR	0.	0.	0.	0.
DCLLE/DR	.03286	.7859	.5281	.2817
DCNLE/DR	-.001777		-.01464	-.008552

TABLE 2

THIN FLAT RECTANGULAR END PLATED WINGS IN GROUND EFFECT

TRIANGULAR END PLATES

AR	.5	.5	.5	.5	.5
ANGLE	2.5	2.5	2.5	2.5	10.
HEIGHT	.05	.075	.1	.2	.15
CDI					
CL	.17246	.092275	.07253	.052065	.5134
CMLE	-.05903	-.02166	-.014725	-.008674	-.1685
XCG	.3419	.2345	.2028	.1664	.3342
DCDI/DH	-.3048	-.036014	-.01303	-.001873	-1.159
DCL/DH	-8.009	-1.252	-.5016	-.08095	-9.766
DCMLE/DH	4.17	.4763	.16144	.022255	5.103
DCDI/DT	.20672	.03788	.01997	.00897	.8454
DCL/DT	3.644	.751	.402	.19	2.589
DCMLE/DT	-2.94	-.621	-.334	-.1576	-2.824
DCDI/DW	.20998	.09346	.06961	.0473	.4145
DCL/DW	3.737	2.072	1.641	1.187	2.685
DCMLE/DW	-1.276	-.4901	-.33497	-.1983	-.8911
DCDI/DQ	.1177	.0619	.048076	.034736	.2709
DCL/DQ	2.009	1.298	1.053	.79916	1.267
DCMLE/DQ	-1.32	-.7262	-.5572	-.3978	-.7967
DCY/DY	0.	0.	0.	0.	0.
DCLLE/DY	0.	0.	0.	0.	0.
DCNLE/DY	0.	0.	0.	0.	0.
DCY/DPHI	.04931	.008571	.003247	.396E-3	.323
DCLLE/DPHI	-.094094	-.0132	-.004679	-.573E-3	-.1769
DCNLE/DPHI	-.004951	-.774E-3	-.279E-3	-.346E-4	-.06163
DCY/DPSI	0.	0.	0.	0.	0.
DCLLE/DPSI	0.	0.	0.	0.	0.
DCNLE/DPSI	0.	0.	0.	0.	0.
DCY/DV	-.07789	-.04339	-.034364	-.02713	-.3155
DCLLE/DV	-.2305	-.09113	-.057076	-.03045	-.3729
DCNLE/DV	-.01291	-.006	-.004153	-.002654	-.0384
DCY/DP	.014634	.0105	.009304	.008284	.04896
DCLLE/DP	-.023794	-.01418	-.01196	-.01008	-.02868
DCNLE/DP	.8248E-3	.2191E-3	.1265E-3	.2634E-4	-.002103
DCY/DR	-.819E-3	.001487	.002095	.002783	-.002221
DCLLE/DR	.6156E-3	.5388E-3	.5647E-3	.5759E-3	.004078
DCNLE/DR	-.0015	-.001289	-.001253	-.001234	-.01567

TABLE 2

THIN FLAT RECTANGULAR END PLATED WINGS IN GROUND EFFECT

TRIANGULAR END PLATES

AR	.5	1.	1.	1.	1.
ANGLE	10.	2.5	2.5	2.5	2.5
HEIGHT	.2	.05	.075	.1	.2
CDI					
CL	.3296	.52843	.253006	.1814829	.11343
CMLE	-.07966	-.20587	-.077247	-.048863	-.025682
XCG	.238	.3891	.305	.269	.2261
DCDI/DH	-.1554	-.96618	-.12725	-.04126	-.00575
DCL/DH	-1.47	-21.274	-4.72168	-1.7216	-.27797
DCMLE/DH	.6366	9.9695	1.990612	.635	.0881888
DCDI/DT	.2715	.6344	.08214	.039785	.0079
DCL/DT	.8401	7.94	1.665	.6059	.147
DCMLE/DT	-.9938	-5.263	-1.1686	-.4362	-.1105
DCDI/DW	.2708	.5719	.23435	.1599	.09588
DCL/DW	1.795	9.403	5.462	4.017	2.5676
DCMLE/DW	-.4458	-3.477	-1.686	-1.09	-.5831
DCDI/DQ	.1854	.27315	.1215283	.08713	.05675
DCL/DQ	.9913	3.8512	2.72429	2.0899	1.44
DCMLE/DQ	-.5527	-2.255	-1.47292	-1.0598	-.68299
DCY/DY	0.	0.	0.	0.	0.
DCLLE/DY	0.	0.	0.	0.	0.
DCNLE/DY	0.	0.	0.	0.	0.
DCY/DPHI	.03836	.16965	.031012	.01134	.001458
DCLLE/DPHI	-.01969	-1.164	-.230795	-.07905	-.009952
DCNLE/DPHI	-.006243	.0065737	.6887E-3	.1522E-3	.5061E-5
DCY/DPSI	0.	0.	0.	0.	0.
DCLLE/DPSI	0.	0.	0.	0.	0.
DCNLE/DPSI	0.	0.	0.	0.	0.
DCY/DV	-.22894	-.067135	-.033468	-.022936	-.01389
DCLLE/DV	-.1257	-.8081	-.409967	-.2431	-.1006
DCNLE/DV	-.01622	.008643	.4812E-2	.002697	.8737E-3
DCY/DP	.04489	.03886	.024212	.019496	.01497
DCLLE/DP	-.02159	-.28985	-.152924	-.1137	-.07991
DCNLE/DP	-.001437	.025185	.9868E-2	.006686	.4052E-2
DCY/DR	.01998	.003252	-.896E-3	-.271E-3	.355E-3
DCLLE/DR	.002863	.01946	.7413E-2	.0052895	.3676E-2
DCNLE/DR	-.01612	-.002389	-.001279	-.001043	-.859E-3

TABLE 2

THIN FLAT RECTANGULAR END PLATED WINGS IN GROUND EFFECT

TRIANGULAR END PLATES

AR	1.	1.	1.	1.	2.
ANGLE	2.5	5.	5.	5.	2.5
HEIGHT	.5	.1	.15	.2	.075
CDI					
CL	.0842	.4946	.3008	.2458	.5667
CMLE	-.01645	-.1715	-.08198	-.06061	-.195
XCG	.1952	.3455	.2716	.2457	.3439
DCDI/DH	-.568E-3	-.5414	-.08124	-.03231	-.11997
DCL/DH	-.03049	-8.868	-1.684	-.7247	-10.026
DCMLE/DH	.009803	4.441	.6864	.26856	4.378
DCDI/DT	.00358	.4013	.0925	.0549	.13047
DCL/DT	.072	3.561	.793	.451	2.84
DCMLE/DT	-.0539	-2.526	-.5841	-.3373	-1.8665
DCDI/DW	.07071	.4447	.2519	.2023	.2166
DCL/DW	1.923	5.088	3.292	2.734	10.92
DCMLE/DW	-.3762	-1.7685	-.9064	-.6797	-3.8165
DCDI/DQ	.04579	.2271	.1414	.1191	.126
DCL/DQ	1.174	2.283	1.678	1.465	4.451
DCMLE/DQ	-.5441	-1.31	-.8599	-.7204	-2.226
DCY/DY	0.	0.	0.	0.	0.
DCLLE/DY	0.	0.	0.	0.	0.
DCNLE/DY	0.	0.	0.	0.	0.
DCY/DPHI	.115E-3	.1232	.02245	.008668	.08229
DCLLE/DPHI	-.813E-3	-.5108	-.08177	-.03042	-2.5695
DCNLE/DPHI	-.168E-5	.004986	.1342E-3	-.488E-5	.01976
DCY/DPSI	0.	0.	0.	0.	0.
DCLLE/DPSI	0.	0.	0.	0.	0.
DCNLE/DPSI	0.	0.	0.	0.	0.
DCY/DV	-.01163	-.09294	-.05826	-.04862	-.003139
DCLLE/DV	-.060926	-.5355	-.2463	-.1642	-.7438
DCNLE/DV	.3702E-3	.008755	.0022385	.5667E-3	.00863
DCY/DP	.013706	.04235	.0325	.02961	.060456
DCLLE/DP	-.06962	-.1627	-.1051	-.09063	-1.899
DCNLE/DP	.003001	.01984	.010736	.0086497	.07261
DCY/DR	.698E-3	-.005389	-.797E-3	.5227E-3	-.003894
DCLLE/DR	.0032	.017275	.01011	.008716	.1117
DCNLE/DR	-.79E-3	-.00473	-.003614	-.003366	-.005086

TABLE 2

THIN FLAT RECTANGULAR END PLATED WINGS IN GROUND EFFECT

TRIANGULAR END PLATES

AR	2.	2.
ANGLE	2.5	2.5
HEIGHT	.1	.2
CDI		
CL	.39916	.2254
CMLE	-.12524	-.06094
XCG	.3136	.2702
DCDI/DH	-.05032	-.008289
DCL/DH	-4.364	-.68396
DCMLE/DH	1.722	.23697
DCDI/DT	.06156	.0135
DCL/DT	.968	.1041
DCMLE/DT	-.6715	-.092
DCDI/DW	.18744	.1267
DCL/DW	8.3634	5.0165
DCMLE/DW	-2.6555	-1.361
DCDI/DQ	.09789	.06684
DCL/DQ	3.5736	2.372
DCMLE/DQ	-1.687	-1.046
DCY/DY	0.	0.
DCLLE/DY	0.	0.
DCNLE/DY	0.	0.
DCY/DPHI	.03412	.004594
DCLLE/DPHI	-1.0535	-.1401
DCNLE/DPHI	.008942	.001405
DCY/DPSI	0.	0.
DCLLE/DPSI	0.	0.
DCNLE/DPSI	0.	0.
DCY/DV	-.004223	-.002897
DCLLE/DV	-.55266	-.2408
DCNLE/DV	.008484	.004463
DCY/DP	.04579	.02908
DCLLE/DP	-1.327	-.7427
DCNLE/DP	.05573	.03361
DCY/DR	-.002407	-.001099
DCLLE/DR	.07013	.03582
DCNLE/DR	-.003571	-.002097

TABLE 2

THIN FLAT RECTANGULAR END PLATED WINGS IN GROUND EFFECT

RECTANGULAR END PLATES

AR	.5	.5
ANGLE	10.	10.
HEIGHT	.15	.2
CDI	.03718	.02188
CL	.4182	.2776
CMLE	-.1429	-.0681
XCG	.3365	.242
DCDI/DH	-.8486	-.1166
DCL/DH	-7.081	-1.174
DCMLE/DH	4.107	.5502
DCDI/DT	2.734	1.607
DCL/DT	12.43	8.862
DCMLE/DT	-9.163	-5.662
DCDI/DW	.2767	.189
DCL/DW	2.0623	1.438
DCMLE/DW	-.7439	-.3761
DCDI/DQ	.2346	.1619
DCL/DQ	1.009	.8329
DCMLE/DQ	-.673	-.4825
DCY/DY	0.	0.
DCLLE/DY	0.	0.
DCNLE/DY	0.	0.
DCY/DPHI	.4005	.04467
DCLLE/DPHI	-.1379	-.01583
DCNLE/DPHI	-.1305	-.0103
DCY/DPSI	0.	0.
DCLLE/DPSI	0.	0.
DCNLE/DPSI	0.	0.
DCY/DV	-.9844	-.3937
DCLLE/DV	-.417	-.1342
DCNLE/DV	-.5264	-.1319
DCY/DP	.04467	.04034
DCLLE/DP	-.02134	-.01615
DCNLE/DP	-.009745	-.004718
DCY/DR	.1347	.1128
DCLLE/DR	.01216	.00701
DCNLE/DR	-.05675	-.07093

TABLE 3

THIN RECTANGULAR WINGS CONNECTED IN TANDEM IN GROUND EFFECT

SEPARATION BETWEEN WINGS = 3 CHORDS

AR	1.	1.	1.	2.	2.
ANGLE	2.5	2.5	2.5	2.5	2.5
HEIGHT	.05	.2	.5	.075	.2
CDI	.01264	.002876	.002092	.01399	.005783
CL	.4127	.1215	.09103	.6237	.2844
CMLE	-.359	-.06798	-.04543	-.8137	-.3083
XCG					
DCDI/DH	-.6448	-.007606	-.827E-3	-.2681	-.01785
DCL/DH	-15.4	-.2852	-.03332	-9.651	-.8339
DCMLE/DH	19.38	.211	.02665	15.7	1.133
DCDI/DT	2.274	.1027	.05347	.6794	.1029
DCL/DT	44.02	2.261	1.182	13.2	1.899
DCMLE/DT	-159.2	-7.004	-3.561	-57.94	-7.288
DCDI/DW	.5075	.1268	.09309	.4824	.2362
DCL/DW	8.475	2.755	2.079	13.05	6.369
DCMLE/DW	-7.393	-1.552	-1.04	-17.65	-6.978
DCDI/DQ	1.568	.3938	.2969	.9832	.5005
DCL/DQ	25.84	8.15	6.278	22.21	12.18
DCMLE/DQ	-89.92	-25.48	-19.06	-89.64	-45.31
DCY/DY					
DCLLE/DY					
DCNLE/DY					
DCY/DPHI					
DCLLE/DPHI					
DCNLE/DPHI					
DCY/DPSI					
DCLLE/DPSI					
DCNLE/DPSI					
DCY/DV					
DCLLE/DV					
DCNLE/DV					
DCY/DP					
DCLLE/DP					
DCNLE/DP					
DCY/DR					
DCLLE/DR					
DCNLE/DR					

TABLE 3

THIN RECTANGULAR WINGS CONNECTED IN TANDEM IN GROUND EFFECT

SEPARATION BETWEEN WINGS = 3 CHORDS

AR	2.	4.	4.	4.
ANGLE	2.5	2.5	2.5	2.5
HEIGHT	.5	.075	.2	.5
CDI	.003824	.01232	.006608	.004901
CL	.188	1.153	.5339	.3478
CMLE	-.1773	-1.963	-.8068	-.4774
XCG				
DCDI/DH	-.00234	-.1626	-.01618	-.002028
DCL/DH	-.1201	-15.45	-1.592	-.2456
DCMLE/DH	.1692	30.21	2.8	.4518
DCDI/DT	.0413	.806	.1319	.05067
DCL/DT	.7274	7.486	.8913	.2869
DCMLE/DT	-2.397	-53.22	-6.308	-1.428
DCDI/DW	.1631	-.06401	.197	.1821
DCL/DW	4.282	22.08	11.73	7.868
DCMLE/DW	-4.044	-38.32	-17.85	-10.83
DCDI/DQ	.3795	.3977	.3083	.2881
DCL/DQ	9.139	16.85	12.08	10.01
DCMLE/DQ	-31.88	-92.51	-56.77	-42.1
DCY/DY				
DCLLE/DY				
DCNLE/DY				
DCY/DPHI				
DCLLE/DPHI				
DCNLE/DPHI				
DCY/DPSI				
DCLLE/DPSI				
DCNLE/DPSI				
DCY/DV				
DCLLE/DV				
DCNLE/DV				
DCY/DP				
DCLLE/DP				
DCNLE/DP				
DCY/DR				
DCLLE/DR				
DCNLE/DR				

TABLE 3

THIN RECTANGULAR WINGS CONNECTED IN TANDEM IN GROUND EFFECT

SEPARATION BETWEEN WINGS = 4 CHORDS

AR	1.	1.	1.	1.	1.
ANGLE	2.5	2.5	2.5	2.5	2.5
HEIGHT	.05	.1	.125	.15	.5
CDI	.01264	.004672	.003881	.00341	.002094
CL	.4127	.1852	.158	.1412	.09106
CMLE	-.4104	-.1384	-.1125	-.09713	-.0537
XCG					
DCDI/DH	-.6449	-.0421	-.02367	-.01509	-.82E-3
DCL/DH	-15.4	-1.412	-.8302	-.543	-.03344
DCMLE/DH	21.88	1.379	.7646	.4905	.03098
DCDI/DT	2.917	.3552	.2420	.1848	.06756
DCL/DT	56.66	7.725	5.31	4.054	1.523
DCMLE/DT	-267.3	-33.11	-22.39	-16.92	-5.983
DCDI/DW	.5076	.2017	.1691	.1493	.09317
DCL/DW	8.48	4.133	3.547	3.186	2.079
DCMLE/DW	-8.439	-3.139	-2.559	-2.212	-1.229
DCDI/DQ	2.05	.797	.6702	.5944	.3816
DCL/DQ	33.47	15.55	13.35	12.	7.991
DCMLE/DQ	-153.2	-67.05	-56.98	-50.82	-32.7
DCY/DY					
DCLLE/DY					
DCNLE/DY					
DCY/DPHI					
DCLLE/DPHI					
DCNLE/DPHI					
DCY/DPSI					
DCLLE/DPSI					
DCNLE/DPSI					
DCY/DV					
DCLLE/DV					
DCNLE/DV					
DCY/DP					
DCLLE/DP					
DCNLE/DP					
DCY/DR					
DCLLE/DR					
DCNLE/DR					

TABLE 3

THIN RECTANGULAR WINGS CONNECTED IN TANDEM IN GROUND EFFECT

SEPARATION BETWEEN WINGS = 4 CHORDS

AR	1.	2.	2.	2.	2.
ANGLE	2.5	2.5	2.5	2.5	2.5
HEIGHT	50.	.075	.1	.2	.5
CDI	.001859	.01399	.009925	.005785	.003829
CL	.0814	.6238	.4663	.2845	.1881
CMLE	-.04153	-1.013	-.707	-.3854	-.2225
XCG					
DCDI/DH	0.	-.2681	-.1007	-.01788	-.002331
DCL/DH	0.	-9.654	-4.07	-.833	-.1198
DCMLE/DH	0.	19.44	7.571	1.41	.2099
DCDI/DT	.0814	.8189	.397	.1231	.04914
DCL/DT	-.001859	16.58	8.053	2.411	.9323
DCMLE/DT	0.	-97.59	-45.17	-12.22	-4.037
DCDI/DW	.08299	.4825	.3714	.2362	.1633
DCL/DW	1.86	13.05	10.09	6.374	4.284
DCMLE/DW	-.9516	-22.	-15.68	-8.723	-5.079
DCDI/DQ	.3533	1.228	.9455	.6272	.4757
DCL/DQ	7.42	27.77	22.32	15.23	11.4
DCMLE/DQ	-29.66	-151.8	-118.7	-77.11	-54.39
DCY/DY					
DCLLE/DY					
DCNLE/DY					
DCY/DPHI					
DCLLE/DPHI					
DCNLE/DPHI					
DCY/DPSI					
DCLLE/DPSI					
DCNLE/DPSI					
DCY/DV					
DCLLE/DV					
DCNLE/DV					
DCY/DP					
DCLLE/DP					
DCNLE/DP					
DCY/DR					
DCLLE/DR					
DCNLE/DR					

TABLE 3

THIN RECTANGULAR WINGS CONNECTED IN TANDEM IN GROUND EFFECT

SEPARATION BETWEEN WINGS = 4 CHORDS

AR	4.	4.	4.	4.
ANGLE	2.5	2.5	2.5	2.5
HEIGHT	.075	.1	.2	.5
CDI	.01233	.009857	.006609	.0049
CL	1.154	.882	.5341	.3479
CMLE	-2.485	-1.828	-1.026	-.6113
XCG				
DCDI/DH	-.1626	-.07234	-.01636	-.002013
DCL/DH	-15.48	-7.533	-1.594	-.2462
DCMLE/DH	37.97	17.9	3.533	.5657
DCDI/DT	.8436	.441	.1388	.05389
DCL/DT	8.852	4.535	1.188	.3586
DCMLE/DT	-91.03	-45.73	-10.82	-2.421
DCDI/DW	-.06367	.1239	.1967	.1821
DCL/DW	22.07	18.09	11.74	7.87
DCMLE/DW	-48.58	-38.1	-22.73	-13.87
DCDI/DQ	.4423	.4156	.362	.34034
DCL/DQ	19.52	17.93	14.32	11.86
DCMLE/DQ	-154.3	-133.2	-95.32	-70.85
DCY/DY				
DCLLE/DY				
DCNLE/DY				
DCY/DPHI				
DCLLE/DPHI				
DCNLE/DPHI				
DCY/DPSI				
DCLLE/DPSI				
DCNLE/DPSI				
DCY/DV				
DCLLE/DV				
DCNLE/DV				
DCY/DP				
DCLLE/DP				
DCNLE/DP				
DCY/DR				
DCLLE/DR				
DCNLE/DR				

TABLE 4

NON-PLANAR WING IN NON-PLANAR GROUND EFFECT

RECTANGULAR RAIL--WING WITH END PLATES
(ILLUSTRATED IN FIGURE 25,B)

AR	.2564
ANGLE	2.5
HEIGHT	.2123
CDI	.006176
CL	.1147
CMLE	-.02437
XCG	.212
DCDI/DH	-.03517
DCL/DH	-.628
DCMLE/DH	.18
DCDI/DT	.01944
DCL/DT	.1673
DCMLE/DT	-.09327
DCDI/DW	.1287
DCL/DW	1.526
DCMLE/DW	-.3094
DCDI/DQ	.05449
DCL/DQ	.6555
DCMLE/DQ	-.3381
DCY/DY	-.09916
DCLLE/DY	.008515
DCNLE/DY	.05774
DCY/DPHI	.02633
DCLLE/DPHI	-.003876
DCNLE/DPHI	-.01129
DCY/DPSI	.1161
DCLLE/DPSI	-.02441
DCNLE/DPSI	-.07429
DCY/DV	-1.415
DCLLE/DV	.165
DCNLE/DV	.3709
DCY/DP	.08047
DCLLE/DP	-.01282
DCNLE/DP	-.01577
DCY/DR	.3587
DCLLE/DR	-.04397
DCNLE/DR	-.2029

TABLE 5

NON-PLANAR WING IN NON-PLANAR GROUND EFFECT

RECTANGULAR RAIL--WING WITH END PLATES
(ILLUSTRATED IN FIGURE 25,B)

```
AR             .2564
ANGLE          5.
HEIGHT         .2452
CDI            .01464
CL             .2042
CMLE           -.04501
XCG            .2191
DCDI/DH        -.07478
DCL/DH         -.9769
DCMLE/DH       .3332
DCDI/DT        .06363
DCL/DT         .1742
DCMLE/DT       -.111
DCDI/DW        .204
DCL/DW         1.693
DCMLE/DW       -.3821
DCDI/DQ        .09632
DCL/DQ         .7523
DCMLE/DQ       -.3859
DCY/DY         -.1516
DCLLE/DY       .01603
DCNLE/DY       .07737
DCY/DPHI       .03889
DCLLE/DPHI     -.006999
DCNLE/DPHI     -.01745
DCY/DPSI       .1308
DCLLE/DPSI     -.03668
DCNLE/DPSI     -.09398
DCY/DV         -1.861
DCLLE/DV       .2457
DCNLE/DV       .5024
DCY/DP         .1134
DCLLE/DP       -.02114
DCNLE/DP       -.02209
DCY/DR         .3741
DCLLE/DR       -.06054
DCNLE/DR       -.2101
```

TABLE 6

NON-PLANAR WING IN NON-PLANAR GROUND EFFECT

RECTANGULAR CHANNEL--WING WITH END PLATES
(ILLUSTRATED IN FIGURE 25,C)

AR	.2936
ANGLE	2.5
HEIGHT	.1327
CDI	.001747
CL	.08862
CMLE	-.03245
XCG	.3658
DCDI/DH	-.002338
DCL/DH	-.1312
DCMLE/DH	.06355
DCDI/DT	.03569
DCL/DT	.4405
DCMLE/DT	-.2019
DCDI/DW	.04464
DCL/DW	1.455
DCMLE/DW	-.5117
DCDI/DQ	.002214
DCL/DQ	.6827
DCMLE/DQ	-.4611
DCY/DY	-.05375
DCLLE/DY	-.005647
DCNLE/DY	.03081
DCY/DPHI	-.007995
DCLLE/DPHI	-.000376
DCNLE/DPHI	.004208
DCY/DPSI	.198
DCLLE/DPSI	.03428
DCNLE/DPSI	-.1115
DCY/DV	-.8762
DCLLE/DV	-.07689
DCNLE/DV	.3999
DCY/DP	-.05897
DCLLE/DP	-.007915
DCNLE/DP	.02434
DCY/DR	.284
DCLLE/DR	.02363
DCNLE/DR	-.2041